TWO-DIMENSIONAL VISCOUS FLOWS WITH LARGE DISTRIBUTED SURFACE INJECTION

Part I. Boundary Layer Flows with Large Injection and Heat Transfer

Part II. Experiments in Supersonic Turbulent Flow with Large Distributed Surface Injection

Part III. The Effect of Finite Plate Length

Thesis by

Fernando Lawrence Fernandez

In Partial Fulfillment of the Requirements

For the Degree of

Doctor of Philosophy

California Institute of Technology

Pasadena, California

1969

(Submitted September 4, 1968)

ACKNOWLEDGEMENTS

Beyond the appreciation due to the members of the GALCIT faculty and staff whose continuing effort underlies every research project, the author is particularly grateful to:

the Aerospace Corporation who, through the Aerospace fellowship program, provided financial support for the author's graduate studies;

the U. S. Army Research Office and the Advanced Research Projects Agency, Contract DA-31-124-ARO(D)-33 for their sponsorship;

the staff of the Aeronautics machine shop and especially Messrs. G. Carlson and E. Dahl for their skill and suggestions in constructing the experimental equipment;

Messrs. S. Roman, J. Van Dijk and P. Baloga for their assistance and guidance in conducting the wind tunnel tests;

Mrs. Truus van Harreveld for her care in the numerical computations;

Mrs. B. Wood, Mrs. Jewel Colbert, Miss J. Greene and Mr. G. van Halewyn for their aid in the preparation of the illustrations presented herein;

Mrs. Elizabeth Fox and Mrs. Virginia Conner for their excellent typing of the manuscript;

Professor Anatol Roshko for his very helpful suggestions in the preparation of this manuscript;

Professors Toshi Kubota, Edward Zukoski, Donald Coles and Wilhelm Behrens for their invaluable guidance in the performance of this research; and to

Professor Lester Lees who, throughout the course of my graduate education, has provided the interest, inspiration and guidance essential to the completion of this research.

With the recognition that their inspiration and perseverance were fundamentally associated with its inception and completion, this work is dedicated to my wife, Carmen, and my children, Lisa and Chris.

ABSTRACT

This report is concerned primarily with the effect of surface injection on viscous two-dimensional flows. More precisely, the investigation centers on surface injection rates where the wall shear has been considerably reduced below the no-injection value, but where the momentum of the injectant is still negligible compared to that in the free stream. Three separate problems are investigated to try to obtain an understanding of the physical mechanisms which control the flow.

For the case of laminar boundary-layer flow, asymptotic solutions are obtained for large injection and heat transfer. It is found in this case that the boundary layer may be divided into two regions: (1) an inner region adjacent to the surface where viscous mixing plays a minor role; (2) a viscous layer where the transition occurs from the inner solution to the inviscid flow outside the boundary layer. In the case of the insulated wall the viscous layer contributes only small corrections to the boundary-layer properties. For the highly-cooled wall the boundary layer is strongly influenced by the viscous mixing between the inviscid outer flow and the high density low-speed gas adjacent to the wall.

For turbulent flow, experiments with constant distributed surface injection at $M_\infty = 2.6$ have been performed. These show that large injection leads to a constant pressure self-similar flow with linear growth. The experimental results are shown to be in good agreement with low Mach number experiments when the normal coordinate is stretched by using a Howarth-Dorodnitsyn transformation

at the same value of the ratio of wall mass flow per unit area to that in the free stream.

Finally, the third part considers the upstream effect of the termination of injection on the flow in the "blown" layer. An analysis, using an integral approach is presented which agrees with the experimentally observed effects. In particular, as injection rates approaching the maximum value which can be entrained by a constant pressure mixing layer are approached, the analysis predicts that virtually the entire porous region experiences a falling pressure. It is postulated that this effect provides for a smooth transition from a boundary-layer flow to one where mixing is negligible, except in a thin layer near the streamline which divides the injected and free-stream gas. Therefore, the analysis provides the step which gives a quantitative estimate for the range of injection rates in turbulent flow where the effect of mixing can be neglected and inviscid flow models utilized.

TABLE OF CONTENTS

TABLE OF CONTENTS (Cont'd)

TABLE OF CONTENTS (Cont'd)

PART I. BOUNDARY LAYER FLOWS WITH LARGE INJECTION AND HEAT TRANSFER*

*This work has been published with Professor T. Kubota of GALCIT in the AIAA Journal, vol. 6, #1, pp. 22-28, January 1968.

List of Tables - Part I

List of Figures - Part I

List of Symbols - Part I

C_p specific heat of gas at constant pressure

f_η u/u_e, dimensionless velocity in boundary layer

$f(\eta)$ stream function defined by $\psi = f(\eta)\sqrt{2\tilde{s}}$, where ψ satisfies boundary-layer continuity equations

f_w injection rate at surface $= -f(0) = \dfrac{\rho_w v_w}{\rho_e u_e \mu_e}\sqrt{2\tilde{s}}$

$\tilde{f}$ inner variable $= f/f_w$

f^* intermediate variable $= \tilde{f}/\nu(\epsilon)$

g $\dfrac{h_o}{h_{oe}}$, dimensionless enthalpy in boundary layer

$\tilde{g}_1, \tilde{g}_2, \ldots$ enthalpy functions in inner expansion for g

G_0, G_1 enthalpy functions in transition expansion for g

g_w dimensionless wall enthalpy $= \left(\dfrac{h_o}{h_{oe}}\right)_{y=\infty}$

h_o total enthalpy $= C_p T + \dfrac{u^2}{2}$

h_{oe} total freestream enthalpy $= C_p T_e + \dfrac{U_e^2}{2}$

H $\dfrac{\delta^*}{\theta}$, ratio of displacement thickness to momentum thickness

k thermal conductivity of gas

M_e Mach number at edge of boundary layer

Pr $\dfrac{\mu C_p}{k}$, Prandtl number

$\tilde{s}$ $\displaystyle\int_0^x \rho_e u_e \mu_e dx$, transformed distance along body

T static temperature

u velocity component parallel to body in boundary layer

u_e velocity component parallel to body at edge of boundary layer

$D_n(Z)$ parabolic cylinder functions

v velocity component perpendicular to body surface in boundary layer

x distance measured along body surface

y distance normal to body surface

Z $(\frac{u}{u_e})^2$

Z_0, Z_1 velocity functions in transition expansion for Z

$\tilde{Z}_0, \tilde{Z}_1$ velocity functions in inner expansion for Z

β pressure gradient parameter, $\frac{2\tilde{s}}{M_e} \frac{dM_e}{d\tilde{s}}$

δ^* $\int_0^\infty (1 - \frac{u}{u_e})\, d\eta$-displacement thickness

ϵ $\frac{1}{f_w^2}$

η $\frac{\rho_e u_e}{(2\tilde{s})^{\frac{1}{2}}} \int_0^y \frac{\rho}{\rho_e}\, dy$-transformed y-variable

ρ gas density

σ $\int_0^\infty (1-g)\, d\eta$-energy thickness

θ $\int_0^\infty \frac{u}{u_e} (1 - \frac{u}{u_e})\, d\eta$-momentum thickness

μ viscosity

ν gauge function; $\sqrt{\epsilon} \ll \nu \ll 1$

ξ $\frac{f}{g_w^{\frac{1}{4}}}$

Subscripts

e edge of boundary layer

w wall, $y = 0$

I. 1 Introduction

This first part concerns itself with the solution of a model equation in laminar flow. Although the conditions required for the flow to satisfy this equation are of doubtful practical interest, the trends observed in the solution can be used to provide insight into the manner in which viscous flows adjust to increasing injection rates.

The effect of large* mass injection rates on the incompressible similar laminar boundary layer with favorable pressure gradient has been examined by Pretsch[1] and, more recently, by Aroesty and Cole[2]. However, since in most circumstances the boundary layer with large injection will be characterized by large normal temperature gradients, the effect of compressibility and heat transfer warrant attention.

The simplest extension of the incompressible analysis can be obtained by assuming Pr = 1 and $\mu \sim T$. In this case, as shown by Lees[3] and Cohen and Reshotko[4], the boundary-layer equations can be reduced to an equivalent incompressible form. These are

$$f_{\eta\eta\eta} + f f_{\eta\eta} + \beta(g - f_{\eta}^2) = 0 \qquad \text{(I. 1)}$$

$$g_{\eta\eta} + f g_{\eta} = 0 \qquad \text{(I. 2)}$$

with boundary conditions: $f_{\eta}(0) = 0$; $g(0) = g_w$; $f(0) = -f_w$; $f_{\eta}(\infty) = g(\infty) = 1$ where

$$g = h_o / h_{oe}$$

---

*"Large", of course, assumes that boundary-layer theory is still valid.

$$
\begin{aligned}
f_\eta &= u/u_e \\
\beta &= \frac{2\tilde{s}}{M_e}\,\frac{dM_e}{d\tilde{s}} \\
\eta &= \frac{\rho_e u_e}{(2\tilde{s})^{\frac{1}{2}}}\int_o^y \frac{\rho}{\rho_e}\,dy \\
\tilde{s} &= \int_o^x \rho_e u_e \mu_e dx
\end{aligned}
\qquad \text{(I. 3)}
$$

If β *and* f_w *are constants, then these equations are ordinary, though* nonlinear.

A direct numerical integration of these equations for large f_w is quite difficult, even with the use of high-speed digital computers. In fact, beyond f_w of about 4. 0 most numerical methods commonly used for solving boundary-value problems of this type completely break down. Numerical computations carried out by Libby[5] have clearly indicated this difficulty.

This section presents an approximate solution to the equations for large f_w using the method of matched asymptotic expansions. Except for the case $g \equiv 1$, the approximate equations still require the use of numerical methods for solution. But, as is shown later in this section, the solutions are much easier to obtain.

Section I. 2 presents the analysis and the resulting approximate equations which are obtained. In Section I. 3, some comparison with "exact" computer solutions are shown which indicate the asymptotic solution is valid within a few percent for f_w as low as 2. 0. Some of the numerical results obtained are also presented, which show the effect of heat transfer. In Section I. 4, approximate

algebraic formulae for the displacement, momentum and energy thicknesses are presented which should be accurate for $f_w >> 2.0$. In Appendices I. A and I. B, the numerical technique used in the computations is discussed, since a somewhat different, iterative approach has been used.

I. 2 Derivation of Equations

Following Aroesty and Cole[2], it is convenient to work in variables defined by

$$Z \equiv (f_\eta)^2; \quad f \equiv f \tag{I. 4}$$

Equations (I. 1) and (I. 2) then become

$$\sqrt{Z}\,\frac{d^2Z}{df^2} + f\frac{dZ}{df} + 2\beta[g-Z] = 0 \tag{I. 5}$$

$$\frac{d}{df}\left[\sqrt{Z}\,\frac{dg}{df}\right] + f\frac{dg}{df} = 0 \tag{I. 6}$$

with boundary conditions

$$\begin{aligned} &Z = 0, \quad f = -f_w \\ &Z = 1, \quad f \to +\infty \\ &g = g_w, \quad f = -f_w \\ &g = 1, \quad f \to +\infty \end{aligned} \tag{I. 7}$$

For the inner region, near the wall, a new independent variable, $\tilde{f} = \frac{f}{f_w} = \sqrt{\epsilon}\, f$ is introduced. Then, Equations (I. 5) and (I. 6) become

$$\epsilon\sqrt{Z}\,\frac{d^2Z}{d\tilde{f}^2} + \tilde{f}\frac{dZ}{d\tilde{f}} + 2\beta[g-Z] = 0 \tag{I. 8}$$

$$\epsilon \frac{d}{d\tilde{f}} \left[\sqrt{Z} \frac{dg}{df} \right] + \tilde{f} \frac{dg}{d\tilde{f}} = 0 \qquad \text{(I. 9)}$$

with boundary conditions

$$\tilde{f} = -1 \left\{ \begin{matrix} Z = 0 \\ g = g_w \end{matrix} \right\} ; \quad \tilde{f} \to \infty \left\{ \begin{matrix} g = 1 \\ Z = 1 \end{matrix} \right\} \qquad \text{(I. 10)}$$

Now, consider an "inner" (wall) solution that is valid for fixed $\tilde{f}$ and $\epsilon \to 0$. Expand Z and g as

$$\begin{aligned} Z(f;\epsilon) &= \tilde{Z}_0(\tilde{f}) + \epsilon \tilde{Z}_1(\tilde{f}) + \epsilon^2 \tilde{Z}_2(\tilde{f}) + \ldots \\ g(f;\epsilon) &= \tilde{g}_0(\tilde{f}) + \epsilon \tilde{g}_1(\tilde{f}) + \epsilon^2 \tilde{g}_2(\tilde{f}) + \ldots \end{aligned} \qquad \text{(I. 11)}$$

If the series (I. 11) are inserted into (I. 8) and (I. 9), a power series in ϵ is obtained which must vanish identically in ϵ; hence the coefficients of the successive powers of ϵ must vanish. * The coefficients are sets of second order differential equations for $\tilde{Z}_i$ and $\tilde{g}_i$. Up to second order in ϵ, these are:

Zero Order in ϵ

$$\tilde{f} \frac{d\tilde{Z}_0}{d\tilde{f}} + 2\beta \left[\tilde{g}_0 - \tilde{Z}_0 \right] = 0 \qquad \text{(I. 12-a)}$$

$$\tilde{f} \frac{d\tilde{g}_0}{d\tilde{f}} = 0 \qquad \text{(I. 12-b)}$$

Boundary Conditions:

$$\tilde{Z}_0(-1) = 0; \; \tilde{g}_0(-1) = g_w \qquad \text{(I. 12-c)}$$

* β is assumed to be O(1).

First Order in ϵ

$$\tilde{Z}_0^{\frac{1}{2}} \frac{d^2\tilde{Z}_0}{d\tilde{f}^2} + \tilde{f} \frac{d\tilde{Z}_1}{d\tilde{f}} + 2\beta[\tilde{g}_1 - \tilde{Z}_1] = 0 \qquad \text{(I. 13-a)}$$

$$\frac{d}{d\tilde{f}} [\tilde{Z}_0^{\frac{1}{2}} \frac{d\tilde{g}_0}{d\tilde{f}}] + \tilde{f} \frac{d\tilde{g}_1}{d\tilde{f}} = 0 \qquad \text{(I. 13-b)}$$

Boundary Conditions: $\tilde{Z}_1(-1) = \tilde{g}_1(-1) = 0$ (I. 13-c)

Second Order in ϵ

$$\tfrac{1}{2} \frac{\tilde{Z}_1}{\tilde{Z}_0^{\frac{1}{2}}} \frac{d^2\tilde{Z}_0}{d\tilde{f}^2} + \tilde{Z}_0^{\frac{1}{2}} \frac{d^2\tilde{Z}_0}{d\tilde{f}^2} + \tilde{f} \frac{d\tilde{Z}_2}{d\tilde{f}} + 2\beta[\tilde{g}_2 - \tilde{Z}_2] = 0 \qquad \text{(I. 14-a)}$$

$$\frac{d}{d\tilde{f}} [\tilde{Z}_0^{\frac{1}{2}} \frac{d\tilde{g}_1}{d\tilde{f}} + \tfrac{1}{2} \frac{\tilde{Z}_1}{\tilde{Z}_0^{\frac{1}{2}}} \frac{d\tilde{g}_0}{d\tilde{f}}] + \tilde{f} \frac{d\tilde{g}_2}{d\tilde{f}} = 0 \qquad \text{(I. 14-b)}$$

Boundary Conditions:

$$\tilde{Z}_2(-1) = \tilde{g}_2(-1) = 0 \qquad \text{(I. 14-c)}$$

As can be seen from Equations (I. 12, I. 13, I. 14), the expansion near the wall as $\epsilon \to 0$ has resulted in a set of equations one order lower than the original equations, (I. 8, I. 9): hence, the boundary conditions at $\tilde{f} \to +\infty$ are abandoned. An examination of the higher order energy equations and boundary conditions gives, immediately

$$\tilde{g}_0 = g_w = \text{constant}$$
$$\tilde{g}_1 = \tilde{g}_2 = \ldots = \tilde{g}_i = 0 \qquad \text{(I. 15)}$$

That is, to all orders in ϵ, the enthalpy ratio, g, is constant in the

inner solution and equal to g_w.

The solution to the zero order momentum equation, (I. 12-a), with the boundary condition (I. 12-c) is

$$\tilde{Z}_0(\tilde{f}) = g_w[1 - (-\tilde{f})^{2\beta}] \tag{I. 16}$$

The solution of the first order equation, (I. 13-a), with the boundary condition (I. 13-c) yields upon integration

$$\tilde{Z}_1(\tilde{f}) = (-\tilde{f})^{2\beta}\, 2\beta(2\beta-1) g_w^{\frac{3}{2}} \int_1^{-\tilde{f}} \frac{[1-t^{2\beta}]^{\frac{1}{2}}}{t^3}\, dt \tag{I. 17}$$

Although the integral can be expressed in terms of a hypergeometric function, in general, little insight is gained from doing this. An important result which can be obtained from (I. 17) is the behavior of $\tilde{Z}_1$ as $\tilde{f} \to 0^-$. Then,

$$\tilde{Z}_1(\tilde{f}) \sim -\beta(2\beta-1) g_w^{\frac{3}{2}} (-\tilde{f})^{2\beta-2} [1 + 0(-\tilde{f}^{2\beta})] \tag{I. 18}$$
$$\tilde{f} \to 0^-$$

In order to determine the shear at the wall, note that, in the usual boundary-layer variables

$$f_{\eta\eta}\Big)_{\eta=0} = \tfrac{1}{2} \frac{dZ}{df}\Big)_{f=-f_w} \tag{I. 19}$$

Differentiating Equations (I. 16) and (I. 17), or using the differential equations, (I. 12) and (I. 13) themselves, yields

$$f_{\eta\eta}\Big)_{\eta=0} = \frac{\beta g_w}{f_w} + O(\epsilon^2) \tag{I. 20}$$

And, as indicated in Equation (I. 15), to all orders in ϵ;

$$\left.\frac{dg}{df}\right)_{f=-f_w} = \left.\frac{dg}{d\eta}\Big/\frac{df}{d\eta}\right)_{\eta=0} = 0 \qquad \text{(I. 21)}$$

hence $\frac{dg}{d\eta} = 0$ to all order in ϵ. Since within the similar boundary-layer assumption

$$\left.\frac{dg}{d\eta}\right)_{\eta=0} \sim \left.\frac{\partial T}{\partial y}\right)_{y=0} \qquad \text{(I. 22)}$$

One concludes, as was found by Libby[5] that, at least for the case Pr = 1, $\mu \sim T$, for any finite β, the heat transfer goes to zero at the wall for large blowing while the shear is still finite.

Another fact worth noting is a result that can be shown by examination of Equations (I. 13) and (I. 14). If $\beta \equiv \frac{1}{2}$, then the zero-order solution Equation (I. 16) is exact to all orders in ϵ since all higher-order solutions contain the factor $(2\beta-1)$. This case, where Z is linear with $\tilde{f}$ near the wall, corresponds to the case investigated numerically by Libby.[5]

Equations (I. 16) and (I. 18) indicate that the inner solution cannot really be continued past $\tilde{f} = 0$. If $g_w = 1$, the solution to (I. 6) with boundary conditions (I. 7) gives g = 1 everywhere. Then, at $\tilde{f} = 0$ the inner solution gives the correct value of Z at infinity. Hence, for the special case $g_w = 1$, the viscous effect is to smooth the discontinuity in the slope in the (Z-f) plane. However, for $g_w \neq 1$, the inner solution gives $\tilde{Z}_0 = g_w \neq 1$ at $\tilde{f} = 0$, and the discontinuity in Z is smoothed by the viscosity in a thin layer around f = 0 (see Fig. (I. 1)

In order to match the inner solution to the outer, uniform flow solution, a transitional expansion is introduced. For this expansion, the physical variable f is appropriate, because this is the region

where viscous terms and inviscid terms are of the same order. Furthermore, the behavior of the inner solution as $\tilde{f} \to 0^-$ suggests an expansion of the form

$$Z(f;\epsilon) = Z_0(f) + \epsilon^{\beta} Z_1(f) + \ldots$$
$$g(f;\epsilon) = G_0(f) + \epsilon^{\beta} G_1(f) + \ldots \qquad \text{(I. 23)}$$

Substituting (I. 23) into Equations (5) and (6) yields

Zero order

$$Z_0^{\frac{1}{2}} \frac{d^2 Z_0}{df^2} + f \frac{dZ_0}{df} + 2\beta (G_0 - Z_0) = 0 \qquad \text{(I. 24-a)}$$

$$\frac{d}{df}\left[Z_0^{\frac{1}{2}} \frac{dG_0}{df} \right] + f \frac{dG_0}{df} = 0 \qquad \text{(I. 24-b)}$$

Order ϵ^{β}

$$\tfrac{1}{2} Z_1 \frac{d^2 Z_0}{df^2} + Z_0 \frac{d^2 Z_1}{df^2} + Z_0^{\frac{1}{2}} f \frac{dZ_1}{df} + 2\beta Z_0 (G_1 - Z_1) = 0 \qquad \text{(I. 25-a)}$$

$$\frac{d}{df}\left[Z_0^{\frac{1}{2}} \frac{dG_1}{df} + \frac{Z_1}{2 Z_0^{\frac{1}{2}}} \frac{dG_0}{df} \right] + f \frac{dG_1}{df} = 0 \qquad \text{(I. 25-b)}$$

As can be seen, Equations (I. 24) are nonlinear while Equations (I. 25) are linear with variable coefficients. The boundary conditions for these equations must be chosen so that the transition solution matches the outer (uniform flow) solution and the inner (inviscid) solution to some prescribed order in ϵ. Consider, first, the behavior of $f \to +\infty$. In this region it is required that $Z = g = 1$ for all ϵ. This suggests that as $f \to +\infty$, the boundary conditions for (I. 24) are that $Z_0 = G_0 = 1$. With these conditions, an examination of (I. 24) reveals an exponential

decay to the required values. Then, for large positive f, Equations (I. 25) give

$$\frac{d^2Z}{df^2} + f\frac{dZ_1}{df} + 2\beta(G_1 - Z_1) = 0 \qquad \text{(I. 26-a)}$$

$$\frac{d^2G_1}{df^2} + f\frac{dG_1}{df} = 0 \qquad \text{(I. 26-b)}$$

Equation (I. 26-a) has a solution in terms of parabolic cylinder functions. (See, for example, Whittaker and Watson, "Modern Analysis.")

$$Z_1(f) - G_1(f) = \left\{\exp(-f^2/4)\left[c_1 D_{-2\beta-1}(f) + c_2 D_{2\beta}(if)\right]\right\} \qquad \text{(I. 27)}$$

where it is to be noted that $G_1(f) \to 0$ exponentially as $f \to +\infty$.

As $f \to +\infty$

$$D_{-2\beta-1}(f) \sim e^{-f^2/4} f^{-1-2\beta}\left[1 + 0(1/f^2) + \ldots\right] \quad f \to +\infty \qquad \text{(I. 28)}$$

$$D_{2\beta}(if) \sim e^{f^2/4} f^{2\beta}\left[1 + 0(1/f^2)\right] \quad f \to +\infty \qquad \text{(I. 29)}$$

The requirement that $Z_1 \to 0$ as $f \to +\infty$ is satisfied only if $c_2 = 0$ in (I. 27). With $c_2 = 0$, it is seen that as $f \to +\infty$, $Z_1 \to 0$ exponentially. The other boundary conditions on Equations (I. 24) and (I. 25) are determined by requiring that an overlap domain exists where the solutions to (I. 24) and (I. 25) match the inner solution.

In order to determine these boundary conditions, an intermediate variable $f^* = f/\nu(\epsilon)$ is introduced where $\left.\begin{matrix}\nu(\epsilon) \to 0 \\ \nu(\epsilon)/\sqrt{\epsilon} \to \infty\end{matrix}\right\} \epsilon \to 0$. Then, the matching condition requires that the $\lim_{\epsilon \to 0}$ (f^* fixed) of the inner and transition solutions match. Note that this limit implies

$\tilde{f} = \nu f^* \to 0^-$ and $f = \dfrac{\nu f^*}{\sqrt{\epsilon}} \to -\infty$ as $\epsilon \to 0$ for negative f^*. Writing the inner solution (Equations I. 16 and I. 18) near $\tilde{f} = 0^-$ in terms of f^*

$$Z(f;\epsilon) \underset{\text{inner}}{\sim} g_w - g_w \nu^{2\beta}(-f^*)^{2\beta} - \frac{1}{f^{*2}}\frac{\epsilon}{\nu^2}\left\{\beta(2\beta-1)g_w^{\frac{3}{2}}(-\nu f^*)^{2\beta}(1+0(-\nu f^*)^{2\beta})\right\} \tag{I. 30-a}$$

$$g(f;\epsilon) \underset{\text{inner}}{\sim} g_w \tag{I. 30-b}$$

On the other hand, the transition solutions become

$$Z_{\text{trans.}} \sim Z_0(\nu f^*/\sqrt{\epsilon}) + \epsilon^\beta Z_1(\nu f^*/\sqrt{\epsilon}) + \ldots \tag{I. 31-a}$$

$$g_{\text{trans.}} \sim G_0(\nu f^*/\sqrt{\epsilon}) + \epsilon^\beta G_1(\nu f^*/\sqrt{\epsilon}) + \ldots \tag{I. 31-b}$$

Hence

$$Z_{\text{trans.}} - Z_{\text{inner}}$$

$$= Z_0(\nu + f^*/\sqrt{\epsilon}) - g_w + \nu^{2\beta}\left[(\sqrt{\epsilon}/\nu)^{2\beta} Z_1(\nu f^*/\sqrt{\epsilon}) + g_w(-f^*)^{2\beta}\right] + O(\epsilon/\nu^2)$$

$$g_{\text{trans.}} - g_{\text{inner}}$$

$$= G_0(\nu f^*/\sqrt{\epsilon}) - g_w + \epsilon^\beta G_1(\nu f^*/\sqrt{\epsilon}) + \ldots$$

Therefore, for matching we must have

$$Z_0(f) = G_0(f) \to g_w$$

$$Z_1(f) \to -g_w(-f)^{2\beta} \qquad \text{as } f \to -\infty \tag{I. 32}$$

$$G_1(f) \to 0$$

That the matching can be accomplished is shown in the following

manner. For large negative f, Equations (I. 25) give, neglecting exponentially small terms

$$\frac{d^2 Z_1}{d\xi^2} + \xi \frac{dZ_1}{d\xi} - 2\beta Z_1 = 0$$

$$\frac{d^2 G_1}{d\xi^2} + \xi \frac{dG_1}{d\xi} = 0 \qquad \text{(I. 33)}$$

where $\xi = f/g_w^{\frac{1}{4}}$

The solution is again given by parabolic cylinder functions

$$\tilde{Z}_1(\xi) = \left\{\exp(-\xi^2/4)\right\} \left[AD_{-2\beta-1}(\xi) + BD_{2\beta}(i\xi)\right] \qquad \text{(I. 34)}$$

Then, from (I. 28) and (I. 29), for large values of ξ

$$\tilde{Z}_1(\xi) \sim B \cdot \xi^{2\beta} = \left(\frac{B}{g_w^{\beta/2}}\right) (-f)^{2\beta} \qquad \text{(I. 35)}$$

which has the required form.

After the transition solution is obtained, the composite solution is constructed by adding the two solutions and subtracting the common part (which is the inner solution in this case). Hence

$$Z(f;\epsilon) = Z_0(f) + (1/f_w)^{2\beta} Z_1(f) \qquad \text{(I. 36)}$$

$$g(f;\epsilon) = G_0(f) + (1/f_w)^{2\beta} G_1(f) \qquad \text{(I. 37)}$$

is a uniformly valid expansion where Z_0, G_0 and Z_1 and G_1 are solutions of Equations (I. 24) and (I. 25) with boundary conditions given by Equation (I. 32).

The effect of heat transfer becomes clear from an examination

of Equations (I. 24). If $g_w \equiv 1$, then a solution to (I. 24-a) and (I. 24-b) satisfying the boundary conditions is $Z_0 = G_0 \equiv 1$. Furthermore, from (I. 25-b) $G_1 \equiv 0$ and the solution to Equation (I. 25-a) is given by parabolic cylinder functions, as shown by Aroesty and Cole[2]. However, if $g_w \neq 1$, then the leading term in the expansion for Z is the solution of nonlinear mixing layer equations (Equations I. 24-a, I. 24-b). Therefore, for the non-adiabatic case, the viscous mixing layer becomes more important.

Since Z_0 represents the solution to the problem of mixing of two parallel streams of different velocity with pressure gradient, β, and does not depend on f_w, these solutions can be tabulated once and for all. Although the governing equation for Z_0 (Equation I. 24-a) is nonlinear and requires numerical integration, it does not possess any singularities and (as will be shown in the next section) the numerical scheme is quite stable. The correction term, Z_1, is the solution to a linear differential equation, and it also can be obtained numerically without any difficulties. An important point which seems worth repeating is that neither Z_0 or Z_1 depend on f_w. The blowing rate enters only as a multiplier in the final solution.

The physical meaning of the solutions Z_0 and Z_1 is clear. Z_0 represents the velocity in the viscous mixing layer. As $g_w \rightarrow 1$, the velocity change across the layer is small. Essentially, this means the flow is turned from the direction normal to the wall primarily by the effect of the pressure gradient. That is, most of the turning occurs prior to mixing. For $g_w << 1$, however, the pressure gradient becomes less important (since the fluid density at the wall

is very high) and it is the mixing of the injected and free stream fluids which accomplishes the main part of the turning. In both cases, Z_1 represents the rounding off of corners in the velocity profiles.

I. 3 Approximate Formulae for Integral Properties

For approximate solutions of non-similar boundary layers with large mass addition at the wall, we may employ the moment integral method which was found successful in separating boundary layers with interaction with supersonic external flow.[18] For that purpose it is useful to have approximate formulae for the integral properties of boundary layer. For $\beta < 1$, this can be done as shown below.

Displacement thickness

$$\delta^* = \int_0^\infty (1-f_\eta)d\eta = \int_{-f_w}^\infty \left(\frac{1}{\sqrt{Z}} - 1\right) df \qquad \text{(I. 38)}$$

Momentum thickness

$$\theta = \int_0^\infty f_\eta(1-f_\eta)d\eta = \int_{-f_w}^\infty (1-\sqrt{Z})\, df \qquad \text{(I. 39)}$$

Total enthalpy thickness

$$\sigma = \int_0^\infty (g-1)d\eta = \int_{-f_w}^\infty (g-1)\frac{df}{\sqrt{Z}} \qquad \text{(I. 40)}$$

When f_w is large, from the asymptotic solution

$$Z \simeq \begin{cases} \tilde{Z}_0(\tilde{f}) = g_w\left[1 - (-f/f_w)^{2\beta}\right] & \text{for } f = O(-f_w) \\ Z_0(f) + (1/f_w)^{2\beta}\, Z_1(f) + \ldots & \text{for } f = O(1) \end{cases}$$

Then it follows that approximations valid uniformly in $-f_w \leq f \leq 0$ for $1/\sqrt{Z}$, $\sqrt{Z}$ and g are given by:

$$\frac{1}{\sqrt{Z}} \simeq \frac{1}{\sqrt{\tilde{Z}_0}} + \frac{1}{\sqrt{Z_0}} - \frac{1}{\sqrt{g_w}} - \frac{1}{2}\left(\frac{1}{f_w}\right)^{2\beta}\left[\frac{Z_1}{Z_0^{\frac{3}{2}}} - \frac{1}{\sqrt{g_w}}(-f)^{2\beta}\right] + \ldots \tag{I. 41}$$

$$\sqrt{Z} \simeq \sqrt{\tilde{Z}_0} + \sqrt{Z_0} - \sqrt{g_w} + \frac{1}{2}\left(\frac{1}{f_w}\right)^{2\beta}\left[\frac{Z_1}{Z_0^{\frac{1}{2}}} - \sqrt{g_w}\,(-f)^{2\beta}\right] + \ldots \tag{I. 42}$$

$$\frac{g}{\sqrt{Z}} \simeq \frac{g_w}{\sqrt{\tilde{Z}_0}} + \frac{G_0}{\sqrt{Z_0}} - \sqrt{g_w} + \left(\frac{1}{f_w}\right)^{2\beta}\left\{\frac{G_1}{\sqrt{Z_0}} - \frac{1}{2}\left[\frac{G_0 Z_1}{Z_0^{\frac{3}{2}}} + \sqrt{g_w}(-f)^{2\beta}\right]\right\} \tag{I. 43}$$

Hence*

$$\delta^* = f_w\delta_0 + \delta_1 - \tfrac{1}{2}\left(\frac{1}{f_w}\right)^{2\beta}\delta_2 + \ldots \tag{I. 44}$$

$$\theta = f_w\theta_0 + \theta_1 - \tfrac{1}{2}\left(\frac{1}{f_w}\right)^{2\beta}\theta_2 + \ldots \tag{I. 45}$$

$$\sigma = f_w\sigma_0 + \sigma_1 + \left(\frac{1}{f_w}\right)^{2\beta}\sigma_2 + \ldots \tag{I. 46}$$

where

$$\delta_0 = \frac{1}{f_w}\int_{-f_w}^{0}\left(\frac{1}{\sqrt{\tilde{Z}_0}} - 1\right)df = -1 + \sqrt{\pi}\,\Gamma\left(\frac{1}{2\beta}\right)\Big/\left[2\beta g_w^{\frac{1}{2}}\,\Gamma\left(\tfrac{1}{2} + \frac{1}{2\beta}\right)\right] \tag{I. 47}$$

$$\delta_1 = \int_{-\infty}^{0}\left(\frac{1}{\sqrt{Z_0}} - \frac{1}{\sqrt{g_w}}\right)df + \int_{0}^{\infty}\left(\frac{1}{\sqrt{Z_0}} - 1\right)df \tag{I. 48}$$

*These expressions are valid if $\beta < 1$. For $\beta > 1$ the last term in these expressions is of higher order than that which would appear due to the next order term in the inner solution $\tilde{Z}_1$. The first two terms in (44-46) are unchanged.

$$\delta_2 = \int_{-\infty}^{0} \left[\frac{Z_1}{Z_0^{\frac{3}{2}}} + \frac{1}{g_w^{\frac{1}{2}}} (-f)^{2\beta} \right] df + \int_0^{\infty} \frac{Z_1}{Z_0^{\frac{3}{2}}} \, df \tag{I. 49}$$

$$\theta_0 = \frac{1}{f_w} \int_{-f_w}^{0} (1-\sqrt{\tilde{Z}_0}) df = 1 - g_w^{\frac{1}{2}} \sqrt{\pi} \; \Gamma(\tfrac{1}{2\beta}) / \left[2(\beta+1) \, \Gamma(\tfrac{1}{2} + \tfrac{1}{2\beta}) \right] \tag{I. 50}$$

$$\theta_1 = - \int_{-\infty}^{0} (\sqrt{Z_0} - \sqrt{g_w}) df + \int_0^{\infty} (1 - \sqrt{Z_0}) \, df \tag{I. 51}$$

$$\theta_2 = \int_{-\infty}^{0} \left[\frac{Z_1}{Z_0^{\frac{1}{2}}} + \sqrt{g_w} \; (-f)^{2\beta} \right] df + \int_0^{\infty} \frac{Z_1}{Z_0^{\frac{1}{2}}} \, df \tag{I. 52}$$

$$\sigma_0 = (g_w - 1) \sqrt{\pi} \; \Gamma(\tfrac{1}{2\beta}) / \left[2\beta g_w^{\frac{1}{2}} \; \Gamma(\tfrac{1}{2} + \tfrac{1}{2\beta}) \right] \tag{I. 53}$$

$$\sigma_1 = \int_{-\infty}^{0} \left(\frac{G_0}{\sqrt{Z_0}} - \sqrt{g_w} \right) df - \int_{-\infty}^{0} \left(\frac{1}{\sqrt{Z_0}} - \frac{1}{\sqrt{g_w}} \right) df + \int_0^{\infty} \frac{(G_0 - 1)}{\sqrt{Z_0}} \, df \tag{I. 54}$$

$$\sigma_2 = \int_{-\infty}^{\infty} \frac{G_1}{\sqrt{Z_0}} \, df - \tfrac{1}{2} \left\{ \int_{-\infty}^{0} \left[\frac{(G_0 - 1) Z_1}{Z_0^{\frac{3}{2}}} + \frac{(g_w - 1)}{\sqrt{g_w}} (-f)^{2\beta} \right] df + \int_0^{\infty} \frac{(G_0 - 1) Z_1}{Z_0^{\frac{3}{2}}} df \right\} \tag{I. 55}$$

The values of δ_i, θ_i and σ_i are given in Table I. 1. It is interesting to consider $\frac{\delta^*}{\theta} = H(\beta, g_w, f_w)$ as $f_w \to \infty$ from Equations (I. 41) and (I. 42).

As $f_w \to \infty$, $\frac{\delta^*}{\theta}$ approaches a constant, $H(\beta, g_w, \infty)$ given by

$$H(\beta, g_w, \infty) = \frac{\left[\frac{\sqrt{\pi}}{2} \frac{\Gamma(\frac{1}{2\beta})}{\Gamma(\frac{\beta+1}{2\beta})} \frac{1}{\beta g_w^{\frac{1}{2}}} - 1 \right]}{\left[1 - \frac{g_w^{\frac{1}{2}}}{\beta+1} \frac{\sqrt{\pi}}{2} \frac{\Gamma(\frac{1}{2\beta})}{\Gamma(\frac{\beta+1}{2\beta})} \right]} \tag{I. 56}$$

For the cold wall, $g_w << 1$ this gives

$$H(\beta, g_w, \infty) \underset{g_w << 1}{\sim} \frac{\sqrt{\pi}}{2} \frac{\Gamma(\frac{1}{2\beta})}{\Gamma(\frac{\beta+1}{2\beta})} \frac{1}{\beta g_w^{\frac{1}{2}}} \left[1 + O(g_w^{\frac{1}{2}})\right] \tag{I. 57}$$

Finally, for $\beta << 1$, this gives to lowest order in β and g_w since as $Z \to \infty$ $\Gamma(Z) \sim \sqrt{2\pi}\ Z^{Z-\frac{1}{2}}\ e^{-Z}$

$$H(\beta, g_w, \infty) \underset{g_w, \beta << 1}{\sim} \sqrt{\frac{\pi}{2\beta g_w}} \tag{I. 58}$$

Numerical calculations indicate that, over the range of β and g_w presented in Table I. 2, Equation (I. 56) is accurate to within $\approx 7\%$ for $f_w > 3.0$. Hence, H becomes independent of f_w quite rapidly and this approximate relation may be useful for large f_w.

I. 4 Accuracy of the Solution

Strictly speaking, the analysis presented in Section (I. 2) is valid only as $f_w \to \infty$. Just how large f_w must be to guarantee an accurate representation of the flow is certainly worth determining. In order to estimate this, solutions obtained from the asymptotic equations were compared with a straightforward integration of Equations (I. 1) and (I. 2). The results are shown in Figs. (I. 1), (I. 2) and (I. 3). For $f_w = 2.0$ the asymptotic solution is already within a few percent of "exact" numerical results.* Hence, for any higher values of f_w, the foregoing analysis is expected to be quite accurate. Since, as mentioned previously, the asymptotic solutions do not depend on f_w

* The straightforward integration was performed with a computer program written by J. Klineberg of GALCIT.

implicitly, then solutions obtained for $f_w = 2.0$ can be used to obtain results for higher f_w. That is, once Z_0 and Z_1 are tabulated for various values of β and g_w, the velocity can be obtained from

$$Z = Z_0 + \left(\frac{1}{f_w}\right)^{2\beta} Z_1$$

$$g = G_0 + \left(\frac{1}{f_w}\right)^{2\beta} G_1$$

for any $f_w > 2.0$ to order $\left(\frac{1}{f_w}\right)^{2\beta}$.

As an example, Figs. (I. 4) and (I. 5) present the functions Z_0, Z_1, G_0, G_1 for various values of β and g_w. In Fig. (I. 6) and Fig. (I. 7) the effect of wall temperature on the velocity and enthalpy profiles for $\beta = 0.1$ and 1.0 is presented. Figs. (I. 8) and (I. 9) present the variation of the values of velocity and total enthalpy along the dividing streamline ($f = 0$) with β and g_w. A remarkable insensitivity to β is observed for $g_w \ll 1$ indicating that a "locally" similar solution may be valid in some cases.

I. 5 Summary

The effect of large mass injection on the compressible similar laminar boundary with favorable pressure gradient has been examined. It is found that for high rates of injection, the boundary layer may be divided into two regions: (1) an inner region adjacent to the surface where the viscosity plays a minor role; (2) the viscous layer where the transition occurs from the inner layer to the inviscid flow outside the boundary layer. Matched asymptotic expansions appropriate for large injection rates have been constructed for each layer and a uniformly valid solution has been obtained. In the case of the insulated

wall, it turns out that the viscous outer layer contributes only small corrections to properties of the boundary layer. In the case of the highly-cooled wall, on the other hand, the boundary layer is dominated by the viscous mixing between the inviscid outer flow and the high density, low-speed gas adjacent to the wall. Simple expressions for heat transfer rates, skin friction and approximations for integral properties of the boundary layer have been derived, which are useful in future application in non-similar boundary-layer calculations.

TABLE I.1

Integral Functions from Asymptotic Solutions for δ^*, θ, σ

g_w	β	δ_1	δ_2	θ_1	θ_2	σ_1	σ_2
.200	0.100	-.454	1.022	-.001	-.022	.624	.548
	.200	-.481	.860	-.013	-.039	.638	.472
	.300	-.500	.726	-.022	-.055	.649	.413
	.400	-.516	.609	-.028	-.073	.659	.362
	.500	-.528	.509	-.034	-.089	.664	.315
	.600	-.538	.403	-.039	-.108	.669	.281
	.700	-.547	.303	-.042	-.129	.674	.239
	.800	-.554	.204	-.046	-.150	.678	.208
	.900	-.560	.096	-.048	-.175	.681	.166
	1.000	-.565		-.051		.684	
	1.500	-.584		-.059		.695	
	2.000	-.596		-.064		.701	
.400	.100	-.118	.433	.007	-.044	.180	.265
	.200	-.125	.318	.002	-.075	.183	.222
	.300	-.131	.216	-.001	-.105	.185	.188
	.400	-.135	.123	-.004	-.138	.186	.158
	.500	-.139	.038	-.006	-.168	.187	.133
	.600	-.142	-.056	-.008	-.205	.188	.108
	.700	-.144	-.151	-.010	-.244	.189	.081
	.800	-.146	-.251	-.011	-.287	.190	.059
	.900	-.148	-.361	-.012	-.335	.191	.032
	1.000	-.150		-.013		.192	
	1.500	-.155		-.017		.193	
	2.000	-.159		-.019		.194	
.600	.100	-.026	.146	.010	-.078	.041	.132
	.200	-.028	.050	.008	-.126	.041	.107
	.300	-.030	-.040	.007	-.172	.041	.088
	.400	-.031	-.124	.006	-.218	.042	.070
	.500	-.032	-.208	.005	-.267	.042	.054
	.600	-.033	-.299	.005	-.321	.042	.039
	.700	-.034	-.395	.004	-.380	.042	.022
	.800	-.034	-.498	.004	-.444	.042	.008
	.900	-.035	-.612	.003	-.517	.042	-.011
	1.000	-.035		.003		.042	
	1.500	-.037		.002		.043	
	2.000	-.038		.001		.043	
.800	.100	-.002	-.031	.004	-.118	.001	.053
	.200	-.002	-.118	.004	-.181	.001	.044
	.300	-.002	-.200	.004	-.243	.001	.034
	.400	-.002	-.281	.003	-.305	.001	.025

TABLE I.1 (Cont'd)

g_w	β	δ_1	δ_2	θ_1	θ_2	σ_1	σ_2
	.500	-.002	-.361	.003	-.369	.001	.029
	.600	-.002	-.453	.003	-.442	.001	.011
	.700	-.002	-.549	.003	-.520	.001	.003
	.800	-.002	-.654	.003	-.607	.001	-.005
	.900	-.002	-.772	.003	-.702	.001	-.013
	1.000	-.002		.003		.001	
	1.500	-.002		.003		.001	
	2.000	-.002		.003		.001	
1.000	.100	0	-.164	0	-.164	0	0
	.200	0	-.239	0	-.239	0	0
	.300	0	-.319	0	-.319	0	0
	.400	0	-.397	0	-.397	0	0
	.500	0	-.476	0	-.476	0	0
	.600	0	-.567	0	-.567	0	0
	.700	0	-.664	0	-.664	0	0
	.800	0	-.771	0	-.771	0	0
	.900	0	-.891	0	-.891	0	0
	1.000	0		0		0	0
	1.500	0		0		0	0
	2.000	0		0		0	0

TABLE I.2

Comparison of Computer Values of $H(\beta, g_w, \delta_w)$ with $H(\beta, g_w, \infty)$ for $\delta_w = 3.0$

f_w	g_w	β	$H = \frac{\delta^*}{\theta}$	$H(\beta, g_w, \infty)$ [Eqn. (I.56)]	% Error = $\frac{H(\infty) - H}{H}$
		0.200	6.66	7.154	7.4%
	0.200	0.600	4.41	4.617	4.1
		1.000	3.72	3.874	4.0
		2.000	3.05	3.174	3.9
3.0		0.200	4.24	4.521	6.6
	0.600	0.600	3.00	3.074	2.3
		1.000	2.61	2.625	0.4
		2.000	2.19	2.148	1.8
		0.200	3.55	3.818	7.6
	1.000	0.600	2.75	2.884	4.7
		1.000	2.54	2.660	2.4
		2.000	2.34	2.496	6.8

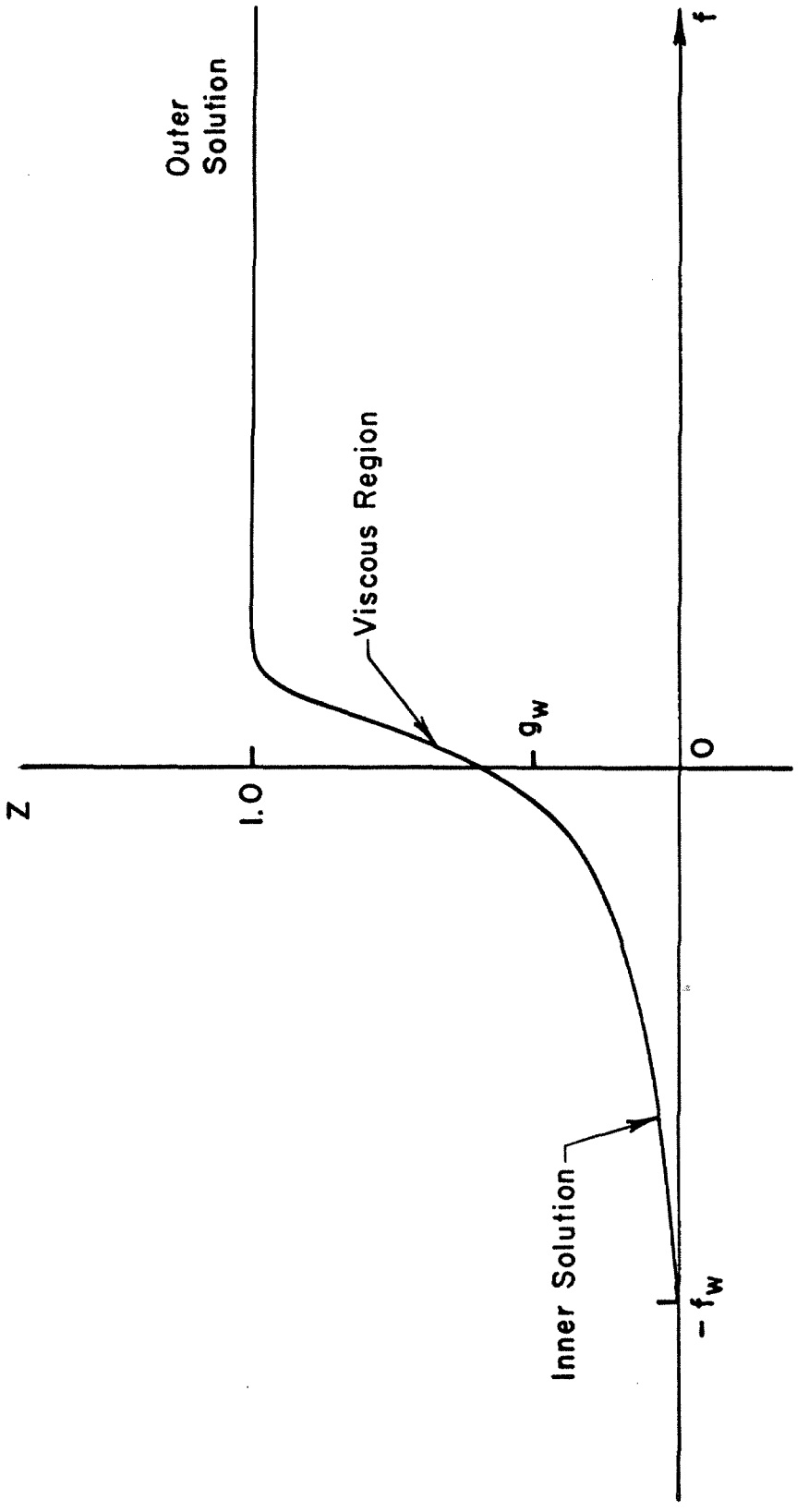

FIG.I.I SKETCH OF INNER AND OUTER SOLUTIONS

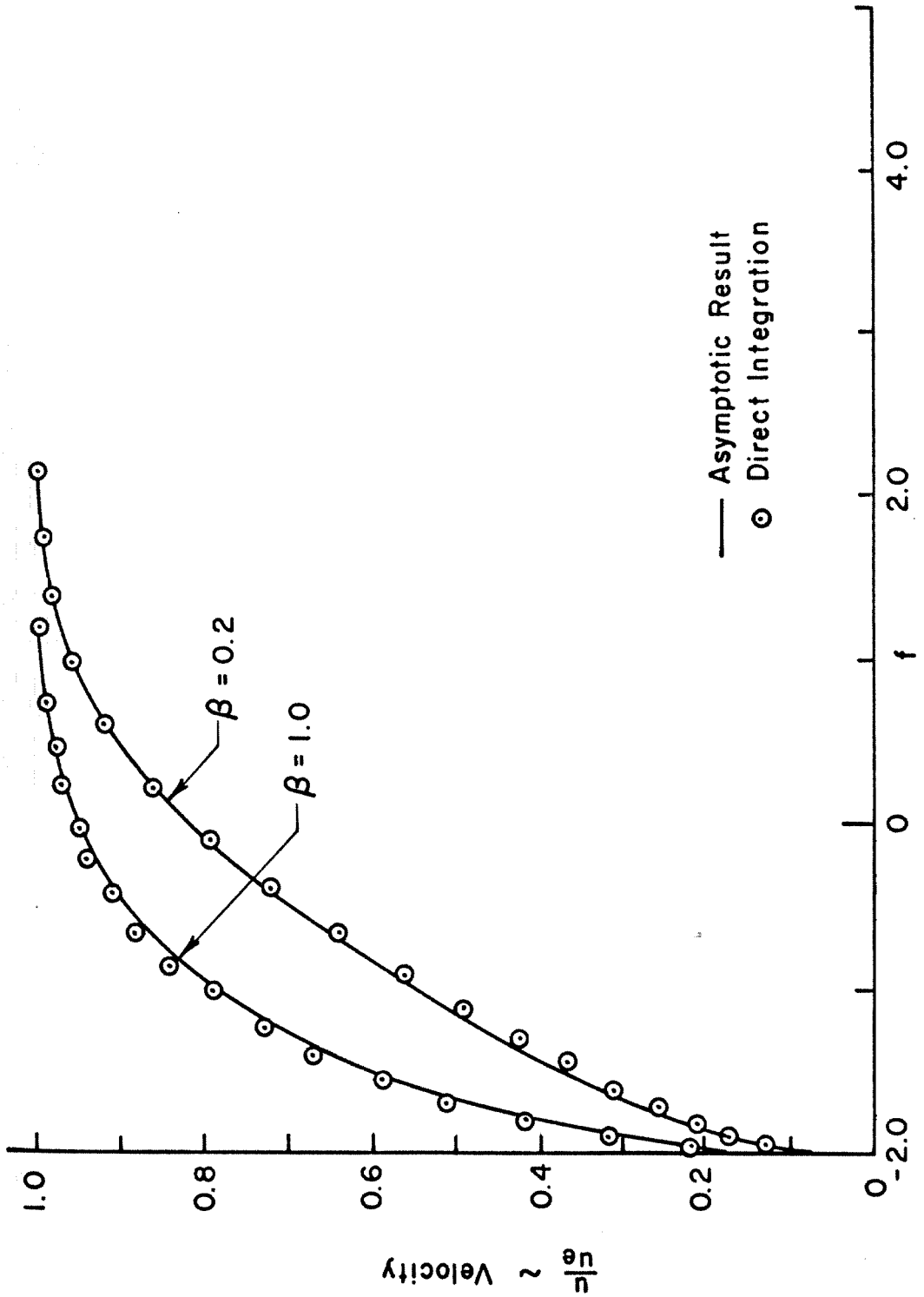

FIG.I.2 COMPARISON OF ASYMPTOTIC SOLUTION WITH EXACT RESULT
$g_w = 1.0$; $f_w = 2.0$

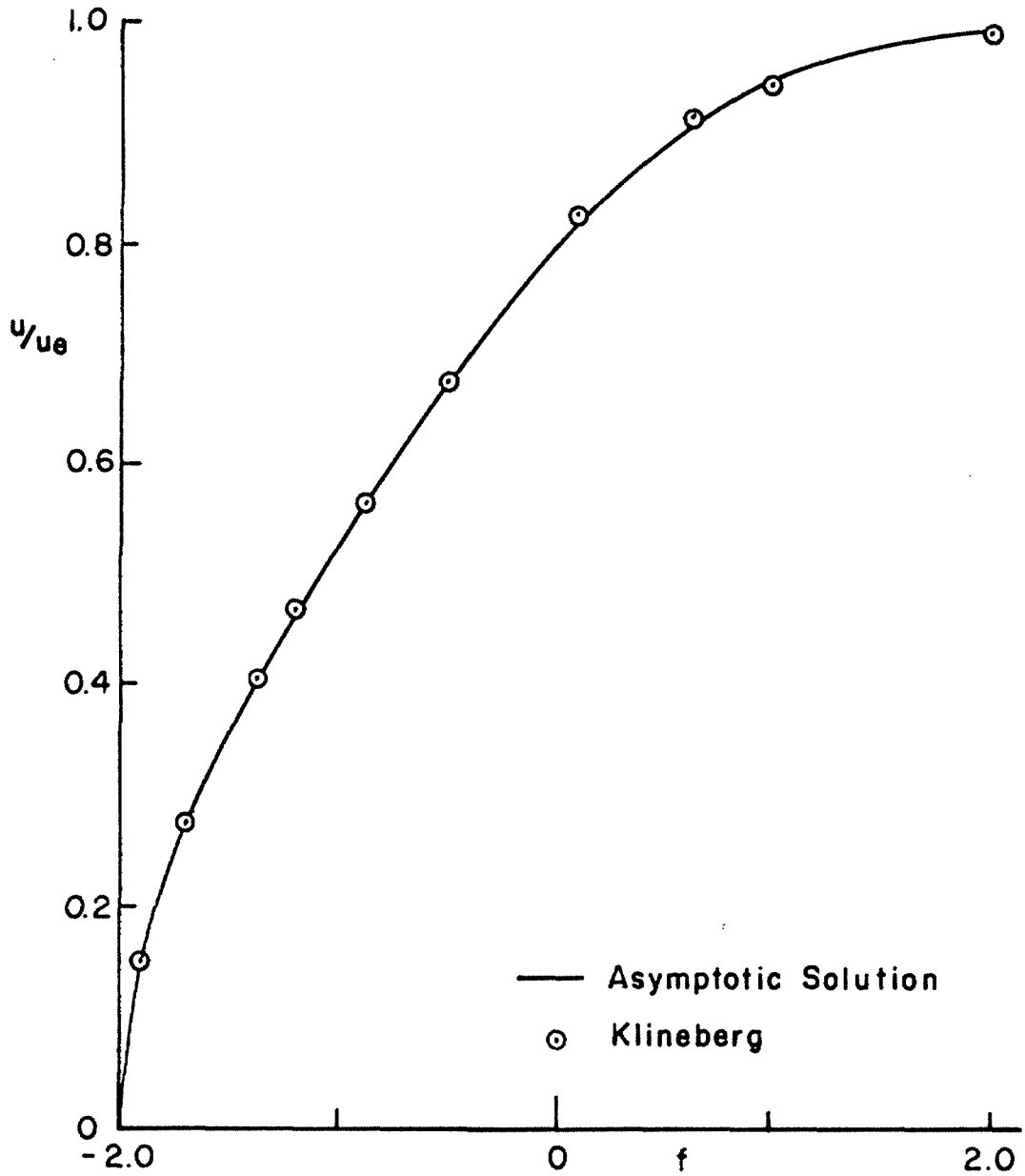

FIG.I.3 COMPARISON OF "EXACT" AND ASYMPTOTIC SOLUTIONS $f_w = 2.0$ $g_w = 0.5$ $\beta = 0.5$

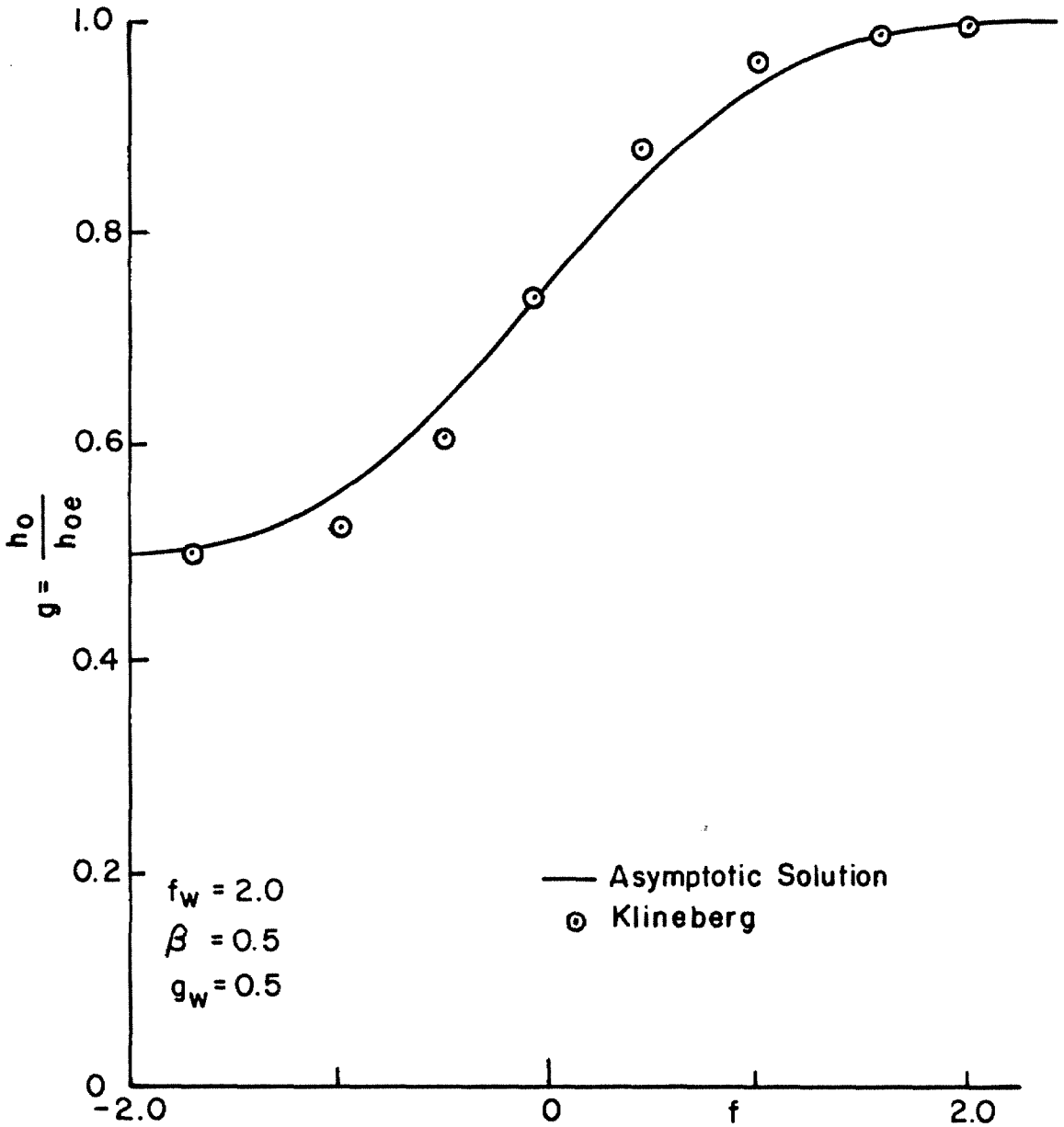

FIG. I.4 COMPARISON OF EXACT AND ASYMPTOTIC SOLUTIONS

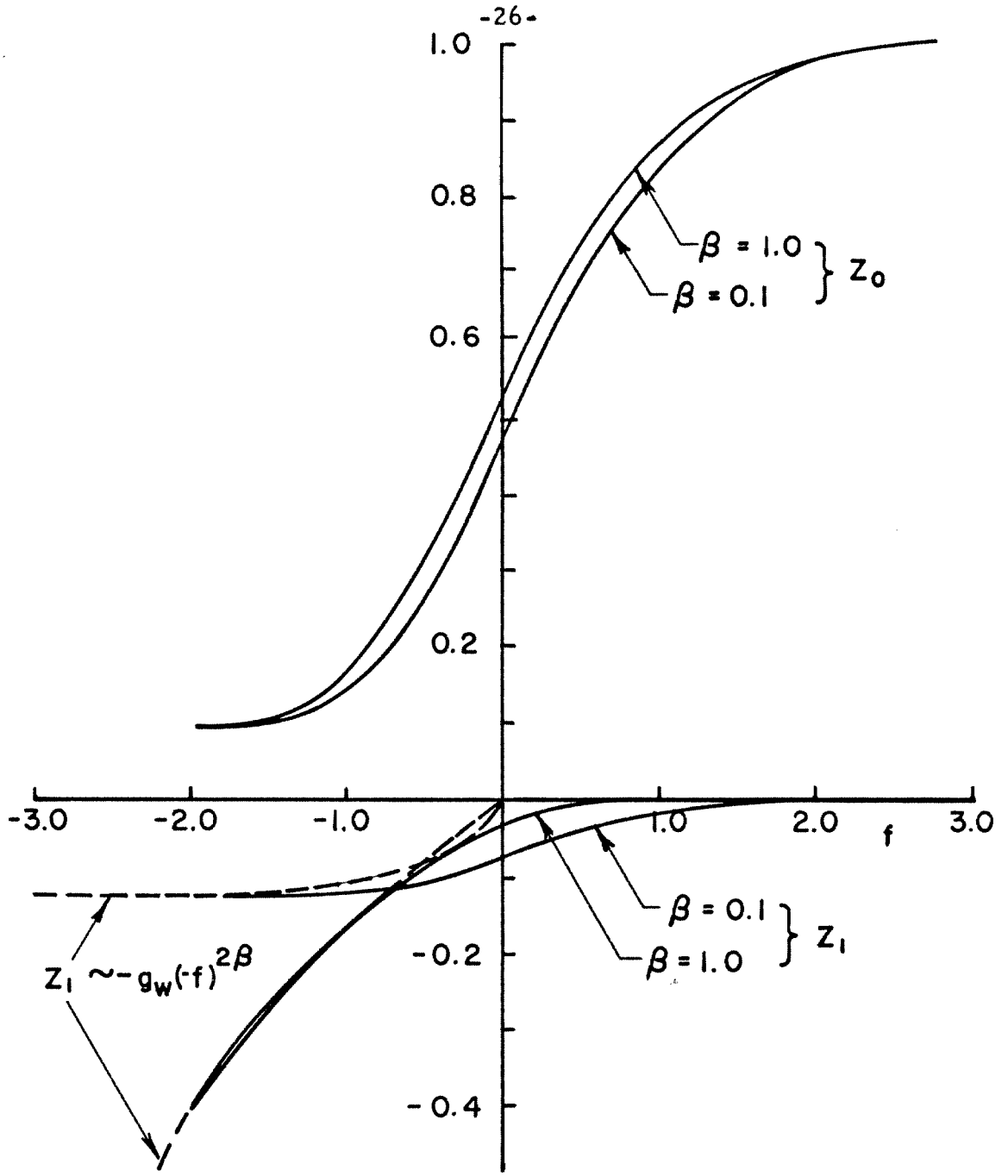

FIG. I.5 VELOCITY FUNCTIONS IN ASYMPTOTIC EXPANSION
Z_0 and Z_1 $g_w = 0.1$

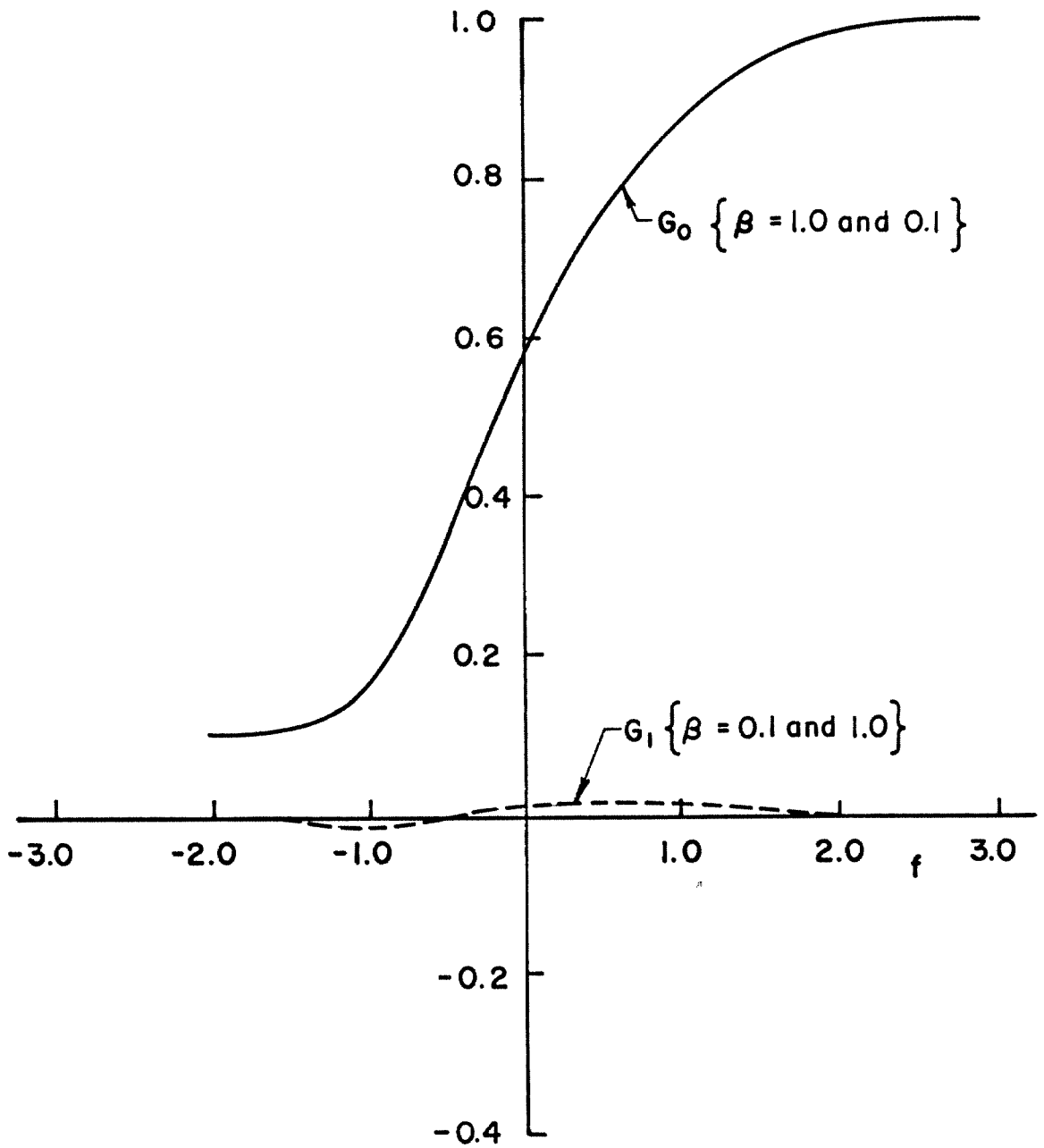

FIG. I.6 ENTHALPY FUNCTIONS IN ASYMPTOTIC EXPANSION $g_w = 0.1$

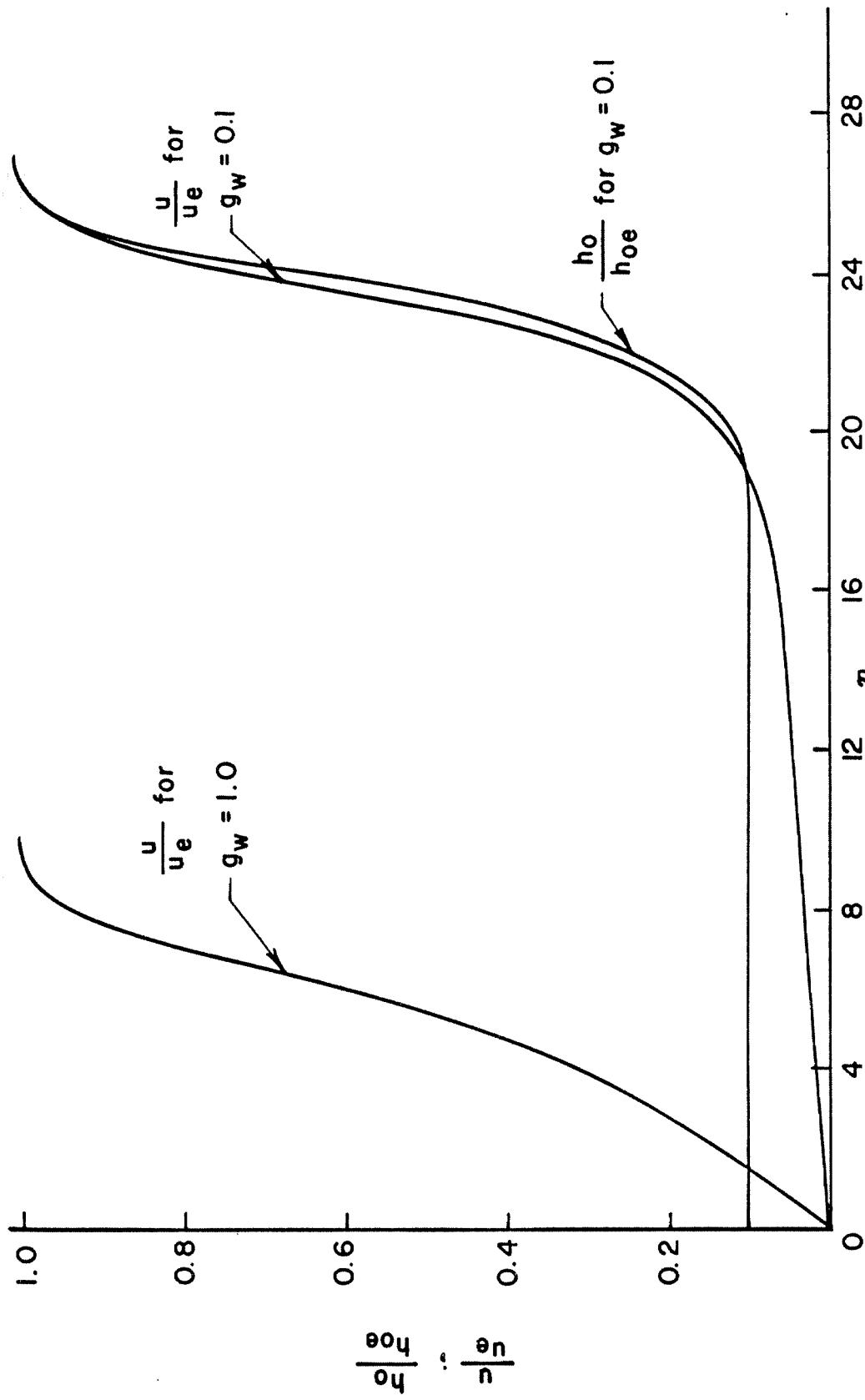

FIG.I.7 WALL COOLING EFFECT $f_w = 2.0$ $\beta = 0.1$

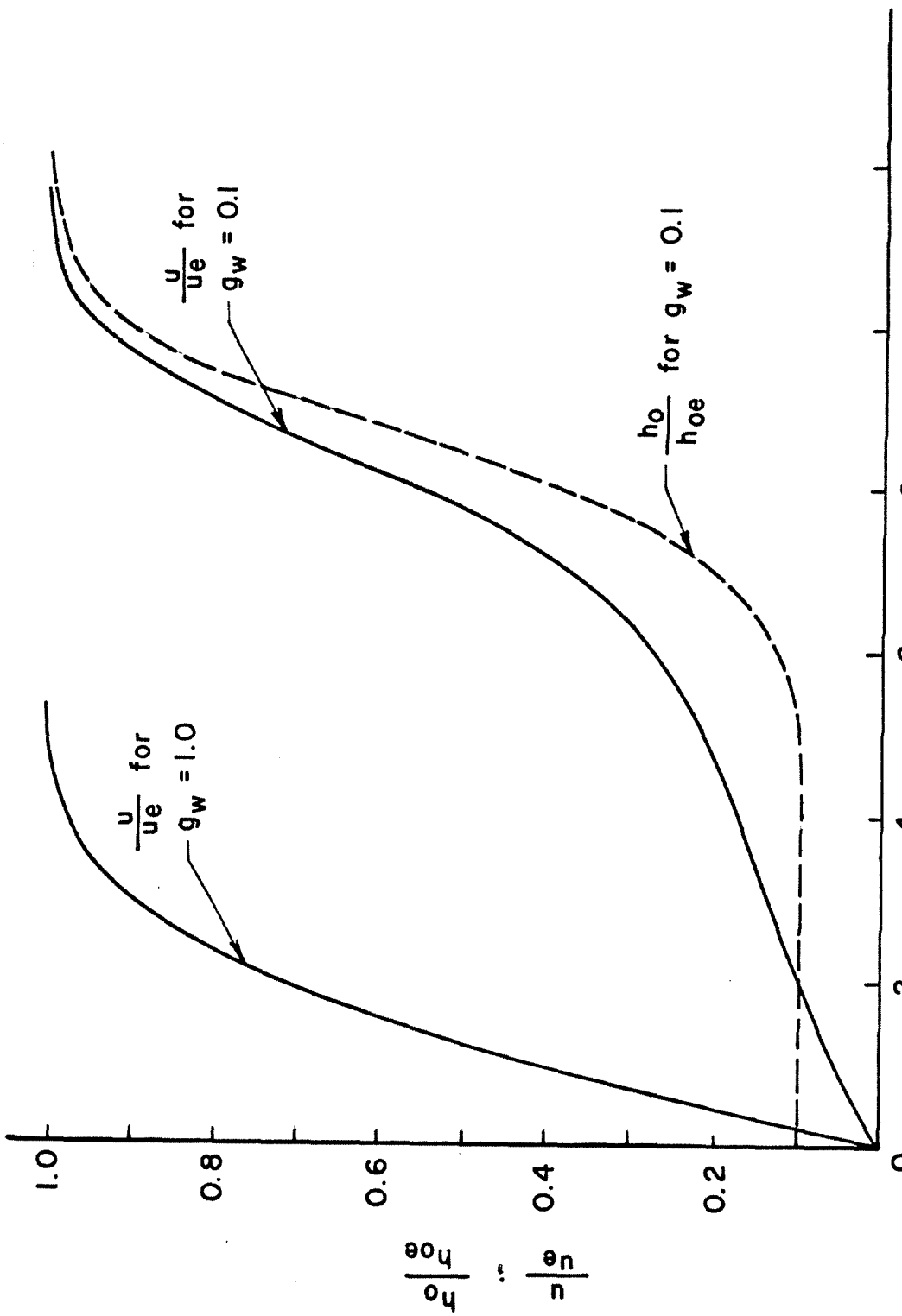

FIG.I.8 WALL COOLING EFFECT $f_w = 2.0$ $\beta = 1.0$

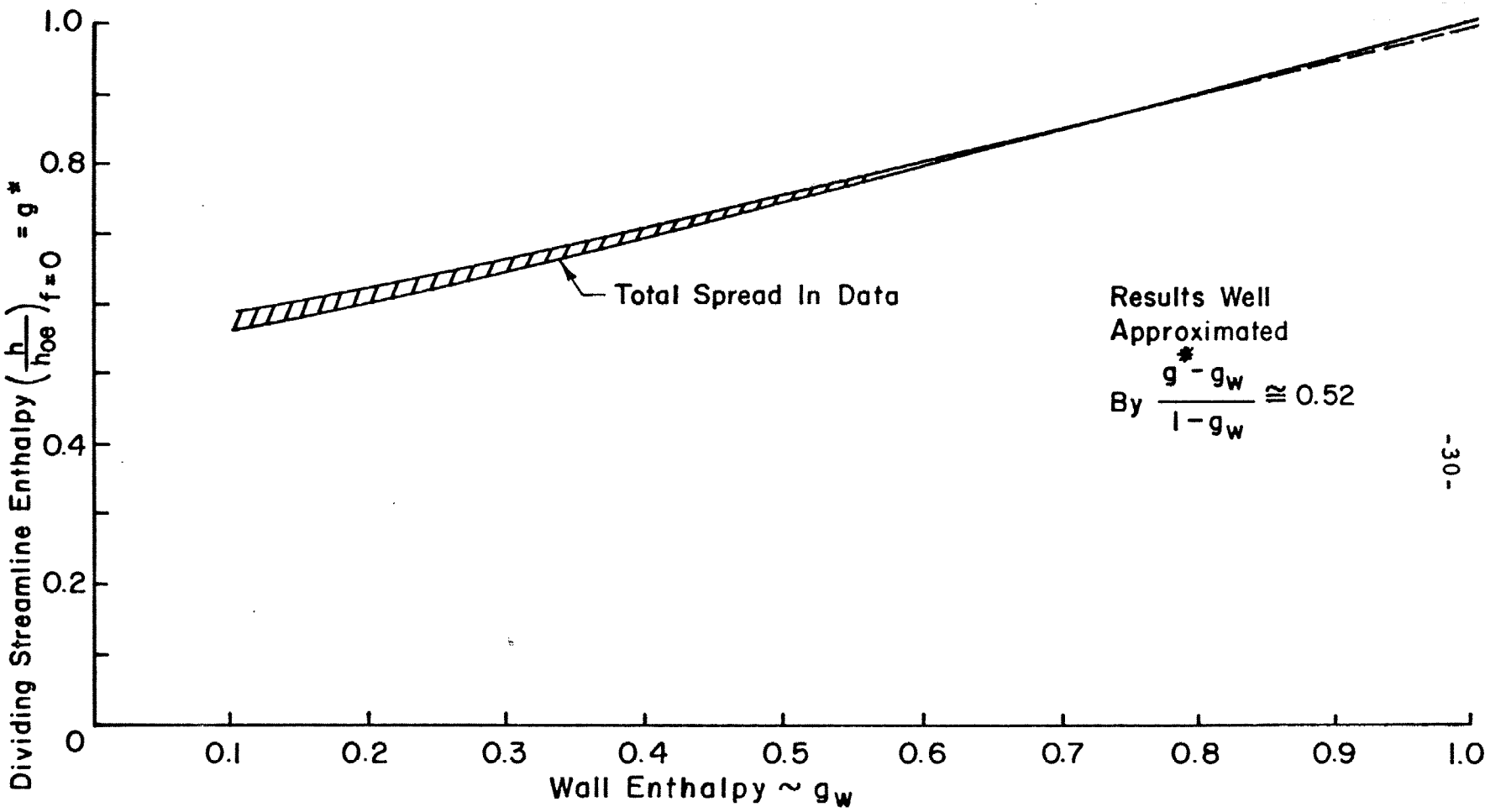

FIG. I.9 EFFECT OF INJECTION AND PRESSURE GRADIENT ON DIVIDING STREAMLINE ENTHALPY $2.0 < f_w < \infty$ (MIXING LAYER SOLUTION) $0.1 < \beta < 2.0$

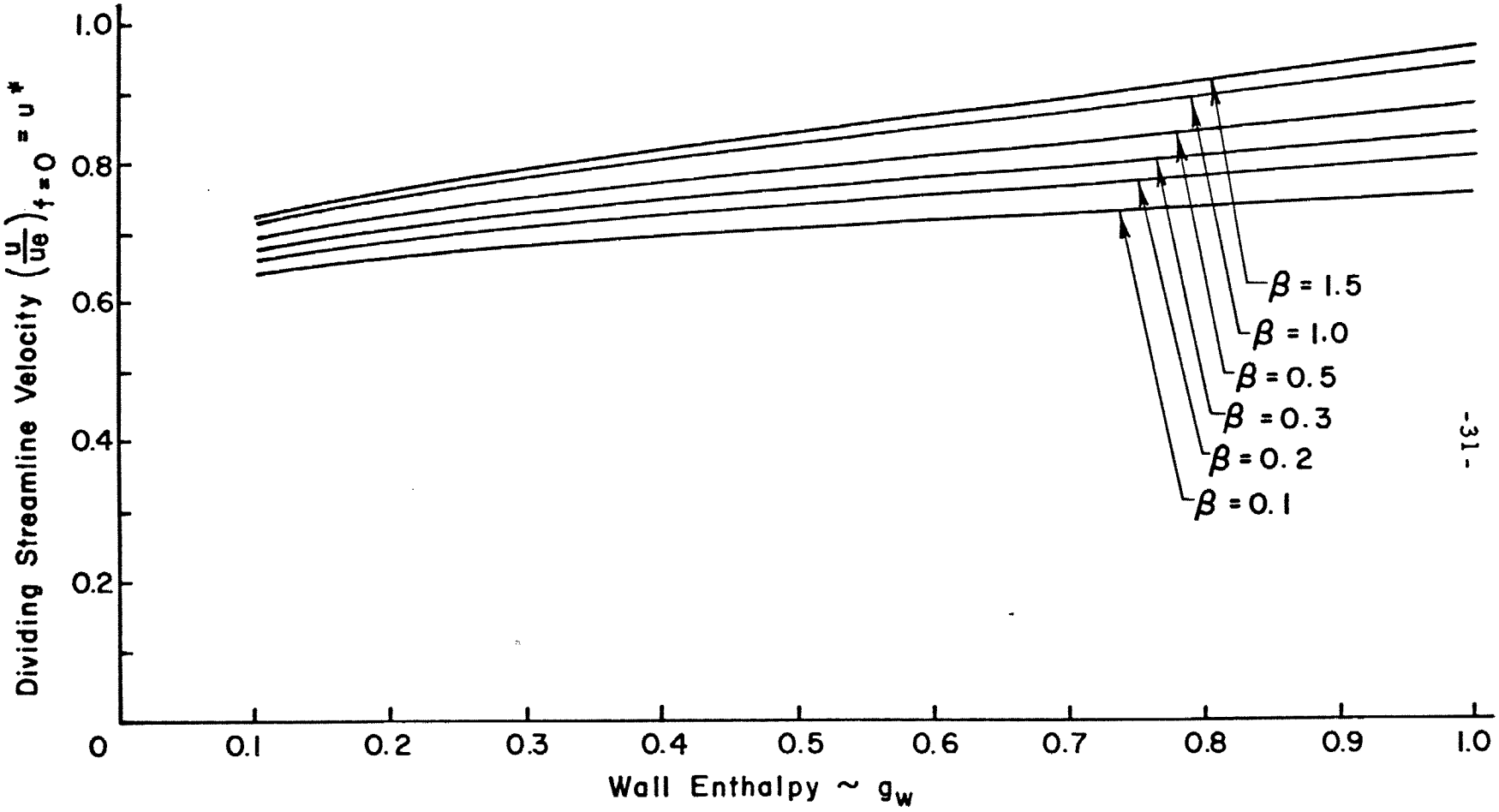

FIG. I.10 DIVIDING STREAMLINE VELOCITY $f_w = 2.0$

APPENDIX I. A

NUMERICAL SOLUTION OF THE EQUATIONS

Equations (I. 24) and (I. 25) constitute two fourth-order systems and are repeated here for clarity.

$$Z_0^{\frac{1}{2}} \frac{d^2 Z_0}{df^2} + f \frac{dZ_0}{df} + 2\beta[G_0 - Z_0] = 0 \qquad \text{(I. A. 1-a)}$$

$$\frac{d}{df}\left[Z_0^{\frac{1}{2}} \frac{dG_0}{df}\right] + f \frac{dG_0}{df} = 0 \qquad \text{(I. A. 1-b)}$$

B. C. $Z_0(\infty) = 1$ $\quad G_0(\infty) = 1$

$Z_0(-\infty) = g_w$ $\quad G_0(-\infty) = g_w$ $\qquad$ (I. A. 1-c)

$$\frac{Z_1}{2} \frac{d^2 Z_0}{df^2} + Z_0 \frac{d^2 Z_1}{df^2} + \sqrt{Z_0}\, f \frac{dZ_1}{df} + 2\beta\sqrt{Z_0}[G_1 - Z_1] = 0 \qquad \text{(I. A. 2-a)}$$

$$\frac{d}{df}\left[\sqrt{Z_0} \frac{dG_1}{df} + \frac{Z_1}{2Z_0} \frac{dG_0}{df}\right] + f \frac{dG_1}{df} = 0 \qquad \text{(I. A. 2-b)}$$

B. C. $Z_1(\infty) = 0$ $\quad G_1(\infty) \to 0$

$Z_1(-\infty) \to -g_w(-f)^{2\beta}$ $\quad G_1(-\infty) \to 0$ $\qquad$ (I. A. 2-c)

The coupling between the two sets is seen to be one way; namely, the solutions of (I. A. 1) enter into (I. A. 2) as coefficients.

The technique used in solving these equations is the method of "quasilinearization" (6) (7). In this scheme, a form is assumed for the solution which satisfies the boundary conditions exactly, and an iterative procedure is developed from the finite difference form of the differential equations. The method possesses distinct

advantages in solving boundary-value problems of this type, since it may be shown that the "shooting" method becomes unstable for large injection rates. However, questions of convergence for non-linear systems are, in general, very difficult to answer.

In order to illustrate the technique used, consider Equations (I. A. 1). Assume solutions F(1) and G(1) to (I. A. 1). Then let

$$F(2) = F(1) + [F(2)-F(1)] = F(1) + \Delta F \qquad \text{(I. A. 3)}$$

If the assumed solution, F(1) of (I.A. 1) is fairly close to the correct solution, $\Delta F \ll F(1)$. Hence Equation (I. A. 1) can be linearized around F(1) to give

$$F''(2)\sqrt{F(1)} + F(2)\left[\frac{F''(1)}{2\sqrt{F(1)}} - 2\beta\right] + fF'(2)$$

$$= \frac{F''(1)\sqrt{F(1)}}{2} - 2\beta G(1) \qquad \text{(I. A. 4)}$$

where primes denote differentiation.

Now, the derivatives in Equation (I. A. 4) are written in finite difference form, where Δf, the interval size, is assumed constant,

$$F''(2,n) = \frac{F(2,n+1) - 2F(2,n) + F(2,n-1)}{(\Delta f)^2} \qquad \text{(I. A. 5-a)}$$

$$F'(2,n) = \frac{F(2,n+1) - F(2,n-1)}{2\Delta f} \qquad \text{(I. A. 5-b)}$$

substituting this into Equation (I. A. 4) and collecting coefficients of F(2, i), gives

$$\left[1 - \frac{(\Delta f)f}{2\sqrt{F(1,n)}}\right] F(2,n-1)$$

$$+\left[\frac{(\Delta f)^2}{\sqrt{F(1,n)}}\left(\frac{F''(1,n)}{2\sqrt{F(1,n)}} - 2\beta\right) - 2\right] F(2,n)$$

$$+\left(1 + \frac{(\Delta f)f}{2\sqrt{F(1,n)}}\right) F(2,n+1)$$

$$= \frac{(\Delta f)^2}{\sqrt{F(1,n)}}\left[\frac{F''(1,n)}{2}\sqrt{F(1,n)} - 2\beta G(1)\right] \qquad \text{(I. A. 6)}$$

If the "interval" $[-\infty \leq f \leq \infty]$ is characterized by f_{min} and f_{max} with N_2 points on the negative f axis and N_1 points on the positive f axis, there is a total of $N_2 + N_1 + 1$ points at which the solution is to be obtained. Equation (I. A. 6) applied at interior points describes a system of $N_1 + N_2 - 1$ equations. The two boundary conditions at f_{max} and f_{min} provide two more equations making this a complete algebraic system. If we change indices from n to I where $I = 1, 2, ---N_2 + N_1 - 1$, Equation (I. A. 6) can be written as a matrix equation

$$A(1,I)U(I-1) + A(2,I)U(I) + A(3,I)U(I+1) = V(I) \qquad \text{(I. A. 7-a)}$$

where

$$A(1,I) = 1 - \frac{(I-N_2)(\Delta f)^2}{2\sqrt{F(1,I+1)}}$$

$$A(2,I) = \frac{(\Delta f)^2}{\sqrt{F(1,I+1)}}\left\{\frac{1}{2(\Delta f)^2\sqrt{F(1,I+1)}}\left[F(1,I+2) - 2F(1,I+1) + F(1,I)\right] - 2\beta\right\} - 2 \qquad \text{(I. A. 7-b)}$$

$$A(3, I) = 2 - A(1, I)$$

$$V(I) = \frac{(\Delta f)^2}{\sqrt{F(1, I+1)}} \left[\frac{\sqrt{F(1, I+1)}}{2(\Delta f)^2} \left(F(1, I+2) - 2F(1, I+1) + F(1, I) \right) - 2\beta G(1, I+1) \right]$$

$$U(I) = F(2, I+1)$$

Here the finite difference form for F'_1, F_1 has been used. The boundary conditions are

$$\left.\begin{aligned} Z_0(\infty) &= 1 \\ Z_0(-\infty) &= g_w \end{aligned}\right\} \Longrightarrow \quad \begin{aligned} U(N_1+N_2) &= 1 \\ U(0) &= g_w \end{aligned} \qquad \text{(I. A. 7-c)}$$

This procedure has been employed for Equations (I. A. 1-b) and (I. A. 2). The iteration procedure used was as follows: An initial guess is made for the function $Z_0(1)$. Using the guess, the energy equation (I. A. 1-b) is solved for $G_0(1)$ subject to the boundary conditions (I. A. 1-c). This solution for $G_0(1)$ and $Z_0(1)$ are substituted into Equation (I. A. 4), which is solved for $Z_0(2)$. The entire procedure is then repeated until the successive solutions satisfy a prescribed convergence criteria. Once the solutions to Equations (I. A. 1) are obtained, Equations (I. A. 2), written in a similar finite difference form, are solved using the solutions of (I. A. 4) as coefficients. With $Z = (f_\eta)^2$ determined as a function of f, the physical distance η can be obtained from

$$\eta = \int_{-f_w}^{f} \frac{df}{\sqrt{Z}} \qquad \text{(I. A. 8)}$$

Since a straightforward numerical integration as given by (I. A. 8) is very difficult near $f = -f_w$ [$Z \to 0$ as $f \to -f_w$], η is computed as follows:

$$\eta = \int_{-f_w}^{-f_w+\Delta f} \frac{df}{\sqrt{Z}} + \int_{-f_w+\Delta f}^{f} \frac{df}{\sqrt{Z}} \qquad \text{(I. A. 8-a)}$$

the second integral poses no numerical problems. For the first integral, near the wall, the "inner" solution, Equation (I. 16), is certainly valid if Δf is small. Using Equation (I. 16)

$$\eta_1 = \frac{1}{g_w^{\frac{1}{2}}} \int_{-f_w}^{-f_w+\Delta f} \frac{df}{\left[1 - \left(-\frac{f}{f_w}\right)^{2\beta}\right]^{\frac{1}{2}}} \qquad \text{(I. A. 9)}$$

letting $w = 1 - \left(-\frac{f}{f_w}\right)^{2\beta}$

$$\eta_1 = \frac{f_w}{2\beta g_w^{\frac{1}{2}}} \int_0^{1-\left(1-\frac{\Delta f}{f_w}\right)^{2\beta}} \frac{(1-w)^{\frac{1-2\beta}{2\beta}}}{w^{\frac{1}{2}}}\, dw$$

If $\frac{\Delta f}{f_w} << 1$, then $w << 1$,

since $0 \le w \le 1 - \left(1 - \frac{\Delta f}{f_w}\right)^{2\beta}$.

Expanding the upper limit and the integrand, we get

$$\eta_1 = \frac{f_w}{2\beta\, g_w^{\frac{1}{2}}} \int_0^{2\beta\frac{\Delta f}{f_w}} \frac{dw}{w^{\frac{1}{2}}} = \left(\frac{2f_w}{\beta g_w}\right)^{\frac{1}{2}} \Delta f \qquad \text{(I. A. 10)}$$

to the order of $\left(\frac{\Delta f}{f_w}\right)^{\frac{3}{2}}$.

This scheme was programmed on the IBM 7094 and the solutions for Z_0, Z_1, G_0 and G_1 were obtained for $0.1 \leq g_w \leq 1.0$ and $0.1 \leq \beta \leq 2.0$. The scheme works quite well with convergence usually obtained in 2-5 iterations. The running time for the most extreme case ($g_w = 0.1$) was under ten seconds.

In all, the success and efficiency of the numerical scheme indicates it may be quite useful for future applications.

APPENDIX I. B

COMPUTER PROGRAM FOR SOLUTION OF EQUATIONS

```
      ASYMPTOTIC SOLUTION OF BOUNDARY LAYER EQUATIONS FOR LARGE INJECTION
      BY THE METHOD OF QUASILINEARIZATION


      DIMENSION F(2,300), G(2,300), A(3,300), V(300),U(300)
      LOGICAL EOD
    1 READ(5,900) BETA, FW, GW, EOD
  900 FORMAT(3F10.0,L10)
      READ(5,901)  FMAX, FMIN, EPS, CONVF, N2, N1, MIT, ITPRT, NSTEP
  901 FORMAT(4F10.0,5I5)
      XI = N1+N2
      DELF = (FMAX+FMIN)/XI
      WRITE(6,329) BETA,FW,GW,  FMAX,  FMIN,DELF,N2,N1,MIT,EPS,CONVF
  329 FORMAT(1H1,5X6HBETA = F9.4,5X4HFW = F5.3,5X4HGW = F5.3/
     15X6HFMAX =   F5.2,5X6HFMIN =   F5.2,5X6HDELF = F5.3,5X4HN2 = I4,
     25X4HN1 = I4/5X10HMAX ITER = I3,5X13HERROR BOUND =F8.1,5X
     313HCONV FACTOR = F3.1//15X17HITERATION COUNTER//)

 BETA = DIMENSIONLESS PRESSURE GRADIENT
 FW =   DIMENSIONLESS INJECTION PARAMETER
 GW =   WALL ENTHALPY RATIO
 FMAX = ESTIMATED VALUE OF F AT TOP EDGE OF MIXING LAYER
 FMIN = ESTIMATED VALUE OF (-F) AT BOTTOM EDGE OF MIXING LAYER
 DELF = INTEGRATION STEP SIZE IN F- PLANE
 EPS = ERROR BOUND FOR SUCCESIVE APPROXIMATIONS
 CONVF = CONVERGENCE FACTOR .GT. 0 AND .LE. 1.0
 N2 = NUMBER OF SUBDIVISIONS FOR NEGATIVE F
 N1 = NUMBER OF SUBDIVISIONS FOR POSITIVE F
 NMAX = TOTAL NUMBER OF PIVOTAL POINTS = N2+N1+1
      = (TOTAL NUMBER OF SUBDIVISIONS) + 1
 MIT  = MAXIMUM NUMBER OF ITERATIONS
 ITPRT = 0 IF PRINT OUT OF SUCCESIVE ITERATION IS NOT DESIRED
       = 1 IF PRINT OUT OF SUCCESIVE ITERATION IS DESIRED
 NSTEP = IF ITPRT=1 SOLUTIONS ARE PRINTED AT EVERY (NSTEP)-
         MULTIPLE OF SUBINTERVAL
      ITM = 0
      ITE =0

 INITIAL APPROXIMATION FOR FZERO AND GZERO

      NMAX = N1+N2+1
      F(1,1) = GW
      DO 2 I = 2,NMAX
      RI =I-N2-1
    2 F(1,I) =GW+(1.-GW)*(SQRT((RI*DELF+FMIN)/(FMAX+FMIN)))
      GO TO 105

 SOLUTION OF MOMENTUM EQUATION

 COMPUTATION OF COEFFICIENT MATRIX FOR MOMENTUM EQUATION

    5 CONTINUE
      K=NMAX-2
      DO 10 I= 1,K
```

```
      RI=I-N2-1
      SI = SQRT(F(1,I+1))
      A(1,I) = 1.0 - RI*DELF**2/(2.0*SI)
      A(2,I) = DELF**2/SI*((F(1,I+2)-2.0*F(1,I+1)+F(1,I))/
     1  (2.0*DELF**2*SI) -2.0*BETA)-2.0
      A(3,I) = 2.0-A(1,I)
   10 V(I) = DELF**2/SI*(SI/(2.0*DELF**2)*(F(1,I+2)-2.0*F(1,I+1)+F(1,I))
     1  -2.0*BETA*G(1,I+1))
      V(1) = V(1) -A(1,1)*GW
      A(1,1) =0.0
      I= NMAX-2
      V(I) =V(I) -A(3,I)
      A(3,I) = 0.0

   SOLUTION OF SIMULTANEOUS(NMAX-2) LINEAR EQUATIONS WITH BANDED MATRIX

      ITM = ITM+1
      IF(ITM.GT.MIT) GO TO 400
      CALL SEQSOV(NMAX-2,3,A,V,5,EPS,U,IT,ILL)
      WRITE(6,330) ITE, ITM, IT
  330 FORMAT(10X15HOUTSIDE LOOP = I3,5X14HINSIDE LOOP = I3,
     1 5X12HSEQSOV IT = I3)
      IF(ILL.EQ.1) GO TO 1000
      F(2,1) = GW
      K = NMAX-1
      DO 20 I =2,K
   20 F(2,I) = U(I-1)
      F(2,NMAX) = 1.0
      IF(ITPRT.EQ.0) GO TO 510
      WRITE(6,502)
  502 FORMAT(1HO,6X1HN,13X2HF1,18X2HF2,18X1HG//)
      DO 500 I=1,NMAX,NSTEP
      WRITE(6,501) I,F(1,I),F(2,I),G(2,I)
  501 FORMAT(I8,1P3E20.5)
  500 CONTINUE
      WRITE(6,503)
  503 FORMAT(1HO,//)
  510 CONTINUE
   35 DO 36 I = 1,NMAX
   36 F(1,I) = F(1,I)+ CONVF*(F(2,I)-F(1,I))

   SOLUTION OF ENERGY EQUATION


  COMPUTATION OF ENERGY COEFFICIENT MATRIX

  105 K=NMAX-2
      DO 110 I = 1,K
      IF(F(1,I+1).LT.0.0)GO TO 1000
      SI = SQRT(F(1,I+1))
      RI=I-N2-1
      A(1,I) = SI/DELF**2 -RI/2.0 -(F(1,I+2)-F(1,I))/(8.0*SI*DELF**2)
      A(2,I) = -2.0*SI/DELF**2
      A(3,I) = -(A(2,I)+A(1,I))
  110 V(I) = 0.0
      V(1) = V(1) -GW*A(1,1)
```

```
      A(1,1) = 0.0
      V(NMAX-2) =V(NMAX-2) - A(3,NMAX-2)
      A(3,NMAX-2) = 0.0
      CALL SEQSOV(NAMX-2,3,A,V,5,EPS,U,IT,ILL)
      IF(ILL.EQ.1) GO TO 1000
      G(2,1) = GW
      K = NMAX-1
      DO 130 I = 2,K
      G(2,I) = U(I-1)
130   CONTINUE
      G(2,NMAX) =1.0
      DO 135 I = 1,NMAX
      IF(ABS(G(2,I)/G(1,I)- 1.0).GE.EPS) GO TO 145
135   CONTINUE
      GO TO 200
145   DO 146 I=1,NMAX
146   G(1,I) = G(2,I)
      GO TO 5

 SOLUTION OF ZERO  ORDER MOMENTUM AND ENERGY EQUATIONS COMPLETED

200   WRITE(6,6670)
670   FORMAT(5X29HZERO ORDER SOLUTION CONVERGED)

 SOLUTION OF FIRST ORDER EQUATIONS

      ITM =0

 INITIAL APPROXIMATION FOR G1

      DO 800 I = 1,NMAX
800   G(2,I) = 0.0
      GO TO  600

 SOLUTION OF FIRST  ORDER ENERGY EQUATION

 COMPUTATION OF COEFFICIENT MATRIX
  6   K= NMAX -2
      DO 11 I = 1,K
      RI = I-N2-1
      SI =SQRT(F(1,I+1))
      DGI =(G(1,I+2)-G(1,I))/(2.0*DELF)
      DFI =(F(1,I+2)-F(1,I))/(2.0*DELF)
      D2GI =(G(1,I+2)-2.0*G(1,I+1)+G(1,I))/DELF**2
      A(1,I) =SI/DELF**2-(RI*DELF+DFI/(2.0*SI))/(2.0*DELF)
      A(2,I) = -2.0*SI/DELF**2
      A(3,I) = -(A(2,I)+A(1,I))
11    V(I) =F(2,I+1)/(4.0*SI**3)*DFI*DGI-DGI*(F(2,I+2)-F(2,I))/
     1   (4.0*DELF*SI)-F(2,I+1)*D2GI/(2.0*SI)
      A(1,1) = 0.0
      A(3,NMAX-2) = 0.0
      ITE = ITE +1
      IF(ITE.GT.MIT) GO TO 400
      CALL SEQSOV(NMAX-2,3,A,V,5,EPS,U,IT,ILL)
      WRITE(6,331) ITE,ITM,IT
331   FORMAT(10X15HOUTSIDE LOOP = I3,5X14HINSIDE LOOP = I3,
```

```
   1  5X12HSEQSOV II = 13)
      IF(ILL.EQ.1) GO TO 1000
      K= NMAX-1
      DO 136 I= 2,K
      IF(ABS(G(2,I)-U(I-1)).GE.EPS) GO TO 147
.36 CONTINUE
      GO TO 201
.47 G(2,NMAX) = 0.0
      G(2,1) = 0.0
      K = NMAX - 1
      DO 148 I=2,K
148 G(2,I) = U(I-1)

 SOLUTION OF FIRST  ORDER MOMENTUM EQUATION


 COMPUTATION OF THE COEFFICIENT MATRIX
>00 K = NMAX-2
      DO 601 I =1,K
      SI = SQRT(F(1,I+1))
      RI = I-N2-1
      ZI = F(1,I+1)/DELF**2
      A(1,I) = ZI -SI*RI/2.0
      A(2,I) = (F(1,I+2)-2.0*F(1,I+1)+F(1,I))/(2.0*DELF**2)
     1   -2.0*BETA*SI-2.0*ZI
      A(3,I) = ZI+SI*RI/2.0
>01 V(I) = -2.0*BETA*G(2,I+1)
      RN = N2
      V(1) = V(1)+A(1,1)*GW*(+RN*DELF)**(2.0*BETA)
      A(1,1) = 0.0
      A(3,NMAX-2) = 0.0
      CALL SEQSOV(NMAX-2,3,A,V,5,EPS,U,IT,ILL)
      IF (ILL.EQ.1) GO TO 1000
      F(2,1) = -GW*(RN*DELF)**(2.0*BETA)
      K= NMAX-1
      DO 602 I=2,K
      F(2,I) = U(I-1)
>02 CONTINUE
      F(2,NMAX) =0.0
      GO TO 6

 SOLUTION OF FIRST  ORDER EQUATIONS COMPLETED

201 WRITE(6,335)
335 FORMAT(5X18HSOLUTION CONVERGED)

 VELOCITY, ENTHALPY DISTRIBUTION, INTEGRAL THICKNESSES

      DELTA =(1.0/ FW)**(2.0*BETA)
      A(1,1) = 0.0
      K = NMAX-1
      DO 210 I=2,K
210 A(1,I) = SQRT(F(1,I)+DELTA*F(2,I))
      A(1,NMAX) =1.0
      V(1) = 0.0
      V(2) = SQRT(2.0*FW*DELF/(BETA*GW))
```

```
      DO 211 I= 3,NMAX
211   V(I) = 2.0*DELF/(A(1,I)+A(1,I-1))
      A(2,1) = GW
      DO 212 I =2,NMAX
212   A(2,I) = G(1,I) +DELTA*G(2,I)
      U(1) = -FW
      U(2) = -FW+DELF
      DO 213 I = 3,NMAX
213   U(I) = U(I-1)+ V(I)*(A(1,I-1)+A(1,I))/2.0
      DELSTR = 0.0
      THETA = 0.0
      SIGMA = 0.0
      DO 214 I = 2,NMAX
      FNBAR = (A(1,I) +A(1,I-1))/2.0
      SNBAR = (A(2,I)+A(2,I-1))/2.0
      DELSTR = DELSTR+(1.0-FNBAR)*V(I)
      THETA = THETA +(FNBAR-FNBAR**2)*V(I)
      SIGMA = SIGMA+(1.0-SNBAR)*V(I)
214   CONTINUE
      H = DELSTR/THETA
      DO 224 I = 1,NMAX
224   A(3,I) = SQRT(F(1,I))
      J = (FMIN-2.0)/DELF+2.0
      ALPHA = 0.0
      DELTA2 = 0.0
      GAMMA = 0.0
      THETA2 = 0.0
      SIGMA1 = 0.0
      SIGMA2 = 0.0
      SIGMA3 = 0.0
      DO 217 I = J,NMAX
      ALPHA = ALPHA +DELF/A(3,I)
      DELTA2 = DELTA2 + F(2,I)*DELF/(A(3,I))**3
      GAMMA = GAMMA-A(3,I)*DELF
      THETA2 = THETA2 + F(2,I)*DELF/A(3,I)
      SIGMA1 = SIGMA1 + (1.0-G(1,I))*DELF/A(3,I)
      SIGMA2 = SIGMA2 + G(1,I)*F(2,I)*DELF/(2.0*A(3,I)**3)
      SIGMA3 = SIGMA3 + G(2,I)*DELF/A(3,I)
217   CONTINUE
      THETA1 = GAMMA+FMAX
      DELTA1 = ALPHA - FMAX
      SIGMA1 = FMIN*(1.0-GW)/SQRT(GW) -SIGMA1
      SIGMA2 = SIGMA3 -SIGMA2 +DELTA2/2.0 +(1.0-GW)*FMIN**(2.0*BETA +1.0
     1)/(2.0*SQRT(GW)*(2.0*BETA+1.0))
      THETA1 = THETA1 +FMIN*SQRT(GW)
      THETA2 = THETA2 +SQRT(GW)*FMIN**(2.0*BETA+1.0)/(2.0*BETA+1.0)
      DELTA1 = DELTA1-FMIN/SQRT(GW)
      DELTA2 = DELTA2 + FMIN**(2.0*BETA+1.0)/(SQRT(GW)*(2.0*BETA+1.0))
      WRITE(6,300) BETA,FW,GW
300   FORMAT(1H1,5X6HBETA = F9.4,5X4HFW = F5.3,5X4HGW = F5.3//7X3HETA
     1  10X1HF,11X2HZ0,10X2HZ1,10X2HFN,10X2HG0,10X2HG1,10X1HG//)
      K=0
      DO 235  I = 1,NMAX
      K= K+1
      V(1) = V(1) + V(I)
      IF(K.NE.52) GO TO 230
```

```
      K = 1
      WRITE(6,315)
  315 FORMAT(5X15H** CONTINUED **/1H1,6X3HETA,10X1HF,11X2HZ0,10X2HZ1,
     1 10X2HFN,10X2HG0,10X2HG1,10X1HG//)
  230 WRITE(6,310) V(1),U(I),F(1,I),F(2,I),A(1,I),G(1,I),G(2,I),A(2,I)
  310 FORMAT(8F12.5)
  235 CONTINUE
      WRITE(6,320) DELSTR,THETA,SIGMA,H,DELTA1,DELTA2,THETA1,THETA2,
     1SIGMA1,SIGMA2
  320 FORMAT(15X9HDELTA* = F10.5,5X8HTHETA = F10.5,5X8HSIGMA = F10.5,
     15X4HH = F10.5,/5X9HDELTA1 = F10.5,5X9HDELTA2 = F10.5,5X9HTHETA1 =
     2F10.5,5X9HTHETA2 = F10.5,/5X9HSIGMA1 = F10.5,5X9HSIGMA2 = F10.5)
    ETA = BOUNDARY LAYER SIMILARITY VARIABLE
    F = SIMILAR STREAM FUNCTION VARIABLE
    Z0 = ZERO ORDER MOMENTUM SOLUTION ( MIXING LAYER SOLUTION)
    Z1 = FIRST ORDER MOMENTUN SOLUTION
    FN = DIMENSIONLESS VELOCITY
    G0 = ZERO ORDER ENERGY SOLUTION ( TOTAL ENTHALPY RATIO)
    G1 = FIRST ORDER ENERGY SOLUTION
    G = DIMENSIONLESS ENTHALPY
    DELTA* = DISPLACEMENT THICKNESS
    THETA = MOMENTUM THICKNESS
    SIGMA = ENERGY THICKNESS
    DELTA(I), THETA(I), SIGMA(I) = COEFFICIENTS IN ASYMPTOTIC
        EXPANSION FOR INTEGRAL THICKNESSES
      GO TO 2000
  400 WRITE(6,410) MIT
  410 FORMAT(1X8HEXCEEDED I3,1X10HITERATIONS)
 1000 K=NMAX-2
      WRITE(6,8238) (I,(A(L,I),L=1,3),V(I),I=1,K)
 8238 FORMAT(1H1,5X,19HSEQSOV TROUBLE DUMP ///(5X,I5,1P3E20.5,5X,1PE20.5
     * ))
 2000 IF(.NOT.EOD) GO TO 1
      STOP
       END
```

```
      SUBROUTINE SEGSOV(N,BNDWTH,BDMTX,V,ITER,EPS,  F, IT, ILL )
      DIMENSION A(3,300),V(300),X(300),F(300),BDMTX(3,300),
     1  R(300),XX(300)
C BDMTX = BAND MATRIX GENERATED ROW-WISE AS FOLLOWING
C   1. FIRST ELEMENT OF ANY ROW MUST BE STORED AS FIRST ELEMENT
C        OF EACH COL.
C   2. DIAGONAL TERMS ARE ALWAYS IN THE MIDDLE ROW
C   3. 1ST COL. HAS LEADING ZEROS, LAST COL. HAS TRAILING ZEROS
C         (USER MUST STORE DATA SO THAT IT LOOKS AS IF THE ARRAY
C            HAS BEEN ROTATED 90 DEG. CLOCKWISE AND DISPLACED
C            UP BY 1 EACH TIME)
C  N = ORDER OF MATRIX,
C  BNDWTH = BANDWIDTH - TOTAL NON - ZERO ELEMENTS / ROW
C  B2 = BNDWTH / 2 + 1 - ROW DEF. WHERE DIAGONAL TERMS ARE STORED
C  B1 = B2 - 1 - NO OF NON - ZERO OFF - DIAGONAL TERMS
      INTEGER BNDWTH, B2, B1
      DOUBLE PRECISION R
C SAVE ORIGINAL BAND MATRIX AND COL. VECTOR V - AX = V
      ILL = 0
      IT = 0
      DO 10 J = 1, N
      X(J) = V(J)
      F(J) = 0.
      DO 10 I = 1, BNDWTH
      A(I,J) = BDMTX(I,J)
   10 CONTINUE
      B2 = BNDWTH / 2 + 1
      B1 = B2 - 1
      N1 = N - 1
C TRIANGULARIZE MATRIX - SAVE MULTIPLYING FACTOR IN MATRIX
      K1 = B1
      DO 60 I = 2,N
      K1 = K1 + 1 - (I+B1-1)/(N+1)
      K = B1
      IF(A(B2,I-1) .EQ.0.) GO TO 200
      DO 55 J = I,K1
      CX = A(K,J) / A(B2,I-1)
      L1 = B2 + 1
      KPB = K + B1
      KP1 = K + 1
      DO 50 L = KP1, KPB
      A(L,J) = A(L,J) - CX * A(L1,I-1)
   50 L1 = L1 + 1
      A(K,J) = CX
      K = K - 1
   55 CONTINUE
   60 CONTINUE

C FORWARD PASS - OPERATE ON RIGHT HAND SIDE AS ON MATRIX
   62 CONTINUE
      IN = B1
      DO 70 I = 2,N
      IN = IN+1 - (I+B1-1)/(N+1)
      K1 = B1
      DO 65 J = I, IN
```

```
      X(J) = X(J) - X(I-1)*A(K1,J)
       K1 = K1 -1
   65 CONTINUE
   70 CONTINUE
BACKWARD PASS - SOLVE FOR AX = B
      XX(N) = X(N) / A(B2,N)
      DO 80 I = 1, N1
      SUM = 0.0
      K = N - I
      L = B2 + 1
      K1 = K+B1-1
      IF(K1.GT. N1) K1 = N1
      DO 75 J = K,K1
      SUM = SUM + A(L,K) * XX(J+1)
      L = L + 1
   75 CONTINUE
      XX(K) = (X(K)-SUM) / A(B2,K)
   80 CONTINUE
      DO 90 I = 1, N
      F(I) = F(I) + XX(I)
   90 CONTINUE
      IF(IT .EQ. ITER) GO TO 100
      IT = IT + 1
      DO 95 I = 1, N
      IF(ABS(XX(I)/F(I)) .GT. EPS) GO TO 150
   95 CONTINUE

FINISHED
  100 CONTINUE
      RETURN


DOUBLE PRECISION MATRIX MULTIPLICATION
  150 CONTINUE
      L = B2
      L2 = BNDWTH
      DO 170 I = 1, N
      R(I) = 0.0D0
      K = I - B2 + L
      DO 160 J = L, L2
      R(I) = R(I) + BDMTX(J,I) * F(K)
      K = K + 1
  160 CONTINUE
      IF (I .LT. B2) L = L - 1
      IF (N-I .LT. B2) L2 = L2 - 1
  170 CONTINUE
      DO 180 I = 1, N
      X(I) = V(I) - R(I)
  180 CONTINUE
      GO TO 62
  200 I1 = I-1
      ILL = 1
      WRITE (6,510) I1
  510 FORMAT(/1X25HERROR RETURN FROM SEQSOV    I10,
     1 35HTH DIAGONAL TERM REDUCED TO ZERO      /)
      RETURN
```

PART II. EXPERIMENTS IN SUPERSONIC TURBULENT FLOW WITH LARGE DISTRIBUTED SURFACE INJECTION*

*A portion of this work has been presented at the AIAA 6th Aerospace Science Meeting in conjunction with Prof. E. E. Zukoski (AIAA Preprint #68-129).

List of Tables - Part II

List of Figures - Part II

List of Figures - Part II (Cont'd)

List of Figures - Part II (Cont'd)

List of Symbols - Part II

C_f	skin friction coefficient, $2\tau_w/\rho_e u_e^2$
C_i	mass fraction of i^{th} species
F	side force
H	form parameter, δ^*/θ
$\overline{H}$	incompressible form parameter, $\overline{\delta}^*/\overline{\theta}$
M	Mach number
$\mathcal{M}_{w_i}$	molecular weight of i^{th} species
Re_θ	Reynolds number, based on edge conditions, $(\rho_e u_e \theta)/\mu_e$
T	temperature
T_t	total temperature
u	velocity component in x-direction
v	velocity component in y-direction
x	distance along plate measured from start of porous region
$\overline{y}/\overline{\theta}$	transformed distance normal to wall, $\overline{y}/\overline{\theta} = \int_0^y \frac{\rho}{\rho_e} d(y/\theta)$
δ^*	displacement thickness, $\int_0^\delta (1-\rho u/\rho_e u_e)dy$
δ	edge of layer
θ	momentum thickness, $\int_0^\delta \rho u/\rho_e u_e (1-u/u_e)dy$
$\overline{\delta}^*$	incompressible displacement thickness, $\int_0^{\overline{\delta}} (1-\overline{u}/\overline{u}_e)d\overline{y}$
Θ	induced flow angle at edge; $\tan\Theta = v_e/u_e$
$\overline{\theta}$	incompressible momentum thickness, $\int_0^{\overline{\delta}} \overline{u}/\overline{u}_e (1-\overline{u}/\overline{u}_e)d\overline{y}$
λ_e	$\rho_w v_w/\rho_e u_e$
λ_∞	$\rho_w v_w/\rho_\infty u_\infty$
μ	viscosity

List of Symbols - Part II (Cont'd)

η, ξ, σ transformation functions

ψ stream function; $\partial\psi/\partial y = \rho u$, $\partial\psi/\partial x = -\rho v$

τ shear stress

ρ density

Subscripts

w wall value

e value at edge of layer

∞ free-stream value

bars above quantities denote values for an incompressible flow ($\overline{\rho}$ = const).

II. 1. Introduction

The normal injection of gas through a porous wall into a two-dimensional turbulent boundary layer bounded by a supersonic stream can produce large changes in flow inclination angles and can induce an appreciable increase in surface pressure.

At least three regimes exist for the uniform blowing problem in a supersonic flow. First, when the skin friction term in the integrated momentum equation is comparable to or larger than the injectant term, both skin friction and injectant flow rate influence the problem. Although the boundary layer theory is applicable, no simple, self-similar solution can be obtained because of the skin friction term. Second, when the injectant term is very large compared with the skin friction term but the injectant momentum flux is small compared with the free-stream momentum flux, the boundary-layer approach is still valid and now self-similar solutions with linear growth and a uniform external flow become possible. Finally, when the momentum flux of the injectant and free stream are comparable, the boundary-layer approach is not applicable.

The problem studied experimentally in this section is the second one where skin friction is negligible, and the terms 'large blowing rate' or 'strong blowing' will be used to describe this second regime in contrast to the first one. The conditions obtained in this study never approach those of the third regime. In this experiment, a similar, two-dimensional turbulent flow is approached by large blowing into a turbulent boundary layer. The mean flow quantities are measured and analyzed to determine the effect of blowing rate

and compressibility.

A survey of the literature indicates that both for incompressible and compressible flow, the effect of injection has been experimentally investigated primarily with the view of determining the effects on skin friction and heat transfer (the first regime). Because of this, the data quoted in the bulk of the literature are for injection rates low enough that the velocity profiles, though altered, can still be regarded as slightly perturbed boundary-layer profiles.

Recent experiments have been performed by Hartunian and Spencer[8] at $M_\infty = 4.5$ for flow that was probably laminar and for truly massive injection rates. On the basis of pictures taken of the resulting flow, they concluded that for large injection rates the mixing region between the injected and free-stream gas appeared to grow linearly. Unfortunately, the nature of their experiment did not allow for careful probing of the layer to determine velocity profiles.

Incompressible data on turbulent flows with fairly large injection have been reported recently by McQuaid[9] Simpson[10] and Mugalev[11]. Mugalev's experiments were conducted on a plate mounted in a free jet. Because velocity profiles are given for only two stations in the flow and no attempt was made to monitor or control the static pressure these data are suspect and are not used in the present report. In more carefully controlled experiments McQuaid used a flexible tunnel wall to maintain the tunnel static pressure constant and made detailed velocity measurements for a wide range of injection rates. Simpson's experiment is characterized

by a very long porous section which allows for careful measurement of boundary-layer growth rates and detailed velocity measurements. For compressible turbulent flows with large injection only some data by Mugalev[12] appear to be available and his few results are included in this report.

The purpose of this experiment is to investigate the behavior of a supersonic turbulent boundary layer with large blowing including both the interaction with the external flow and the effect of compressibility.

II. 2 General Description of the Experiments

II. 2. 1 Tunnel and Model Description

The experiments were conducted in the Supersonic Wind Tunnel of the Graduate Aeronautical Laboratories, California Institute of Technology (GALCIT). The tunnel test section is 2 inches by 2 inches and the tunnel operates at a nominal Mach number of 2. 6. The stagnation conditions for all runs were a pressure of 742 mm Hg ($\pm$ 5 mm) and a temperature of 80°F ($\pm$ 5°F). The boundary layer on the tunnel wall was tripped near the nozzle throat to ensure turbulent flow in the test section. Subsequent to these experiments, an independent experimental investigation by Segal[13] has shown that for these conditions tripping of the boundary layer is not necessary to produce turbulent flow in the test section and, furthermore, that no measurable difference seems to exist between the tripped boundary layers and the ones obtained through natural transition. At the start of injection, the boundary layer is about 0. 12 inch thick. Three models were used in the experiment. The first was a uniformly

porous, stainless-steel insert, approximately 3.5 inches long and 2 inches wide, which formed part of the test section wall and was separated from the tunnel side walls by swept fences. Figure II-1 presents a detailed description of the first model with the pertinent dimensions. Figure II-2 is a schematic of the first model mounted in the tunnel. The other two models employed in the experiment represent an attempt to obtain a check on the results obtained with the first model and an extension of the experiment to higher injection rates than those obtained using the insert model.

The idea* used in constructing these models was to realize that if, for large injection, a boundary layer with linear growth is approached, then it appears feasible to perform an experiment on a model where the wall is pitched down from the oncoming flow at a set angle and the injection is increased until uniform free-stream conditions are obtained at the outer edge. A schematic of this concept is shown in Figure II-3. Angles of 10° and 20° were used and a half nozzle was employed in both cases to make maximum use of available test section.

The primary advantage of this form of an experimental arrangement for the GALCIT supersonic tunnel is the virtual elimination of the strong shock produced by the onset of blowing with the first model and the problem of its reflection from the opposite tunnel wall,

---

*This unique experimental innovation, which was suggested to the author by Prof. Donald Coles of GALCIT, would appear to be particularly useful for incompressible experiments with large injection and may eliminate many of the difficulties associated with maintaining constant pressure in such flows.

which effectively shortens the available working section for any set tunnel dimensions. The disadvantage of these two models lies in the fact that only one injection rate meets the required conditions for each angle. For injection rates substantially lower than those necessary to produce a uniform external flow, separation (reverse flow) is produced on the porous plate by the turning of the flow at the end of injection. For injection rates substantially higher than the optimum, the reflected shock from the opposite tunnel wall impinges on the blowing region because of the small half tunnel size (1"). Figures II-4 and II-5 present a detailed description of the manner in which models 2 and 3 are constructed. A 25μ porous plate was used for model #1 and a 10μ plate for the other models. The thickness of porous plate used for each porosity was determined by requiring that the pressure drop across the plate be much greater than the variation in pressure expected in the flow external to the plate. Hence the mass flow per unit area is insensitive to the induced flow conditions. The porous plates were separately examined to determine uniformity and mass flow per unit area. This investigation is discussed in Section II. 3. Room temperature air was used as the primary injectant in the experiments, although some data on model #1 was also obtained using helium as injectant. Figure II-6 is a schematic of the air and helium supply system employed in the experiments. As is seen in Figure II-6 a dual flowmeter system wasused because of the wide range of mass flow required. With this system both low flow rates and high flow rates can be measured accurately and a check on the individual flowmeter calibrations can be obtained by allowing for

cross calibration of one flowmeter against the other in the flow range where they overlap.

The total mass flow through the plate was measured, along with the temperature in the model plenums and the back-face temperature of the porous plate. Both of these temperatures were found to be within a few degrees of the tunnel stagnation temperature for all runs. The ratio of wall mass flow per unit area to that of the free stream was varied from 0 to 0.045.

The measurements taken during the experiments included schlieren photographs to determine the induced shock angles, centerline Pitot-tube measurements, static pressure measurements, and hot wire fluctuation measurements. * The instrumentation is described in Section II. 3. In reducing the data, the total temperature of the flow was assumed constant.

II. 2. 2 Description of the Resulting Flow

II. 2. 2. 1 Model #1

The first set of tunnel runs was made to determine crudely the nature of the flow field, and only schlieren photographs were taken (with and without side fences). These photographs showed remarkably straight shocks and linear growth of the mixing layers, and hence indicated the possibility that a similar flow field had been established. However, the photographs also indicated that transition regions existed at either end of the porous

---

*The author is indebted to Dr. W. Behrens of GALCIT for his invaluable guidance and help in obtaining the fluctuation measurements.

plate. Figure II-7 presents a schematic of the flow field for model #1. At the upstream end, the transition region required for adjustment of the initial turbulent layer to the injection appeared to occupy about 5-10 initial boundary-layer thicknesses. At the downstream end, the expansion required by the end of injection appeared to propagate upstream over the porous plate a distance of about two final boundary-layer thicknesses.

Care was necessary at the higher blowing rates to ensure that events occurring downstream of the porous plate (such as reflected shocks or probe movement) did not cause separation on the porous plate itself. A large region of separated (reverse) flow behind the porous plate was characterized by extreme sensitivity of the overall flow field (both on and off the porous plate) to any measuring probes which were placed in the region. This would, of course, invalidate any measurements made with these probes. Separation was prevented by removing the standard tunnel diffuser, replacing it with one of constant area and by increasing the pumping capacity of the tunnel.

In addition to this problem of downstream separation, a separation of the initial boundary layer upstream of the porous plate was encountered when the turning angle produced by blowing was greater than about 14°. This result is to be expected from earlier studies of turbulent boundary-layer separation. [14]

When all separation phenomena are avoided, the external flow produced by injection resembles that produced by a wall which turns toward the flow through a small angle and then, after a space, returns to its original direction. The transition regions at both

turns and the uniform flow region in between are present. This general picture of the flow is confirmed by Pitot pressure measurements discussed later.

II. 2. 2. 2 Models #2 and #3

The behavior of the flow fields for models 2 and 3 is interesting enough to warrant a separate discussion. For model #2 (the 10^{o} ramp), the flow field with and without injection is shown schematically in Figure II-8. As shown in this figure, there exists a drastic difference between the flows with and without injection. Without injection, the rapid expansion around the sharp corner causes a very abrupt change in boundary-layer thickness and pressure which, for turbulent flow seems to originate from a region near the corner which is a fraction of a boundary-layer thickness in extent. With injection, there is a weak compression (due to the fact that injection starts right at the corner), followed by an expansion to free-stream conditions. For this case, longitudinal surveys taken across the wave indicated less than 1% change in total pressure; hence the entire compression-expansion process can be considered isentropic. This corner region is followed by a region of constant pressure as shown in Figure II-8 and then a falling pressure region which seemed to affect the last inch of porous plate. For model #3 (the 20^{o} ramp), the resulting flow fields are shown schematically in Figure II-9. In this case, without injection, the expansion is so rapid that the initial boundary layer virtually disappears and both schlieren and Pitot surveys indicated the growth of a new, thin viscous layer whose origin appeared to be at the corner. With injection, it was found that with

the maximum amount of injection which still allowed for the process near the corner to be considered isentropic, a falling pressure existed over virtually all of the porous region. As will be discussed later, for the 20^{o} case, similarity was not observed in the porous region.

Hence, model #2 provided a reasonable sized region of similar flow while with model #3, no such region was realized. These results are discussed in more detail in Section II. 4.

II. 3 Instrumentation and Porous Plate

II. 3. 1 Porous Plate Characterization

The porous plates used in the experiments were prepared from sintered stainless steel particles by the Mott Metallurgical Corporation of Hartford, Connecticut and, according to the vendor, possess an average porosity of 40-45 percent. As was mentioned previously, the plate thicknesses were chosen so that mass flow would be insensitive to the spatial pressure variations encountered during tunnel runs (as, for example, the expansion observed near the rear end of injection). For all of the conditions, pressure ratios of from 10-40:1 were maintained across the plate (plate plenum pressure to pressure in turbulent layer), the lower value corresponding to the lowest injection rate investigated. For these pressure ratios, the porous plate is not choked in the sense that there is a Mach 1 flow at the plate exit. However, the plate mass flow is quite insensitive to spatial variations in tunnel conditions.

Since there is some question about the mechanism of "choking" in porous plates, it might be appropriate here to mention that

Emanuel[15] has performed an analysis of this flow problem and some of his results may be used here to obtain an estimate of the pressure ratios required to choke porous plates. If reasonable estimates are made as to the form of the drag coefficients in the plate by using experimental data on the overall mass flow characteristics of the plates, then it seems that pressure ratios which are of the order of 200:1 are necessary to choke the porous plates employed. However, the analysis also shows that at pressure ratios as low as 5:1, a 10 per cent change in ambient condition produces only a 1 per cent change in mass flow; that is, for $p_o/p_{exit} \gtrsim 5$

$$\dot{m}_{plate} \sim P_0^2 \left[1 - (p_{exit}/p_0)^2 + \ldots\right]$$

So it can be concluded that the mass flow through the plate under the conditions employed ($p_0/p_{exit} \approx 10\text{-}40$) is determined only by the plenum pressure. Furthermore, the average Mach number of the flow at the tunnel side of the porous plate is quite low ($\lesssim 0.1$) and hence the flow possesses negligible momentum compared to the free-stream momentum.

Determination of spatial uniformity is not as straightforward. The plates were first inspected visually by immersing the models in a bath, injecting through the plate and noting the resulting bubble pattern formed. This crude inspection should indicate any large scale non-uniformities. The fine scale non-uniformities are more difficult to characterize. For model #1 (which should possess the largest non-uniformities because of the larger pore size) detailed surveys near the plate were made. Although the porous section is

best calibrated under actual tunnel operating conditions, this was not found practical in the present experiments, and instead, the assembled 25μ plate and plenum configuration was surveyed under atmospheric external conditions using a constant-temperature, hot-wire anemometer (DISA Model 55A01) and a specially-constructed, plate-facing Pitot tube. The wire used was 0.1 mil diameter platinum-rhodium, mounted between two needles approximately .030 inch apart. The Pitot tube used was composed of thin-wall stainless steel tubing with an outside diameter of about .040 inch.

Very close to the surface, some large spatial non-uniformities (as high as 50 per cent for the 25μ plate) in velocity were observed with both the Pitot and hot-wire probes. The wavelength of the fluctuations (for the hot-wire surveys) was about 0.04 inch and the mean velocities, calculated for lengths of this order, were found to be within $\pm$ 5 per cent of the overall plate average value, indicating no large-scale non-uniformity. Futhermore, the fluctuations decayed rapidly with distance from the surface, and at a distance of 0.1 inch were within $\pm$ 5 per cent of the overall mean value. The decay with distance away from the plate would be expected to be more rapid in the low-density tunnel operating conditions. Finally, and perhaps most important, the overall mean injection velocity at the plate calculated directly from the hot-wire measurements agreed in all cases within $\pm$ 5 per cent with the values obtained by taking the measured total mass flow to the plate and dividing by the ambient density and the measured plate surface area. Under tunnel operating conditions, the same agreement should exist between the mass flow per unit area

determined by dividing the total (measured) mass flow to the plate by the plate area and the mass flow measured directly. Hence, the quoted values of λ_∞ which follow can be considered accurate to within $\pm$ 5 per cent (including flowmeter inaccuracies). In all, however, it must be concluded that use of bench mounted hot-wire surveys to determine spatial uniformity of the porous plates leads to an inconclusive result as far as the details of the non-uniformities are concerned because of the complexity of the flow at the plate surface but may provide an indication of any large scale, spatial trends towards non-uniformity in injection.

II. 3. 2 Pitot and Hot-wire Instrumentation

The Pitot probes and hot-wire probes used in the experiments are shown in Figures II-10 and II-11. The Pitot tube tips used in the experiments were fabricated from 0. 065 o. d. stainless steel tubing with a tip flattened to 0. 008 inch by 0. 080 inch and an opening of about 0. 004 inch. Thus, readings to within 0. 004 inch from the wall were possible. The Pitot was pitched down at an angle of about 10° to the horizontal to allow minimum angle-of-attack effect within the injection layer. Experiments showed that the probes used in these tests were insensitive to angle-of-attack variations of $\pm 10^\circ$ for subsonic and supersonic flows. The hot-wire probes were constructed as shown in Figure II-11 and were used only to obtain qualitative fluctuation measurements in the layers; hence no pre-calibration was necessary.

The Pitot pressure and y-position data were recorded using a Statham pressure transducer (PA-208TC 50084; 0-10 psia) and a 40-turn Helipot (Model E) whose outputs were connected directly to

a Moseley x-y plotter. The horizontal and vertical Pitot drives used were accurate to within 0.001 inch. Pitot tube contact with the wall was determined electrically. Very near the surface of the plate, where the streamlines are strongly curved, the Pitot readings will have large errors because of the large angle of attack of the flow relative to the Pitot probe axis. The electronic instrumentation for the hot-wire fluctuation measurements has been described by Behrens[16] and both the spectrum (1-320KC) and mean square fluctuation signals were recorded for various of the test conditions.

II. 3. 3 Static Pressure Measurements

Wall static pressures were measured directly ahead of and behind the porous plate region. The pressure taps consisted of a 0.021 hole drilled into the wall which opened, after about 1/16" depth, into a larger section to maximize response time and minimize any possible leak effects. All static pressures were measured using mercury manometers which allowed for a repeatable reading within $\frac{1}{2}$ mm Hg. For the tunnel conditions in this experiment the error thus obtained is never greater than 2%.

In the porous region, the static pressure is quite difficult to measure directly. The use of standard pressure taps in the porous region may give results which are in error due to blowing, and, furthermore, any such taps may cause large non-uniformities in the injection distribution. In an attempt to circumvent this problem, pressure taps were installed on the fences of model #1 as shown in

Figures II-1 and II-2. The question now becomes one of determining the correlation between the values of pressure as measured by the fence taps and the porous-plate static pressure. For no injection, the fence pressure-tap values agreed with the normal static taps ahead of and behind the model within a few per cent.

For the case of injection, the following procedure was followed. First, Pitot traces were taken from the wall out to and across the induced shock wave for the injection rates of interest. Figure II-12 shows a typical Pitot trace taken (with side fences) at an intermediate injection rate. Two points are worth mentioning. The first is that the raw Pitot traces were found to be similar when scaled with the thickness as determined from the maximum slope intercept shown in Figure II-12. The second is that, unlike normal turbulent boundary-layer Pitot profiles, the traces for large injection are quite inflected near the wall (i. e., slowly varying).

Using the measured jump in Pitot pressure across the shock wave and knowing free-stream conditions, the static pressure and flow deflection angle just behind the shock wave were calculated from the oblique shock equations. The angle was checked with that measured from the schlieren photographs. As seen, the flatness of the Pitot trace from the boundary-layer edge to the shock for various x-stations and the uniformity of the shock Pitot-pressure jump indicate a uniform (constant pressure) flow behind the shock.

Secondly, the fact that the Pitot pressure is slowly varying near the wall indicates that, regardless of angle of attack, the flow near the wall has a very small dynamic pressure, and the Pitot

reading should be close to the static pressure. If this is so, then very near the wall there should be only a negligible effect of Pitot orientation. To verify this idea, a Pitot tube with an opening facing the plate was constructed and vertical traverses made. Near the wall, good agreement was found between pressure measurements obtained with the modified and standard probes. This result indicates the validity of the above hypothesis.

Finally, all four of these pressure values, i.e., the fence values, the values deduced from the shock jump, the plate-facing Pitot value, and the value for the standard Pitot at the wall, were compared in the region where similar flow was observed from the raw Pitot data. For all injection rates, these data agreed within 8 per cent, and thus show that the fence taps give a valid value of plate static pressure and indicate the absence of any appreciable y-pressure gradient.

In the region near the end of the plate, where the abrupt cessation of injection dominates the flow and causes severe streamline curvature, the readings from the fences were used alone to determine the pressure. As would be expected from the preliminary discussion, a positive pressure gradient in the y-direction was indicated in this region by the side-fence taps, and this gradient shows the effect on the flow of the rapid expansion near the end of the injection.

Figure II-13 is a composite of the static pressure data obtained

in this manner for the various injection rates investigated. * The good agreement obtained for model #1 indicated that for the ramp models (#2 and #3) the value of pressure determined from the wall Pitot value and the value deduced from the Pitot edge value would give an adequate value of the static pressure in the similar region and hence the fences for these models were not fitted with fence pressure taps as for model #1.

II. 3. 4 Data Reduction Procedure

The Pitot data were reduced by using the measured static pressure and the Rayleigh Pitot formula to calculate the Mach number distribution. No corrections were made for the effect of angle of attack on the Pitot data, since at least two other effects must be included in this region to correct the Pitot data accurately. The first is the effect of Reynolds number on the reading, because the region of high angle of attack is also the region of low flow velocities and low densities. The second effect is that of the wall on this measurement. Hence, the data presented can be expected to be in error (large relative error but small absolute error) near the wall.

The final assumption made concerns the total temperature distribution in the layer. Since both the tunnel and model plenums are at room temperature, it was assumed that the total temperature everywhere in the layer was equal to room temperature. With these assumptions, then, the velocity profiles were obtained and relevant

---

*Note that for the highest injection rate, a small, but noticeable, pressure drop seems to exist over most of the porous plate. This effect will be referred to in later sections.

integral properties were calculated using standard integration techniques and formulae.

II. 4 Experimental Results

II. 4. 1 Similarity

The Pitot tube traces, the schlieren photographs and the hot-wire fluctuation measurements discussed in the previous section suggest that a region of flow over the porous plate exists where the velocity profiles are self-similar for models #1 and #2, i. e., scale linearly with the distance along the surface, x. Examples of this similarity are shown in Figures II-14-17 for model #1 and Figure II-18 for model #2. Note that in Figure II-17 ($\lambda_e \approx .029$) the approach to similarity is not as well defined as in the previous figures. This effect might be expected since, for this injection rate a small, but noticeable, pressure gradient exists on most of the porous plate (Figure II. 13). In these figures, the momentum thickness has been used to normalize the y-coordinate, simply because it is subject to minimum experimental error as compared, for example, with the mixing layer edge. For both models #1 and #2 it is seen that in about 5-10 initial boundary thicknesses the velocity profiles become independent of x. This similarity continues until one reaches the rear region of the plate where the effect of the rapid expansion destroys the similarity. Of course, the fact that mean flow profiles appear similar does not necessarily indicate a self-similar turbulent flow and the small physical scale of this experiment could certainly be subject to criticism.

In order to try and verify this approach to similarity, hot-wire surveys were made at various stations on the porous plate for both models #1 and #2. Figures II-19-21 show some of the results. In Figures II-19-21 the mean square fluctuation value of the hot-wire voltage is plotted as a function of distance normal to the wall, y/δ. The value of δ used to normalize the y scale was obtained from the maximum slope intercept of the hot-wire data. Although quantitative reduction of the hot-wire data is extremely difficult in this flow, the raw hot-wire output can be used to check for similarity. These figures show traces taken at various stations on the plate at bandwidth of 1-320 KC. The rapid adjustment of the fluctuations from the no-blowing values to a reasonably similar trace would seem to verify the previous conclusions drawn from the mean flow data. Note that Figure II-21 represents the data obtained on model #1 for injection with helium and also indicates this rapid approach to similarity.

Several other interesting results can be obtained from the hot-wire data. In Figure II-22, the edge of the hot-wire signal is compared with that obtained from Pitot surveys for an intermediate injection rate (both edges determined from the maximum slope intercept). For the same injection rate, Figure II-23 shows measured hot-wire fluctuation readings as a function of the mean flow velocities. Unfortunately, this result, which is representative of the results for most injection rates, indicates that both the mean velocity levels and the hot-wire fluctuation measurements are low near the wall; hence any accurate determination of the relative magnitude of

velocity fluctuations in this region will be quite difficult. Figure II-23 shows that the peak value of fluctuation intensity occurs when $u/u_e \approx 0.75$. This is to be compared with the point of maximum shear stress which occurs at $u/u_e \approx 0.6$ (Figure II-40).

Finally, if the flows are indeed approaching a self-similar state, then spectrum measurements taken at, say, the peak point in the fluctuation data should be invariant with distance. Figures II-24 and II-25 present such typical results for models #1 and #2. The spectra are seen to be quite close except at low frequencies which might indicate the effect of the finite initial boundary-layer thickness. In these figures the integral quantity $u_e/L \equiv 4\int_0^\infty \frac{E}{E(0)}\,df$ has been used to normalize the frequency scale, where E is the mean square signal strength, E(0) is the value at zero frequency. The integration has actually been terminated at f = 320 KC, the limit of the instrumentation. For the injection rates shown in Figures II-24 and II-25 the quantity u_e/L calculated as shown above is initially a function of distance along the plate and seems to approach a constant. If the induced flow angles are measured then u_e can be obtained and, hence, L. For the injection rates shown in Figure II-25 L varies from 1.9×10^{-2} inch (x = 0.4 inch) to 2.5×10^{-2} inch ($x \gtrsim 1.6$ inch). For Figure II-24 L varies from 4.8×10^{-2} inch (x = 0.37 inch) to $L = 4.6 \times 10^{-2}$ inch ($x \gtrsim 1.0$ inch). The fact that L approaches a constant in both these cases would seem to indicate that the contribution to the integral scale from the low frequencies is less important as one approaches a similar flow.

For the 20^{o} ramp configuration (model #3) it was found that a constant pressure region could not be maintained and that similar flow could not be achieved as with the other two models. It is felt that this is primarily due to the effect of cessation of injection, an effect which is discussed in more detail in Part III. Since this result is anomalous to the ones observed for both models #1 and #2, a discussion of the data obtained on model #3 is left to the end of this section and is discussed in more detail therein.

II. 4. 2 Two Dimensionality and Induced Flow Angles

The question of two-dimensionality of the flow is not as straightforward to decide as is similarity. For example, if the flow is two-dimensional, spanwise pressure measurements taken ahead of and behind the model should be uniform (as indeed they are in these experiments). The converse, however, is not true. Two methods were used to check for the two-dimensionality of the flow. The first was to integrate the continuity equation from the wall to the edge of the layer for model #1 and model #2. In this case, one obtains

$$\frac{v_e}{u_e} \equiv \tan \Theta = \frac{d\delta^*}{dx} + \lambda_\infty \frac{\rho_\infty u_\infty}{\rho_e u_e} - \frac{(\delta - \delta^*)}{\rho_e u_e} \frac{d}{dx}(\rho_e u_e) \qquad \text{(II. 1)}$$

where $\delta^* = \int_0^\delta (1 - \rho u/\rho_e u_e)dy$

$\lambda_\infty = \rho_w v_w / \rho_\infty u_\infty$ (II. 2)

Θ = the inviscid flow angle at the edge of the layer

δ = the location of the edge of the layer

and where the subscripts (e) refer to quantities at the edge*. The quantities contained on each side of equation (II. 1) can be obtained independently from experimental measurements, and for constant edge pressure, the last term in equation (II. 1) contributes nothing. Figure II-26 presents a check of this equation for model #1. In Figure II-26, the angle Θ deduced from the schlieren-measured shock angle and the results obtained by evaluating the right side of equation (II. 1) from the measured velocity profiles are plotted as a function of λ_∞. The good agreement between the values of Θ calculated by the two methods indicates that the flow is very close to two-dimensional.

Figure II-26 also shows independently one of the more interesting results of the experiment: Θ, the induced angle of flow deflection due to surface injection. It is seen that for λ_∞ as low as 0. 03, deflection angles greater than 10° are induced, and these large angles produce significant pressures and side forces. The value of Θ increases very nearly linearly with λ_∞ up to about $\Theta = 12^\circ$ at $\lambda_\infty = 0.03$ and more slowly for larger values of λ_∞. The maximum value obtained for model #1 is fixed by the upstream separation phenomena described in Section II. 2. 2. 1.

For model #2, the resulting plots of δ^* is shown in Figure II-27. Since, for this model, the angle is fixed at 10°, the calculations shown in Figure II-27 show the resulting mass balance. The

---

*Since there may be some confusion concerning the notation used in these equations, and those which follow, the convention will be summarized here. Subscript (∞) always refers to the free stream. Subscript (e) always refers to quantities at the edge of the layer. For model #1, $M_\infty \neq M_e$ because of the shock, while for model #2 $M_\infty \approx M_e$.

results for the 10^{o} ramp cannot be plotted on the same graph as those for the flat plate model because, for this flow angle and edge Mach number, they essentially represent flat plate flow at $M_{\infty} \approx 3.3$.

A second check of two-dimensionality is to consider the integrated x-momentum equation. Assuming a boundary-layer type flow, one obtains, for zero x-pressure gradient, the result

$$\frac{d\theta}{dx} = \lambda_e \left[1 + C_f/2\lambda_e\right] \tag{II. 3}$$

where $\theta = \int_0^{\delta} \frac{\rho_u}{\rho_e u_e}(1-u/u_e)dy$, $C_f = \tau_w/\frac{1}{2}\rho_e u_e^2$, $\lambda_e = \rho_w v_w/\rho_e u_e$

For the injection rates of this experiment, it can easily be shown that $C_f/\lambda_e << 1$, so that to a first approximation,

$$\frac{d\theta}{dx} \cong \lambda_e \quad \text{or} \quad \theta = \theta_0 + \lambda_e x \tag{II. 4}$$

if the flow is two-dimensional. Figures II-28 and II-29 present the values of θ obtained from the flat plate and 10^{o} ramp velocity profiles plotted versus x and the slopes required to agree with equation (II. 4). At the highest injection rate, where the uncertainty in calculating θ is a maximum, the deviation is about 10 per cent, and it is much less at lower injection rates.* Hence, both methods indicate that a reasonably two-dimensional flow has been achieved. (Note that without the fences, agreement achieved by either method was noticeably worse.)

---

*As noted previously, at the highest injection rate a falling pressure was observed over a good deal of the porous plate. As will be shown later (Equation II. 21) this falling pressure (Figure II-13) is sufficient to produce the noted discrepancy.

To illustrate the importance of fences, Figure II-30 presents the values of $\Delta\theta/\Delta x$ obtained for the flat plate without fences and the resulting discrepancy in slopes required for two dimensionality.

II. 4. 3 Similar Flow Profiles

Since it has been shown that a similar, two-dimensional flow is approached, the velocity profiles measured in the similar region should be unique, i. e., should be independent of such incidental experimental details as the initial boundary-layer thickness, and should depend only on such parameters as Mach number or blowing rate. From equation (II. 1), it is seen that the natural parameter for the blowing rate is $\lambda_e = \rho_w v_w / \rho_e u_e$, where the subscripts e denote conditions at the edge of the layer. Plots of u/u_e versus y/θ are shown in Figure II-31 for the flat plate. By increasing the value of λ_e, a whole range of profile shapes can be obtained. At the highest injection rates, the velocity profiles are fully inflected and seem to approach the free mixing-layer curve. Note that despite the great change in profile shape, the thickness of the layer, in terms of the momentum thickness, does not change greatly and remains close to $10\,\theta$ for $\lambda_e \gtrsim 0.004$ (compared with the no injection value at this Mach number $\delta \approx 13\,\theta$).

Figure II-32 presents the velocity profiles for the 10^o ramp and those for a similar injection rate for the flat plate. The difference in these profiles at the same value of λ_e will be shown in a following section to be well accounted for by the compressibility effect due to difference in edge Mach number as indicated in Figure II-32.

Table II. 1 presents the value of Pitot pressure for the data presented in Figures II-31 and II-32 together with the calculated velocity profiles and integral parameters. In Table II. 2, the non-similar data are presented for completeness.

II. 4. 4 Compressibility and Turbulent Mixing

Two difficult questions which have not yet been answered for this type of flow are: first, the question of the effect of density variation across the layer on the mean flow quantities; and second, the process by which the turbulent fluid motion entrains the mass injected at the wall and mixes it with the external flow. Since a direct experimental explanation of the second question in supersonic flow is extremely difficult, it is useful to attempt first to determine the overall effects of compressibility on the mean flow properties. If this can be done, then low-speed experiments, where direct, quantitative measurements of turbulent shearing stress are considerably simplified, can be used to help understand the mixing. As stated previously, the data of McQuaid[9] include moderately high injection rates, and his careful monitoring of pressure by adjusting the tunnel walls ensures a minimum pressure gradient in the flow direction. In addition, because the results of Figure II-31 indicate that boundary-layer velocity profiles approach the free-mixing layer values for large injection rates, the mixing-layer data of Liepmann and Laufer[17] will also be useful for comparison with the results obtained at the high injection rates.

According to Coles[18], sufficient conditions for transformation of a boundary-layer flow from a low-speed or incompressible

flow (barred quantities) to a compressible flow are:

$$\bar{\psi}/\psi = \sigma(x); \quad d\bar{x}/dx = \xi(x); \quad \bar{\rho}\partial\bar{y} = \eta(x)\rho\partial y \tag{II. 5}$$

A result of this transformation is

$$\bar{u} = [\sigma(x)/\eta(x)]\, u \tag{II. 6}$$

which implies that at corresponding points

$$u/u_e = \bar{u}/\bar{u}_e \tag{II. 7}$$

From (II. 5)

$$\bar{\rho}\,\bar{y} = \eta(x) \int_0^y \rho dy \tag{II. 8}$$

where we assume $\bar{y}\,(y = 0) = 0$, i. e., assume wall transforms into wall. The momentum thickness is given by:

$$\theta \equiv \int_0^\infty \rho u/\rho_e u_e\,(1-u/u_e)dy = \frac{1}{\eta(x)} \int_0^\infty \bar{u}/\bar{u}_e(1-\bar{u}/\bar{u}_e)\bar{\rho}/\rho_e\, d\bar{y}$$

or

$$\bar{\rho}\,\bar{\theta} = \eta(x)\, \rho_e\theta \tag{II. 9}$$

Combining (II. 8) and (II. 9), one obtains

$$\bar{y}/\bar{\theta} = \int_0^y \rho/\rho_e\, d(y/\theta) \tag{II. 10}$$

at corresponding stations, which is a general form of the Howarth-Dorodnitsyn transformation.

If the transformation shown in equation (II. 10) is applicable and if the only relevant parameter is the mass flow at the wall

normalized by the edge value, λ_e, then the velocity profile $u/u_e(\bar{y}/\bar{\theta})$ obtained at $M_\infty = 2.6$ should agree with the low-speed data obtained for the same value of λ_e (for large injection where $C_f/\lambda_e << 1$). *

Figure II-33 shows a comparison of the present data with the subsonic data for the injection rates closely corresponding to McQuaid's[9] experiments. Also shown are the profiles obtained at the largest injection values and the data of Liepmann and Laufer[17]. The good agreement indicates that for large injection rates the normalized velocity profiles do depend only on the properly normalized mass flow rate. Note that at $M_\infty = 2.6$ (compare Figures II-31 and II-33), the transformation shown in equation (II.10) gives a reduction in scale of about a factor of two. Hence, the good agreement between compressible and incompressible data is a sensitive check on the transformation.

The profile obtained at the highest injection value also agrees well with the data of Liepmann and Laufer except near the wall. This discrepancy is to be expected, since the maximum injection rate shown is about 10-20 per cent lower than the value obtained for their mixing layer. It should be noted that in comparing the profiles for this case the $u/u_e = 0.5$ line has been picked to match.

Another check on the effect of compressibility can be obtained from the data shown in Figure II-32, which compares model #1 and #2. If the scale normal to the wall is transformed as shown in

---

*Note that this statement represents an assumption which must be verified by comparison with low-speed results. It is not a necessary condition.

equation (II. 10), the profiles in II-32 can be shown to collapse onto each other as shown in Figure II-34. This good agreement shows the consistency of the transformation for fixed λ_e and varying edge Mach number.

The success of the transformation in comparing the velocity profiles suggests that the form parameter $H = \delta^*/\theta$ can be similarly correlated. With the assumption of constant total temperature and the transformation of equation (II. 10), one can show that

$$H = \delta^*/\theta = \left[\frac{\gamma-1}{2} M_e^2 + \left(1 + \frac{\gamma-1}{2} M_e^2\right) \overline{H}\,(\overline{\lambda}_e)\right] \qquad \text{(II. 11)}$$

where $\overline{H} = \overline{\delta}^*/\overline{\theta}$ is the value for an incompressible flow.

Equation (II. 11) is valid for, say, air to air injection. For the injection of a foreign gas, an estimate can be made for the transformation of the form parameter, H, if it is assumed that the momentum, mass and energy diffusivities are equal. As is shown in Appendix II-A, the induced angle for the flow with injection is approximated by

$$\mathrm{Tan}\Theta \cong \lambda_e\left(1 + \frac{\gamma-1}{2} M_e^2\right)\left[1 + \frac{\mathcal{M}_{w_{air}}}{\mathcal{M}_{w_{inJ}}} \overline{H}\right] \qquad \text{(II. 12)}$$

where $\mathcal{M}_w$ is the molecular weight of the gases in question. For air to air injection, where velocity profiles are available, equation (II. 11) can be used to give $\overline{H}$. For foreign gas injection, equation (II. 12) should provide a reasonable estimate of the variation of $\overline{H}$ with the

injection parameter, λ_e. If direct concentration, velocity and temperature measurements are available, equation (II. 12) is not necessary and $\overline{H}$ can be calculated directly from the data.

In order to test the density transformation, helium was injected through model #1 and the resulting induced flow angles were recorded from schlieren data. Then, using equation (II. 12), $\overline{H}$ as a function of λ_e can be calculated for any set of known freestream conditions by iteration. Figure II-35 shows the values of $\overline{H}$ determined from equation (II. 11) using the measured values of M_e, δ^*, and θ at $M_\infty = 2.6$, and the values for helium injection obtained from equation (II. 12). These are to be compared with the results of McQuaid (M = 0). Also included in Figure II-35 are the values of $\overline{H}$ calculated directly from the data of Mugalev[12] at $M_\infty = 2.5$ for air to air and CO_2-air injection, the results of Danberg[19] at $M_\infty = 6.2$, and the results obtained herein on the 10^o ramp (model #2). The agreement is good for the range where overlap exists. Furthermore, at the highest injection rate where the boundary layer is nearly separated, the value of $\overline{H}$ obtained from the experiments is close to the value for separated flows (~4).[33] Hence, it appears that $\overline{H}$ can be expressed solely as a function of λ_e for large injection rates regardless of density variation, and that the limiting velocity profile reached at $\lambda_e \cong 0.03$ is the mixing-layer profile.

II. 4. 5 Flow Angle and Shear Stress Distribution

With similar flow established, it is possible to use the velocity profiles shown in Figure II-31 to calculate the flow angles through the layer and the shear stress distribution if one assumes boundary-layer

flow. The equations in the zero pressure-gradient similar region are:

continuity $$(\rho u)_x + (\rho v)_y = 0 \qquad \text{(II. 13)}$$

momentum $$\rho u u_x + \rho v u_y = \tau_y \qquad \text{(II. 14)}$$

Integrating (II. 13) from y = 0 to $y = \tilde{y}$,

$$\frac{v}{u}(\tilde{y}) = \lambda_e \left(\frac{\rho_e u_e}{\rho u}\right) - \frac{\rho_e u_e}{\rho u} \frac{d}{dx} \left\{ \int_0^{\tilde{y}} \rho u / \rho_e u_e dy \right\} + \frac{d\tilde{y}}{dx} \qquad \text{(II. 15)}$$

For similar flow, $\rho u/\rho_e u_e = f(y/\theta)$ and $d\theta/dx \cong \lambda_e$, so equation (II. 15) gives

$$\frac{v}{u} = \lambda_e \left[\frac{\rho_e u_e}{\rho u} - \frac{\rho_e u_e}{\rho u} \int_0^{\tilde{y}/\theta} \rho u/\rho_e u_e d(y/\theta) + \tilde{y}/\theta \right] \qquad \text{(II. 16)}$$

Similarly, integrating equation (II. 14) and using equation (II. 16), one gets

$$\frac{\tau - \tau_w}{\rho_e u_e^2} = \lambda_e \left\{ \frac{u}{u_e} - \frac{u}{u_e} \int_0^{\tilde{y}/\theta} \rho u/\rho_e u_e d(y/\theta) + \int_0^{y/\theta} \frac{\rho u^2}{\rho_e u_e^2} d(y/\theta) \right\} \qquad \text{(II. 17)}$$

where τ_w is the wall shear stress. Equations II. 7 and II. 10 can be combined with equation II. 17 to yield a density invariant at corresponding stations. Combining these we get

$$\frac{\tau - \tau_w}{\lambda_e \rho_e u_e^2} = \frac{\overline{\tau} - \overline{\tau}_w}{\overline{\lambda}_e \overline{\rho}\, \overline{u}_e^2} \qquad \text{(II. 17-a)}$$

at corresponding stations in the flows. This result is the basis for some of the plots of shear stress shown later in the text (Figures II-38-II-40). Figures II-36 and II-37 show the results of equations (II. 16) and (II. 17) as applied to the data presented in Figure II-30. From these equations, one sees that the minimum value of v/u and the maximum value of $\tau - \tau_w/\rho_e u_e^2$ occur when

$$\int_0^{y/\theta} \rho u/\rho_e u_e d(y/\theta) = 1 \qquad \text{(II. 18)}$$

The dividing streamline ($\psi = 0$) is defined by

$$\int_0^y \frac{\rho u}{\rho_e u_e} dy = \int_0^x \frac{\rho_w v_w}{\rho_e u_e} dx \qquad \text{(II. 19)}$$

For constant injection and similar flow with $\frac{d\theta}{dx} = \lambda_e$, equations (II. 18) and (II. 19) are the same if the initial boundary layer is zero thickness. The effect of finite initial boundary-layer thickness is to cause a discrepancy in the calculated maximum in shear stress and the dividing streamline location as determined from equation (II. 19). Hence, for a truly similar flow, independent of initial boundary-layer thickness, the maximum value of shear stress, and the minimum flow angles should occur along the dividing streamline. In Figures II-36 and II-37, the point $\psi = 0$ determined from (II. 19) (a mass balance) is plotted. The close agreement with the maximum of τ and minimum of v/u is still another check on the two-dimensional, similar nature of the experimental flow. It should be emphasized that in using equation (II. 19), x is the actual distance from the beginning of the porous plate and has not been corrected for any virtual origin effects. It might also be noted that factors other than the initial boundary-layer thickness might cause the small bias shown in Figures (II. 36) and (II. 37), for example, the assumption of constant total temperature or the effect of Pitot probe angle of attack might be responsible.

Figure II-36 also indicates the region where large errors in the Pitot tube readings are important because of angle-of-attack effects. The most important result shown in Figure II-37 is that, although the shear stress at the wall is expected to be quite small, the maximum shear stress in the layer is several times the maximum value in the boundary layer with no injection, and this result emphasizes the importance of turbulent mixing in this problem. For example, for the

approaching boundary layer at the Reynolds number and Mach number of these tests ($Re\theta \approx 2000$, $M_e = 2.6$), $C_{f0} = 2\tau_w/\rho_e u_e^2 \cong 0.0025$. At the highest injection rate shown in Figure II-37, $\tau_{max}/\rho_e u_e^2$ $\lambda_e = .029 \approx .01$, and this value is about four times larger than C_{f0}. If one assumes Newtonian shearing stress, then at the wall one obtains (from Figure II-31)

$$\left.\frac{\partial(u/u_e)}{\partial y/\theta}\right)_{\lambda_e \approx .03} < .05$$

So,

$$\left.\frac{\tau_w}{\rho_e u_e^2}\right)_{\lambda_e \approx .03} = \frac{1}{Re\theta}\,\frac{\mu_w}{\mu_e}\,\frac{\partial(u/u_e)}{\partial(y/\theta)} < 5 \times 10^{-6}$$

for $\theta \approx .09''$ and $Re/inch \approx 2.2 \times 10^5$. Hence, for these high injection rates, the wall stress is of no importance.

As a further check on the compressibility, the maximum value of $\frac{1}{\lambda_e}\,\frac{\tau}{\rho_e u_e^2}$ is plotted as a function of λ_e in Figure II-38 and compared with the results of McQuaid[9] and Simpson[10]. As is shown in Appendix B of this part $\frac{1}{\lambda_e}\,\frac{\tau_{max}}{\rho_e u_e^2}$ should be an invariant for a free shear layer ($\tau_w = 0$) and Figure II-38 shows the variation of this quantity with injection rate and the asymptotic value of Liepmann and Laufer at $M = 0$.

An interesting plot of the data is shown in Figures II-39 and II-40 where τ/τ_{max} is plotted as a function of velocity for various injection rates. In Figure II-40, the incompressible data of Simpson[10] and Liepmann and Laufer[17] are also included. The plot shows

an interesting insensitivity of the normalized shear stress curve to both density and injection rate when $C_f/\lambda_e << 1$. This insensitivity is most apparent in the outer (wake) portion of the layer, where $u/u_e \gtrsim 0.5$. The determination of an eddy viscosity from mean flow profiles involves differentiating data and is thus subject to large errors. Nevertheless, such information may be useful for future applications. Figure II. 41 presents the value of the derived eddy viscosity normalized by the maximum value for the velocity profiles previously presented. In differentiating the data, a five point smoothing was used. A quartic was least squares fitted to successive sets of points and the derivative was calculated for the central point in a set by differentiating the resulting polynomial. The shear stress was calculated using equation (II. 17) and the eddy viscosity was obtained from $\epsilon = \tau/\rho \frac{\partial u}{\partial y}$. In Figure II. 41, the transformed eddy viscosity is plotted $[\tilde{\epsilon}/\tilde{\epsilon}_{max} = (\rho/\rho_e)^2 \epsilon/\epsilon_{max}]$. For completeness both the transformed and untransformed values of eddy viscosity are tabulated in table II-1. The maximum value of $\tilde{\epsilon}$ is included in section III, Figure III-6. Although there is considerable scatter, it appears as if $\tilde{\epsilon}/\tilde{\epsilon}_{max}$ certainly varies across the layer with a roughly parabolic shape. This effect has been experimentally observed in other types of flows with low skin friction. [39, 40]

Finally a physical picture of the flow field can be obtained from the data presented thus far. Figures II-42 or II-43 show the streamline pattern calculated for an intermediate injection rate. In Figure II-43 the effect of the termination of injection is quite

pronounced and is discussed in more detail in Part III of this thesis.

II. 4. 6 Induced Side Forces

Another result which can be obtained from the data is the induced side forces caused by the interaction of the injectant with the external stream. Assuming that $C_f/\lambda_e << 1$ and that $\overline{H} = \overline{\delta}^*/\overline{\theta}$ can be expressed only as a function of λ_e (regardless of density ratio across the layer) and using a Crocco integral relation for the total enthalpy in the layer, Lees[20] has combined the integral form of the boundary-layer continuity and momentum equations to obtain the following expression for the induced angle:

$$\text{Tan}\Theta = \lambda_e \left[1 + \frac{\gamma-1}{2} M_e^2\right]\left[1 + Tw/T_{t\infty}\, \overline{H}\,(\lambda_e)\right] \qquad \text{(II. 20)}$$

By an iterative process, it is possible to obtain $\Theta(\lambda_e, M_e)$ or $\Theta(\lambda_\infty, M_\infty)$ from the above equation and Figure II-35.

Calculations of the total side force produced by injection were made without taking account of up- and downstream end effects, and consequently the total force for a plate of length L and unit width was calculated from $F = (P_e(\Theta) - P_\infty)L$. Values of F normalized by the thrust of a sonic jet of the same mass flow rate flowing into a vacuum, F_{sv}, were calculated for $2.6 \leq M_\infty \leq 8$; $0 \leq \Theta \leq 14^o$, $\gamma = 1.4$ and $0.33 \leq T_w/T_{t\infty} \leq 1.5$.

As would be expected from the excellent agreement between calculated and measured values of $\Theta(\lambda_\infty)$, shown in Figure II-26, calculated and experimental values of F/F_{sv} for the $M_\infty = 2.6$ case agree well. The thrust ratio increased from 2. 9 for very small

values of λ_e to 3.5 at the maximum blowing rate of 0.03 = λ_e. In addition, calculated values of F/F_{sv} were within $\pm$ 10 per cent of 3.2 for the whole range of parameters examined in the calculations. This value is slightly larger than similarly normalized side forces obtained experimentally for concentrated injection of gases from narrow slots and into supersonic streams. (21)

Hence, it appears as if the thrust ratio obtained by injection into a supersonic stream is quite insensitive to the manner in which the fluid is injected (slot or porous plate). This result may have some interesting implications for future design of control surfaces.

II. 4. 7 Results Obtained on Model #3 (20° Ramp)

As has been mentioned previously, it was not possible to obtain a similar flow region for the 20° ramp model. This model configuration was chosen on the basis of the results obtained previously. For Mach number ≈ 2.6 it should represent a fully "blown off" condition for constant pressure. Experimentally it was observed that the pressure in the layer was always dropping. Furthermore, if the effect of falling pressure is neglected, neither a mass nor momentum balance can be achieved. Figures II-44 and II-45 present the computed displacement thickness and momentum thickness variations observed for this model and indicate the large discrepancy between these results and the behavior expected for a constant pressure flow. Although the variation appears linear, it was found that the velocity profiles could not be scaled with, say, y/θ (Figure II-46). However, and this result may have some bearing on mixing layer experiments,

if the velocity profiles are plotted from some arbitrary point as origin, instead of the wall (where it is known u = 0), then it would appear that the flow is similar for $.2 < u/u_e < .95$ (Figure II-47). Thus, care must be exercised in interpreting compressible mixing layer experiments. The low velocity tails on the profiles can have large effects on the deduced entrainment values and, unfortunately, are subject to large experimental errors. Table II. 3 presents a summary of the data obtained for model #3 and shown in Figures (II-42 - II-47).

It is postulated here that this behavior observed on the 20^o model was due primarily to the falling pressure induced by the termination of injection. That is, an a priori assumption of constant pressure in the transition region from the porous to the non-porous section requires that the slope of the momentum thickness and the slope of the shape factor H possess jump discontinuities which are determined from, say, equation II. 1 and II. 4. Such discontinuities cannot be tolerated by a viscous flow and, hence, unless special care is taken in tailoring the geometry of the non-porous section, a pressure gradient will be generated due to viscous inviscid interaction similar to that observed in flow approaching an expansion corner. For example, at this injection rate, including the pressure gradient term the integrated momentum equation becomes

$$\lambda_e - \frac{d\theta}{dx} \cong \frac{\theta}{M_e} \frac{dM_e}{dx} \frac{H + 2 - M_e^2}{(1 + \frac{\gamma-1}{2} M_e^2)} \qquad \text{(II. 21)}$$

using $\lambda_e = 0.04$

$$\frac{d\theta}{dx} = 0.028$$

$$H \approx \frac{\gamma-1}{2} M_e^2 + (1 + \frac{\gamma-1}{2} M_e^2)H_i, \quad H_i \approx 4 \text{ (for a separated flow)} \tag{II. 22}$$

$$M_e = 2.67$$

gives

$$\frac{\theta}{M_e} \frac{dM_e}{dx} \approx .005 \tag{II. 23}$$

at the midpoint of the plate $\Delta x \approx 2''$, $\theta \approx .05''$

$$\frac{\Delta M_e}{M_e} \approx 20\%$$

So, the discrepancy between $d\theta/dx$ and λ_e can be accounted for by an overall change of about 20% in the Mach number over the plate which is of the order of that which was observed. This may possibly be alleviated by redesign of the region downstream of injection to approximate the final streamline leaving the wall. The difficulty in calculating the proper streamline shape stems from the fact that the actual flow for which the shape is to be calculated is not known. However, assuming that for model #3 it is very close to a mixing layer and using the compressibility transformation cited in the text, a first approximation to the shape can be computed from, say, the data of Liepmann and Laufer.[17] This shape can now, conceivably, be iterated upon to try and maintain a constant pressure region.

II. 4. 8 Effect of Finite Plate Length for Model #1

This short section may be considered as a prologue to the

third part of this thesis and repeats some of the results already cited in some of the previous sections. However, it is felt that the effect of the end of injection is important enough to warrant several further comments.

Since the effect of large injection is to cause inflection of the mean velocity profiles and to move the sonic line away from the wall, the fact that the porous plate is finite in length could be felt upstream. The termination of injection causes an abrupt expansion of the flow with noticeable pressure variations normal to the wall and large pressure gradients in the streamwise direction. This effect is also readily observed in the velocity profiles.

For all injection rates examined, the effect of the rapid expansion is felt about two layer thicknesses upstream. Since the induced angles depend only on λ_e and M_e, it seems reasonable to suppose that, in any experiment which attempts to investigate higher injection rates than the present values, the "few" thicknesses which are influenced by the end of the porous region will essentially cover the entire porous plate. For example, if the induced angle is 20°, and if the corner effect propagates upstream 2-3 layer thicknesses, then it is easily seen that regardless of the plate length, about 75-100 per cent of the plate will be dominated by the effect of the termination of injection (see for example Section II. 4. 5).

Hence, any theoretical analysis of the flow field produced by injection rates much larger than the maximum used here must include this downstream interaction region. In this case, the flow will not be similar over most of the injection region.

II. 4. 9 Some Comments on Constant Pressure Mixing

The results quoted in the experiments which have been described seem to indicate that as injection is increased the boundary-layer velocity profile approaches a free mixing layer shape. The value of mass injection at which this seems to occur is close to the value of entrainment which has been observed for the incompressible mixing layer.

However, an important discrepancy exists between these results and the correlation Alber[22] obtained for compressible mixing layers. In examining available data on these layers Alber found that the mass entrained on the low speed side of these layers was proportional to the square of the density ratio across the layer. In the blowing experiments, the ratio of edge density to that at the wall is about two. If the maximum amount of mass which can be entrained by the constant pressure boundary layer corresponds to the free shear layer entrainment value (which is the case for laminar flow)[23, 24] Alber's correlation predicts an entrainment rate about 300% too low. *

The experimental data used by Alber in his correlation came from two sources: supersonic experiments by Maydew and Reed[25] and by Sirieix and Solignac.[26] In an attempt to explain the discrepancy, a careful study of these two sets of data was performed.

---

*The data of Danberg[19] presented in Figure II-35 is at an injection rate which according to Alber's correlation is already 3 times that which can be entrained by the mixing layer at that edge Mach number. Clearly, Danberg's results do not represent a "blown off" boundary layer.

The data from Maydew and Reed in an axisymmetric experiment were treated by Alber as two-dimensional. The first point worth mentioning concerns the actual discrepancy in the momentum thickness variation obtained directly from Maydew and Reed's data and that of the present report (Model #1) at the highest injection rate (for the same edge Mach number). Assuming a two-dimensional flow for their data, the author has re-calculated $\frac{d\theta}{dx}$ from their data and found that $\frac{d\theta}{dx}_{M_e \approx 2.0} = 0.015 \pm 0.002$. For the present work, at the highest injection date, $\frac{d\theta}{dx}_{Max} \approx 0.025$ (see Figure II-28). Hence, Alber's correlation underpredicts the data for this case. A second point is that the data were obtained in the potential core region of flow exiting from a circular pipe. Because of this, two effects are evident in the data which, it is felt, may strongly influence the discrepancy in entrainment. The first is the axisymmetric effect. The fact that the zero streamline must be displaced a few degrees in order to satisfy the symmetry boundary condition on the pipe centerline has been investigated and can be shown to cause an increase of about 30% in the entrainment values deduced from considering only the growth of momentum thickness. That is, if, for axisymmetric flow, θ is defined in the manner used throughout the text, $\frac{d\theta}{dx} \neq \lambda_e$. The effect of the zero streamline displacement enters directly into the determination of the low-speed side mass entrainment rate. If this 30% difference is applied to the previously mentioned results, the difference in entrainment rates for these two experiments is less than 30%. Hence, no great discrepancy actually seems to exist between the two sets of data if they are properly interpreted. Secondly, and perhaps

more importantly, it has been calculated that the induced flow at the low-speed side of the layer is not characterized by zero longitudinal velocity ($u_{-\infty}$) (see for example, Taylor[27]). This may be an important difference between the mixing layer results and those obtained using a porous plate where a no slip condition (u = 0) seems quite reasonable.

The data of Sirieix and Solignac[26], are believed to be subject to the second effect. If so, the geometry of the low-speed region is open to question and may have strongly influenced the deduced entrainment rates. Furthermore, their results indicate a very slowly growing layer which may have been strongly influenced by the initial boundary layer.

The conclusion is that the question of the mass entrained by variable density turbulent mixing layers is still unresolved but appears to be limited by the Liepmann and Laufer[17] value of $\lambda_e = \rho_{-\infty} v_{-\infty} / \rho_e u_e \approx .035$. However, the results included in Appendix II-B show that there may be strong effects of small secondary velocities for highly compressible flows. Clearly, further experiments are required in which the boundary condition of $u_{-\infty} = 0$ is assured at the low-speed end, or at least in which $u_{-\infty}$ is measured. It is felt that using porous plates to supply the mass (at low momentum) may provide the answer to this experimental difficulty.

Furthermore, the present injection experiments indicate that the effect of termination of injection seems to influence the flow strongly at injection rates near the constant pressure mixing layer

limit. It may be possible that the downstream (reattachment) boundary condition on most experimental mixing layer experiments may, in fact, dominate the experimental results obtained.

Finally, a plea is made to the experimenters who obtain data on mixing layers. The practice of trying to fit a measured compressible flow velocity profile to an incompressible analytical estimate by using a simple affine transformation of the scales is not only incorrect, but quite misleading. If a reference incompressible profile is used, it should be an experimental one, not a theoretical error function estimate of such. The effect of compressibility is certainly not a linear one and if scales are to be stretched, the stretching should be performed by using some rational integral transformation such as a Howarth-Dorodnitsyn transformation instead of a constant factor.

II. 5 Conclusions

(1) A self-similar, two-dimensional flow field with linear growth has been established experimentally for uniform injection on a flat surface and its mean flow properties have been investigated.

(2) The results obtained at $M_\infty = 2.6$ can be brought into agreement with the available incompressible data on boundary layers with moderately large injection by using a Howarth-Dorodnitsyn type transformation.

(3) At the highest injection rate obtained without upstream separation, the mean velocity profiles approach the free mixing-layer results. However, the amount of mass entrained at this point seems

to be close to that for the constant density layer ($\rho_w v_w / \rho_e u_e \approx .03$).

(4) Forces obtained with distributed injection are comparable to those obtained with injection through a slot for a given total mass flow rate.

(5) For any finite, porous-plate length, the effect of the discontinuity in injection at the end of the region is felt farther upstream as λ_e is increased and is expected to dominate the entire flow field for induced flow angles of about 20^o or larger, regardless of the plate length.

II. 6 Future Work

The following related experimental investigations are recommended:

(1) An investigation of the flow field in an incompressible boundlayer layer with injection rates approaching the entrainment value for a mixing layer ($\lambda_e \approx .03$). The geometry recommended for this is the ramp with the addition of a variable angle capability.

(2) Further investigation as to the effect of compressibility on flows with large injection using a cold wall or a heavy (large molecular weight) injectant. This should allow one to approach the limiting λ_e with a minimum effect of the finite plate length, since the induced flow angle will be much smaller for a given injection rate.

(3) An investigation of the flow field with large injection on an axisymmetric body (e. g. , a cone) with emphasis on the possible effects of transverse curvature.

(4) A more detailed investigation of the effect of compressibility on a two-dimensional mixing layer than has been performed to date.

NOMENCLATURE FOR TABLES II. 1, II. 2 AND II. 3

M_∞	freestream Mach number
P_∞	freestream pressure (cm. Hg.)
λ_∞	$\rho_w v_w / \rho_\infty u_\infty$
λ_e	$\rho_w v_w / \rho_e u_e$
P_e	pressure at edge of layer (cm. Hg.)
M_e	Mach number at edge of layer
H	form factor - δ^*/θ
$\overline{H}$	transformed form factor $\overline{\delta}^*/\overline{\theta}$
θ	momentum thickness
Θ	induced flow angle - $\tan \Theta = v_e/u_e$
y	distance normal to wall - inches
x	distance along plate - inches
P/P_{T_2}	ratio of static pressure to Pitot pressure
$\overline{y}/\overline{\theta}$	transformed distance normal to wall
u/u_e	velocity ratio
$\frac{\tau - \tau_w}{\rho_e u_e^2}$	normalized shear stress
$\frac{\epsilon}{u_e \theta}$	normalized eddy viscosity
$\frac{\overline{\epsilon}}{\overline{u}_e \overline{\theta}}$	transformed eddy viscosity = $(\frac{\rho}{\rho_e})^2 \frac{\epsilon}{u_e \theta}$

TABLE II. 1. 1

TABULATION OF SIMILAR EXPERIMENTAL DATA (MODEL #1)

$M_\infty = 2.600$ $\lambda_\infty = 0$ $P_e = 3.800$ $H = 4.490$ $\theta = 0.008502$

$P_\infty = 3.800$ $\lambda_e = 0$ $M_e = 2.60$ $\overline{H} = 1.334$ $\circledcirc = 0$

y	P/P_{T_2}	$\overline{y}/\theta$	u/u_e	$\frac{\tau-\tau_w}{\rho_e u_e^2}^*$	$\frac{\epsilon}{u_e\theta}^*$	$\frac{\overline{\epsilon}}{\overline{u}_e\overline{\theta}}^*$
0	1.0000	.0000	.0000	.0000	.0000	.000000
.005	.396	.288	.636			
.010	.317	.627	.712			
.015	.271	.991	.761			
.020	.253	1.371	.781			
.025	.238	1.761	.799			
.030	.224	2.161	.816			
.035	.209	2.572	.834			
.040	.198	2.993	.848			
.045	.188	3.425	.862			
.050	.181	3.865	.872			
.055	.173	4.314	.884			
.060	.167	4.773	.894			
.065	.160	5.240	.905			
.070	.154	5.717	.914			
.075	.150	6.202	.922			
.080	.144	6.697	.932			
.085	.139	7.202	.942			

*Not calculated for this case

TABLE II. 1. 1 (Cont'd)

y	P/P_{T_2}	$\overline{y}/\overline{\theta}$	u/u_e	$\frac{\tau-\tau_w}{\rho_e u_e^2}^*$	$\frac{\epsilon}{u_e\theta}^*$	$\frac{\overline{\epsilon}}{\overline{u}_e\overline{\theta}}^*$
.090	.136	7.715	.948			
.095	.131	8.238	.957			
.100	.128	8.769	.963			
.105	.124	9.310	.970			
.110	.120	9.860	.978			
.115	.118	10.418	.988			
.120	.115	10.985	.989			
.125	.113	11.558	.993			
.130	.111	12.138	.996			
.135	.110	12.723	1.000			

*Not calculated for this case

TABLE II. 1. 2

TABULATION OF SIMILAR EXPERIMENTAL DATA (MODEL #1)

$M_\infty = 2.59$ $\lambda_\infty = 0.0039$ $P_e = 4.551$ $H = 4.701$ $\theta = 0.0155$

$P_\infty = 3.80$ $\lambda_e = 0.0036$ $M_e = 2.45$ $\overline{H} = 1.591$ $\Theta = 1.160$

y	P/P_{T_2}	$\overline{y}/\overline{\theta}$	u/u_e	$\frac{\tau-\tau_w}{\rho_e u_e^2}$	$\frac{\epsilon}{u_e\theta}$	$\frac{\overline{\epsilon}}{\overline{u}_e\theta}$
.000	1.000	0	0	0	0	0
.010	.722	.307	.285	.00143	0	0
.020	.569	.639	.382	.00180	.0145	.00415
.030	.469	.994	.453	.00200	.0328	.0105
.040	.403	1.365	.497	.00207	.0455	.0158
.050	.358	1.752	.537	.00210	.0515	.0193
.060	.318	2.155	.583	.00210	.0508	.0208
.070	.276	2.579	.638	.00204	.0502	.0230
.080	.246	3.025	.682	.00196	.0529	.0265
.090	.222	3.490	.721	.00185	.0577	.0314
.100	.202	3.975	.758	.00172	.0591	.0349
.110	.186	4.479	.793	.00156	.0592	.0377
.120	.173	5.002	.824	.00140	.0584	.0398
.130	.163	5.541	.853	.00123	.0562	.0408
.140	.153	6.098	.881	.00104	.0513	.0395
.150	.145	6.671	.907	.000849	.0453	.0370
.160	.139	7.261	.931	.000654	.0394	.0339
.170	.133	7.865	.953	.000459	.0311	.0281
.180	.129	8.483	.970	.000295	0	0
.182	.127	8.608	.976	.000234	0	0

TABLE II. 1. 3

TABULATION OF SIMILAR EXPERIMENTAL DATA (MODEL #1)

$M_\infty = 2.54$ $\lambda_\infty = 0.008$ $P_e = 5.20$ $H = 5.116$ $\theta = .0231$

$P_\infty = 4.20$ $\lambda_e = 0.0077$ $M_e = 2.270$ $\overline{H} = 2.012$ $\circledR = 2.689$

y	P/P_{T_2}	$\overline{y}/\overline{\theta}$	u/u_e	$\frac{\tau-\tau_w}{\rho_e u_e^2}$	$\frac{\epsilon}{u_e\theta}$	$\frac{\overline{\epsilon}}{\overline{u}_e\overline{\theta}}$
.000	1.000	0	0	0	0	0
.010	.929	.216	.203	.00156	0	0
.020	.867	.436	.281	.00213	.0197	.00519
.030	.806	.660	.343	.00256	.0377	.0104
.040	.759	.889	.386	.00283	.0471	.0134
.050	.707	1.122	.431	.00308	.0569	.0168
.060	.646	1.361	.481	.00332	.0634	.0198
.070	.608	1.605	.511	.00343	.0716	.0231
.080	.559	1.853	.549	.00355	.0775	.0262
.090	.520	2.108	.580	.00360	.0776	.0273
.100	.479	2.369	.617	.00363	.0780	.0290
.110	.435	2.636	.646	.00362	.0693	.0271
.120	.391	2.911	.681	.00355	.0621	.0257
.140	.301	3.497	.775	.00317	.0487	.0244
.160	.235	4.142	.853	.00257	.0429	.0262
.180	.195	4.846	.906	.00192	.0395	.0282
.200	.169	5.603	.947	.00123	.0324	.0265
.220	.152	6.409	.977	.000523	.0178	0
.240	.141	7.255	.999	-.000102	-.00512	0

TABLE II. 1. 4

TABULATION OF SIMILAR EXPERIMENTAL DATA (MODEL #1)

$M_\infty = 2.550$ $\lambda_\infty = 0.0147$ $P_e = 6.15$ $H = 6.085$ $\theta = 0.033$

$P_\infty = 4.150$ $\lambda_e = 0.0126$ $M_e = 2.18$ $\overline{H} = 2.632$ $\circledH = 5.102$

y	P/P_{T_2}	$\overline{y}/\overline{\theta}$	u/u_e	$\frac{\tau-\tau_w}{\rho_e u_e^2}$	$\frac{\epsilon}{u_e\theta}$	$\frac{\overline{\epsilon}}{\overline{u}_e\overline{\theta}}$
.000	1.000	0	0	0	0	0
.010	.997	.155	.044	.00055	0	0
.020	.992	.311	.069	.00087	.0175	.0046
.030	.984	.466	.097	.00122	.0242	.0064
.040	.976	.622	.119	.00148	.0257	.0069
.050	.953	.779	.167	.00205	.0338	.0091
.060	.932	.937	.204	.00247	.0367	.0101
.070	.911	1.096	.232	.00280	.0449	.0124
.080	.872	1.256	.280	.00332	.0550	.0156
.090	.848	1.418	.307	.00359	.0620	.0179
.100	.820	1.581	.336	.00387	.0709	.0209
.110	.788	1.746	.367	.00414	.0688	.0207
.120	.750	1.914	.402	.00443	.0675	.0209
.130	.707	2.084	.440	.00470	.0673	.0216
.140	.661	2.256	.478	.00494	.0698	.0232
.150	.615	2.433	.516	.00514	.0744	.0258
.160	.572	2.613	.550	.00528	.0762	.0275
.170	.532	2.797	.582	.00537	.0803	.0303
.180	.492	2.985	.620	.00542	.0869	.0346

TABLE II. 1. 4 (Cont'd)

y	P/P_{T_2}	$\overline{y}/\overline{\theta}$	u/u_e	$\frac{\tau-\tau_w}{\rho_e u_e^2}$	$\frac{\epsilon}{u_e\theta}$	$\frac{\overline{\epsilon}}{\overline{u}_e\,\overline{\theta}}$
.190	.456	3.178	.646	.00542	.0889	.0368
.200	.424	3.374	.668	.00539	.0891	.0382
.210	.384	3.576	.701	.00528	.0805	.0366
.220	.353	3.782	.732	.00512	.0715	.0344
.230	.327	3.996	.761	.00492	.0684	.0349
.240	.299	4.216	.794	.00462	.0641	.0351
.250	.274	4.443	.822	.00429	.0601	.0351
.260	.253	4.678	.848	.00394	.0586	.0365
.270	.232	4.922	.875	.00351	.0542	.0363
.280	.216	5.173	.896	.00310	.0509	.0361
.290	.200	5.432	.918	.00262	.0473	.0358
.300	.188	5.699	.936	.00217	.0432	.0346
.310	.178	5.973	.951	.00133	.0391	.0329
.320	.170	6.254	.965	.00133	.0334	.0294
.330	.163	6.541	.977	.00089	0	0
.337	.159	6.745	.984	.00061	0	0

TABLE II. 1. 5

TABULATION OF SIMILAR EXPERIMENTAL DATA (MODEL #1)

$M_\infty = 2.55$ $\lambda_\infty = 0.026$ $P_e = 7.20$ $H = 7.088$ $\theta = 0.0417$

$P_\infty = 3.95$ $\lambda_e = 0.0189$ $M_e = 2.12$ $\overline{H} = 3.259$ $\circledR = 8.684$

y	P/P_{T_2}	$\overline{y}/\overline{\theta}$	u/u_e	$\frac{\tau-\tau_w}{\rho_e u_e^2}$	$\frac{\epsilon}{u_e\theta}$	$\frac{\overline{\epsilon}}{\overline{u}_e\overline{\theta}}$
0	1.000	0	0	0	0	0
.050	.986	.633	.091	.00172	0	0
.075	.966	.951	.143	.00266	.0876	.0248
.100	.960	1.271	.157	.00289	.0928	.0264
.125	.941	1.591	.190	.00344	.0984	.0282
.150	.906	1.915	.243	.00423	.0926	.0272
.175	.862	2.242	.296	.00496	.0941	.0284
.200	.804	2.575	.357	.00567	.0966	.0303
.210	.778	2.710	.382	.00593	.0976	.0312
.220	.750	2.847	.408	.00617	.0964	.0315
.230	.720	2.985	.435	.00639	.0950	.0318
.240	.686	3.124	.465	.00660	.0938	.0323
.250	.652	3.266	.493	.00676	.0925	.0328
.260	.615	3.410	.523	.00689	.0923	.0338
.270	.578	3.557	.553	.00698	.0877	.0333
.280	.541	3.706	.583	.00703	.0858	.0338
.290	.503	3.858	.619	.00702	.0862	.0356
.300	.468	4.014	.647	.00696	.0871	.0376
.320	.399	4.336	.698	.00671	.0808	.0378

TABLE II. 1. 5 (Cont'd)

y	P/P_{T_2}	$\overline{y}/\overline{\theta}$	u/u_e	$\frac{\tau-\tau_w}{\rho_e u_e^2}$	$\frac{\epsilon}{u_e\theta}$	$\frac{\overline{\epsilon}}{\overline{u}_e\overline{\theta}}$
.340	.335	4.675	.763	.00611	.0669	.0354
.360	.280	5.037	.828	.00519	.0547	.0333
.380	.235	5.424	.883	.00408	.0468	.0326
.400	.201	5.839	.930	.00283	.0379	.0301
.420	.180	6.278	.963	.00171	.0290	.0255
.430	.170	6.506	.979	.00105	.0227	.0211
.440	.164	6.739	.989	.00060	.0178	.0171
.450	.162	6.976	.994	.00037	.0205	0
.460	.160	7.214	.996	.00023	.0284	0

TABLE II. 1. 6

TABULATION OF SIMILAR EXPERIMENTAL DATA (MODEL #1)

$M_\infty = 2.60$ $\lambda_\infty = .0436$ $P_e = 8.20$ $H = 7.644$ $\theta = 0.0623$

$P_\infty = 3.70$ $\lambda_e = 0.029$ $M_e = 2.010$ $\overline{H} = 3.781$ $\circledR = 14.084$

y	P/P_{T_2}	$\overline{y}/\overline{\theta}$	u/u_e	$\frac{\tau-\tau_w}{\rho_e u_e^2}$	$\frac{\epsilon}{u_e\theta}$	$\frac{\overline{\epsilon}}{\overline{u}_e\overline{\theta}}$
0	1.000	0	0	0	0	0
.050	.998	.444	.039	.00114	0	0
.100	.989	.889	.083	.00240	.0819	.0252
.150	.975	1.335	.127	.00359	.1130	.0351
.200	.956	1.783	.168	.00466	.1384	.0434
.250	.922	2.235	.226	.00602	.1619	.0519
.300	.886	2.692	.275	.00704	.1730	.0567
.350	.833	3.155	.337	.00803	.1720	.0584
.400	.774	3.628	.398	.00884	.1403	.0497
.420	.729	3.820	.440	.00919	.1183	.0434
.440	.680	4.017	.483	.00945	.1058	.0403
.460	.621	4.217	.533	.00962	.0972	.0390
.480	.562	4.424	.583	.00962	.0972	.0390
.500	.500	4.637	.640	.00943	.0866	.0397
.520	.435	4.858	.689	.00906	.0798	.0393
.540	.378	5.088	.738	.00847	.0727	.0389
.560	.328	5.329	.793	.00753	.0627	.0371
.580	.287	5.583	.844	.00640	.0539	.0354
.600	.252	5.850	.887	.00513	.0459	.0334

TABLE II. 1. 6 (Cont'd)

y	P/P_{T_2}	$\bar{y}/\bar{\theta}$	u/u_e	$\frac{\tau-\tau_w}{\rho_e u_e^2}$	$\frac{\epsilon}{u_e\theta}$	$\frac{\bar{\epsilon}}{\bar{u}_e\bar{\theta}}$
.620	.223	6.131	.927	.00370	.0370	.0298
.640	.198	6.426	.962	.00213	.0261	.0233
.660	.183	6.735	.985	.00095	.0179	.0171
.680	.177	7.051	.997	.00024	0	0
.690	.176	7.211	.998	.00013	0	0

TABLE II. 2. 1

TABULATION OF NON-SIMILAR DATA (MODEL #1)

$M_\infty = 2.590 \quad \lambda_\infty = .0039$

$P_\infty = 3.800$

$P_e = 4.450$	$x = .900$	$P_e = 4.500$	$x = 1.410$	$P_e = 4.55$	$x = 2.410$
y	P/P_{T_2}	y	P/P_{T_2}	y	P/P_{T_2}
0.	1.0000	0.	1.000	0.	1.000
0.010	0.610	0.010	0.662	0.010	0.758
0.020	0.454	0.020	0.517	0.020	0.607
0.030	0.368	0.030	0.429	0.030	0.506
0.040	0.311	0.040	0.366	0.040	0.433
0.050	0.2696	0.050	0.317	0.050	0.386
0.060	0.237	0.060	0.276	0.060	0.337
0.070	0.212	0.070	0.243	0.070	0.299
0.080	0.193	0.080	0.220	0.080	0.268
0.090	0.178	0.090	0.198	0.090	0.243
0.100	0.166	0.100	0.182	0.100	0.223
0.110	0.155	0.110	0.170	0.110	0.207
0.120	0.146	0.120	0.158	0.120	0.192
0.130	0.139	0.130	0.150	0.130	0.180
0.140	0.133	0.140	0.142	0.140	0.169
0.150	0.128	0.150	0.136	0.150	0.158
0.153	0.127	0.160	0.132	0.160	0.150
				0.170	0.143

TABLE II. 2. 1 (Cont'd)

y	P/P_{T_2}	y	P/P_{T_2}	y	P/P_{T_2}
				0.180	0.138
				0.190	0.133
				0.194	0.131

TABLE II. 2. 2

TABULATION OF NON-SIMILAR DATA (MODEL #1)

$M_\infty = 2.600$ $\quad$ $_\infty = .0146$

$P_\infty = 3.650$

$P_e = 5.70$	$x = .304$	$P_e = 5.25$	$x = 2.67$	$P_e = 4.35$	$x = 3.06$
y	P_e/P_{T_2}	y	P_e/P_{T_2}	y	P_e/P_{T_2}
0.	1.000	.0	1.000	0.	1.000
0.010	0.786	.025	.981	0.025	0.946
0.020	0.648	.050	.913	0.050	0.879
0.030	0.543	.075	.861	0.075	0.820
0.040	0.458	.100	.808	0.100	0.763
0.050	0.389	.125	.750	0.125	0.702
0.060	0.322	.150	.603	0.150	0.649
0.070	0.271	.175	.528	0.175	0.600
0.080	0.233	.200	.447	0.200	0.537
0.090	0.208	.225	.368	0.225	0.470
0.100	0.191	.250	.299	0.250	0.406
0.110	0.178	.275	.240	0.275	0.343
0.120	0.167	.300	.200	0.300	0.290
0.130	0.157	.325	.173	0.325	0.244
0.140	0.149	.350	.153	0.350	0.206
0.150	0.144	.375	.141	0.375	0.175
0.160	0.142	.400	.138	0.400	0.153
0.170	0.141	.420	.136	0.425	0.137
0.175	0.141	.430	.135	0.450	0.126

TABLE II. 2. 2 (Cont'd)

y	$P_e P_{T_2}$	y	P_e/P_{T_2}	y	P_e/P_{T_2}
		.440	.134	0.475	0.120
		.450	.134	0.500	0.119
		.460		0.525	0.118
		.470		0.550	0.118
				0.575	0.117
				0.600	0.117

TABLE II. 2. 3

TABULATION OF NON-SIMILAR DATA (MODEL #1)

$M_\infty = 2.550$ $\quad$ $_\infty = .0260$

$P_\infty = 3.950$

$P_e = 7.250$	$x = .695$	$P_e = 7.200$	$x = 1.0880$
y	P_e/P_{T_2}	y	P_e/P_{T_2}
0.	1.000	0.	1.000
0.050	0.967	0.050	0.980
0.075	0.929	0.075	0.941
0.100	0.879	0.100	0.917
0.110	0.848	0.125	0.878
0.120	0.801	0.140	0.847
0.130	0.751	0.150	0.823
0.140	0.694	0.160	0.791
0.150	0.639	0.170	0.754
0.160	0.578	0.180	0.716
0.180	0.466	0.190	0.670
0.200	0.367	0.200	0.626
0.220	0.290	0.210	0.576
0.240	0.231	0.220	0.529
0.260	0.194	0.230	0.480
0.280	0.172	0.240	0.436
0.300	0.160	0.260	0.355
0.310	0.157	0.280	0.285
0.320	0.156	0.300	0.232

TABLE II. 2. 3 (Cont'd)

y	P_e/P_{T_2}	y	P/P_{T_2}
0. 330	0. 156	0. 320	0. 196
		0. 340	0. 174
		0. 350	0. 167
		0. 360	0. 162
		0. 370	0. 160
		0. 380	0. 158

TABLE II.2.4

TABULATION OF NON-SIMILAR DATA (MODEL #1)

$M_\infty = 2.600$ $\lambda_\infty = .0436$

$P_\infty = 3.700$

$P_e = 8.500$	$x = 1.115$	$P_e = 8.300$	$x = 1.480$
y	P_e/P_{T_2}	y	P_e/P_{T_2}
0.	1.000	0.	1.000
0.050	0.992	0.050	0.995
0.100	0.964	0.100	0.982
0.120	0.944	0.150	0.958
0.140	0.928	0.200	0.918
0.160	0.908	0.250	0.858
0.180	0.886	0.300	0.790
0.200	0.859	0.320	0.755
0.220	0.827	0.340	0.722
0.240	0.788	0.360	0.664
0.260	0.742	0.380	0.606
0.280	0.693	0.400	0.537
0.300	0.635	0.420	0.464
0.320	0.574	0.440	0.398
0.340	0.503	0.460	0.342
0.360	0.423	0.480	0.293
0.380	0.352	0.500	0.253
0.400	0.295	0.520	0.220
0.420	0.249	0.540	0.197

TABLE II. 2. 4 (Cont'd)

y	P_e/P_{T_2}	y	P_e/P_{T_2}
0. 440	0. 214	0. 560	0. 183
0. 460	0. 188	0. 580	0. 177
0. 480	0. 177	0. 590	0. 176
0. 490	0. 176	0. 600	0. 175

TABLE II. 3. 1

TABULATION OF NON-SIMILAR DATA (MODEL #3)

$M_\infty = 2.610$ $P_\infty = 3.660$

$\lambda_\infty = .0354$

P_e=4.100	x = 0.4	P_e = 3.800	x = 0.785	P_e = 3.380	x = 1.180
y	P_e/P_{T_2}	y	P_e/P_{T_2}	y	P_e/P_{T_2}
0	1.000	0	1.000	0	1.000
0.0805	0.993	0.162	0.987	0.188	0.958
0.0855	0.988	0.172	0.979	0.238	0.939
0.0905	0.976	0.182	0.969	0.278	0.914
0.0955	0.965	0.192	0.955	0.303	0.883
0.1005	0.943	0.202	0.938	0.328	0.824
0.1055	0.921	0.212	0.916	0.333	0.814
0.1105	0.882	0.217	0.900	0.338	0.795
0.1155	0.845	0.222	0.880	0.343	0.777
0.1205	0.804	0.227	0.850	0.348	0.756
0.1255	0.752	0.232	0.826	0.353	0.735
0.1305	0.701	0.237	0.795	0.358	0.712
0.1355	0.646	0.242	0.769	0.363	0.690
0.1405	0.590	0.247	0.735	0.368	0.663
0.1455	0.536	0.252	0.704	0.373	0.644
0.1505	0.485	0.257	0.670	0.378	0.617
0.1555	0.434	0.262	0.639	0.383	0.591
0.1605	0.392	0.267	0.603	0.388	0.591
0.1655	0.353	0.272	0.571	0.393	0.537

TABLE II. 3. 1 (Cont'd)

y	P_e/P_{T_2}	y	P_e/P_{T_2}	y	P_e/P_{T_2}
0. 1705	0. 319	0. 277	0. 539	0. 398	0. 508
0. 1755	0. 291	0. 282	0. 503	0. 403	0. 483
0. 1805	0. 269	0. 287	0. 466	0. 408	0. 457
0. 1855	0. 249	0. 292	0. 432	0. 413	0. 431
0. 1905	0. 234	0. 297	0. 398	0. 418	0. 405
0. 1955	0. 219	0. 302	0. 369	0. 423	0. 380
0. 2005	0. 206	0. 307	0. 341	0. 428	0. 358
0. 2055	0. 195	0. 312	0. 313	0. 433	0. 336
0. 2105	0. 185	0. 317	0. 288	0. 438	0. 314
0. 2155	0. 176	0. 322	0. 267	0. 443	0. 296
0. 2205	0. 168	0. 327	0. 248	0. 448	0. 278
0. 2255	0. 161	0. 332	0. 233	0. 453	0. 261
0. 2305	0. 155	0. 337	0. 220	0. 458	0. 245
0. 2355	0. 149	0. 342	0. 207	0. 463	0. 230
0. 2405	0. 144	0. 347	0. 196	0. 468	0. 217
0. 2455	0. 139	0. 352	0. 187	0. 473	0. 205
0. 205	0. 134	0. 357	0. 178	0. 478	0. 195
0. 2555	0. 130	0. 362	0. 170	0. 483	0. 185
0. 2605	0. 126	0. 367	0. 163	0. 488	0. 177
0. 2655	0. 122	0. 372	0. 157	0. 493	0. 169
		0. 377	0. 151	0. 498	0. 161
		0. 382	0. 145	0. 503	0. 155
		0. 387	0. 140	0. 508	0. 149

TABLE II. 3.1 (Cont'd)

y	P_e/P_{T_2}	y	P_e/P_{T_2}	y	P_e/P_{T_2}
		0.392	0.135	0.513	0.143
		0.397	0.131	0.518	0.138
		0.402	0.127	0.523	0.133
		0.407	0.123	0.528	0.129
		0.412	0.120	0.533	0.124
		0.417	0.117	0.543	0.117
		0.422	0.115	0.548	0.114
		0.427	0.114	0.553	0.111
				0.558	0.109
				0.563	0.108

TABLE II. 3. 2

TABULATION OF NON-SIMILAR DATA (MODEL #3)

$M_\infty = 2.610$

$P_\infty = 3.660$

$\lambda_\infty = 0.0354$

$P_e = 3.180$ $x = 1.570$		$P_e = 3.080$ $x = 1.970$		$P_e = 2.900$ $x = 2.750$	
y	P_e/P_{T_2}	y	P_e/P_{T_2}	y	P_e/P_{T_2}
0	1.000	0	1.000	0	1.000
0.278	0.978	0.208	0.994	0.270	0.990
0.478	0.909	0.408	0.978	0.520	0.973
0.528	0.909	0.488	0.962	0.840	0.951
0.548	0.896	0.558	0.948	0.900	0.935
0.558	0.883	0.608	0.928	0.940	0.921
0.568	0.871	0.658	0.906	0.970	0.906
0.578	0.855	0.708	0.880	1.02	0.879
0.588	0.837	0.718	0.868	1.07	0.817
0.598	0.811	0.728	0.856	1.08	0.795
0.608	0.776	0.738	0.844	1.09	0.773
0.618	0.740	0.748	0.828	1.10	0.744
0.628	0.704	0.758	0.800	1.11	0.716
0.638	0.662	0.768	0.770	1.12	0.682
0.648	0.620	0.778	0.739	1.13	0.647
0.658	0.580	0.788	0.700	1.14	0.611
0.668	0.536	0.798	0.658	1.15	0.574
0.678	0.493	0.808	0.622	1.16	0.542

TABLE II. 3.2 (Cont'd)

y	P_e/P_{T_2}	y	P_e/P_{T_2}	y	P_e/P_{T_2}
0.688	0.451	0.818	0.581	1.17	0.509
0.698	0.405	0.828	0.540	1.18	0.475
0.708	0.366	0.838	0.501	1.19	0.446
0.718	0.330	0.848	0.463	1.20	0.414
0.728	0.299	0.858	0.428	1.21	0.384
0.738	0.268	0.868	0.392	1.22	0.358
0.748	0.242	0.878	0.360	1.23	0.330
0.758	0.219	0.888	0.328	1.24	0.305
0.768	0.198	0.898	0.299	1.25	0.282
0.778	0.178	0.908	0.271	1.26	0.259
0.788	0.162	0.918	0.247	1.27	0.241
0.798	0.150	0.928	0.224	1.28	0.222
0.808	0.139	0.938	0.205	1.29	0.206
0.818	0.130	0.948	0.186	1.30	0.190
0.828	0.123	0.958	0.170	1.31	0.176
0.838	0.116	0.968	0.156	1.32	0.163
0.848	0.110	0.978	0.144	1.33	0.151
0.858	0.107	0.988	0.135	1.34	0.141
0.868	0.104	0.998	0.126	1.35	0.132
		1.008	0.119	1.36	0.124
		1.018	0.113	1.37	0.117

TABLE II. 3. 2 (Cont'd)

y	P_e/P_{T_2}	y	P_e/P_{T_2}	y	P_e/P_{T_2}
		1. 028	0. 108	1. 38	0. 111
		1. 038	0. 104	1. 39	0. 106
		1. 048	0. 101	1. 40	0. 102
				1. 41	0. 0993

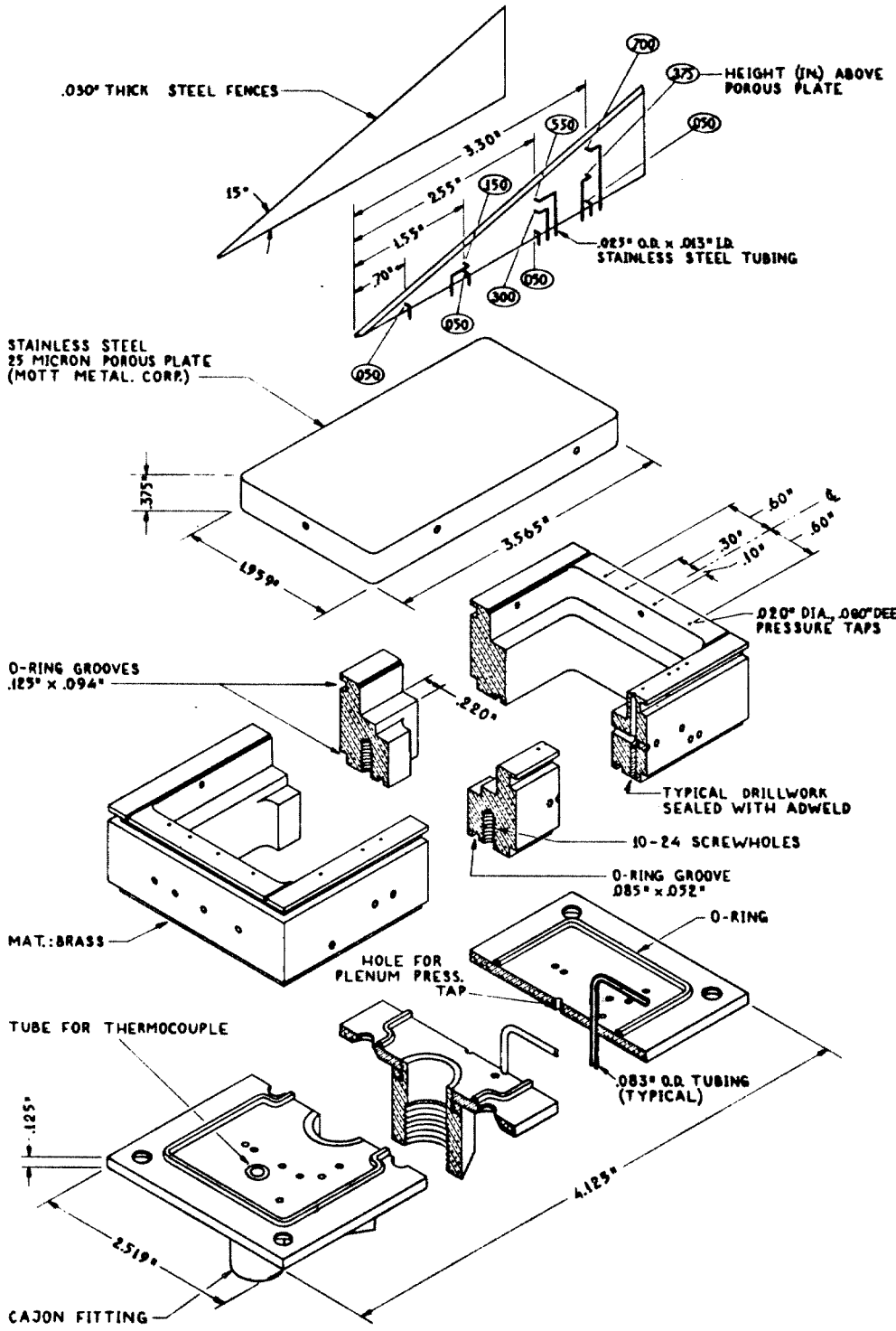

Fig.II.1 DETAIL DRAWING, MODEL #1

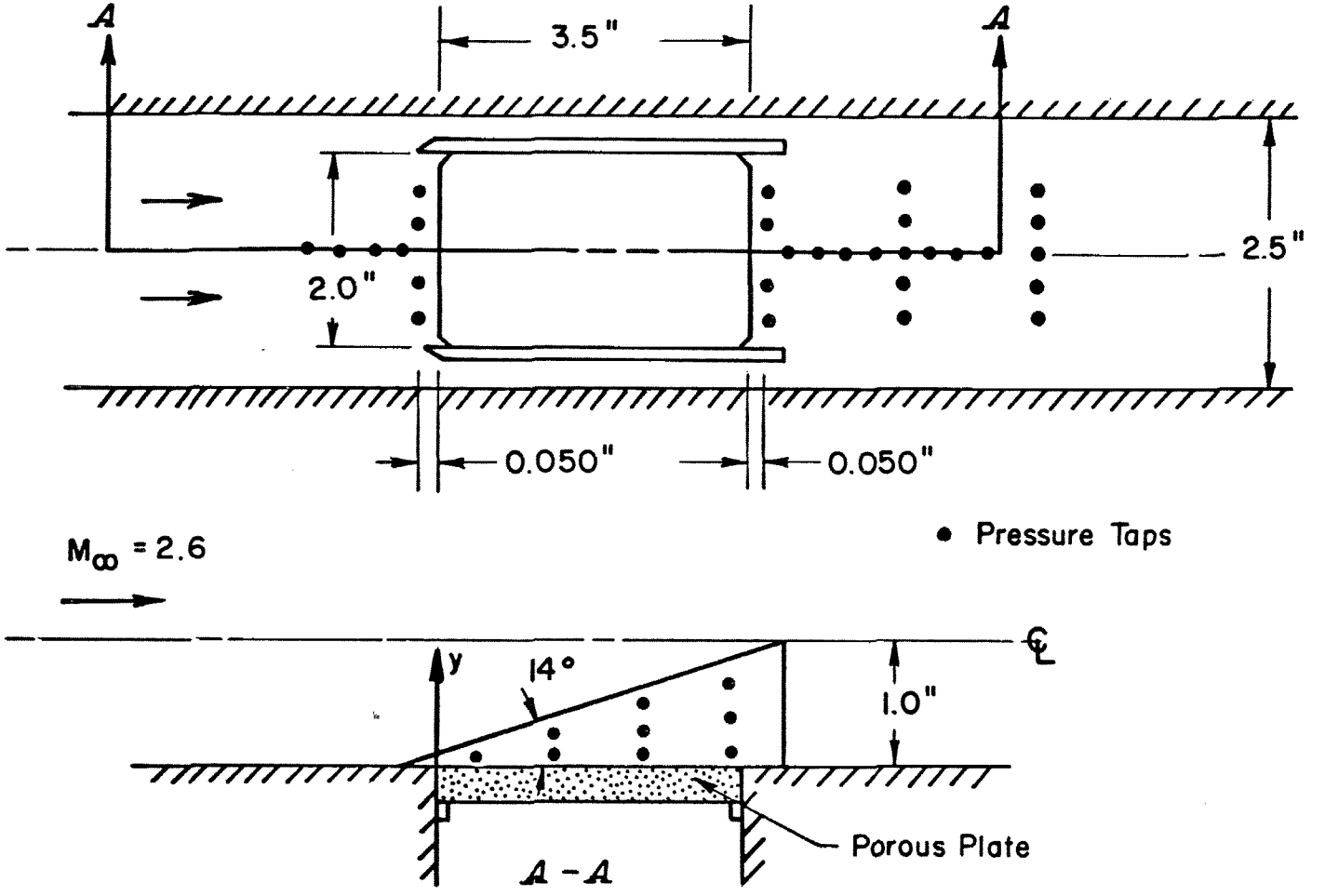

FIG. II.2 SCHEMATIC OF MODEL # 1 IN TUNNEL

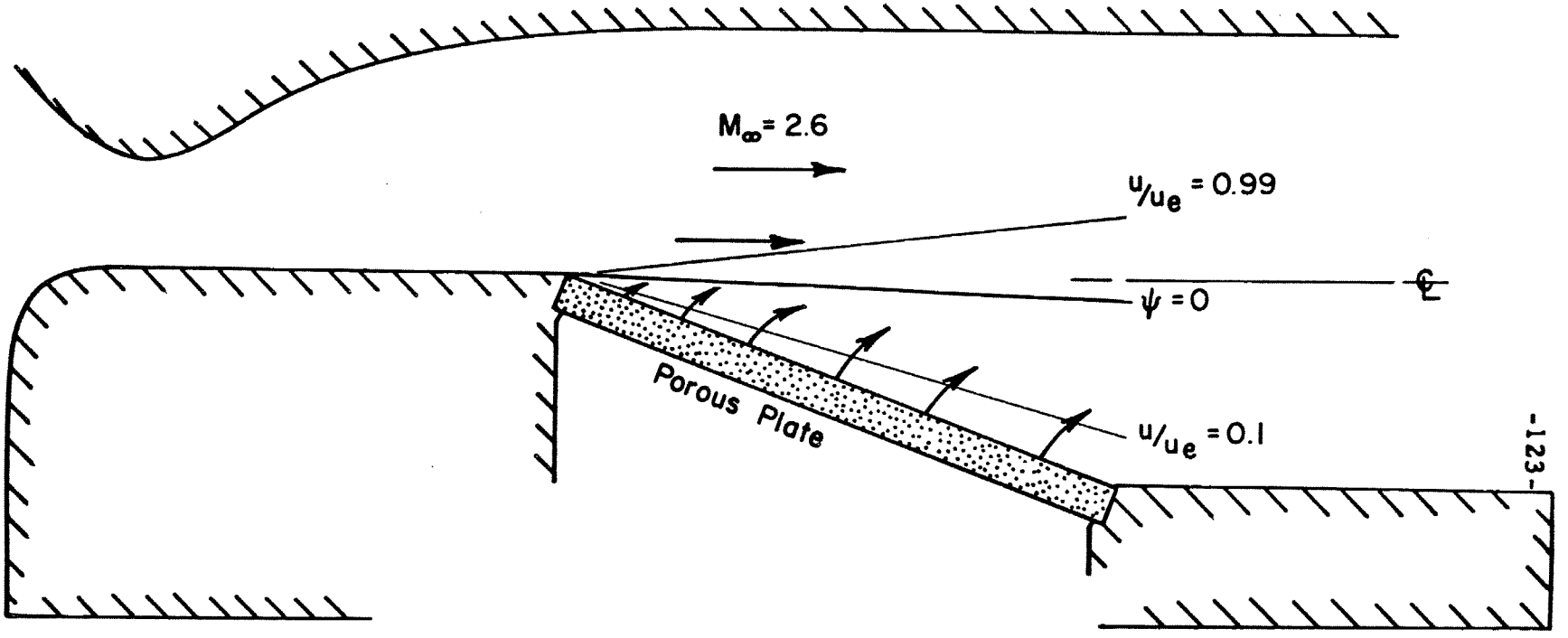

FIG. II.3 SCHEMATIC OF IDEALIZED FLOW PAST RAMP WITH INJECTION

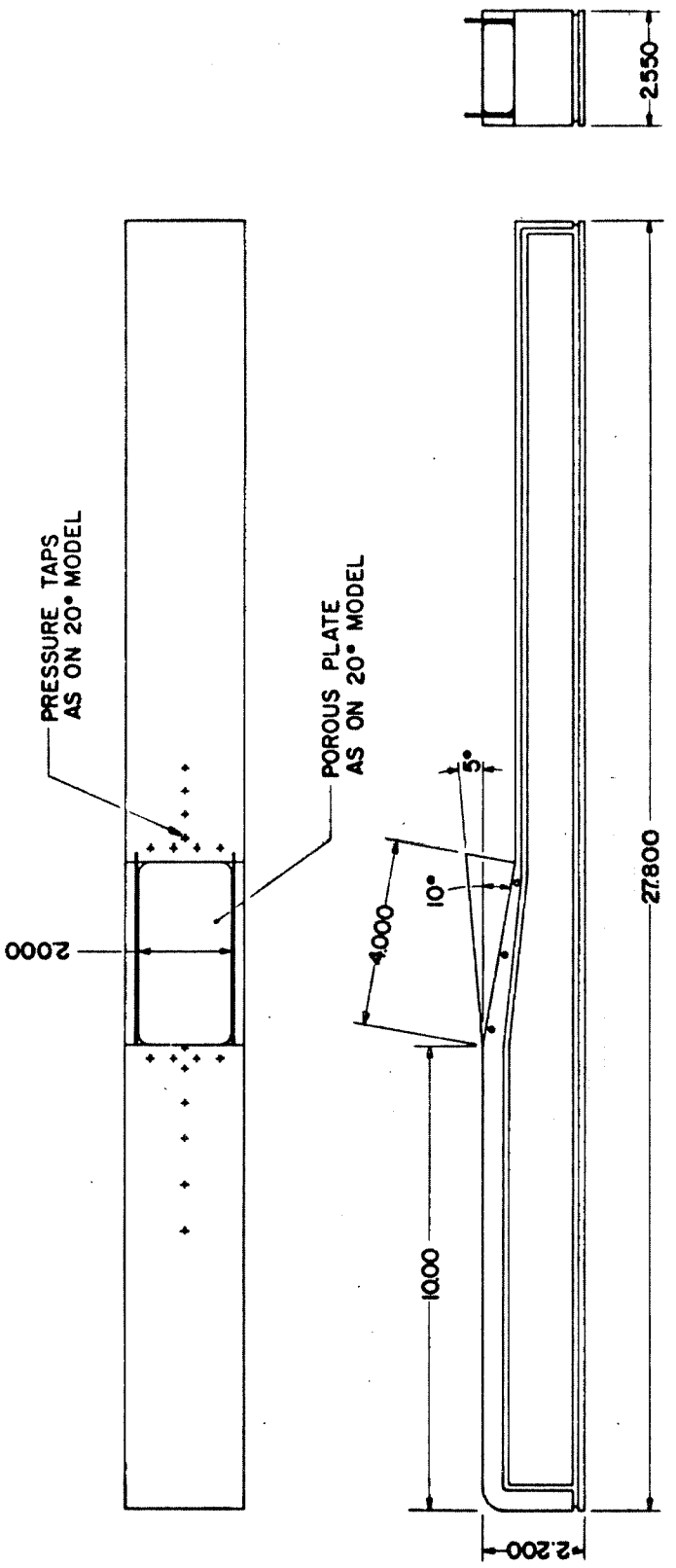

Fig. II.4 DETAIL OF MODEL #2

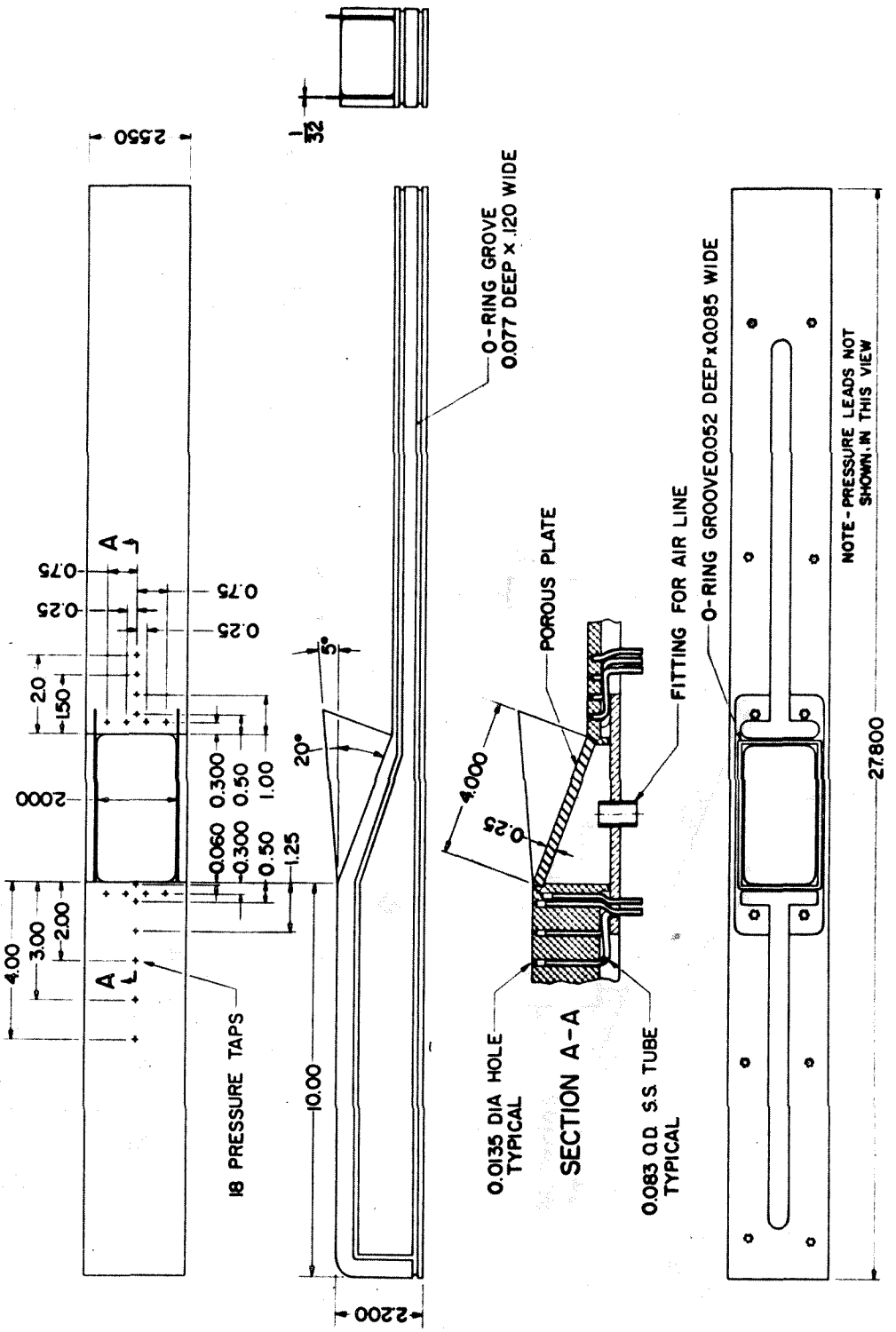

Fig. II. 5 DETAIL DRAWING, MODEL #3

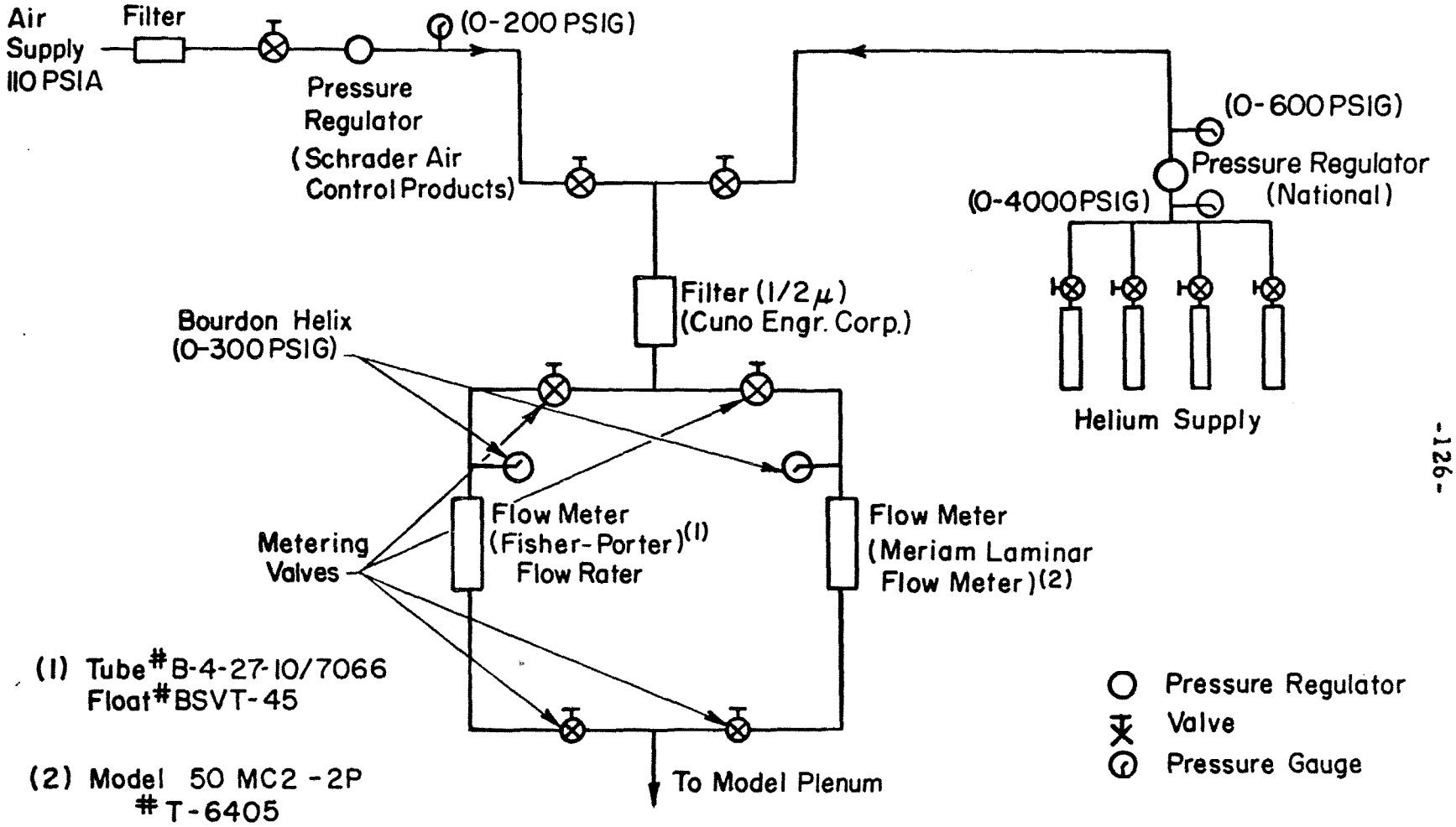

FIG. II.6 FLOW SYSTEM FOR MODEL SUPPLY

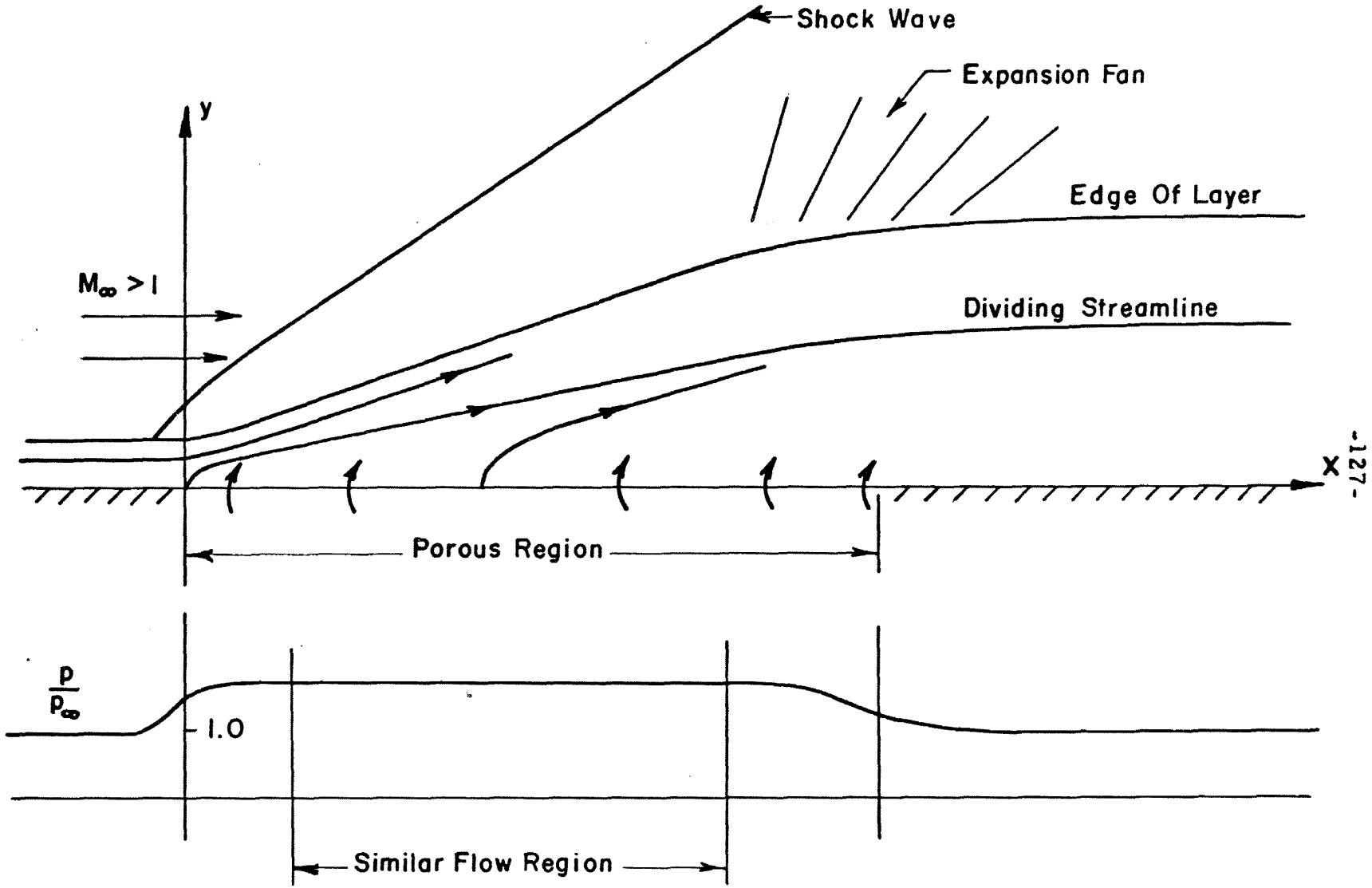

FIG.II.7 SCHEMATIC OF FLOW FIELD FOR MODEL # 1

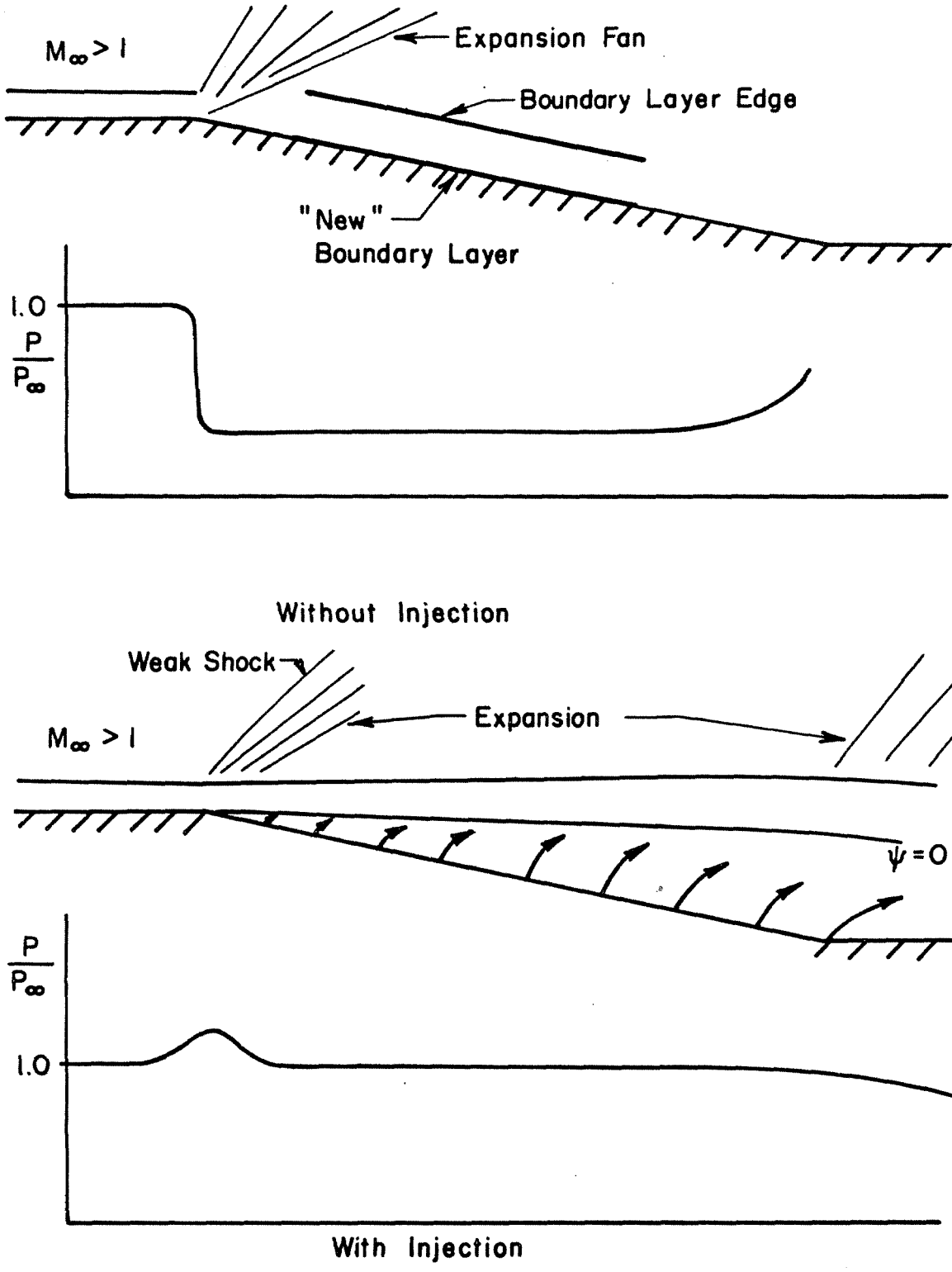

FIG. II.8 SCHEMATIC OF FLOW FIELD FOR MODEL # 2 (10° RAMP)

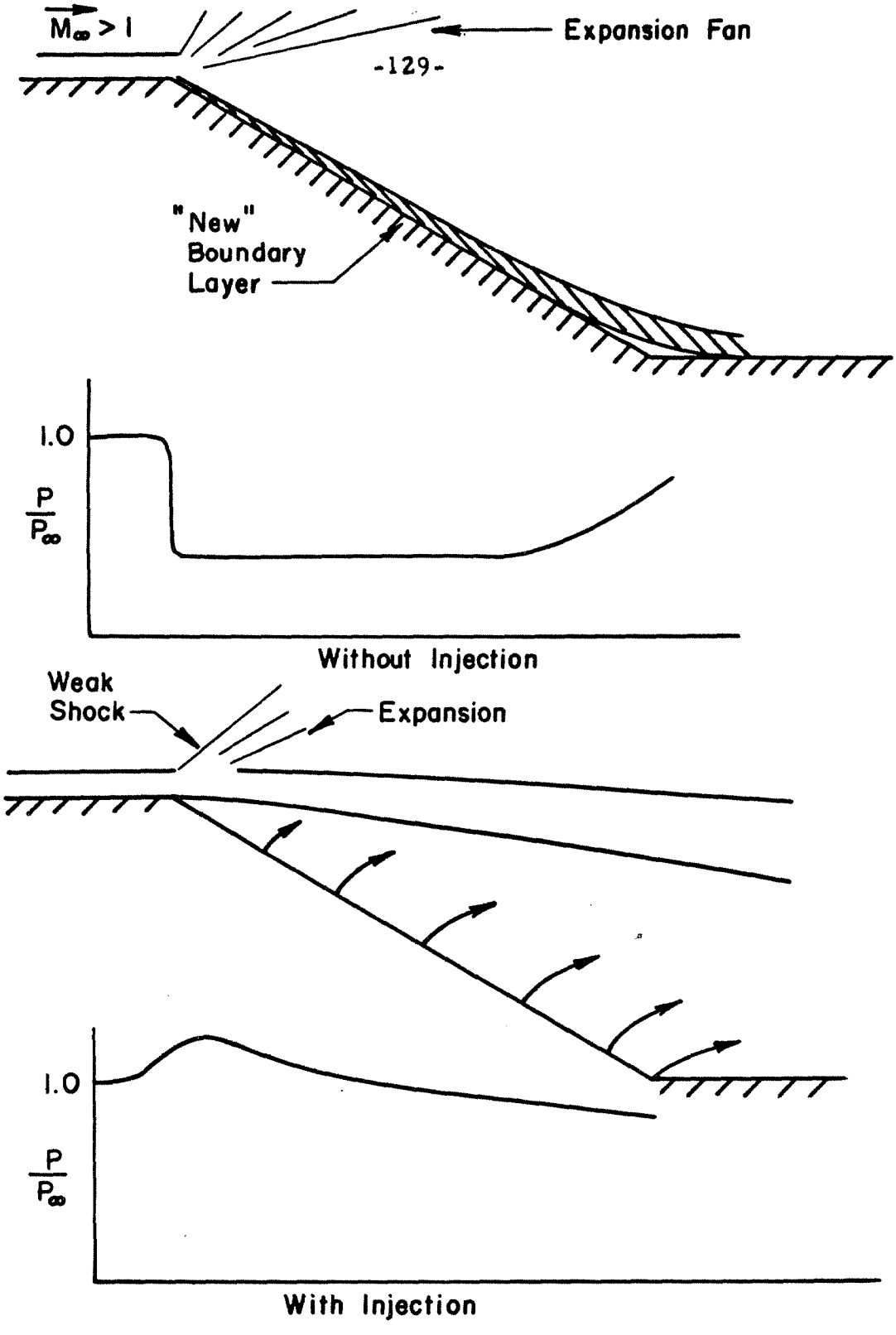

FIG.II.9 SCHEMATIC OF FLOW FIELD FOR MODEL # 3
(20° RAMP)

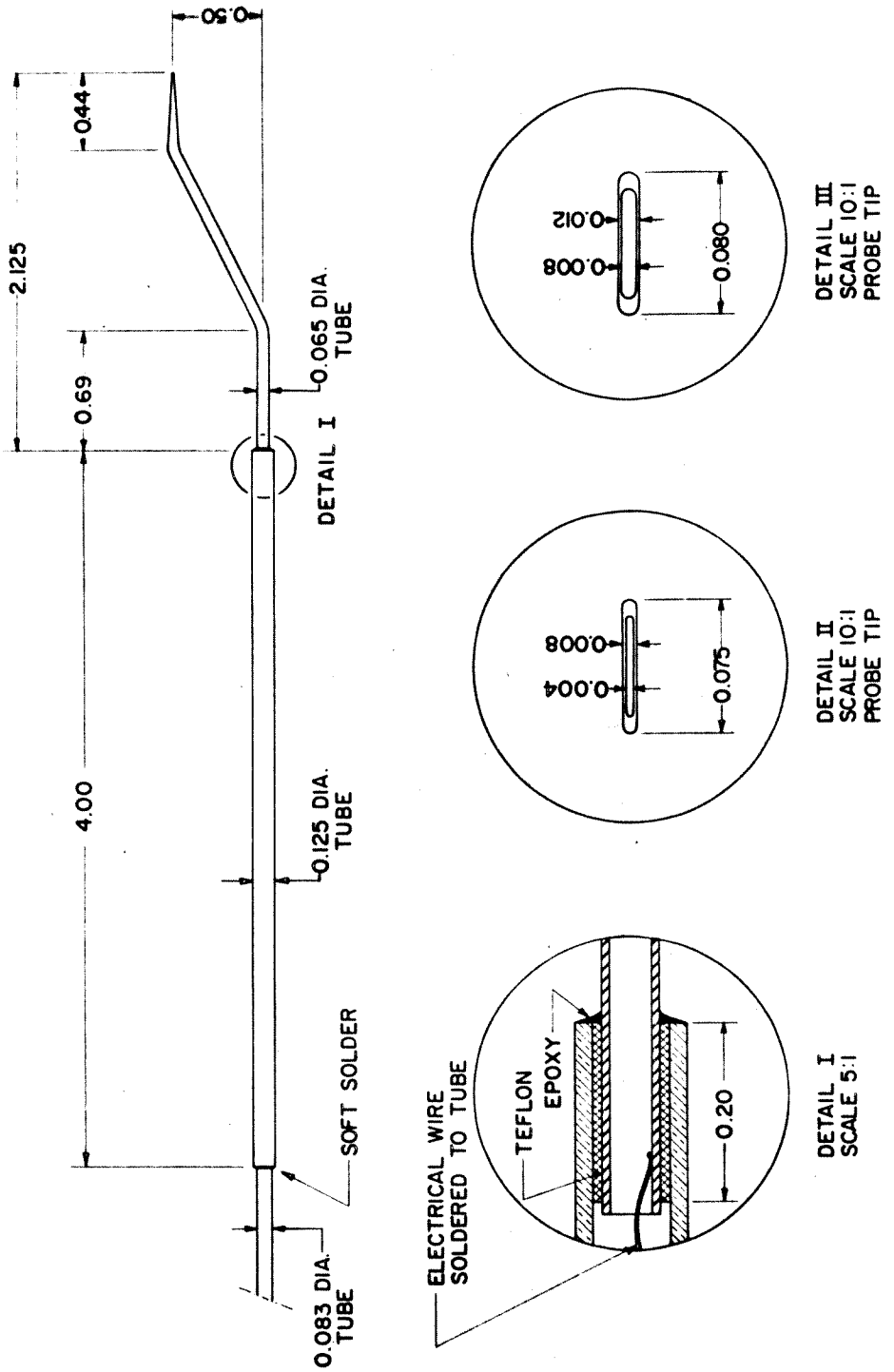

Fig.II.10 DETAIL OF PITOT PROBE

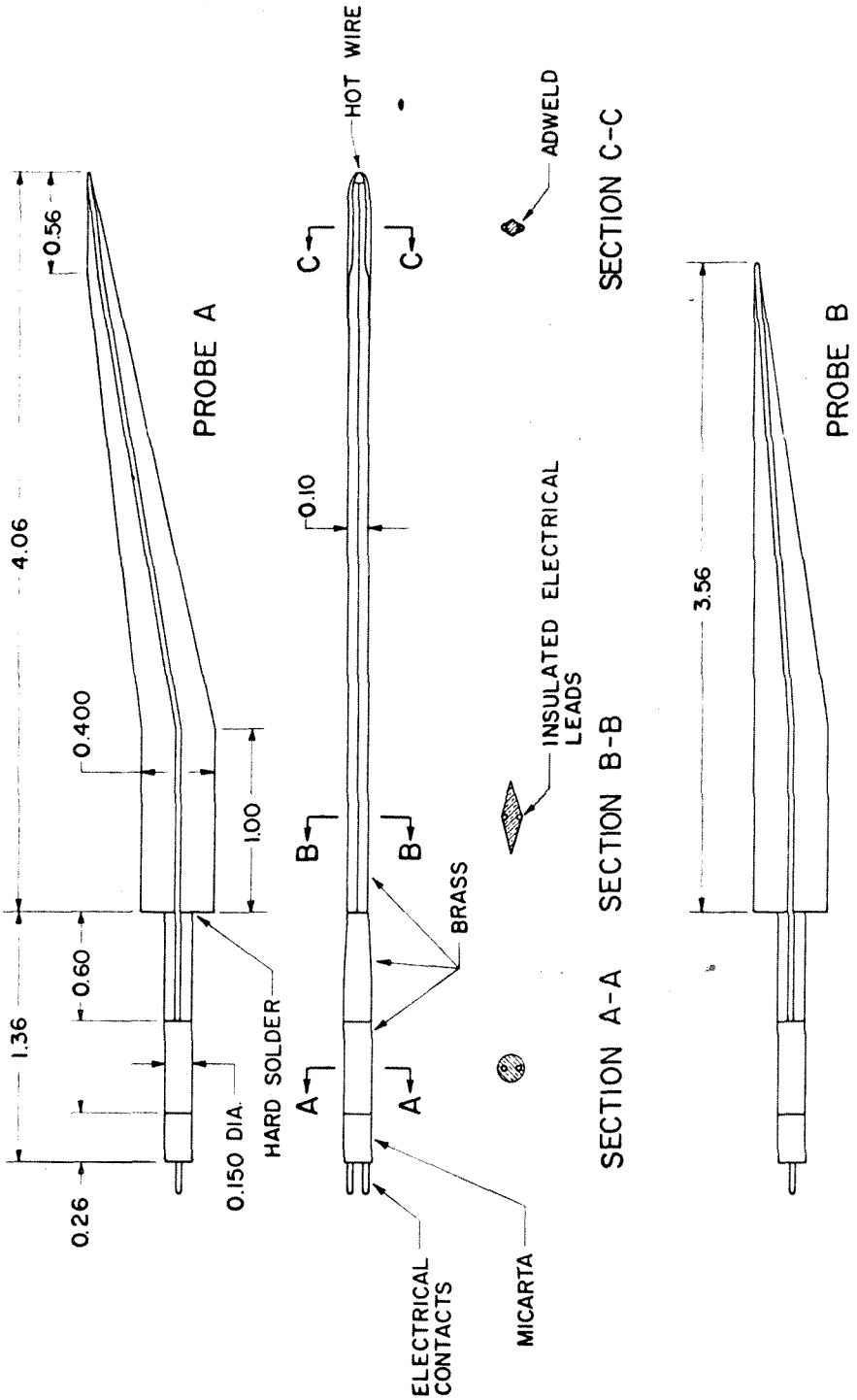

Fig II. II DETAIL OF HOT WIRE PROBES

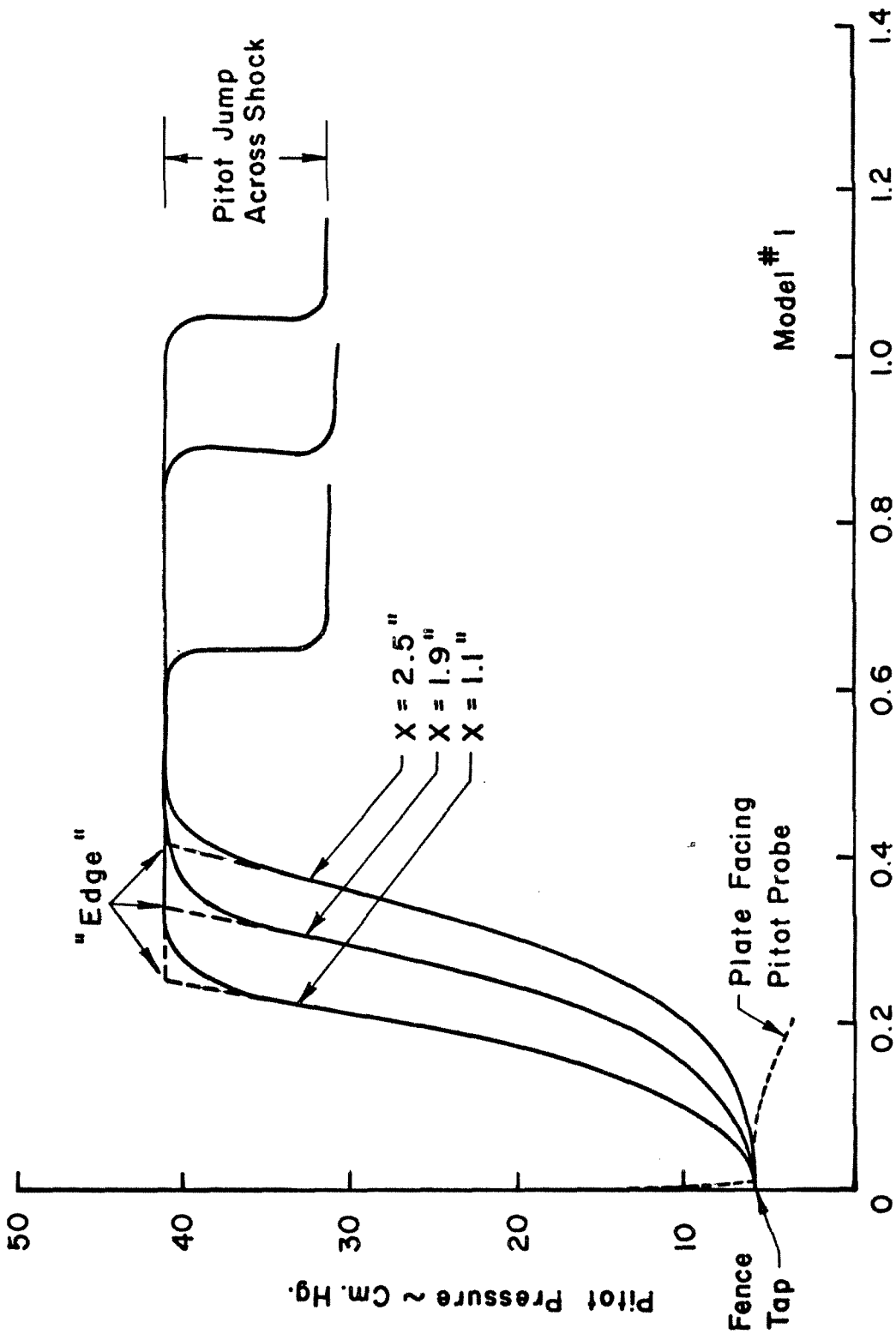

FIG. II.12 PITOT TRACES SHOWING CHECK FOR FENCE PRESSURE TAP READING ($\lambda_\infty = 0.015$)

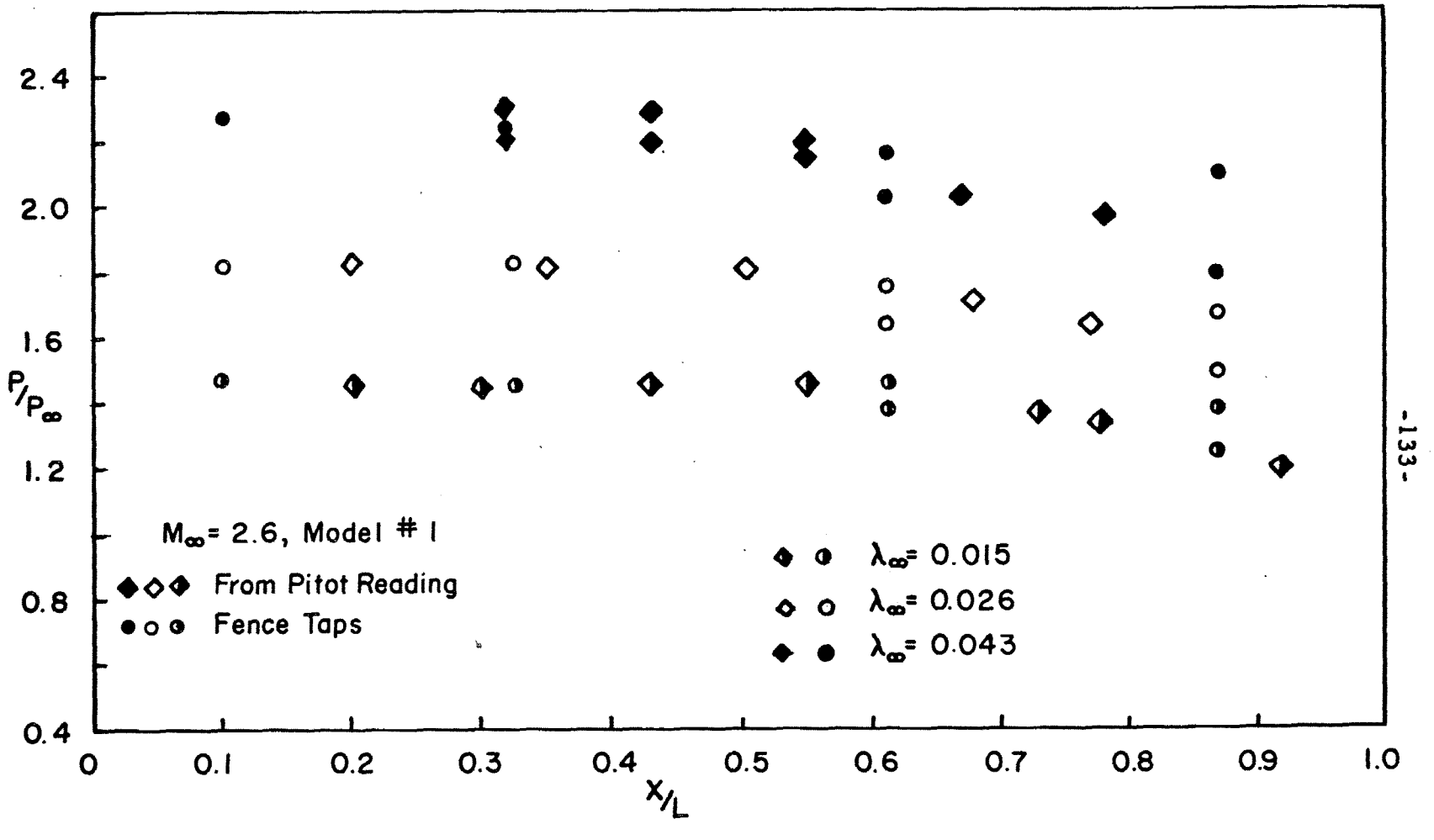

FIG.II.13 PRESSURE DISTRIBUTION ON POROUS PLATE

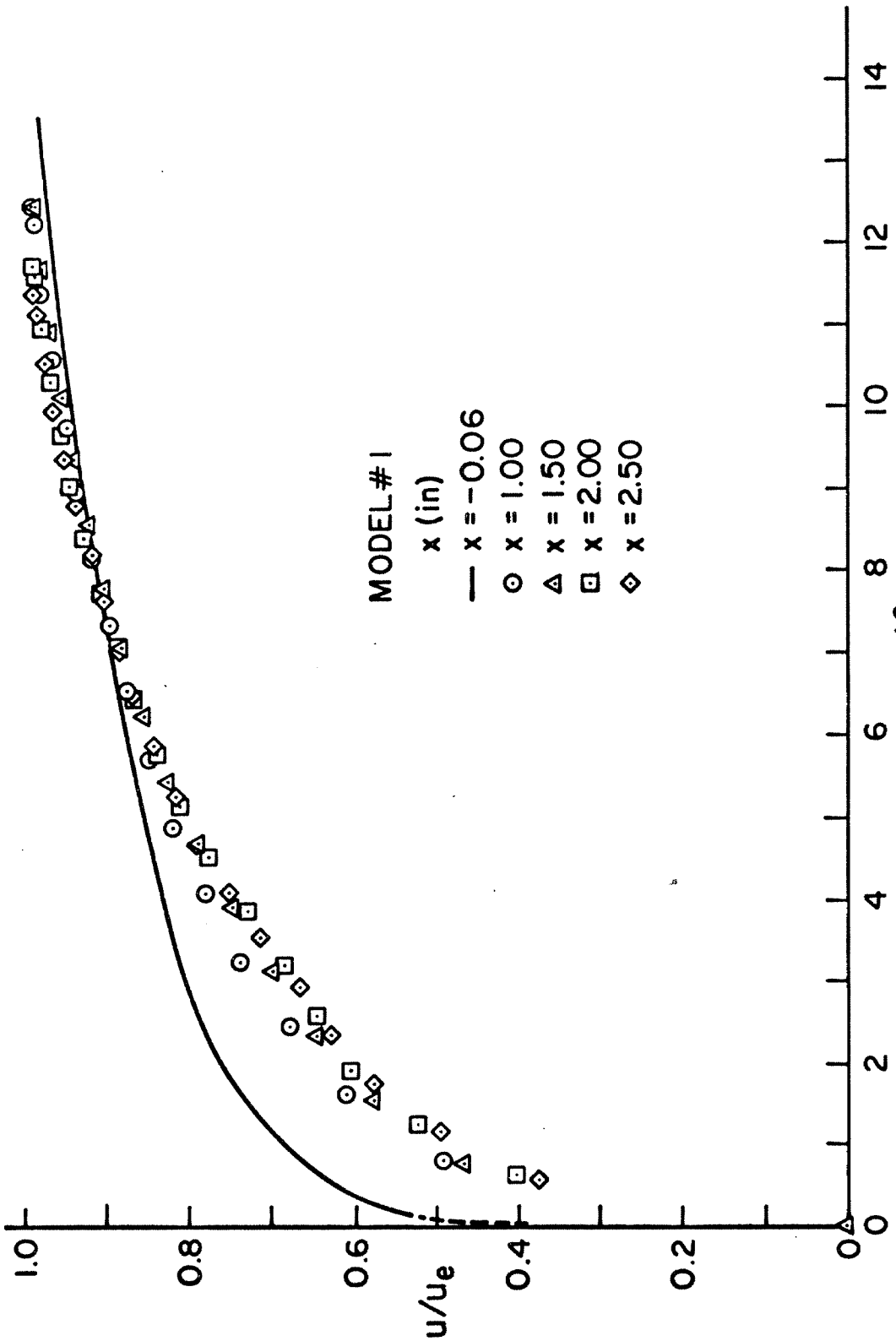

Fig.II.14 APPROACH TO SIMILAR FLOW ($\lambda e = 0.004$)

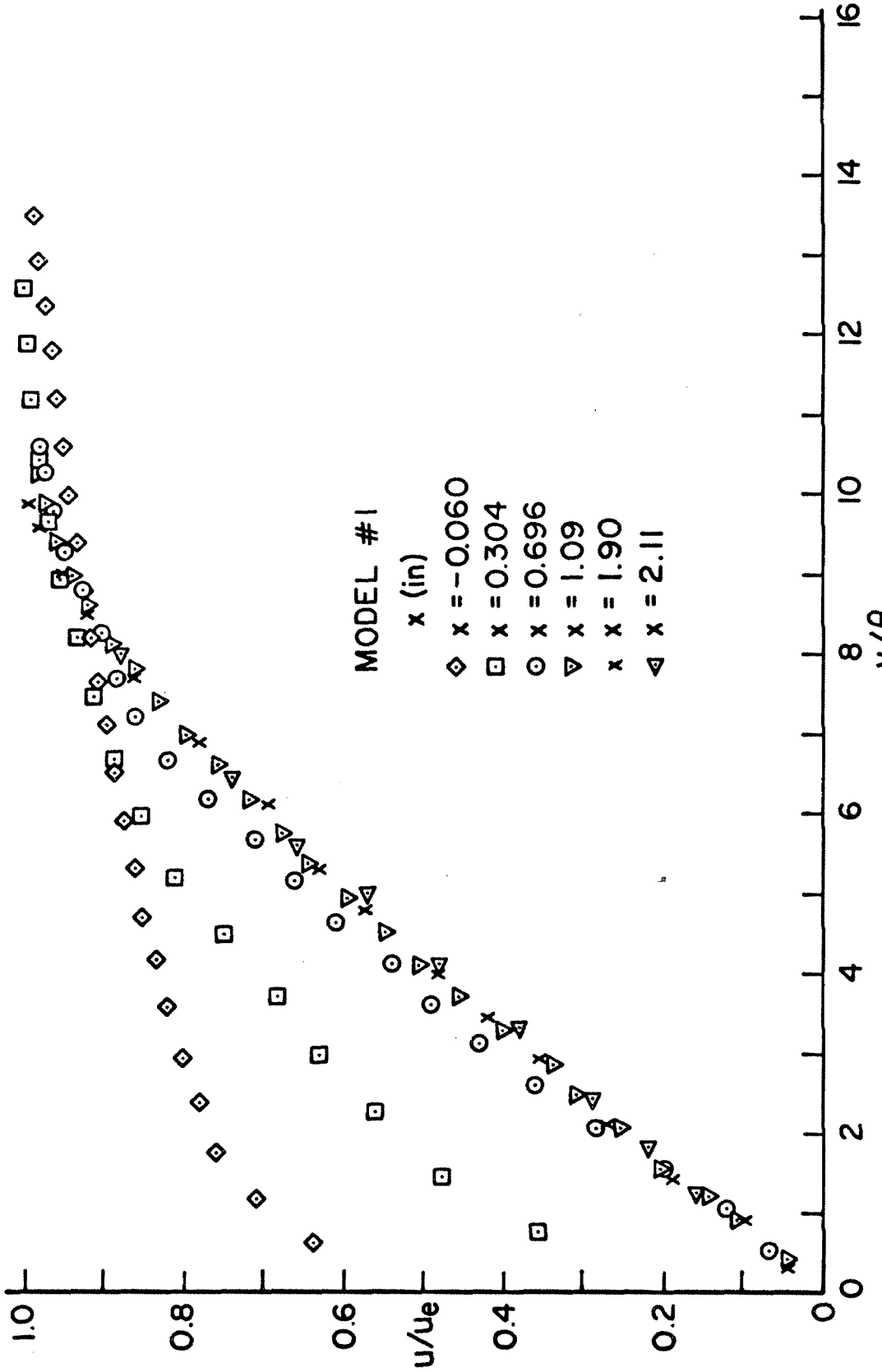

Fig. II.15 APPROACH TO SIMILAR FLOW ($\lambda_\infty = 0.015$, $\lambda_e = 0.0126$)

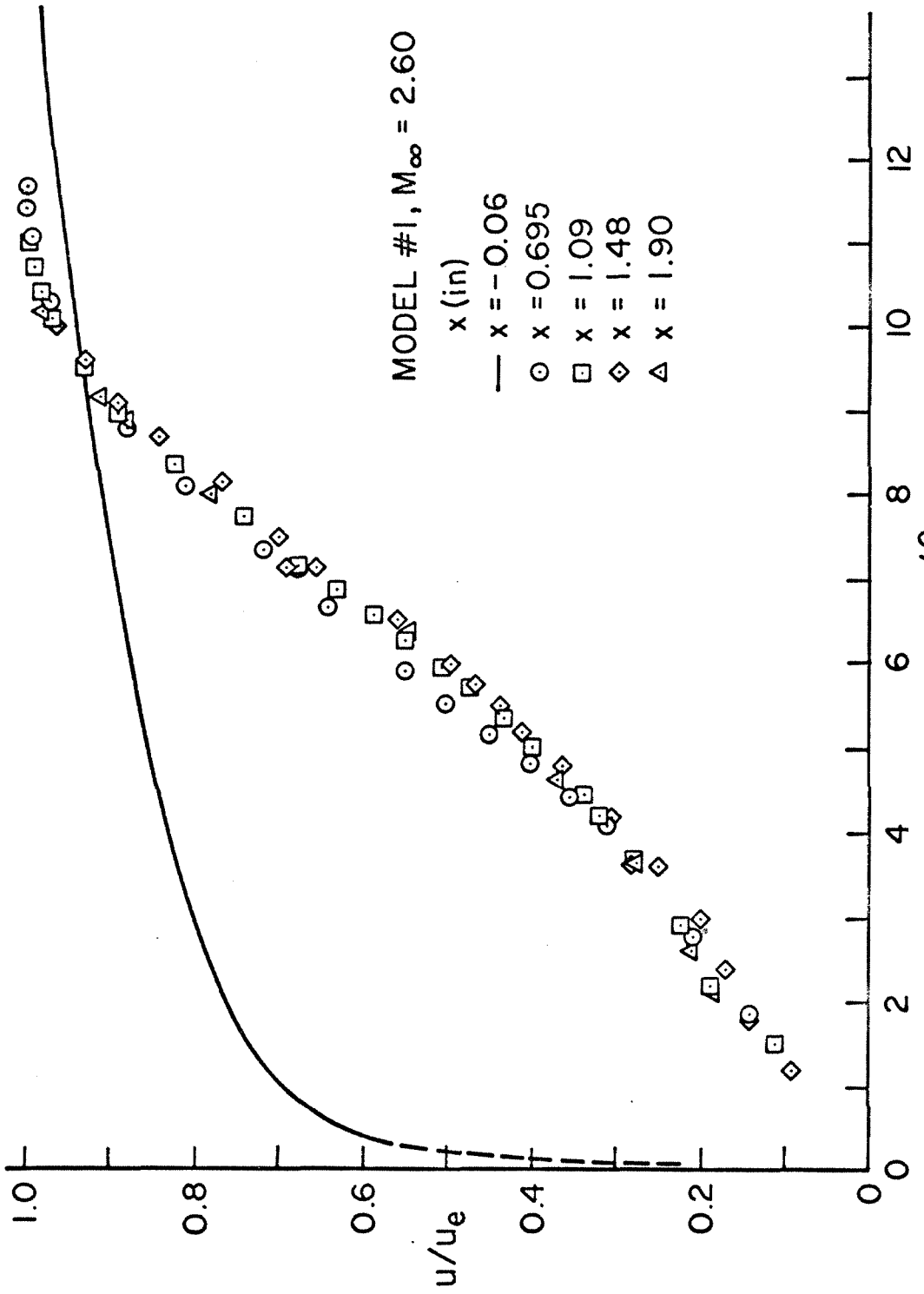

Fig. II.16 APPROACH TO SIMILAR FLOW (λ_e = 0.019)

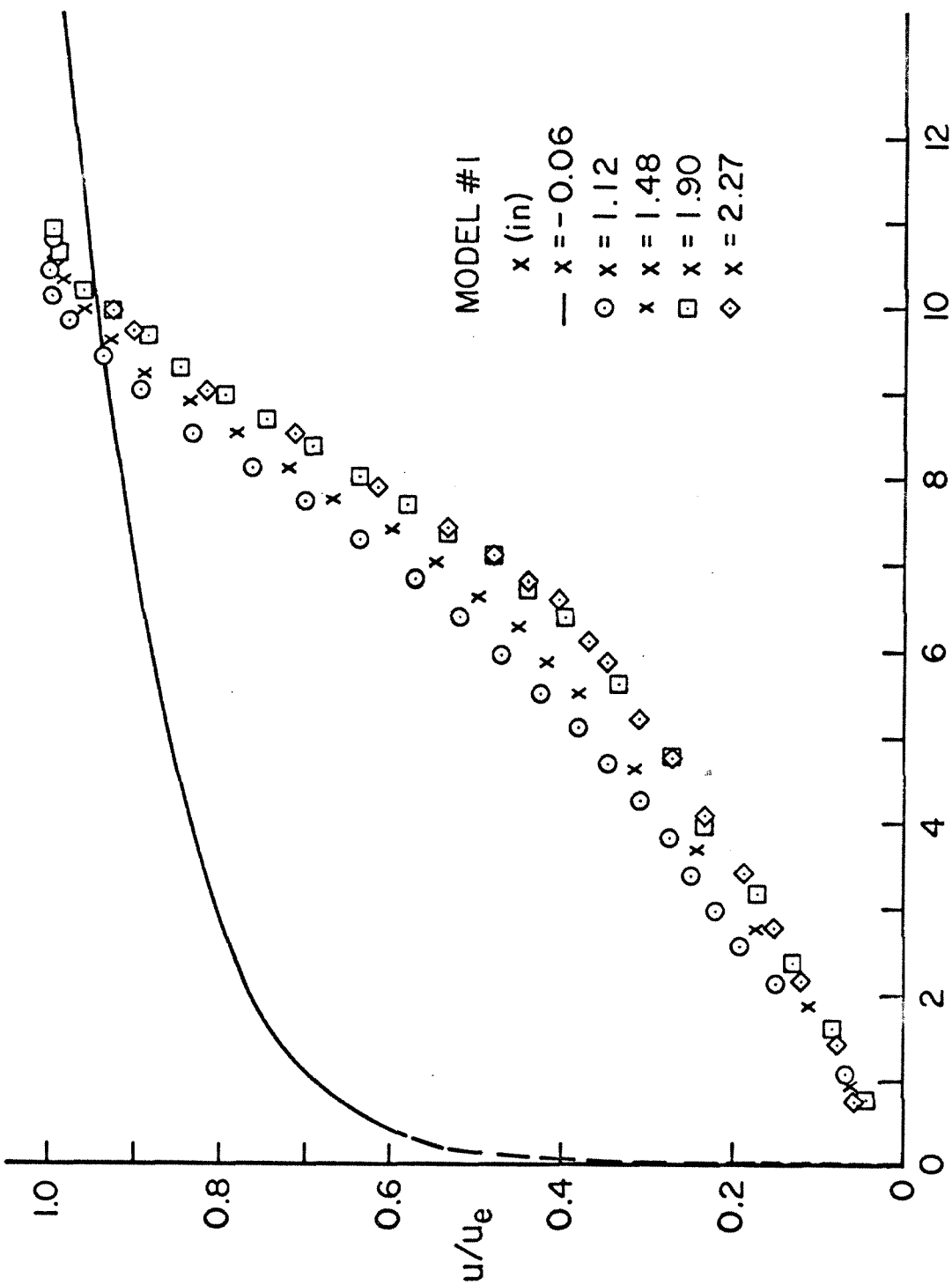

Fig. II.17 APPROACH TO SIMILAR FLOW ($\lambda_e = 0.029$)

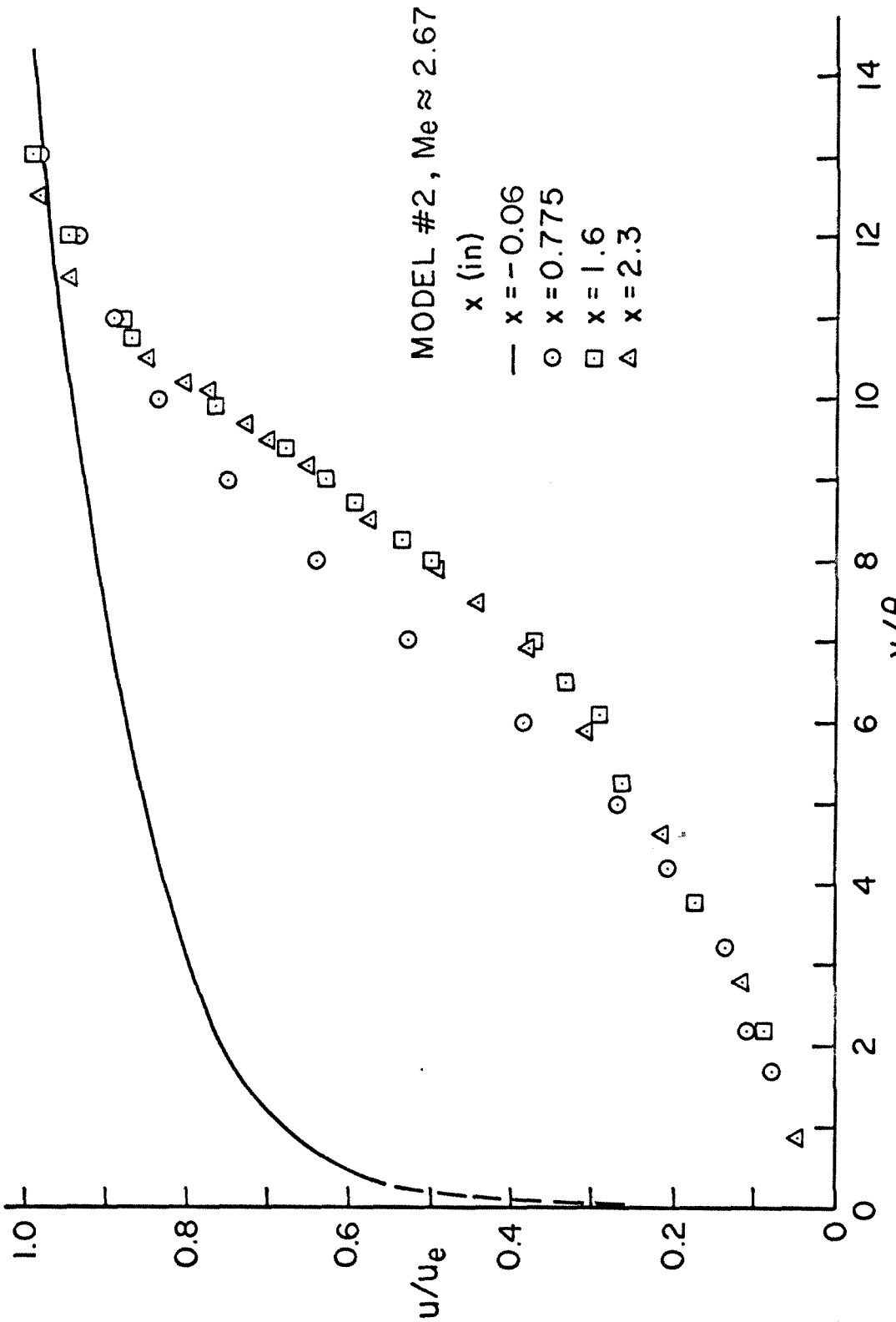

Fig. II.18 APPROACH TO SIMILAR FLOW ($\lambda e = 0.019$)

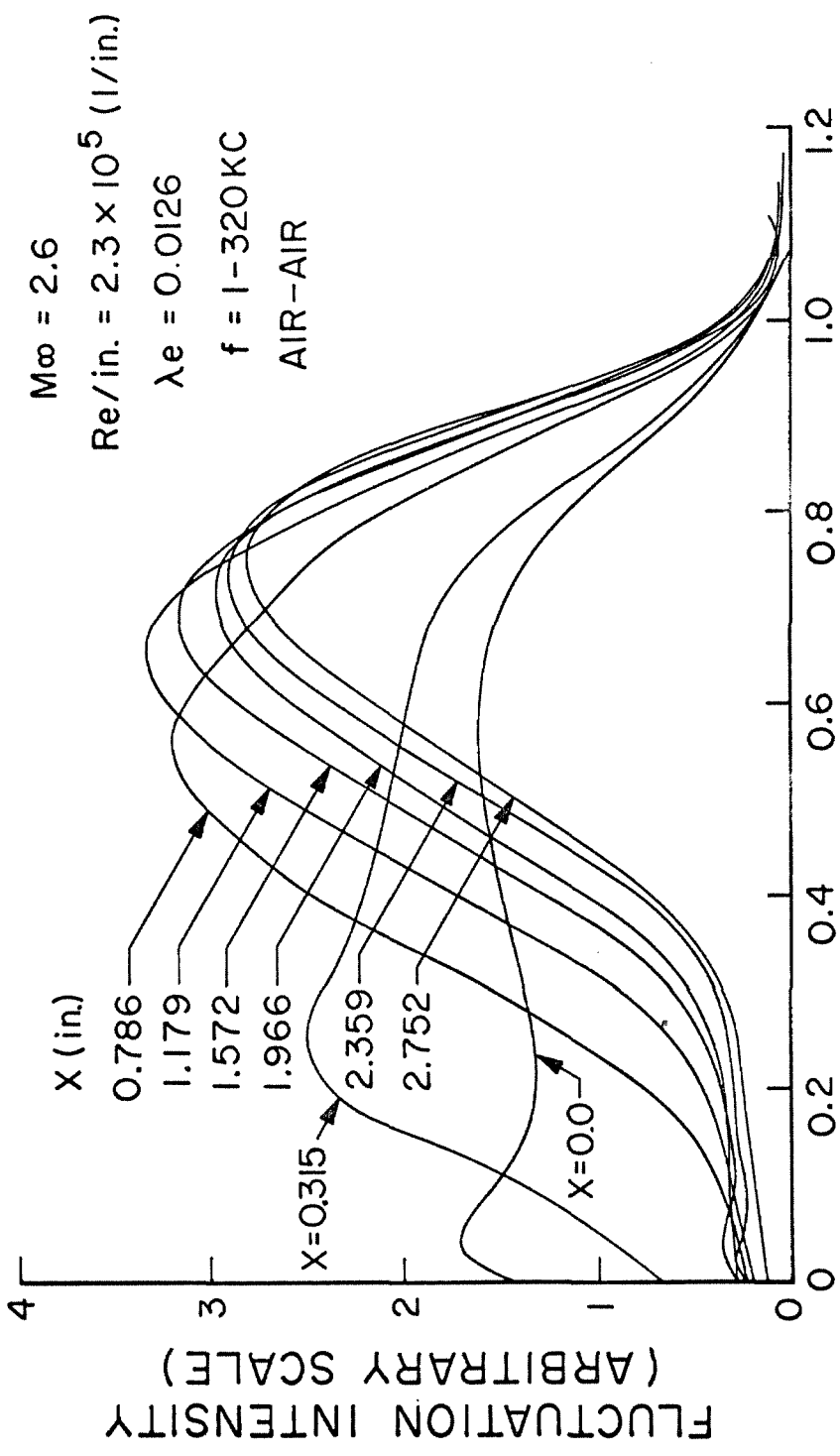

Fig.II.19 HOT WIRE FLUCTUATION MEASUREMENTS, MODEL #1

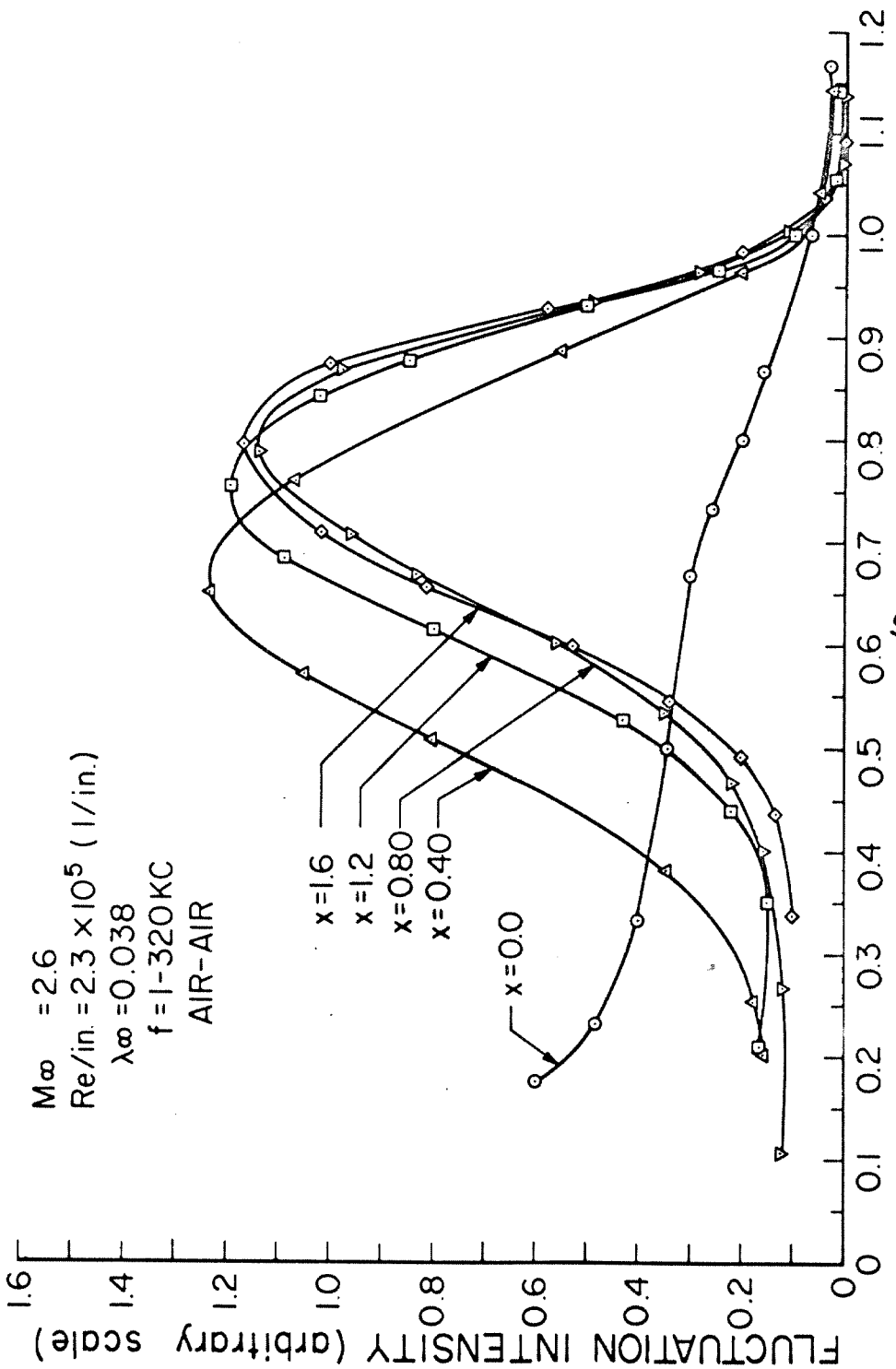

Fig.II.20 HOT WIRE FLUCTUATION MEASUREMENTS, MODEL #1

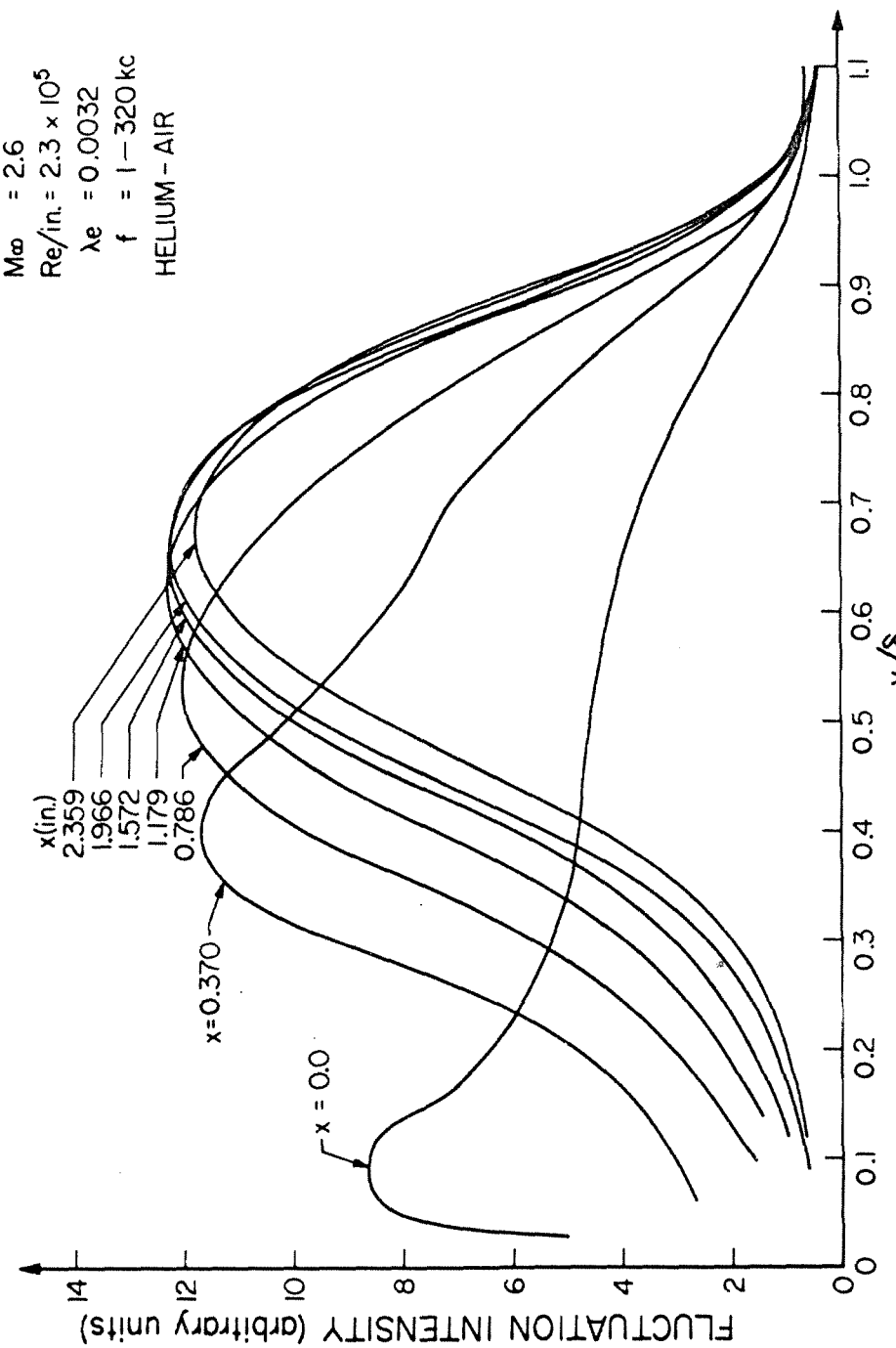

Fig. II.21 HOT WIRE FLUCTUATION MEASUREMENTS, MODEL #1

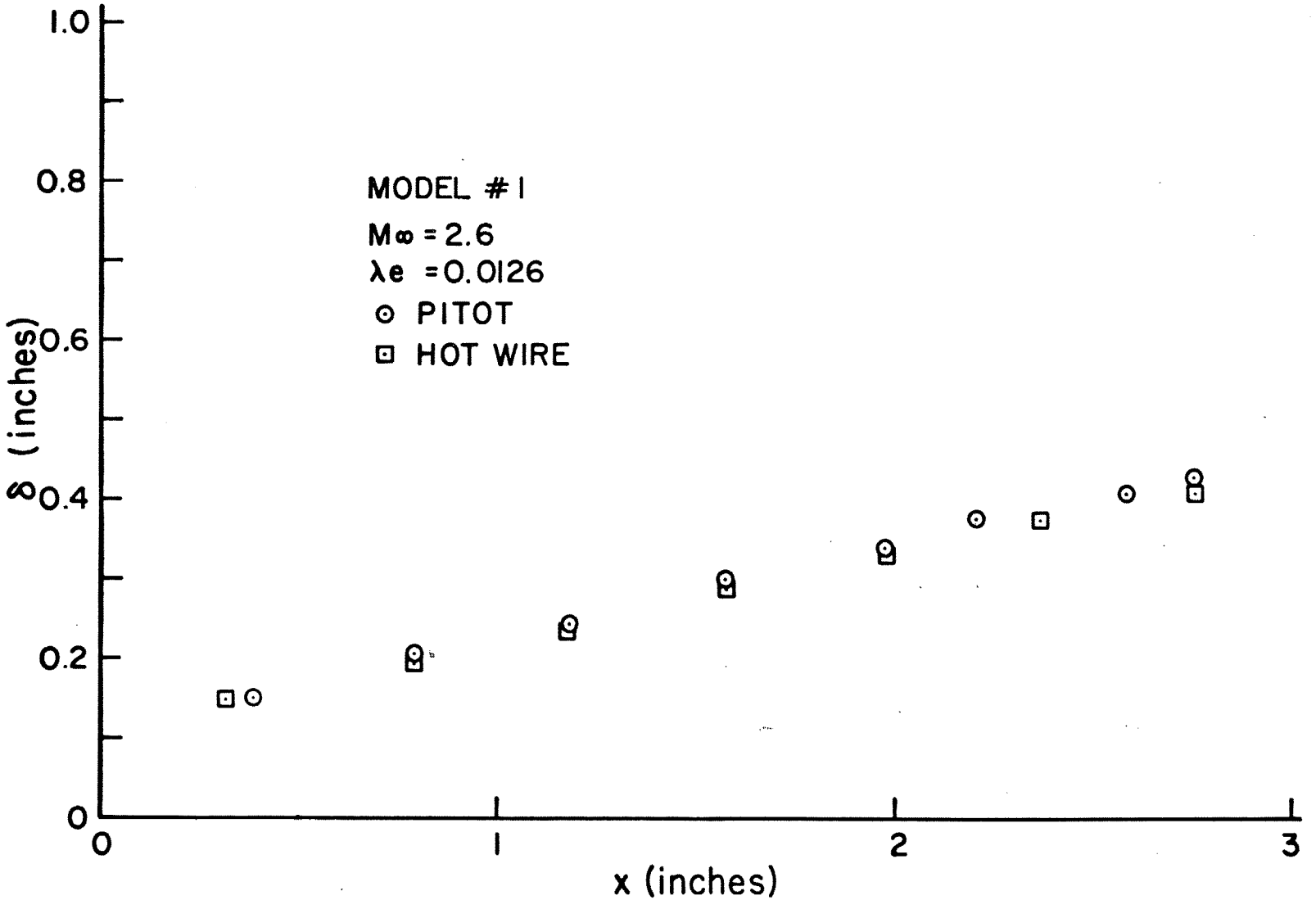

Fig.II.22 COMPARISON OF PITOT AND HOT WIRE "EDGE"

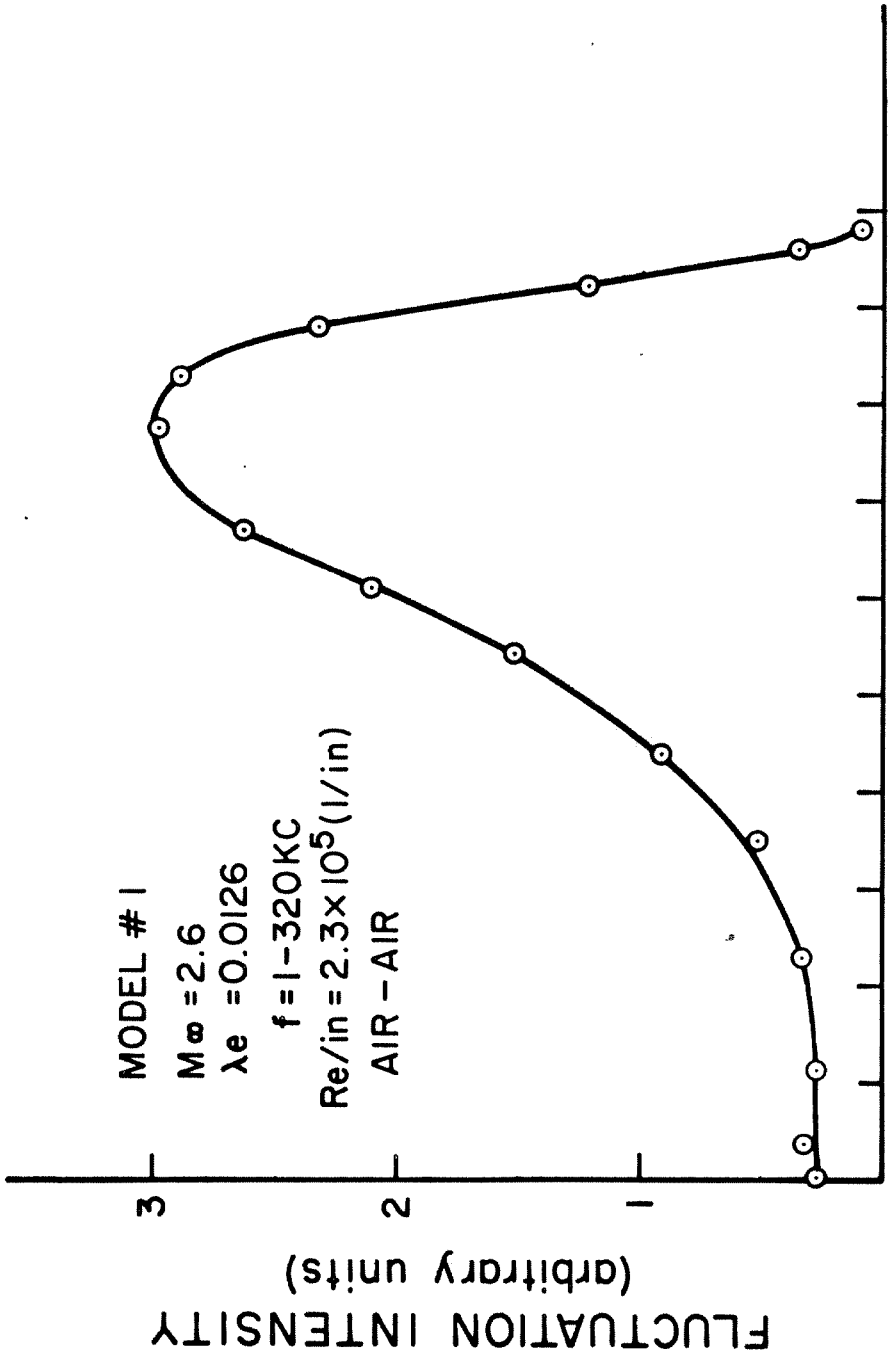

Fig.II.23 FLUCTUATION INTENSITY AS A FUNCTION OF VELOCITY

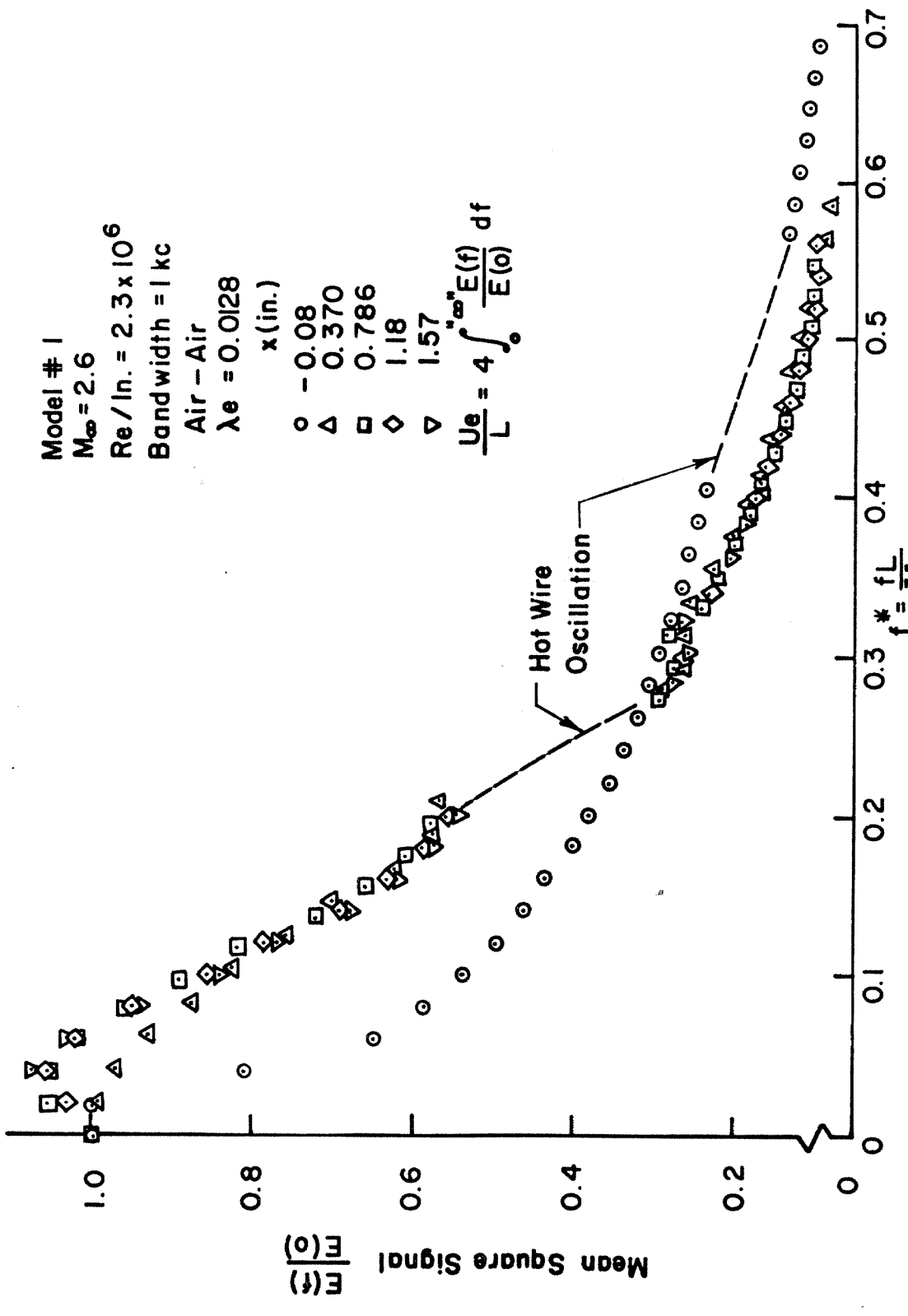

FIG. II. 24 FREQUENCY DISTRIBUTION OF PEAK FLUCTUATION INTENSITY

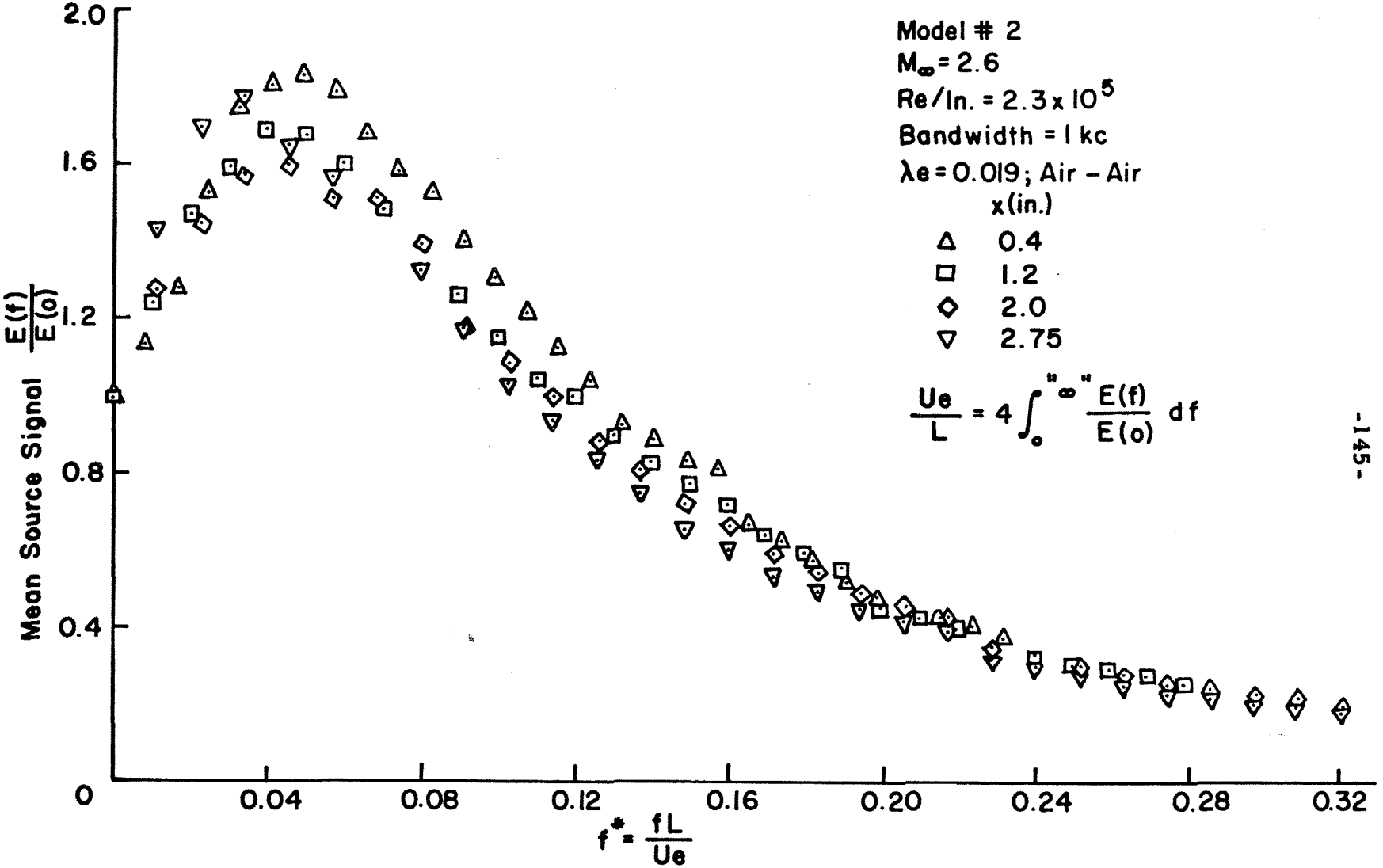

FIG. II.25 FREQUENCY DISTRIBUTION OF PEAK FLUCTUATION EXTENSITY

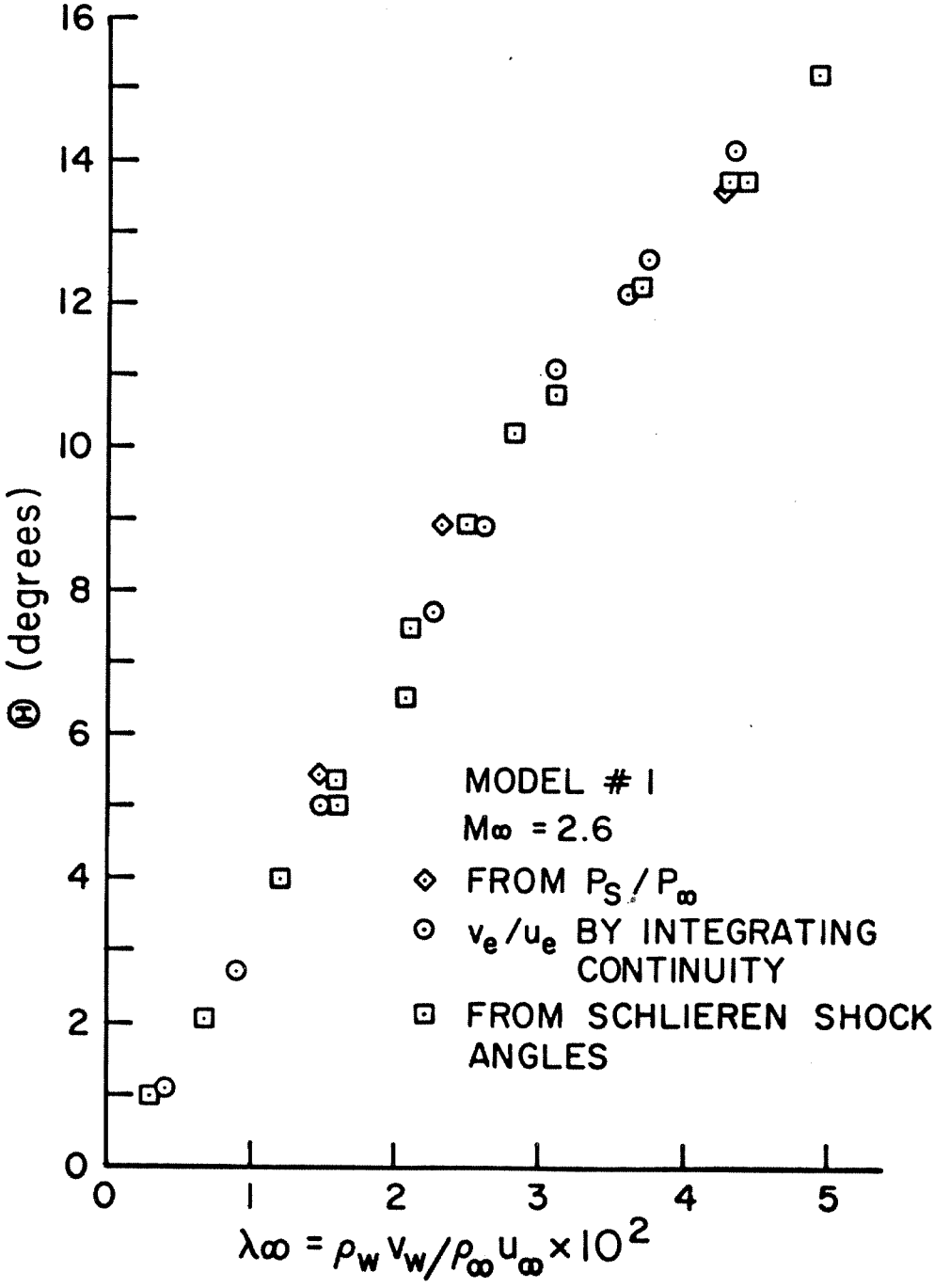

Fig.II.26 INDUCED FLOW ANGLE

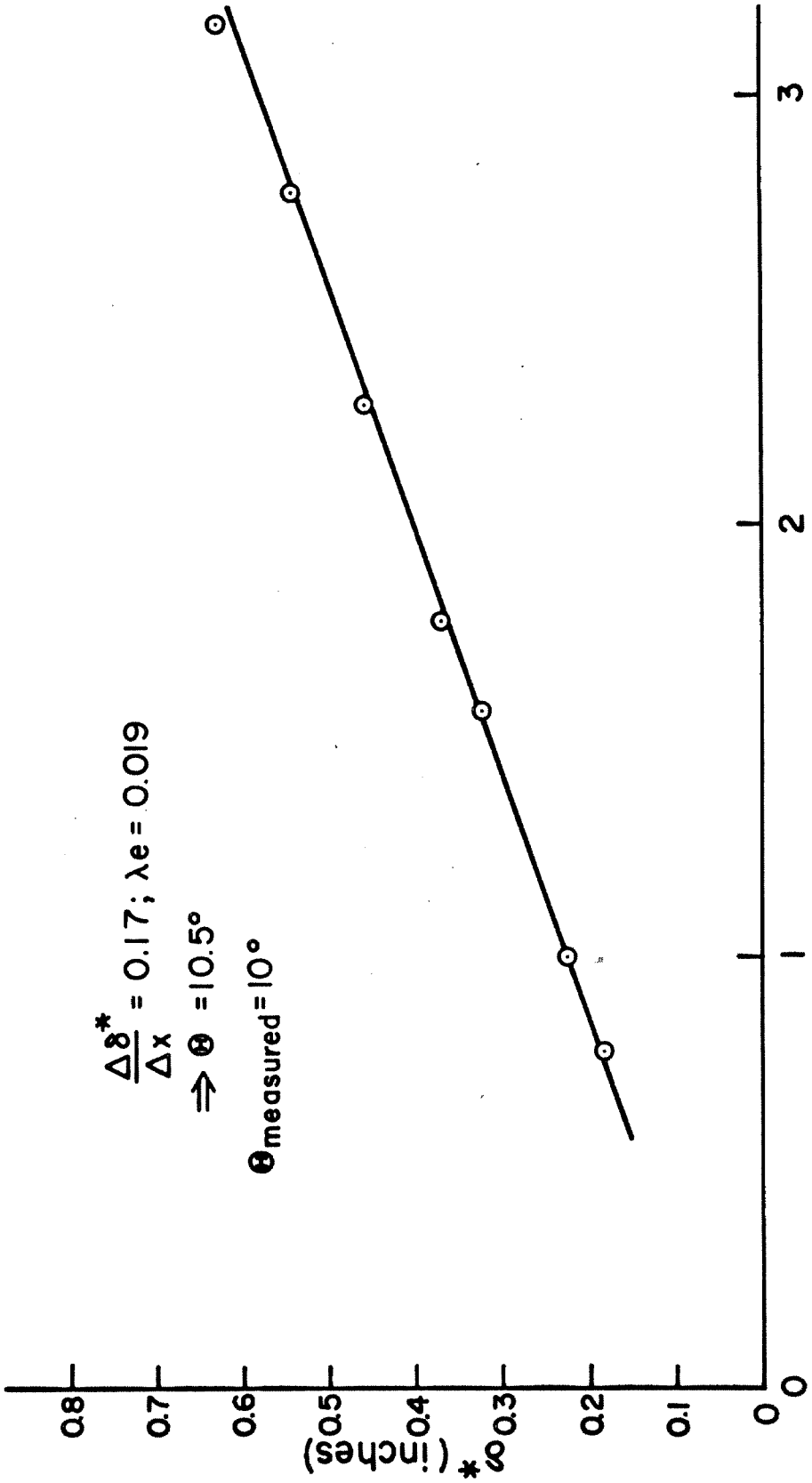

Fig.II.27 MASS BALANCE FOR 10° RAMP

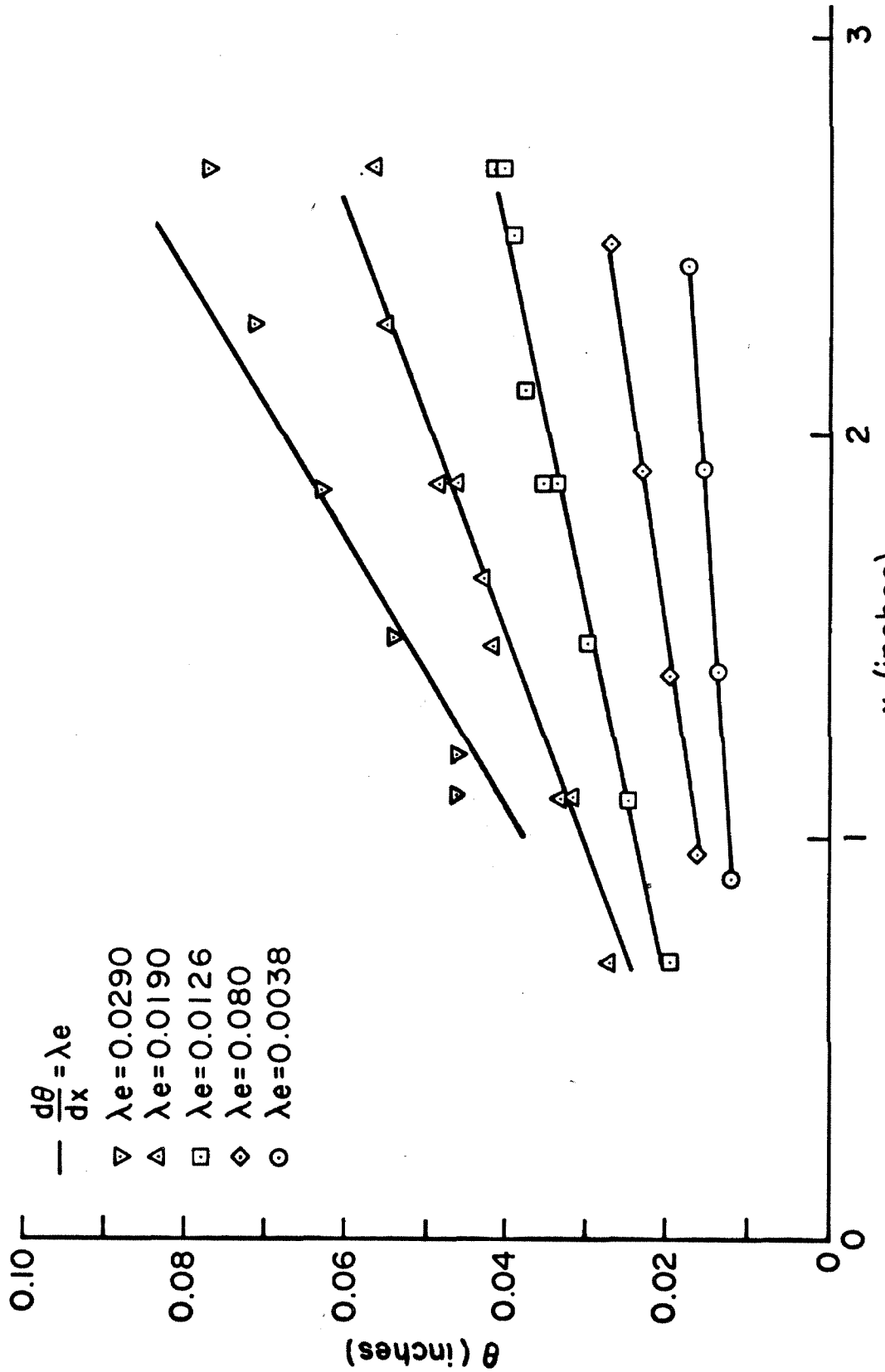

Fig.II.28 MOMENTUM THICKNESS, MODEL # 1

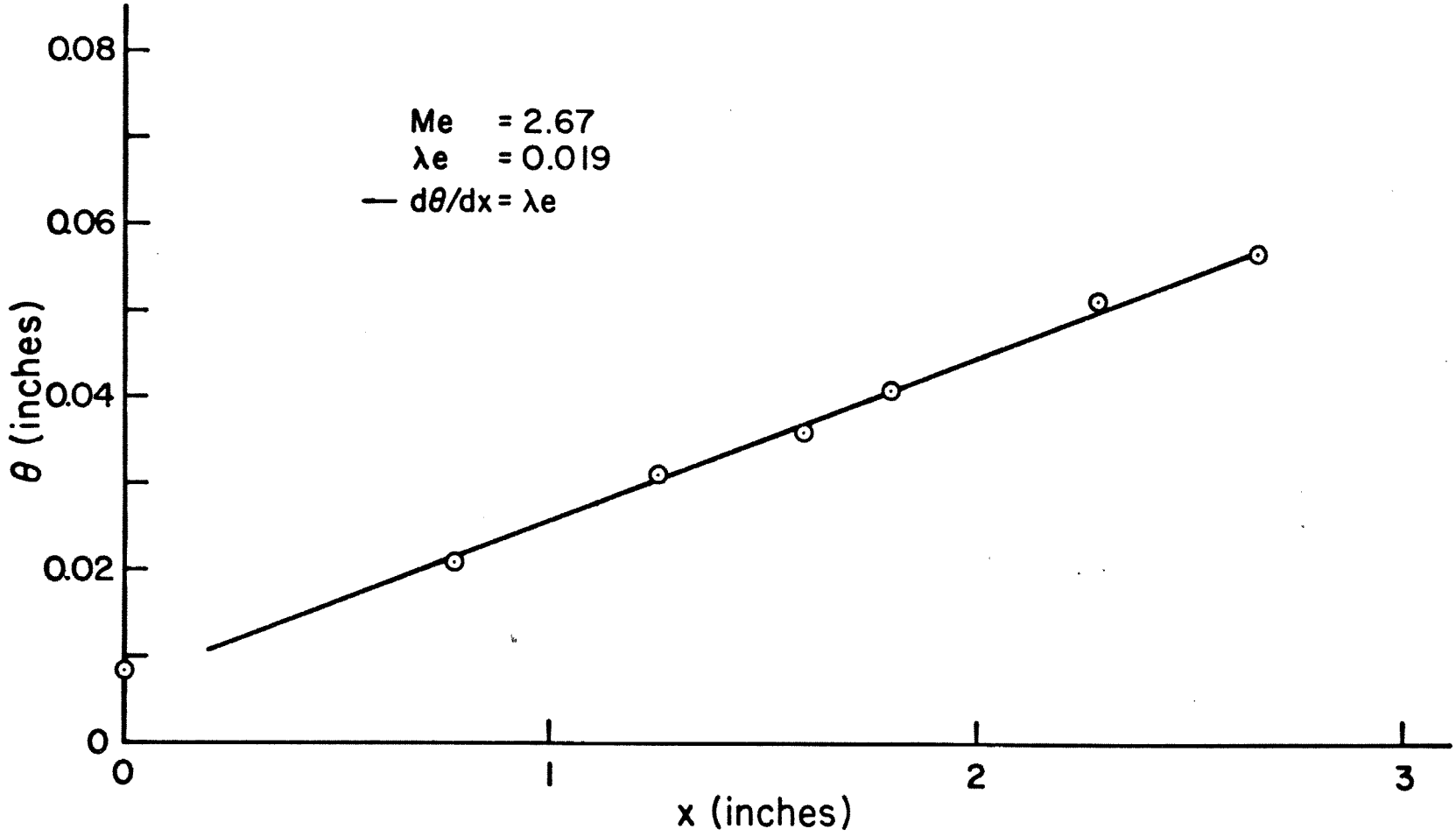

Fig. II.29 MOMENTUM THICKNESS, MODEL #2

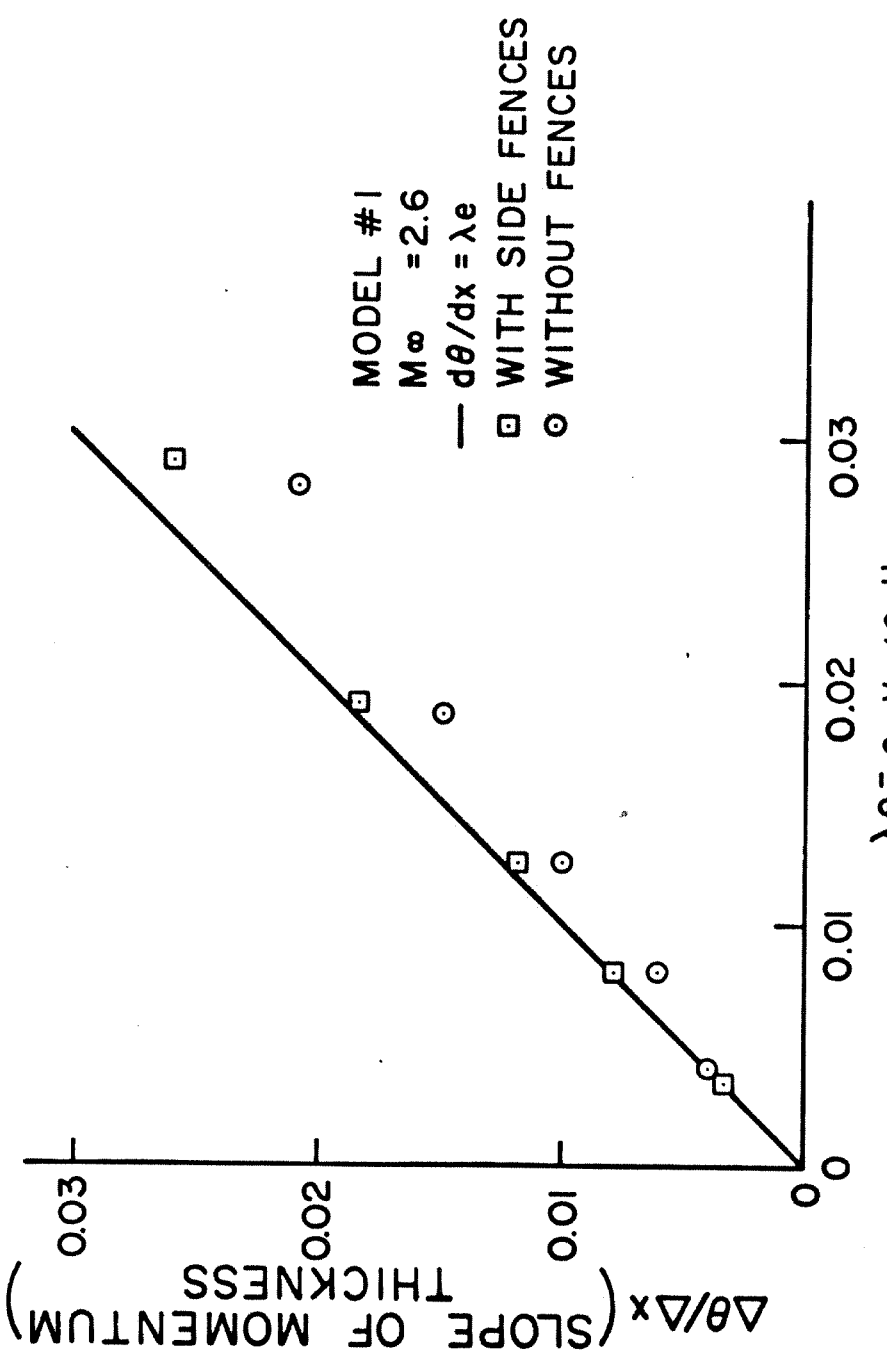

Fig.II.30 EFFECT OF SIDE FENCES ON MOMENTUM BALANCE

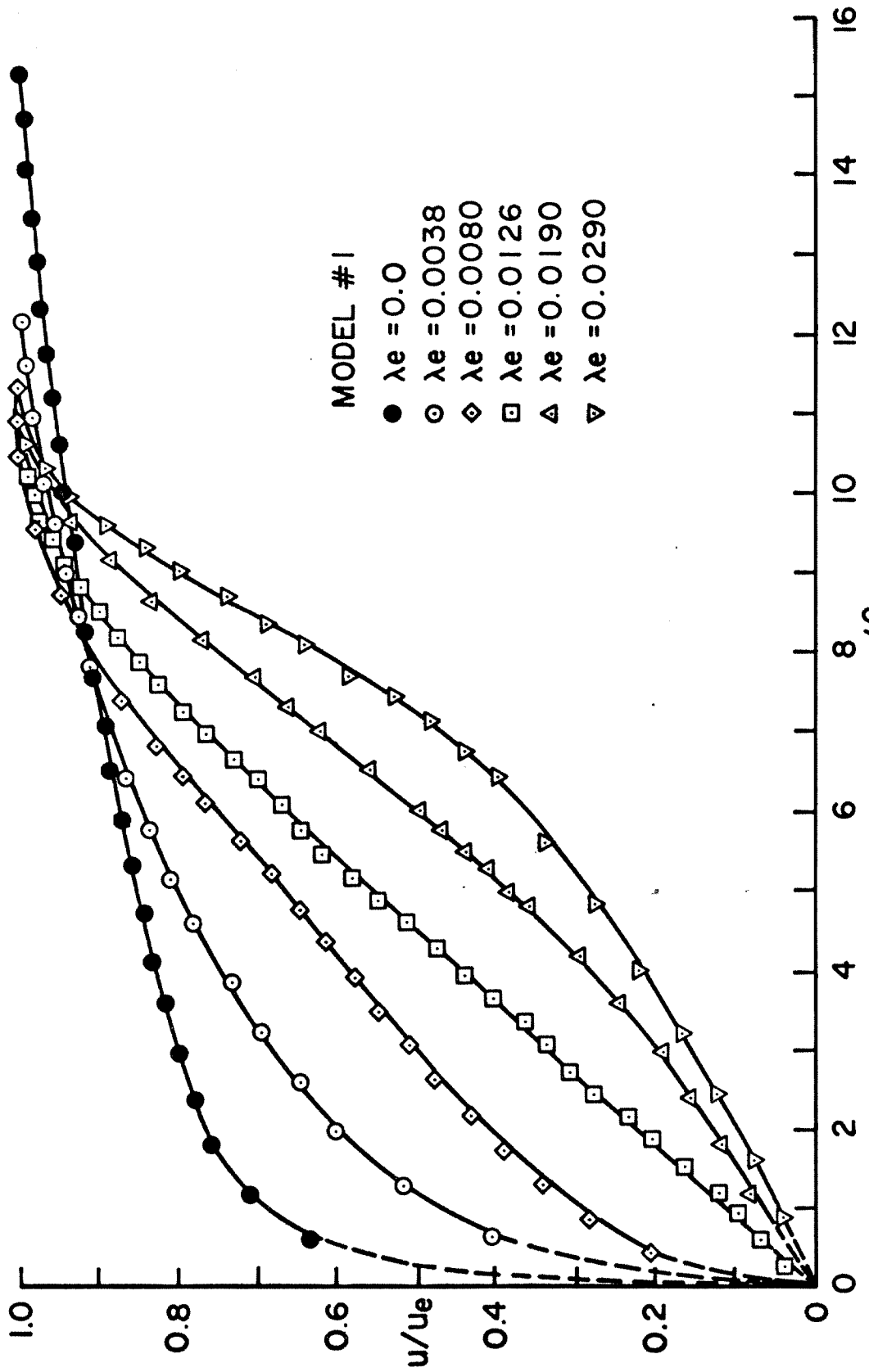

Fig.II.31 EFFECT OF INJECTION ON MEAN VELOCITY PROFILES

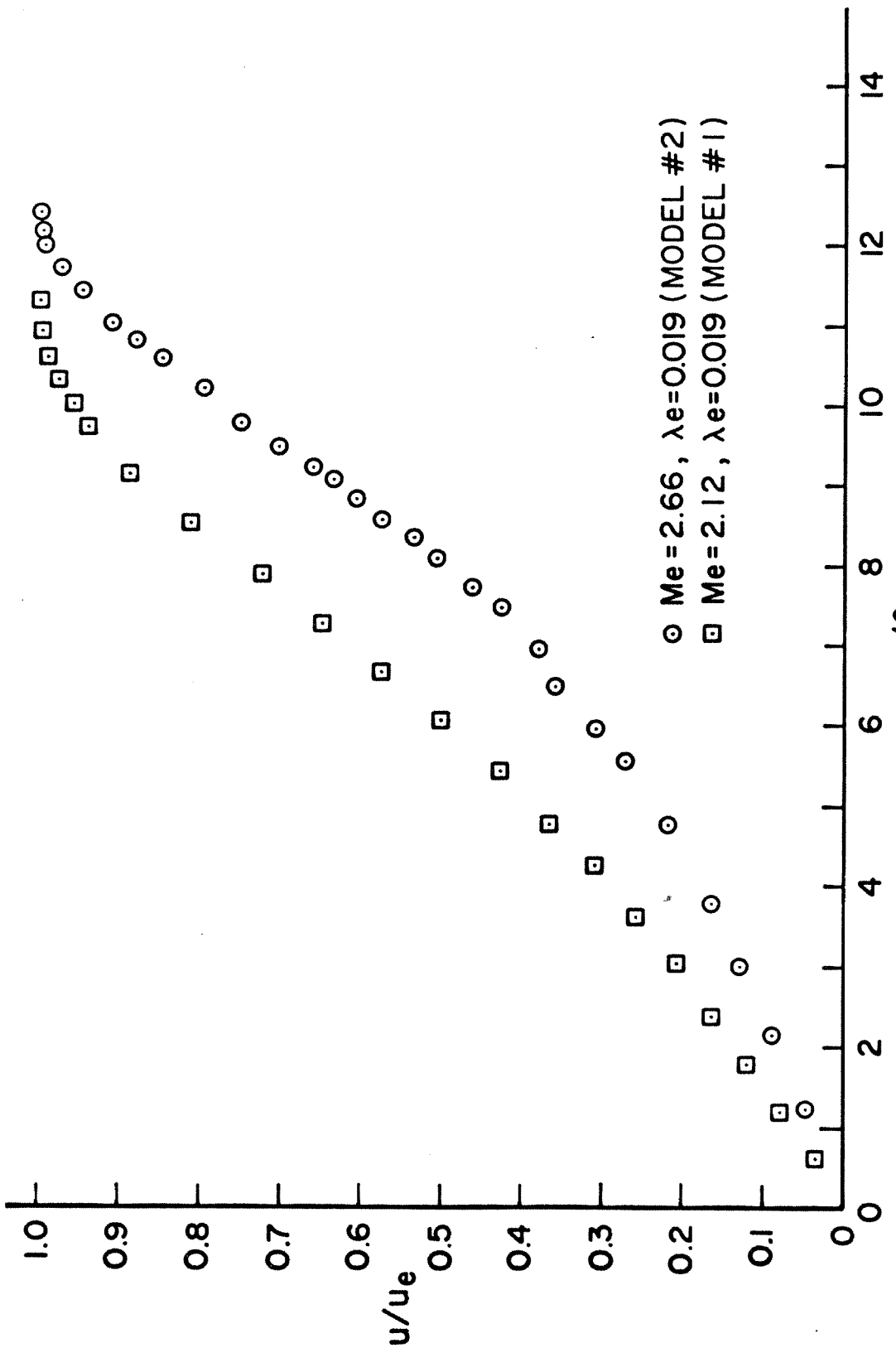

Fig.II.32 VELOCITY PROFILES; MODEL #1 AND #2

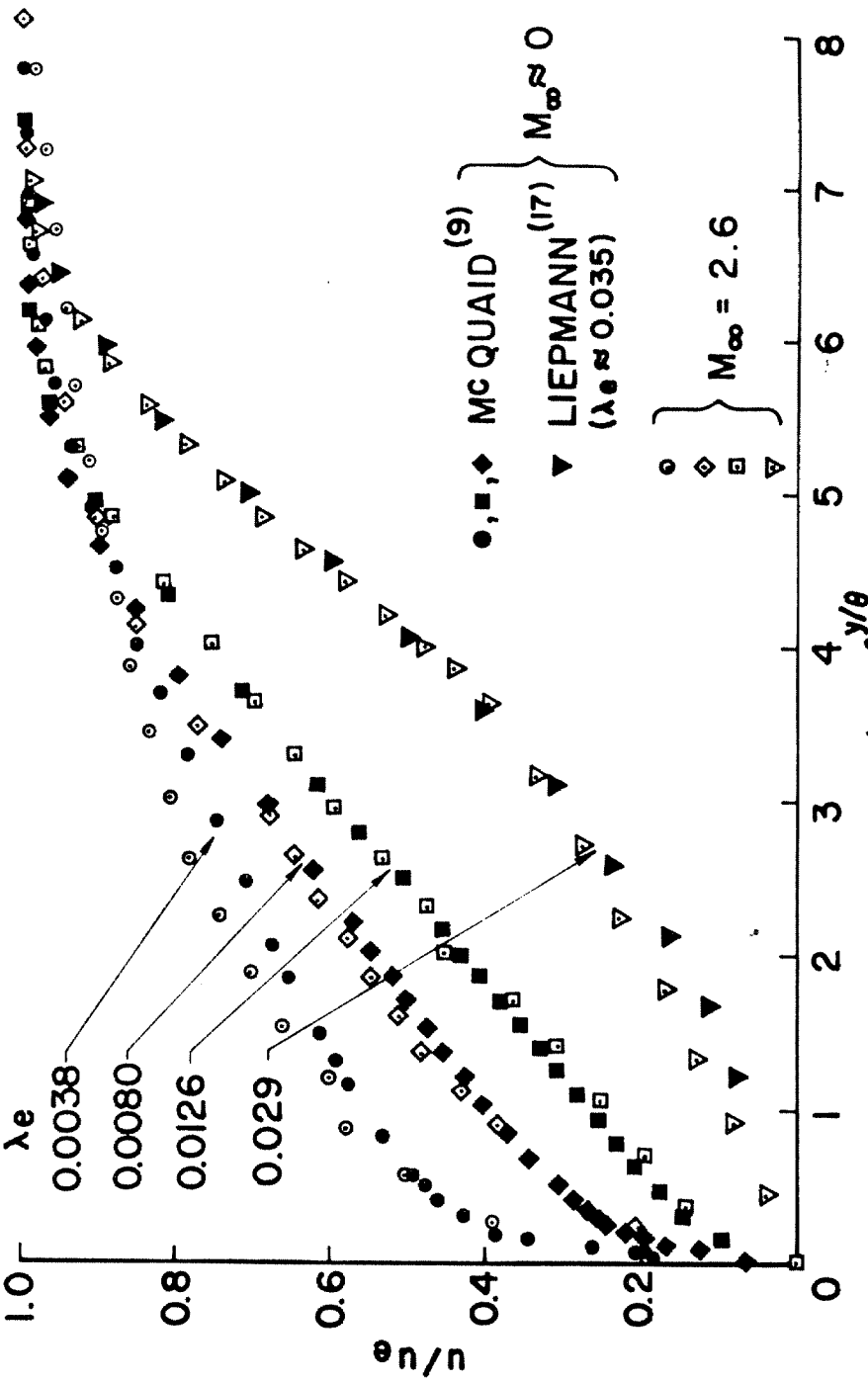

Fig.II.33 COMPARISON WITH LOW SPEED DATA, MODEL #1

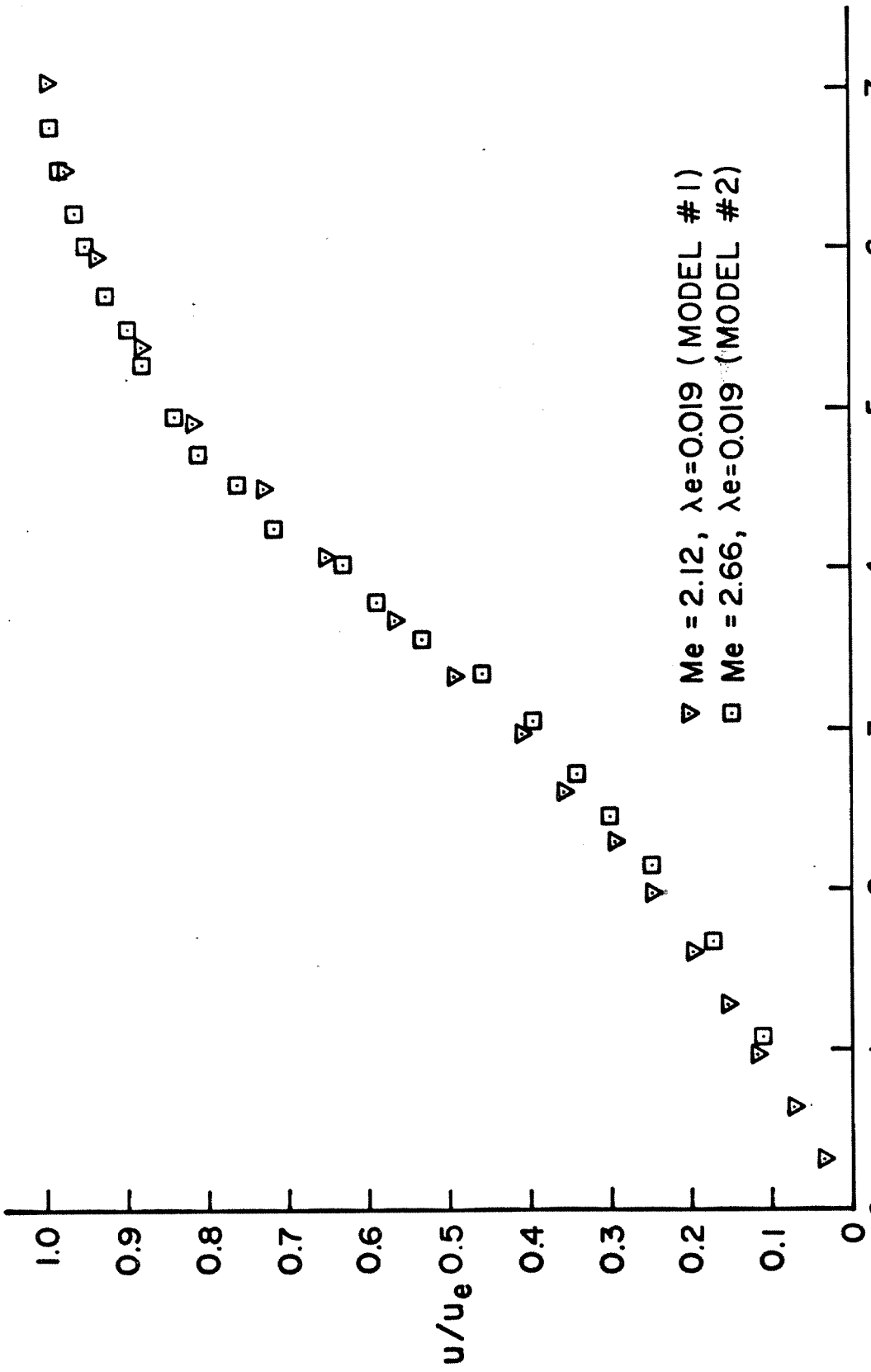

Fig.II.34 VELOCITY PROFILES, MODELS #1 AND #2

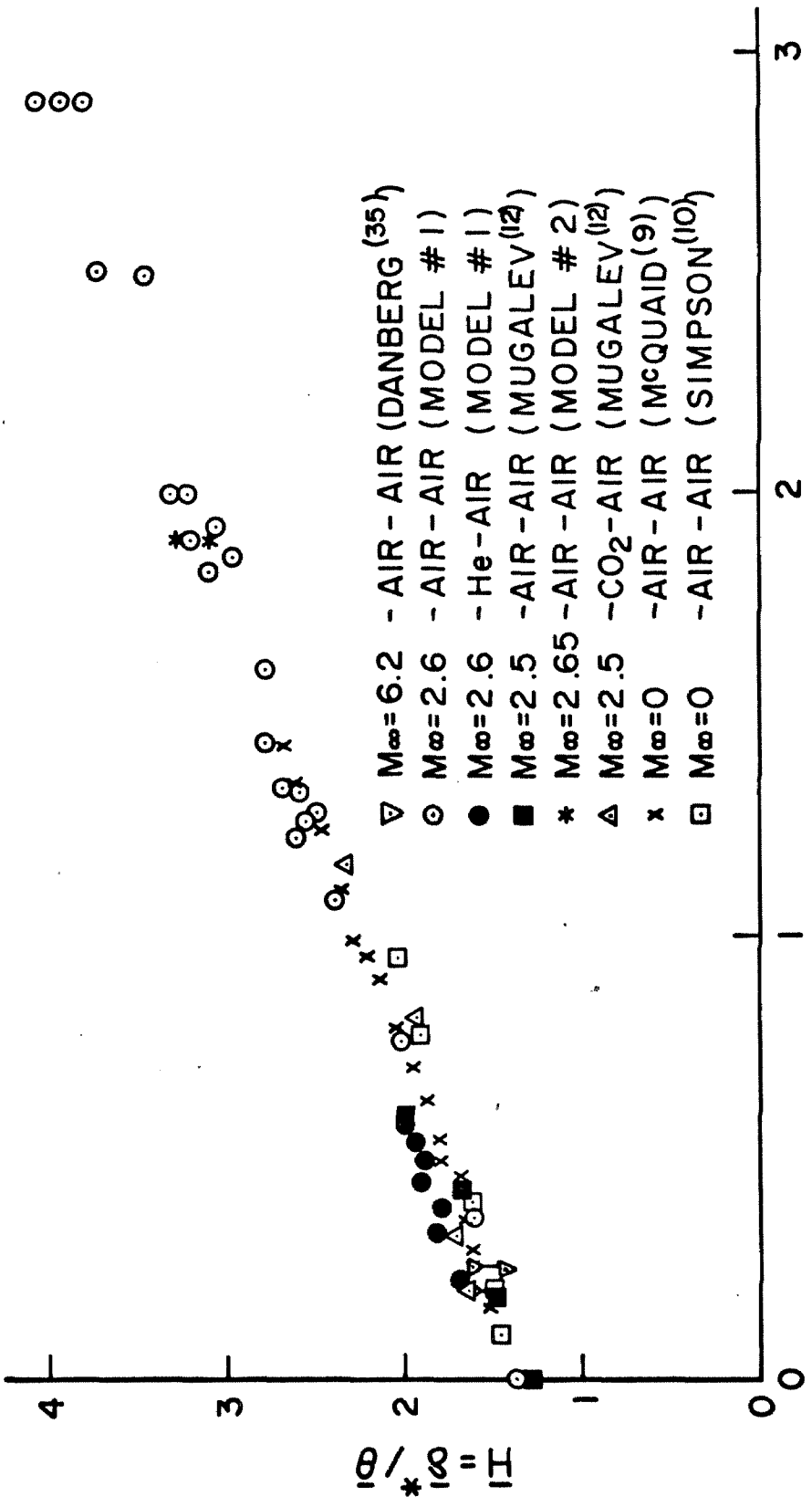

Fig.II.35 FORM PARAMETER COMPARISON

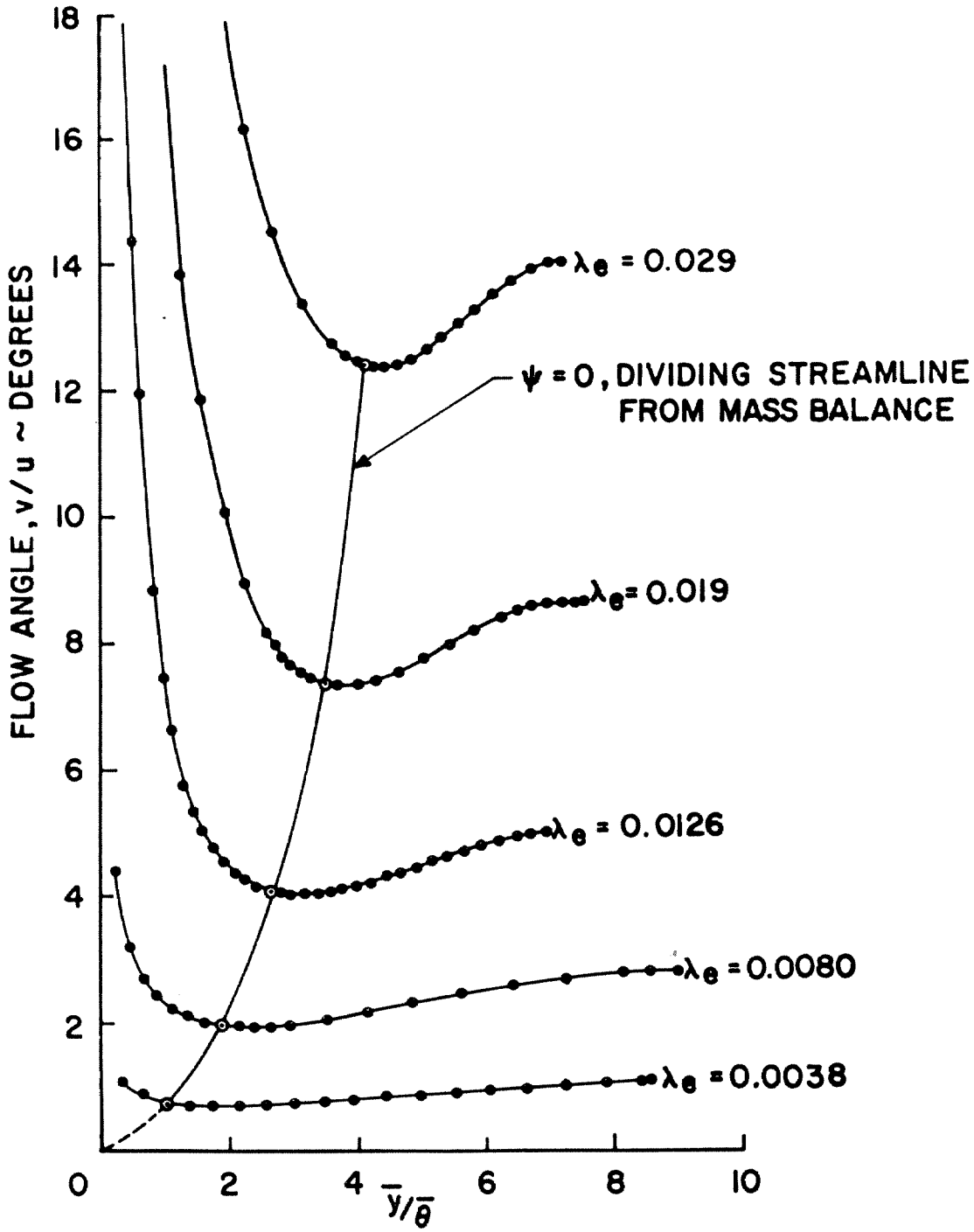

Fig.II.36 FLOW ANGLES, MODEL#1

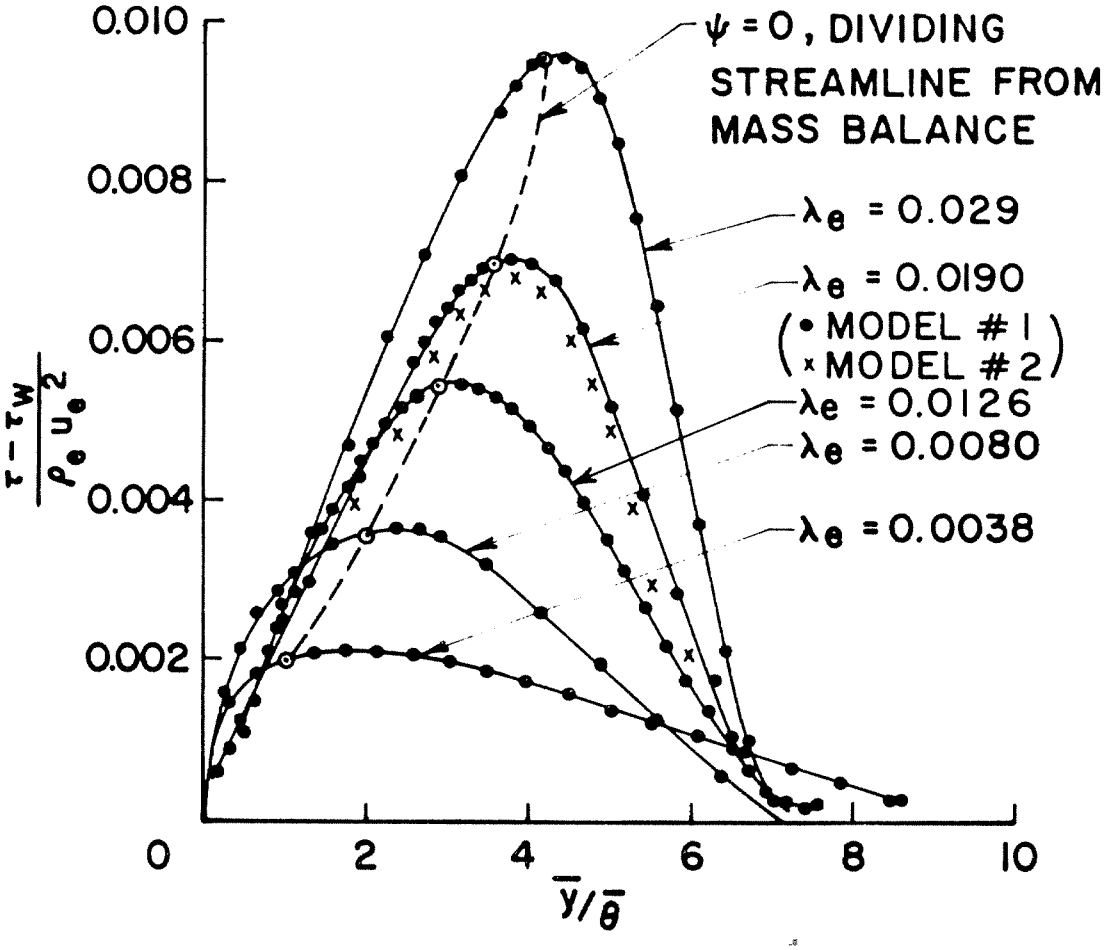

Fig.II.37 BOUNDARY LAYER SHEAR STRESS

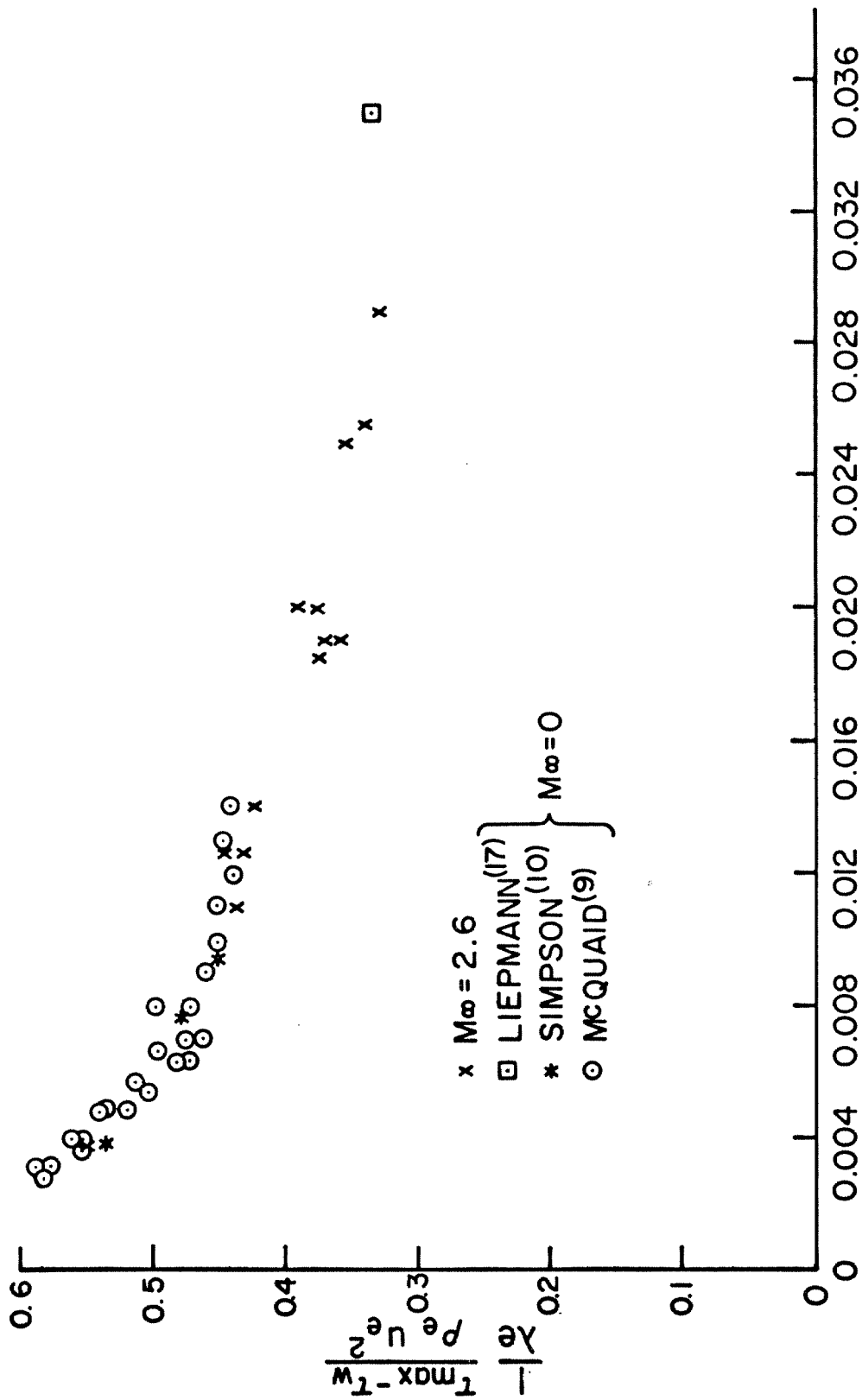

Fig. II.38 MAXIMUM SHEAR STRESS IN LAYER

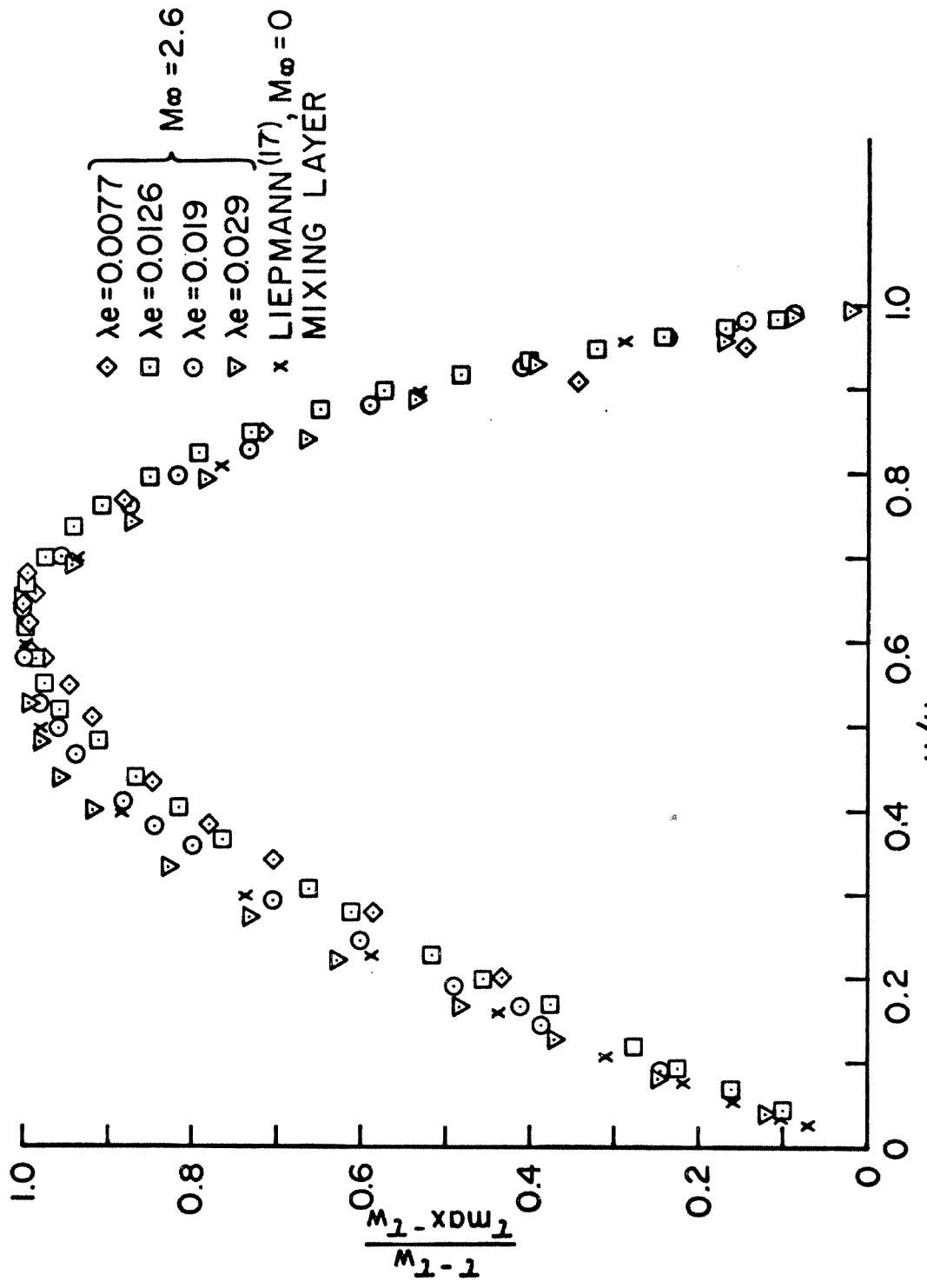

Fig.II.39 SHEAR STRESS VERSUS VELOCITY

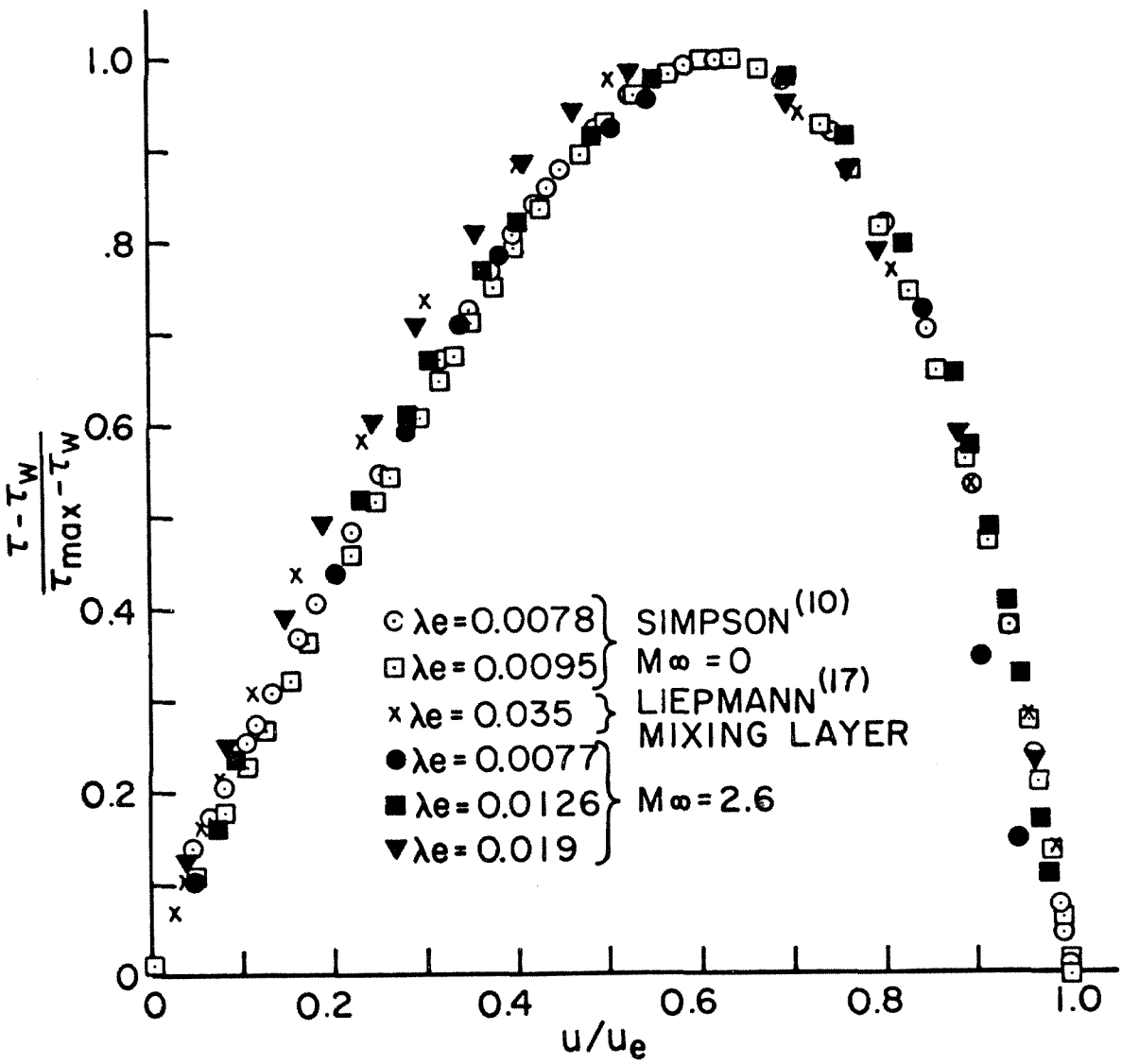

Fig. II.40 SHEAR STRESS VERSUS VELOCITY

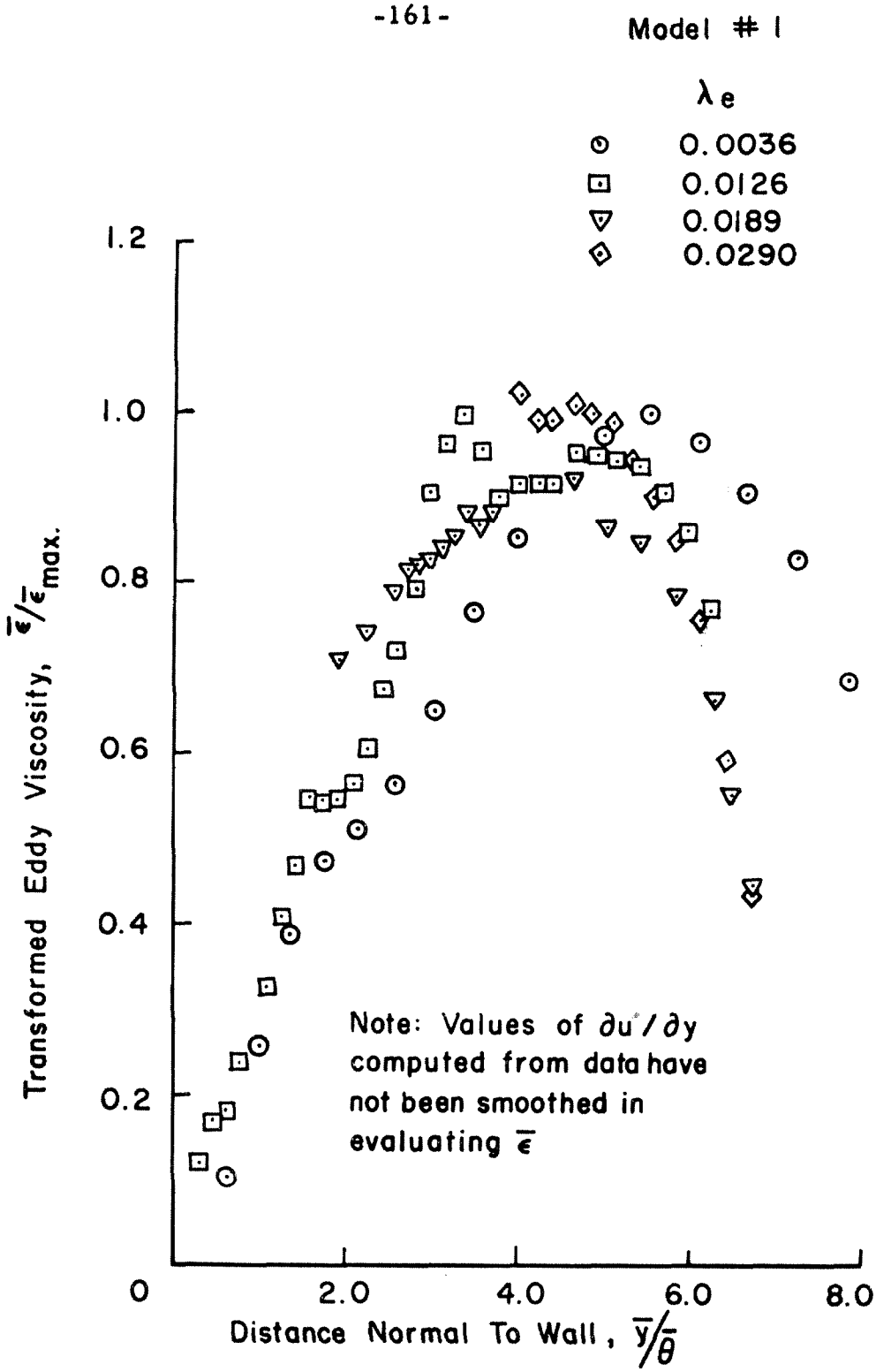

FIG. II.41 EDDY VISCOSITY

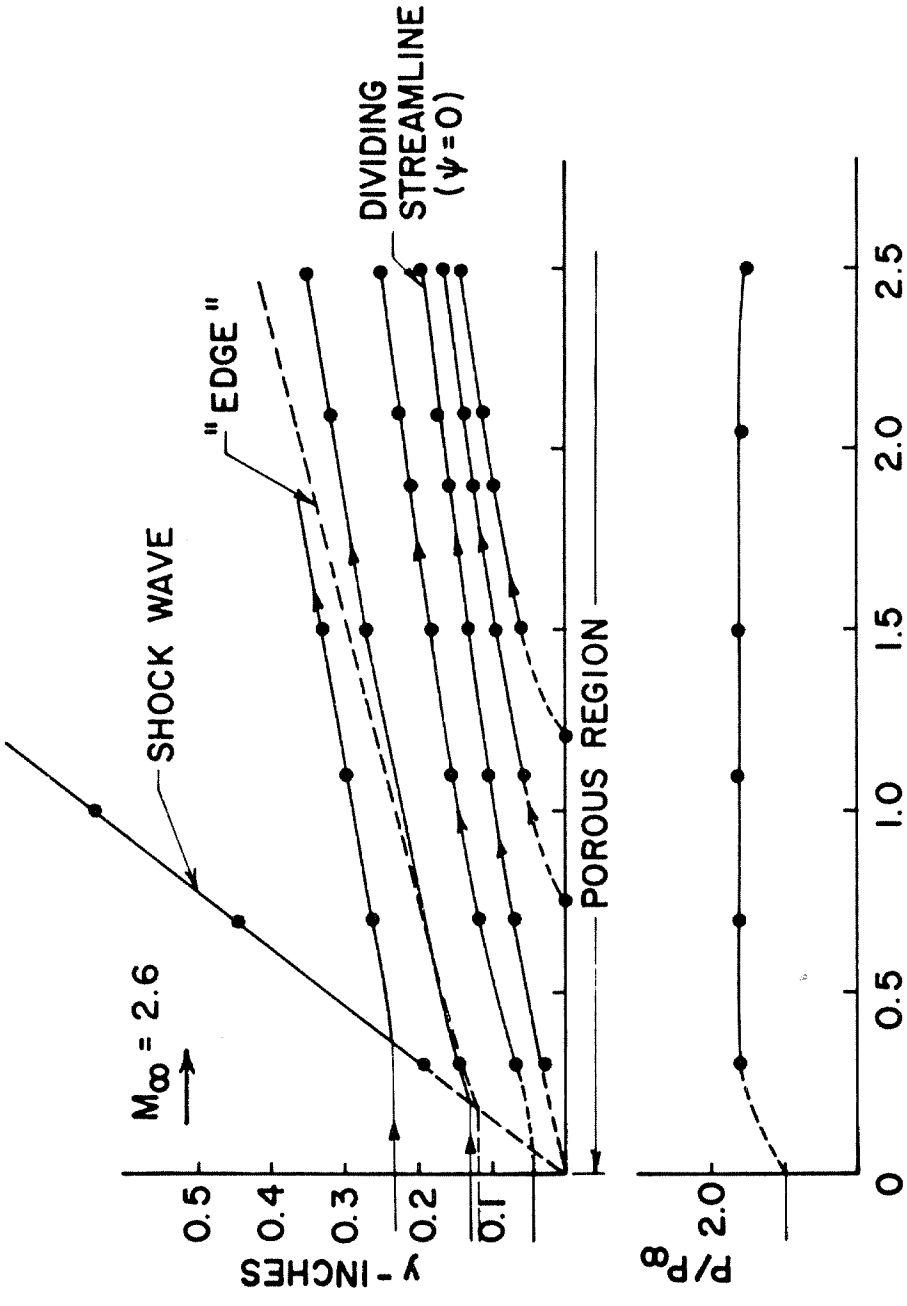

FIG. II.42 FLOW FIELD - MODEL # 1

$\lambda_\infty = \rho_w v_w / \rho_\infty u_\infty = 0.015$

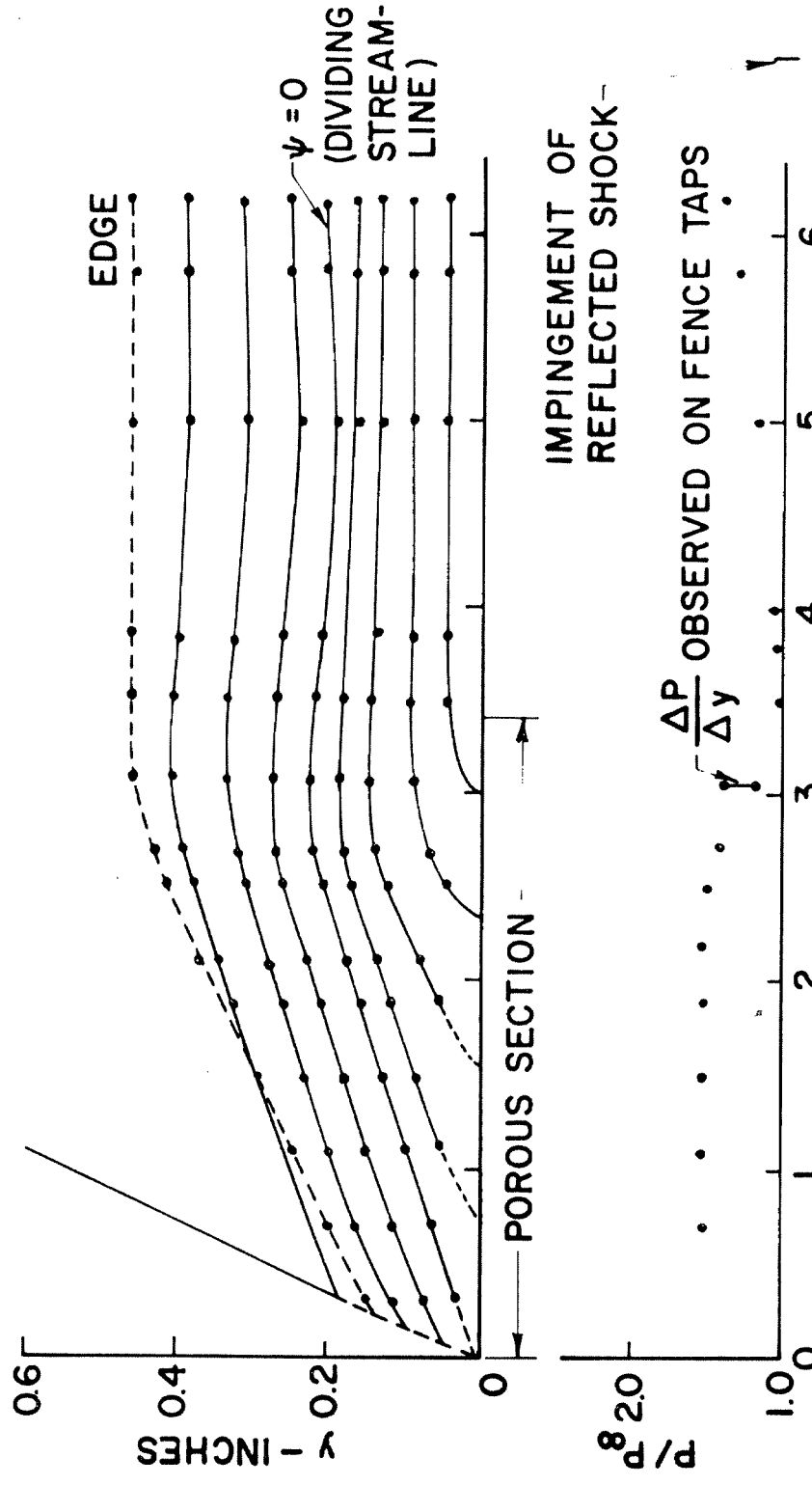

FIG. II.43 FLOW FIELD - MODEL # 1

$\lambda_\infty = \rho_w v_w / \rho_\infty u_\infty = 0.015$

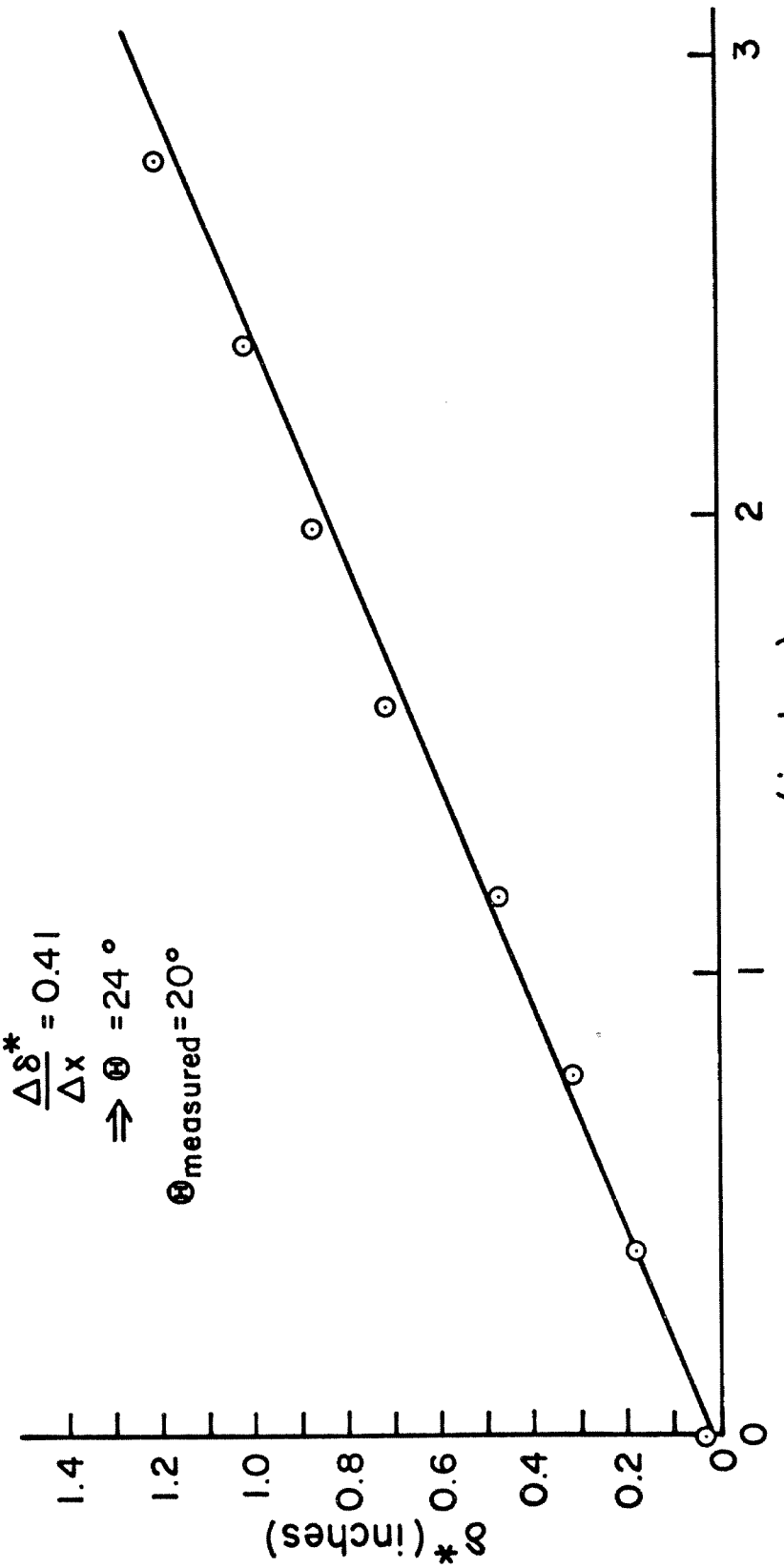

Fig.II.44 MASS BALANCE - 20° RAMP

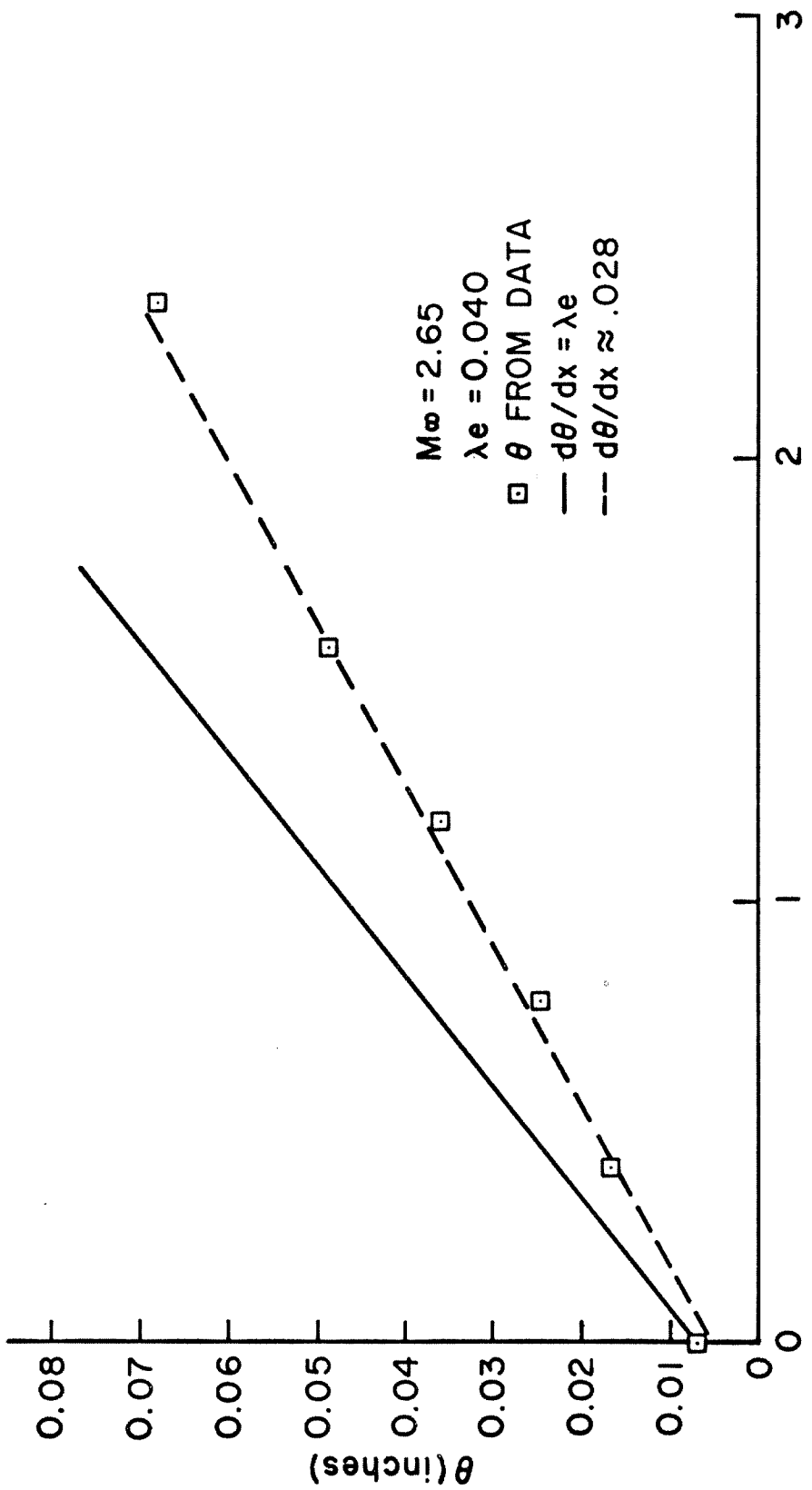

Fig.II.45 MOMENTUM BALANCE - 20° RAMP

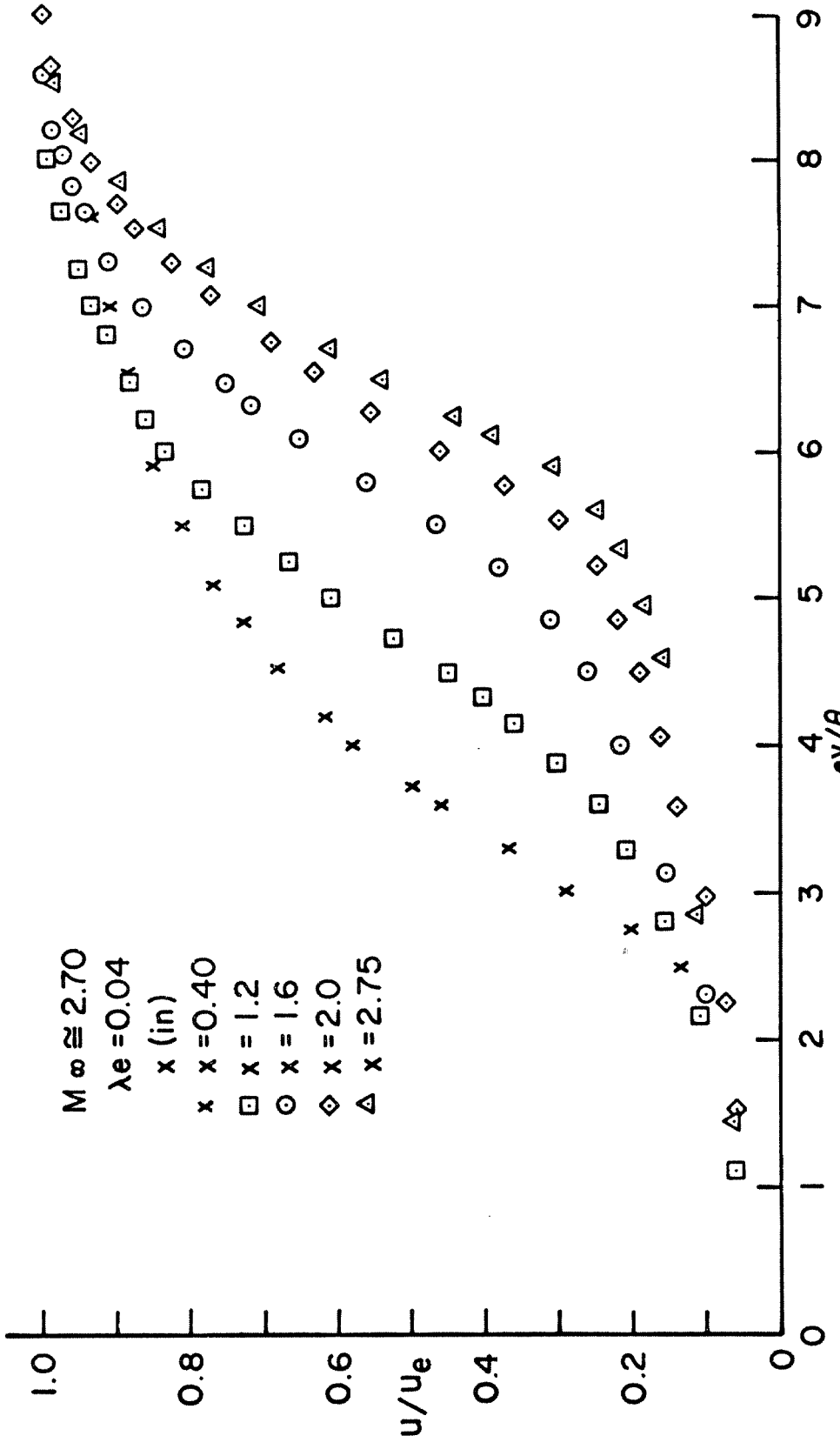

Fig.II.46 VELOCITY PROFILES - 20° RAMP

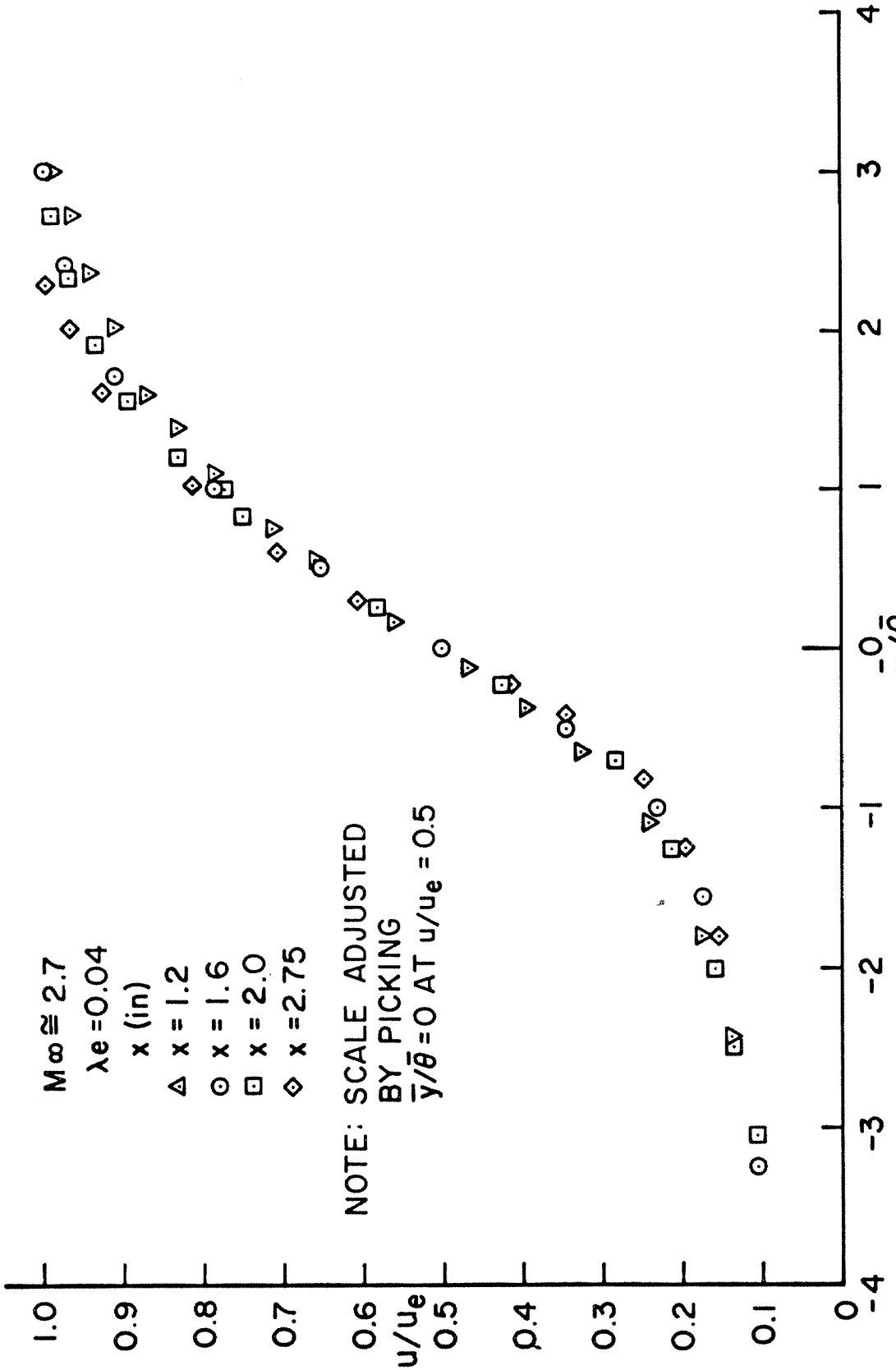

Fig. II.47 VELOCITY PROFILES - 20° RAMP

Appendix II. A

An Approximate Expression for the Induced Flow Angle with Foreign Gas Injection

For the case of zero pressure gradient, and $C_f/\lambda_e << 1$ the continuity equations (II. 13) and (II. 14) can be integrated across the layer and combined to give[20]

$$\tan \Theta = \lambda_e [1 + H^*] \qquad \text{(II. A. 1)}$$

where $H^* = \delta^*/\theta$.

Defining $d\bar{y} = \rho/\rho_e \, dy$

$$\delta^* = \int_0^\delta (1 - \frac{\rho_e}{\rho_e u_e}) dy = \int_0^\delta (\frac{\rho_e}{\rho} - \frac{u}{u_e}) \, d\bar{y} \qquad \text{(II. A. 2)}$$

$$\theta = \int_0^\delta \frac{\rho u}{\rho_e u_e} (1 - u/u_e) dy = \int_0^\delta \frac{u}{u_e} (1 - u/u_e) d\bar{y} \qquad \text{(II. A. 3)}$$

for a perfect gas mixture at constant pressure,

$$\frac{\rho_e}{\rho} = \frac{M_e}{M} \frac{T}{T_e} \; ; \; M = [\Sigma C_i/M_i]^{-1}$$

C_i = mass fraction

M_i = Mol. Wt. of the Species $\qquad \text{(II. A. 4)}$

Assuming an air-injected gas mixture with air only at the edge of the layer ($C_{gas} = 1 - C_{air}$)

$$\frac{\rho_e}{\rho} = \frac{T}{T_e} \left\{ C_{air} + (1 - C_{air}) \frac{M_{air}}{M_{gas}} \right\} \qquad \text{(II. A. 5)}$$

For simplicity assume

$$C_{air} = u/u_e \qquad \text{(II. A. 6)}$$

$$H = H_w + (H_e - H_w)u/u_e \qquad \text{(II. A. 7)}$$

where

$$H = \Sigma C_i h_i + u^2/2$$

$$h_i = C_{p_i} T_i \qquad \text{(II. A. 8)}$$

and where the individual gases are assumed to behave like perfect elements (C_p = const, zero heat of formation).

Then, assume for the GALCIT tunnel

$$T_w = T_e + \frac{u_e^2}{2C_{p_e}} \qquad \text{(II. A. 9)}$$

(i. e., the wall is at the same temperature as the plenum which is at room temperature). This, combined with equation (II. A. 7) implies that T_0 is constant across the layer. Combining (II. A. 7) and (II. A. 9 with the definition of total enthalpy (II. A. 8), one obtains (letting subscript g refer to the injected gas, a to the air)

$$\frac{T}{T_e}\left\{\frac{u}{u_e} + \frac{M_g}{M_a}\frac{C_{p_g}}{C_{p_a}}(1-u/u_e)\right\}$$

$$= \frac{\gamma-1}{2} M_e^2 \left\{-(u/u_e)^2 + \frac{C_{p_g}}{C_{p_a}}\frac{M_g}{M_a} + u/u_e\left(1 - \frac{C_{p_g}}{C_{p_a}}\frac{M_g}{M_a}\right)\right\}$$

$$+ \frac{u}{u_e} + \frac{M_g}{M_a}\frac{C_{p_g}}{C_{p_a}}(1 - u/u_e) \qquad \text{(II. A. 10)}$$

where C_{p_i} is the molal specific heat at constant pressure.

Then, using (II. A. 5) and (II. A. 6), get

$$\frac{\rho_e}{\rho} = \left\{\frac{u/u_e+(1-u/u_e)\mathcal{M}_a/\mathcal{M}_g}{u/u_e(1-u/u_e)C_{p_g}\mathcal{M}_a/C_{p_a}\mathcal{M}_g}\right\}\left\{\frac{\gamma-1}{2}\,M_e^2(u/u_e-(u/u_e)^2)\right.$$
$$\left.+(1+\frac{\gamma-1}{2}\,M_e^2)\,\frac{C_{p_g}}{C_{p_a}}\,\frac{\mathcal{M}_a}{\mathcal{M}_g}\,(1-u/u_e)+u/u_e\right\} \qquad \text{(II. A. 11)}$$

If both gases are diatomic, then $C_{p_g}/C_{p_a} \approx 1$. For helium injection, $C_{p_g}/C_{p_a} \approx 5/7$. However, for $u/u_e = \epsilon << 1$ it can be shown that this effect is not important to order ϵ. For $u/u_e = 1-\epsilon$, the effect causes an error $\approx 15\%$ for these test conditions. In view of the approximations made thus far, it seems justifiable to neglect this effect. Then, equation (II. A. 11) becomes

$$\frac{\rho_e}{\rho} - \frac{u}{u_e} \approx \frac{\gamma-1}{2}\,M_e^2(u/u_e-(u/u_e)^2) + (1+\frac{\gamma-1}{2}M_e^2)\,\frac{\mathcal{M}_a}{\mathcal{M}_g}\,(1-u/u_e) \qquad \text{(II. A. 12)}$$

Combining this with (II. A. 1) and (II. A. 2) gives

$$H^* = \dot{\delta}^*/\theta = \frac{\gamma-1}{2}\,M_e^2 + (1+\frac{\gamma-1}{2}\,M_e^2)\,\frac{\mathcal{M}_a}{\mathcal{M}_g}\,\overline{H} \qquad \text{(II. A. 13)}$$

where $\overline{H} = \overline{\delta}^*/\overline{\theta}$, $\overline{\delta}^* = \int_0^{\sigma} (1-u/u_e)d\overline{y}$

Then, the expression for the induced angle (II. A. 1) gives

$$\tan\Theta \approx \lambda_e(1+\frac{\gamma-1}{2}\,M_e^2)\left\{1+\frac{\mathcal{M}_{air}}{\mathcal{M}_{gas}}\,\overline{H}\right\} \qquad \text{(II. A. 14)}$$

Of course, equation (II. A. 14) can only be expected to give approximate answers, but should be useful in obtaining a reasonable estimate of the effect of varying molecular weight of the injected gas. Table II. A. 1 summarizes the results obtained using schlieren photographs to obtain Θ and equation (II. A. 14) to obtain $\overline{H}(\lambda_e)$.

Table II. A. 1

Shock Angles, Helium Injection ($M_\infty = 2.55$)

λ_∞	θ_s	θ_w	λ_e	$\overline{H}$ (Eqn. II. A. 14)	Injectant
.0027	26.5	4.2	.0023	1.75	Helium
.0038	27.5	5.3	.0032	1.85	
.0059	29.5	7.8	.0045	1.91	
.005	28.5	6.7	.004	1.83	
.0067	30	8.3	.005	1.90	
.007	30.5	8.9	.0053	1.96	
.008	31.5	10.0	.0058	2.02	
.0143	27.5	5.3	.0124	2.61	AIR (Check Case for Eq. (II. A. 14))

Appendix II. B

An Invariant for Constant Pressure Mixing

B. 1 Preliminary Discussion

Although the analysis presented in this appendix does not directly relate to the problem investigated in this section, the conclusions arrived at seem general enough to warrant presentation. We consider the ideal case of constant pressure mixing between two fluid streams. One has density and velocity ρ_1, u_1. The other has density, velocity ρ_2, u_2.

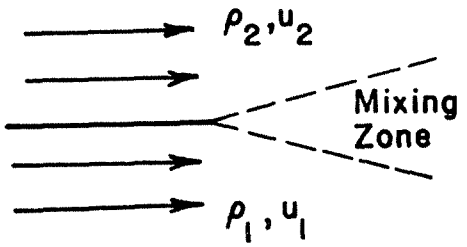

We assume boundary-layer equations are valid for the mean flow

$$\frac{\partial}{\partial x}(\rho u) + \frac{\partial}{\partial y}(\rho v) = 0 \qquad \text{(IIB. 1)}$$

$$\rho u \frac{\partial u}{\partial x} + \rho v \frac{\partial u}{\partial y} = \frac{\partial \tau}{\partial y} \qquad \text{(IIB. 2)}$$

Assuming a turbulent layer where viscous stresses are neglected, the only parameters in the problem are ρ_1, u_1, ρ_2, u_2. There is no length scale in this problem so postulate that the flow must be similar. Since y/x is the only dimensionless quantity involving lengths, the layer must be linear in x, i. e., u, ρ are functions only of $y/x = \xi$.

The coordinate system is taken to be along the streamline

which divides the two fluids. By definition, this streamline originates from the origin of the mixing region and is a straight line for constant pressure mixing. Since the coordinate system is located on this line, $\xi = y/x = 0$ along this streamline ($\psi = 0$). Hence, u, ρ are constant along $\psi = 0$. Then, from equation (II. B. 2) since u = constant along this line, $\frac{\partial \tau}{\partial y} = 0$ which implies τ has an extremum (a maximum in this case).

Integrating equation (II. B. 2) and using (II. B. 1) we get

$$\tau_{max} = \tau(0) = \int_0^{\infty} \rho u(u_2 0u) d(y/x) \qquad \text{(II. B. 3)}$$

using a stream function ψ: $\frac{\partial \psi}{\partial y} = \rho u$, $\frac{\partial \psi}{\partial x} = \rho v$, equation (II. B. 3) can be written as

$$\tau_{max} = \int_0^{\infty} \frac{\psi}{x} \frac{\partial u}{\partial y} \, dy \qquad \text{(II. B. 4)}$$

II. B. 2 Analysis

The sufficient conditions for transforming an incompressible (barred) flow to a compressible flow given by Coles[18] are

$$\begin{aligned} \bar{\psi} &= \sigma(x)\psi \\ d\bar{x} &= \xi(x)dx \\ \bar{\rho}\, \partial \bar{y} &= \eta(x)\rho\, \partial y \end{aligned} \qquad \text{(II. B. 5)}$$

We will assume y = 0 transforms into $\bar{y} = 0$. From these equations it then follows that

$$\frac{u_2}{u_1} = \frac{\bar{u}_2}{\bar{u}_1} = \text{const}$$

is necessary for the two flows to transform into each other. Furthermore, from (II. B. 5) (see Coles[18])

$$\rho_1 \bar{v}_1 = \frac{\sigma}{\xi} \rho_1 v_1 \left\{1 + \frac{x}{\sigma}\frac{d\sigma}{dx} + \frac{u_1}{v_1}\left\{\frac{y}{\sigma}\frac{d\sigma}{dx} - \frac{\overline{\rho u}_1}{\rho u}\frac{1}{\sigma}\frac{\partial \bar{y}}{\partial x}\right\}\right\} \qquad \text{(II. B. 6)}$$

and

$$\frac{\xi\eta}{2}\,\bar{\tau} = \tau + \frac{1}{}\frac{d}{dx}\int_y^\infty \psi \frac{\partial u}{\partial y}\,dy \qquad \text{(II. B. 7)}$$

in particular, when $y = 0$, $\tau = \tau_{max}$ and (II. B. 7) together with (II. B. 4) gives

$$\frac{\xi\eta}{\sigma^2}\,\bar{\tau}_{max} = \tau_{max}\left[1 + \frac{x}{\sigma}\,\frac{d\sigma}{dx}\right] \qquad \text{(II. B. 8)}$$

For conical flow, with some manipulation of equation (II. B. 6) and using the fact that $\frac{\sigma}{\eta} = \text{const}$, equation (II. B. 6) becomes

$$\bar{\rho}\,\bar{v}_1 = \frac{\sigma}{\xi}\rho_1 v_1 \quad (1 + \frac{x}{\sigma}\frac{d\sigma}{dx})\,(1 + \frac{u_1}{v_1} I) \qquad \text{(II. B. 9)}$$

where $I = \int_0^\infty (\rho/\rho_1 - 1)\,d(y/x)$ (II. B. 10)

Then, using (II. B. 8) and (II. B. 10), we get, letting $\lambda_e = \rho_1 v_1/\rho_2 u_2$; $\bar{\lambda}_e = \bar{v}_1/\bar{u}_2$

$$\frac{\bar{\tau}_{max}}{\bar{\rho}\,\bar{u}_2^2\,\bar{\lambda}_e} = \frac{\tau_{max}}{\rho_2 u_2^2 \lambda_e\left\{1 + \frac{u_1}{v_1} I\right\}} \qquad \text{(II. B. 11)}$$

So, since these are constants it follows that

$$\frac{\tau_{max}}{\rho_2 u_2^2 \lambda_e \left\{1 + \frac{u_1}{v_1} I\right\}} = \text{const.}^{*} \qquad \text{(II. B. 12)}$$

For the special case where $u_1 \equiv 0$, (II. B. 12) gives

$$\frac{\tau_{max}}{\rho_2 u_2^2 \lambda_e} = \text{const} = 0.34 \text{ (using the data of Liepmann-Laufer [17])} \qquad \text{(II. B. 13)}$$

which is the analogue of Coles' "Law of Corresponding Station."[18] More importantly, equation (II. B. 12) indicates the sensitivity of the shear stress-entrainment ratio for flows with large density gradients and small, but finite secondary flows ($u_1 \neq 0$), because an incompressible flow equation (II. B. 12) shows that a secondary flow will have no effect on the ratio.

---

*This result is as general as the equation used initially. No assumption as to the form of the density variation or shear stress function has been made. It should apply to flows with more than one gas, or variable Mach number.

PART III. THE EFFECT OF FINITE PLATE LENGTH

List of Figures - Part III

List of Symbols - Part III

B	function defined in equation (III. 12)
C_f	skin friction coefficient = $2\tau_w/\rho_e u_e^2$
C_p	specific heat at constant pressure
D	function defined in equation (III. 28)
f	function defined in equation (III. 12)
H	θ_i/δ_i^* - form factor = $1/\bar{H}$
J	integral function = $\frac{1}{\delta_i^*} \int_0^{\delta_i} u/u_e \, (1-(u/u_e)^2) dY$
K_θ	eddy viscosity coefficient ($\rho^2 \epsilon = K_\theta \rho_R^2 u_e \theta$)
K	perturbation parameter in equation (III. 36)
L	length of porous plate
M	Mach number
m	$\frac{\gamma-1}{2} M^2$
$N_{1,2,3}$	functions defined in equations (III. 25-III. 27)
P	static pressure
R	integral function = $\frac{2}{\lambda_e} \int_0^{\delta_i} \frac{\tau}{\rho_e u_e^2} \frac{\partial(u/u_e)}{\partial Y} dY$
T	static temperature
u	velocity component in x-direction
v	velocity component in y-direction
x	distance along plate measured from start of porous region
y	distance normal to plate
Y	transformed distance normal to wall, $dY = \frac{a_e \rho}{a_2 \rho_2} dy$
Z	integral function = $\frac{1}{\delta_i^*} \int_0^{\delta} u/u_e \, dY$
δ^*	displacement thickness = $\int_0^{\delta} (1 - \frac{\rho u}{\rho_e u_e}) dy$

List of Symbols - Part III (Cont'd)

δ edge of layer

θ momentum thickness, $\int_0^{\delta} \frac{\rho u}{\rho_e u_e}(1-u/u_e)dy$

δ_i^* transformed displacement thickness, $\int_0^{\delta_1}(1-u/u_e)dY$

θ^{**} integral function, $\int_0^{\delta} \frac{\rho u}{\rho_e u_e}(1-(u/u_e)^2)dy$

δ_u integral function, $\int_0^{\delta}(1-u/u_e)dy$

Θ induced flow angle at edge, $\tan\Theta = v_e/u_e$

λ_e $\rho_w v_w/\rho_e u_e$

λ_∞ $\rho_w v_w/\rho_\infty u_\infty$

η, ξ, σ transformation functions

μ viscosity

ψ stream function, $\partial\psi/\partial y = \rho u$, $\partial\psi/\partial x = -\rho v$

τ shear stress

ρ density

Subscripts

w wall value

e value at edge of layer

∞ free stream value

i transformed quantities

2 value at reference station (similar region)

Bars above quantities denote values for an incompressible flow ($\bar{\rho}$ = constant)

PART III

THE EFFECT OF FINITE PLATE LENGTH

III. 1. Introduction

This final part of the report concerns itself with an analytical investigation of the effect of the abrupt cessation of injection which occurs at the end of any finite length porous plate in supersonic turbulent flow. The experimentally observed importance of this effect at the larger injection rates has been briefly referred to in the previous section, and in this part a physically rational yet mathematically simplified approach is adopted to predict the observed pressure and velocity profile variations caused by the adjustment of the flow to the end of injection.

The reason for establishing an analytical model which can predict the extent and magnitude of the observed induced favorable pressure gradient ($\frac{\partial p}{\partial x} < 0$) upstream of the termination of injection can be found in the results obtained in Part I. Although the analysis presented in Part I was for similar laminar flow, certain qualitative aspects can be expected to carry over to the turbulent case. In particular, there is the very important conclusion that for any finite favorable pressure gradient there is no singularity in the boundary-layer equations as injection is increased, as compared to the zero pressure gradient case (Blasius equation) where such a singularity does exist for a particular value of injection. An analysis of this singularity has been performed by Catherall, Stewartson and Williams[23] who show that for laminar flow the singularity occurs at a value of mass injection very close to the value obtained for a

constant pressure mixing layer. (See, for example, Lock[28] and Chapman[24]). One would like to determine, then, whether a flow with (initially) constant pressure exists and rapidly "blows off" (exhibits a singular behavior) as injection is increased beyond a certain critical value, or whether a pressure gradient will be generated because of viscous-inviscid interactions which will prevent this blow-off and allow, instead, for a gradual transition to a flow where viscous forces are negligible everywhere except perhaps along a thin shear layer around the dividing streamline (the inviscid limit). Furthermore, for turbulent flow, if this latter result prevails, one would like to establish quantitative bounds on the regimes of injection rates for which mixing, both pressure gradient and mixing, and only pressure gradient determine the solution.

Hence, the question becomes one of determining what mechanism will generate the pressure gradient. One possibility is the effect of induced nose bluntness caused by injection from a leading edge, which would provide a falling pressure. However, for any fixed injection rate beyond the constant pressure "blowoff" value it seems that this effect could be minimized by making a porous section long enough so that eventually one would arrive back at the situation of constant pressure and an injection rate greater than that which can be tolerated by a constant pressure boundary layer. A second and more plausible mechanism involves the effect of termination of injection on the flow as a means of inducing a favorable pressure gradient. This effect should be similar to that experienced by a flow approaching a rapid expansion corner. This explanation seems more physically

appealing since the thickness of the layer itself near the end of injection is expected to be the dominant length scale in determining the upstream induced pressure field. Since the layer thickness is itself proportional to the plate length, this effect may not be as easy to negate simply by going to a longer injection region. This second mechanism is, therefore, investigated here for the turbulent case.

The difficulty involved in analyzing this problem stems from two main causes: the fact that any realistic analysis of this effect must involve a simultaneous solution of the coupled viscous and inviscid equations; and, secondly, the viscous layer in question is a compressible, turbulent flow, which possesses its own complications.

In order to incorporate the important interaction of the external (inviscid) and viscous flow, at least approximately, the integral approach proposed by Lees and Reeves[29] and extended later to turbulent wake flows by Alber[22] seems most promising. In turbulent flow additional complexity is added to the problem in that there is, in general, no strict one-parameter equivalent to the Falkner-Skan similarity solutions used by Lees and Reeves[29] to characterize the velocity profiles. Furthermore, a completely specified transformation is not available a priori to reduce the compressible flow equations to an equivalent incompressible form.

However, for large injection the experimental data obtained in Section II indicates that in the constant pressure region the velocity profiles and, hence, the integral functions which will appear in any moment-integral description, are well represented as a one-parameter

family. Under these conditions the effect of the viscous sublayer is negligible. That is, the effect of wall shear can be neglected. Lees and Chapkis[20] have employed this idea in formulating a theory for the constant pressure region which has successfully predicted the experimentally observed trends. Although their formulation employed an eddy viscosity model for the turbulent shear stress, this assumption is not essential and, in fact, is not made in the analysis which follows. What is assumed, however, is that even in the non-similar region near the end of injection a one-parameter representation of the flow profiles is adequate. This is the crucial assumption made in this analysis. Its only real justification must lie in the agreement of the theory with experimental observations.

With this assumption, the most logical source for the "similar solutions" which will be used to characterize the integral functions is the constant pressure experimental data itself. Use of this data obviates the need for an eddy viscosity model and provides the necessary information as to the effect of compressibility.

In summary, the approach to be taken involves a moment integral description of the flow assuming a one-parameter family of flow profiles which will be derived from the experimental data obtained in the constant pressure region. The effects of compressibility will also be deduced from the correlations of the present data with incompressible experiments in the constant pressure region. Using these assumptions, the attempt is made to predict the observed pressure field in the non-similar region near the end of injection.

Section III. 2 presents a derivation of the governing equations, and the compressibility transformation employed. Section III. 3 outlines the analytical approach used to treat the flow in the vicinity of the end of injection. Finally, in Section III. 4 the results of the computations are compared with the experimental data and conclusions are drawn for higher injection rates.

III. 2 Governing Equations

III. 2. 1 Derivation and Transformation of the Equations

The equations for the mean flow quantities are assumed to be the boundary-layer equations of a perfect gas (γ, C_p = constant) with a constant total temperature

$$(\rho u)_x + (\rho v)_y = 0 \tag{III. 1}$$

$$\rho u u_x + \rho v u_y = \tau_y - P_x \tag{III. 2}$$

$$P_y = 0 \tag{III. 3}$$

$$C_p T + u^2/2 = C_p T_e + U_e^2/2 = \text{constant} \tag{III. 4}$$

where the subscript e refers to quantities at the edge of the viscous layer. The assumption of constant total temperature is not a necessary one but is consistent with the data to be predicted (Section II).

Equations (III. 1) and (III. 2) and the equation obtained by multiplying equation (III. 2) by u are now integrated across the layer ($y = 0-\delta$) to give (for isentropic external flow)

$$\tan \Theta \equiv v_e/u_e = \frac{d\delta^*}{dx} + \frac{\delta^* - \delta}{\rho_e u_e} \frac{d}{dx} \rho_e u_e + \lambda_e \tag{III. 5}$$

$$\frac{1}{\rho_e u_e^2}\frac{d}{dx}(\rho_e u_e^2\theta) + \frac{\delta^*}{u_e}\frac{du_e}{dx} = \lambda_e[1 + C_f/2\lambda_e] \qquad \text{(III. 6)}$$

$$\frac{1}{\rho_e u_e^3}\frac{d}{dx}(\rho_e u_e^3\theta^{**}) + \frac{2}{u_e}\frac{du_e}{dx}\{\delta^* - \delta_u\} = \lambda_e\left[1 + \frac{2}{\lambda_e}\int_0^\delta \frac{\tau}{\rho_e u_e^2}\frac{\partial(u/u_e)}{\partial y}\,dy\right] \qquad \text{(III. 7)}$$

where subscripts e refer to quantities at the edge ($y = \delta$) and subscripts w refer to wall values, where $\lambda_e = \rho_w v_w/\rho_e u_e$, $C_f/2 = \tau_w/\rho_e u_e^2$ and where δ^*, δ_u, θ and θ^{**} are defined by

$$\delta^* = \int_0^\delta (1 - \frac{\rho u}{\rho_e u_e})dy, \quad \theta = \int_0^\delta \frac{\rho u}{\rho_e u_e}(1-u/u_e)dy$$

$$\theta^{**} = \int_0^\delta \frac{\rho u}{\rho_e u_e}(1-(u/u_e)^2)dy, \quad \delta_u = \int_0^\delta (1-u/u_e)dy \qquad \text{(III. 8)}$$

At this point, in equation (III. 6) it is assumed that in the blowing region $C_f/2\lambda_e \ll 1$ and this term is neglected. However, the last term in equation (III. 7) which represents the turbulent energy production is retained since mixing is assumed to be important in the layer, although wall shears are negligible.

Now equations (III. 5-III. 7) are to be transformed into an equivalent low-speed form in order to remove the implicit Mach number dependence from the integral properties appearing in the equations. In order to do this, define a variable $dY = \frac{a_e\rho}{a_2\rho_2}\,dy$, where the subscript (2) refers to some reference point in the flow (which will be taken to be the similar region upstream of the end of injection where $dP/dx = 0$).

Using this transformation and manipulating the equation, one obtains for constant total temperature

$$B\frac{d\delta_i^*}{dx} + \delta_i^*\frac{dH}{dx} + f\frac{\delta_i^*}{M_e}\frac{dM_e}{dx} = \frac{a_e\rho_e}{a_2\rho_2}\left[\frac{\tan\Theta}{m_e} - \frac{\lambda_e}{m_e}\right] \qquad \text{(III. 9)}$$

$$H\frac{d\delta_i^*}{dx} + \delta_i^*\frac{dH}{dx} + (2H+1)\frac{\delta_i^*}{M_e}\frac{dM_e}{dx} = \lambda_e\left(\frac{\rho_e a_e}{\rho_2 a_2}\right) \qquad \text{(III. 10)}$$

$$J\frac{d\delta_i^*}{dx} + \delta_i^*\frac{dJ}{dx} + \frac{3J\delta_i^*}{M_e}\frac{dM_e}{dx} = \lambda_e[1+R]\left(\frac{\rho_e a_e}{\rho_2 a_2}\right) \qquad \text{(III. 11)}$$

where $B = H + \frac{1+m_e}{m_e}$; $m_e = \frac{\gamma-1}{2}M_e^2$

$$f = \left[2 + \frac{\gamma+1}{\gamma-1}\left(\frac{m_e}{1+m_e}\right)\right]H + \left[\frac{M_e^2-1}{m_e(1+m_e)}\right]Z + \frac{3\gamma-1}{\gamma-2}$$

$$Z = \frac{1}{\delta_i^*}\int_0^{\delta_i} u/u_e\,dY; \quad J = \frac{1}{\delta_i^*}\int_0^{\delta_i} u/u_e(1-(u/u_e)^2)dY$$

$$\delta_i^* = \int_0^{\delta_i}(1-u/u_e)dY; \quad \theta_i = \int_0^{\delta_i} u/u_e(1-u/u_e)dY$$

$$H = \theta_i/\delta_i^*; \quad R = \frac{2}{\lambda_e}\int_0^{\delta_i}\frac{\tau}{\rho_e u_e^2}\frac{\partial(u/u_e)}{\partial Y}\,dY$$

Now it must be shown that the integral functions Z, J and R which appear in equations (III. 9-III. 11) are not implicitly dependent on Mach number.

This can be done by recalling the transformation of Coles[18] used in Part II

$$\overline{\psi} = \sigma(x)\,\psi \qquad \text{(III. 13)}$$

$$d\bar{x} = \xi(x)\, dx \tag{III. 14}$$

$$\bar{\rho}\, \partial\bar{y} = \eta(x)\, \rho\, \partial y \tag{III. 15}$$

where σ, ξ, η are three unknown scaling functions.* An immediate consequence of equations (III. 13-III. 15) was shown in Part II to be that at corresponding points in the flow for any $\eta(x)$, $u/u_e = \bar{u}/\bar{u}_e$. Since the quantities Z and J are formed by ratios of integrals over the transformed variable $\bar{Y}$ and the integrals involve only velocity ratios, $u/u_e = u/u_e$, these functions are already in a form independent of density effects and are independent of the choice of $\eta(x)$.

The argument for R is somewhat more complicated. In general, the quantity R which appears in equation (III. 11) does not transform in a simple manner. However, if the effect of wall shear can be neglected, as shown in Part II, equation II. 17-a, the quantity $\frac{\tau}{\rho_e u_e^2} \frac{1}{\lambda_e}$ is an invariant under the transformation (III. 13-III. 15) at corresponding stations for constant pressure flows. Then, the integral R is indeed independent of density or of the choice of $\eta(x)$. Hence, the integrals R, J and Z which appear in equations (III. 9-III. 11) are density invariant at corresponding points in the two flows.

The problem now becomes one of determining what is meant by "corresponding points." That is, what is the relationship between λ_e and $\bar{\lambda}_e$, the injection rates in the compressible and incompressible

---

*As pointed out by Coles[18], these equations make no assumption as to the nature of the shear stress function, τ, or of the energy equation. Their restriction lies in the assumption of boundary-layer equations. In order to specify the functions and hence the transformation, more information about these quantities is necessary.

flows?

This information is provided by the experimental data. As was shown in Part II, the velocity profiles for both the incompressible and compressible flows (u/u_e vs. $\bar{y}/\bar{\theta}$) can be shown to agree for large injection and constant pressure at $\lambda_e = \bar{\lambda}_e$, where λ_e, $\bar{\lambda}_e$ are the ratio of mass flow per unit area at the wall to that in the free stream for the compressible and incompressible flows, respectively. Hence, $\lambda_e = \bar{\lambda}_e$ characterizes the corresponding points in the two flows for large injection with

$$C_f/\lambda_e << 1 \; ; \qquad \bar{C}_f/\bar{\lambda}_e << 1$$

where C_f, $\bar{C}_f$ are the skin friction coefficients in the two flows.

Now, it is assumed that this relationship holds ($\lambda_e = \bar{\lambda}_e$) even when the pressure is not constant. That is, the compressibility transformation is not affected by the pressure gradient.

Furthermore, at this point it is assumed that the quantities Z, R and J appearing in equations (III. 9-III. 11) can be expressed as functions of one-parameter $H = \theta_i/\delta_i^*$, and that the functional dependence can be obtained from the constant pressure similar flow solutions (experiments). A one-parameter representation is valid if in this region there is only one scale to the problem. However, the region downstream of injection, where wall viscosity effects again become important probably requires a two-parameter presentation.

Finally, a relation between M_e and $\tan\Theta$ is needed to complete the set of equations. Following Lees and Reeves[29], since this is

expected to be an expansion starting from a uniform flow region, Prandtl-Meyer flow is assumed. Then, the relation between induced flow angle and Mach number is

$$\Theta(x) - \Theta(x_2) = \int_{M_e}^{M_2} \frac{\sqrt{M^2-1}}{1 + \frac{\gamma-1}{2}M^2} \frac{dM}{M} \qquad \text{(III. 16)}$$

where $\Theta(x_2)$ is the inviscid flow angle in the similar region, which can be calculated as shown in Part II (equation II. 20).

Equations (III. 9-III. 11) together with the relation (III. 16) and the definitions (III. 12) form a set of three ordinary differential equations for the three unknowns M_e, δ_i^*, H. Once these are obtained, the pressure and physical displacement thickness can be computed by standard methods.

It is important to note at this point that in the constant pressure region where H, M_e are constant, H is directly determined as a function of λ_e. In the non-similar region near the end of injection, however, the profile will be "unhooked" from λ_e. That is, the dependence of J, dJ/dH, Z, R on H is maintained, but now H is obtained from a solution of the three equations (III. 9-III. 11).

III. 2. 2 Evaluation of Integral Functions

In the similar flow regime, M_e, H = const., equations (III. 9-III. 11) reduce to

$$B \frac{d\delta_i^*}{dx} = \frac{\tan\Theta}{m_e} - \frac{\rho_w v_w}{\rho_2 u_2} \qquad \text{(III. 17)}$$

$$H \frac{d\delta_i^*}{dx} = \frac{\rho_w v_w}{\rho_2 u_2} \qquad \text{(III. 18)}$$

$$J \frac{d\delta_i^*}{dx} = \frac{\rho_w v_w}{\rho_2 u_2} [1 + R] \qquad \text{(III. 19)}$$

H, J, and Z are calculated from the measured velocity profiles with minimum error. However, a direct calculation of R is difficult since it involves differentiating experimental data. Therefore R was evaluated by combining equations (III. 18) and (III. 19) to give

$$J/H = 1 + R$$

or

$$R = J/H - 1 \qquad \text{(III. 20)}$$

so, for any H and J, R is determined.

Since there is some scatter in the experimental data for, say, H, J and Z in the similar region (see Part II), the results obtained have been approximated with a least square fit. dJ/dH was obtained by spline fitting the curve of J vs. H and then least square fitting the resulting derivatives. Figure III-1 presents the curve for H obtained from the data as a function of λ_e, the injection parameter. Figures III-2-III-5 present the quantities Z, J, $\frac{dJ}{dH}$ and R as a function of H obtained as indicated above.

A point worth mentioning at this stage is that if the eddy viscosity model proposed by Lees and Chapkis[20] is assumed, and the reference density is taken to be equal to the edge value, the only term which changes in equations (III. 9-III. 11) is R. For their formulation (see (20)),

$$R = \frac{K_\theta H R'}{\lambda_e}$$

where

$$R' = \delta_i^* \int_0^{\delta_i} G(Y/\theta_i) \left[\frac{\partial (u/u_e)}{\partial Y}\right]^2 dY$$

With an eddy viscosity formulation, R', J, can be obtained as a function of H from the resulting similar equation regardless of the value of K_θ. Then, if one uses the experimental curve of H vs. λ_e, K_θ can be obtained from

$$K_\theta(\lambda_e) = \frac{\lambda_e}{2H(\lambda_e)R'(H)} \left[\frac{J(H)}{H(\lambda_e)} - 1\right] \qquad \text{(III. 21)}$$

Figure III-6 presents the resulting curve obtained using the experimentally determined curve of H as a function of λ_e and the integral functions J and R' obtained from the similar solutions of Lees and Chapkis[20]. * It is interesting to note that K_θ thus obtained is a slight function of λ_e, and at high injection rates seems to be approaching the free shear layer value used by Lees[20] ($K_\theta \approx .06$). However, some caution is necessary at this point in interpreting this trend in K_θ, since a distribution function $G(Y/\theta_i)$ for the variation of the eddy viscosity across the layer was assumed, a priori, by Lees and Chapkis[20] in their formulation. The form chosen for this variation influences the value of K_θ obtained using equation (III. 25). Hence,

---

*Also included in Figure III-6 is the value of K_θ obtained by directly evaluating the eddy viscosity from the experimental data and taking K_θ to be the maximum value in the layer. In view of the errors involved in differentiating experimental data, the agreement can be considered quite good.

the approach taken from here on in is to use the integral functions determined as shown previously without employing an eddy viscosity model.

III. 3 Analytical Considerations

III. 3. 1 Subcritical-Supercritical Behavior of Equations

Under certain conditions the effect of a disturbance in a boundary layer can be felt upstream of the point of disturbance through the coupling of the inviscid pressure field and the viscous flow. Within the framework of the integral formulation, the flow can be divided into two regions, subcritical and supercritical. Subcritical flows exhibit an upstream sensitivity to disturbances while supercritical flows do not.

The boundary can be obtained by considering equations (III.9-III. 11) as a set of linear algebraic equations for the three derivatives

$$\frac{\delta_i^*}{M_e}\frac{dM_e}{dx} = \frac{N_1(M_e,H)}{D(M_e,H)} \qquad \text{(III. 22)}$$

$$\delta_i^*\frac{dH}{dx} = \frac{N_2(M_e,H)}{D(M_e,H)} \qquad \text{(III. 23)}$$

$$\frac{d\delta_i^*}{dx} = \frac{N_3(M_e,H)}{D(M_e,H)} \qquad \text{(III. 24)}$$

where, in this case

$$N_1 = \frac{a_e\rho_e}{a_2\rho_2}\frac{\tan\Theta}{m_e}(H_{J'}-J) + \lambda_{e_2}\frac{M_2}{M_e}\left\{\frac{1+m_e}{m_e} - \frac{(H_{J'}-J)}{m_e} - (B_{J'}-J)\right\} \qquad \text{(III. 25)}$$

$$+ R\lambda_{e_2}\frac{M_2}{M_e}\left(\frac{1+m_e}{m_e}\right)$$

$$N_2 = \frac{\tan\Theta}{m_e}\frac{a_e\rho_e}{a_2\rho_2}J(1-H) + \lambda_{e_2}\frac{M_2}{M_e}\left\{3JB-(2H+1)B+\frac{3HJ}{m_e}+fH-\frac{(2H+1)J}{m_e}-fJ\right\}$$

$$+ R\lambda_{e_2}\frac{M_2}{M_e}\{fH-B(2H+1)\} \qquad \text{(III. 26)}$$

$$N_3 = \frac{\tan\Theta}{m_e}\frac{a_e\rho_e}{a_2\rho_2}\{3J-J'(2H+1)\} + \lambda_{e_2}\frac{M_2}{M_e}\left\{(2H+1)-f(1-J')\right.$$

$$\left.-3J-\frac{(3J-(2H+1)J')}{m_e}\right\}$$

$$+R\lambda_{e_2}\frac{M_2}{M_e}\{2H+1-f\} \qquad \text{(III. 27)}$$

$$D = f\{HJ'-J\} - J(H-1) + B\{3J-(2H+1)J'\};\ \lambda_{e_2} = \rho_w v_w/\rho_2 u_2 \qquad \text{(III. 28)}$$

As shown by Lees and Reeves[29] and Klineberg[30], the curve $D(M_e, H) = 0$ is the dividing line between super- and sub-critical flows. For values of M_e, H on one side of this line the end of injection will have no calculable effect on the flow upstream of the termination and for values on the other side an effect will be observed. If the integral quantities are known as a function of H in equation (III. 28), then this dividing line can be obtained by iteration. Figure III-7 is a plot of the critical line for this flow. Since the problem under consideration starts with a similar flow, then initially, H is known as a function of λ_e and Figure III-8 shows the critical line in this manner. Finally, since the similar region is characterized by a straight shock (linear growth), then equation (III. 17) and (III. 18) can be combined to give the critical line in terms of freestream

values, $\lambda_\infty = \rho_w v_w / \rho_\infty u_\infty$ and M_∞, by using the shock relations to obtain $\Theta(x_2)$ and solving these equations by an iteration process. This is shown in Figure III-9. Note that in performing these calculations (Figures III-8 and III-9) the crucial step is to establish a relationship between H and λ_e. Hence, as is seen from Figure III-8 at $M_\infty = 2.6$, any $\lambda_\infty \gtrsim .007$ will result in a flow which has a finite region near the end of the porous plate that influenced by termination of injection.

With the subcritical nature of the flow established for a given free stream Mach number, the next question is how to obtain a solution to equations ((III. 22)-(III. 24)).

III. 3. 2 Analogy with Flow Around a Corner

The approach taken here is to note that in the case of subcritical flow past a sharp corner, (also a rapid expansion), Ko and Kubota[31] were very successful in approximating the flow field by assuming the moment equations possessed an integrable singularity at the corner. In reality, as shown by Victoria[32], the corner is the region where a transition from subcritical to supercritical flow occurs. Essentially, this observation means that in equations ((III. 22)-(III. 24)) Ko and Kubota allowed $D \to 0$ while N_1, N_2, N_3 remained finite. What really happens is that both D and $N_i \to 0$, but until one is very close to the corner $N_i/D \gg 1$. In view of the fact that the equations themselves are questionable in this region, the simpler approach of Ko and Kubota[31] is used in this analysis.

One expects the effect of the end of injection to be similar to that for a flow effectively approaching a sharp expansion corner. That is, for

an initially subcritical flow on the porous plate, the end of injection should cause a rapid expansion of the flow (an effective "corner"). Hence, consider solutions to equations ((III. 22)-(III. 24)) which possess integrable, sink-type, singularities in the gradients of M_e, H, δ_i^*. This should be a valid approximation *if the flow becomes supercritical very* near the end of injection.

III. 3. 3 Existence of a Singular Solution

Two questions have yet to be answered for the equations ((III.22)-(III. 24)) before the solutions can be obtained in a logical fashion. The first is whether solutions of the type required exist for these equations and the second is to establish a consistent method of obtaining these solutions numerically. Fortunately, the similarity between these equations and those treated by Ko and Kubota[31] make the answer to the first question quite straightforward to obtain. If one looks for solutions where

$$\frac{dM_e}{dx} \sim (L-x)^{-\alpha}$$

$$\frac{d\delta_i^*}{dx} \sim (L-x)^{-\beta} \qquad \text{(III. 29)}$$

$$\frac{dH}{dx} \sim (L-x)^{-\gamma}$$

near x = L, then requiring finite H_L, M_{e_L}, $\delta_{i_L}^*$ at x = L means that

$$0 < \alpha, \beta, \gamma < 1 \qquad \text{is necessary}$$

By linearizing the equations about H_L, M_{e_L}, $\delta_{i_L}^*$ it can be shown that to lowest order

$$\alpha = \beta = \gamma = \frac{1}{2}$$

Then

$$M_e = M_{e_L} - k_1 (L-x)^{\frac{1}{2}}$$

$$H = H_L - k_2 (L-x)^{\frac{1}{2}} \qquad \text{(III. 30)}$$

$$\delta_i^* = \delta_{i_L}^* + k_2 (L-x)^{\frac{1}{2}}$$

near x = L, where k_1, k_2 and k_3 are positive constants which can be obtained in terms of conditions at x = L. Hence, solutions with a sink type behavior exist for equations ((III. 26)-(III. 28)).

The second question involves the determination of a consistent perturbation procedure for obtaining these solutions starting with a similar flow (M_e, H = constant). In the vicinity of the end of injection, a small but relatively rapid change occurs in the boundary layer and the perturbation in the external flow must be considered simultaneously with that in the boundary layer. Assuming $\epsilon = (\frac{\gamma-1}{2})^2 M_2^3 \lambda_{e_2} << 1$, * then the analysis of Ko and Kubota[31] for laminar flow

---

*The assumption $[(\gamma-1)/2]^2 M_2^3 \lambda_{e_2} << 1$ is not as restrictive as it may first appear to be. For hypersonic flow, Lees[17] has shown that even for $M_\infty^3 \lambda_\infty >> 1$ the induced flow angle in the similar region, Θ, approaches a limiting value where $\Theta \sim \lambda_e^{1/3}$. Since in this case $M_2 \sim 1/\theta$, the quantity $[(\gamma-1)/2]^2 M_2^3 \lambda_{e_2}$ approaches a constant given by

$$\epsilon_{max} \rightarrow \left[\frac{\gamma(\gamma-1)}{2}\right]^{\frac{1}{2}}$$

For $\gamma = 1.4$, $\epsilon_{max} \approx .53$ which is still small compared to unity. Hence, this perturbation scheme can be expected to work for most of the Mach numbers and injection rates of interest.

can be directly applied to this problem. Assuming the change takes place over a small scale, let

$$\hat{x} = \frac{x-x_2}{\epsilon}$$

where $\hat{x}$ is assumed order 1; $x-x_2 << 1$. That is, assume the change takes place over a distance of order $M_2^3 \lambda_{e_2}$ which, for hypersonic flow with large injection, is of order (Mach number) x (boundary-layer thickness), so boundary-layer equations are still applicable. For supersonic flow, the dependence of boundary-layer thickness on Mach number is more complicated but is less than M_2^2. In this case, the validity of the boundary-layer equations may be questionable but they will be assumed to apply in the analysis.

Near the similar flow region (subscripts 2), let

$$\begin{aligned} \delta_i^* &= \delta_{i_2}^* + \lambda \hat{\delta} \\ H &= H_2 + \lambda \hat{H} \\ M_e &= M_2 + \lambda \hat{M} \end{aligned} \qquad \text{(III. 31)}$$

where $\lambda << 1$ and $\hat{}$ quantities are assumed of O(1). Then a substitution of (III. 31) into the equations ((III. 22)-(III. 24)) yields directly, to lowest order

$$\begin{aligned} \hat{\delta}/\delta_{i_2}^* &= -K\left[(1+2H_2)J_2' - 3J_2\right] \\ \hat{H} &= K\left[(1-H_2)J_2\right] \\ \hat{M}/M_2 &= K\left[H_2 J_2' - J_2\right] \end{aligned} \qquad \text{(III. 32)}$$

where K represents an arbitrary, but small, perturbation of the similar flow variables, H_2, M_{e_2}, $\delta^*_{i_2}$, i.e., Equation (III. 32) relates the change in any two variables if one is given small change. This result is the same as that obtained by Ko and Kubota[31] and Victoria[32] for laminar flow for weak interaction where $(\frac{\gamma-1}{2})^2 \frac{M_\infty^3}{\sqrt{Re_x}} = (\frac{\gamma-1}{2})^2 \chi << 1$ is assumed. The analogy to the corner solution of (31)(32) requires that in our case $(\frac{\gamma-1}{2})^2 M_2^3 \lambda_e << 1$. So, in flows with large injection, the analogue of χ is $M_e^3 \lambda_e$.

III. 4 Results

III. 4. 1 Numerical Solution and Comparison with Experiment

With the background presented, the equations ((III. 22)-(III. 24)) can now be integrated in a systematic way to the end of the porous plate. An important point to note in this problem is that, unlike the laminar flow case, in equations ((III. 22)-(III. 24)) N_1, N_2 and N_3 are only functions of M_e and H. Hence, the equations are invariant to an affine transformation $\tilde{x} = x/x_2$, $\tilde{\delta} = \delta_i^*/x_2$. This means that at the beginning of the integration x_2 can be chosen arbitrarily. Then, using the perturbations on δ_i^*, H, M_e from the similar solution, a solution is generated which has a proper behavior. Numerically this is accomplished by picking a positive value of K so that the solution obtained corresponds to an expansion (M_e, H increasing, δ_i^* decreasing).* At the point where, say $\frac{dH}{dx}$ gets larger than a predetermined number,

---

*Note also that since N_1, N_2, N_3 do not depend on δ_i^*, the equations can be solved without reference to the particular value of K chosen. That is, the effect of varying K can be scaled out of the solution as long as K is small so that the relations (equation 32) are valid.

the solution is continued by simply considering x as a function of H and inverting the integration procedure. Since neither N_1, N_2 or $N_3 \rightarrow 0$, the solution then proceeds smoothly. The singular point can then be rightly called the plate length, L. Computed pressure variations obtained in this way can be plotted solely as a function of x/L for any set of freestream Mach number and injection rate.

Solutions were obtained for three of the higher injection rates used in the experiments using a 7094 computer and standard integration routines. The results are shown in Figure III-10 and compared with the experimentally observed pressure distribution. The agreement is fairly good although significant $\frac{dP}{dy}$ were observed very close to the corner in the experiments and, of course, the equations do not provide for this. At the highest injection rate the theory seems to somewhat overpredict the observed pressure gradient. More importantly, the simple one-parameter representation seems to predict accurately the scale of upstream influence in pressure produced by termination of injection. In fact, for the highest injection rate a good portion of the plate is strongly influenced by the finite length effect. Figure III-11 presents a comparison between the observed and predicted variation of the form parameter, H. The disagreement in the region near the beginning of the porous plate is caused by the fact that in the experiment a finite thickness boundary layer is present at the start of injection while the theory assumes zero initial boundary-layer thickness. The observed initial variation in H is, then, the adjustment of the initial boundary layer to the injection. Conceivably,

this effect might be amenable to analysis using ideas similar to those employed herein.

III. 4. 2 Implication of the Analytical Results

If the analysis presented is plausible, then there are some rather startling conclusions. First, as indicated by the equations, for large injection where $C_f/\lambda_e << 1$, the solutions are functions only of x/L. This means that experimentally, a doubling of porous plate length will not decrease the fraction of plate influenced by this downstream effect. That is, since the similar layer grows linearly and since the only scale height in the equations is δ^*, the effect will scale with this height and thus always cover the same percentage of plate. Of course, the absolute length of similar region is increased but only in proportion to the length of plate. The second effect is shown more clearly in Figure III-12, where a parametric study has been performed for various injection rates. Here it becomes clear that, at least at $M_\infty = 2.6$, when $\lambda_\infty \approx 0.050$ which corresponds to $\lambda_e \approx .033$, virtually the entire plate is influenced by the pressure gradient produced by the termination of injection. This value of injection parameter approaches the entrainment rate of the incompressible constant pressure free shear layer (expected to be the "blowoff" value for the turbulent boundary layer). It is not expected that solutions would exist for constant pressure beyond this value. However, if qualitatively, at least, the turbulent flow solutions behave like the laminar ones, then the analysis presented in Part I would indicate that no singularity will be observed for any small negative pressure gradient and such a pressure gradient has been provided by the effect of

termination of injection.

Moreover, the laminar solutions of Part I indicated that for adiabatic flow at values of injection parameter about twice the value which would normally "blow off" the zero pressure gradient boundary layer, the lowest order asymptotic solutions (which are essentially an inviscid flow approximation) give a valid representation of the flow.* If the analogy can be stretched to the turbulent case, one would expect that at $M_\infty \approx 2.6$ for adiabatic flow, an inviscid flow model will adequately characterize the flow for $\lambda_\infty \gtrsim 0.1$ ($\lambda_e \gtrsim .06$). If the effect of compressibility observed on $M_\infty = 2.6$ can be used at very high Mach numbers, then at $M_\infty \gg 1$ for $\lambda_\infty \gtrsim 0.4$ ($\lambda_e \gtrsim .06$), the same should be true.** However, for injection rates this high at Mach numbers greater than 7 or 8, for adiabatic flow, the effect of the momentum of the injected gas will become important and may invalidate the neglect of $\partial p/\partial y$ in the analysis.

Hence, the analysis has provided the step which gives a quantitative estimate for the range of injection in turbulent flow where the effect of mixing can be neglected and inviscid flow models utilized. It also indicates that inviscid solutions for a semi-infinite plate with constant injection may not comprise a rational approximation to the

---

*For a cold wall, however, the effects of mixing will influence the flow to higher injection rates.

**It might be mentioned here that the above analysis is also applicable to laminar flow. In this case, one expects that the termination of injection will influence the flow for much smaller injection rates than mentioned herein, since the limiting value of entrainment for a laminar mixing layer is $O(1/\sqrt{Re})$.

physical flow. For constant injection, the proper limiting inviscid models would seem to be those which properly account for the discontinuity in boundary conditions which exists at the end of injection for any finite plate length. Perhaps this may explain the difficulties encountered by theoreticians who have attempted the former inviscid approach[34, 35] and the ease with which solutions are obtained by those who employ the latter[36, 37].

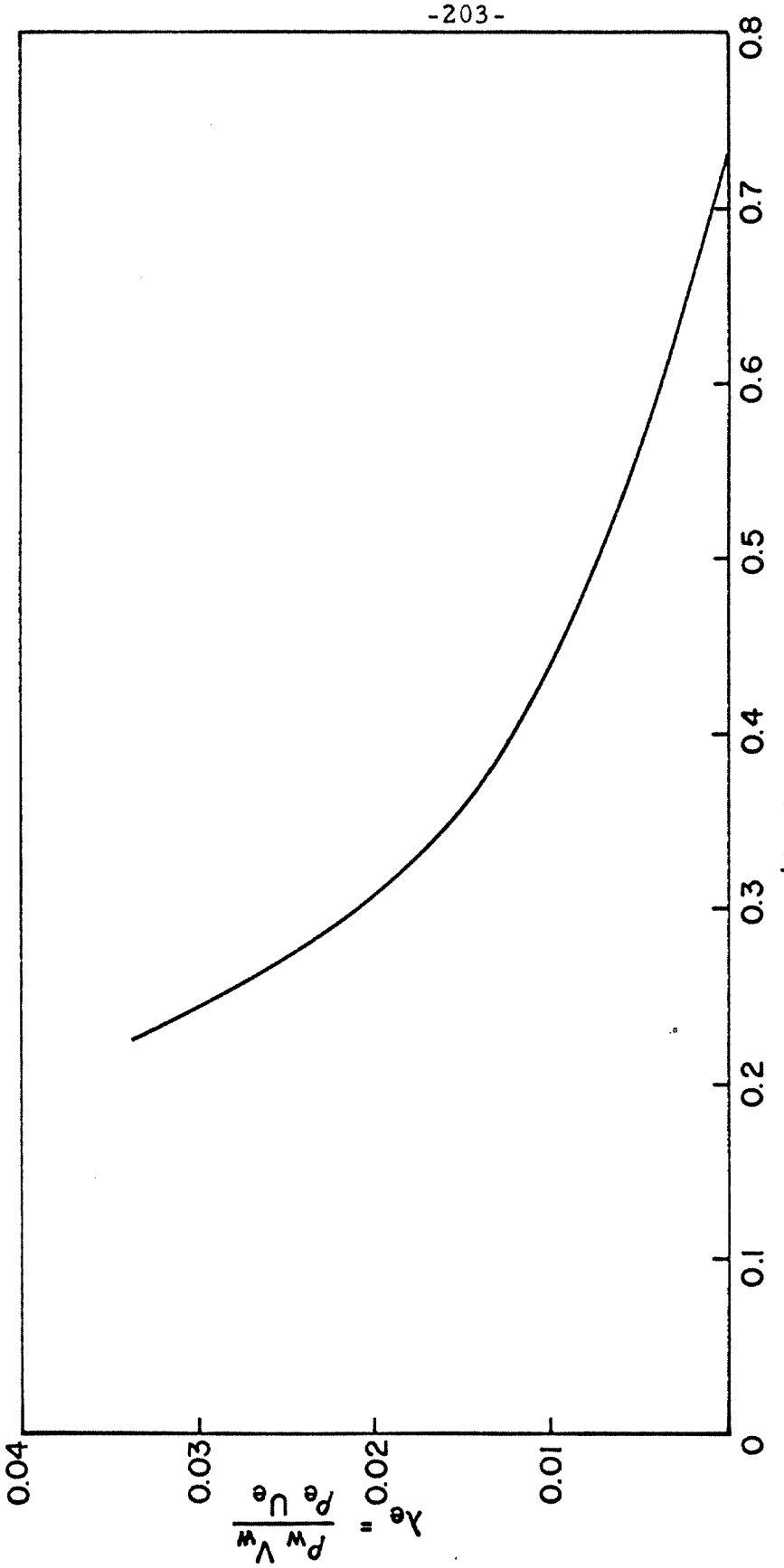

FIG. III.1 CURVE FIT OF DATA FOR $\mathcal{H}$ IN SIMILAR REGION

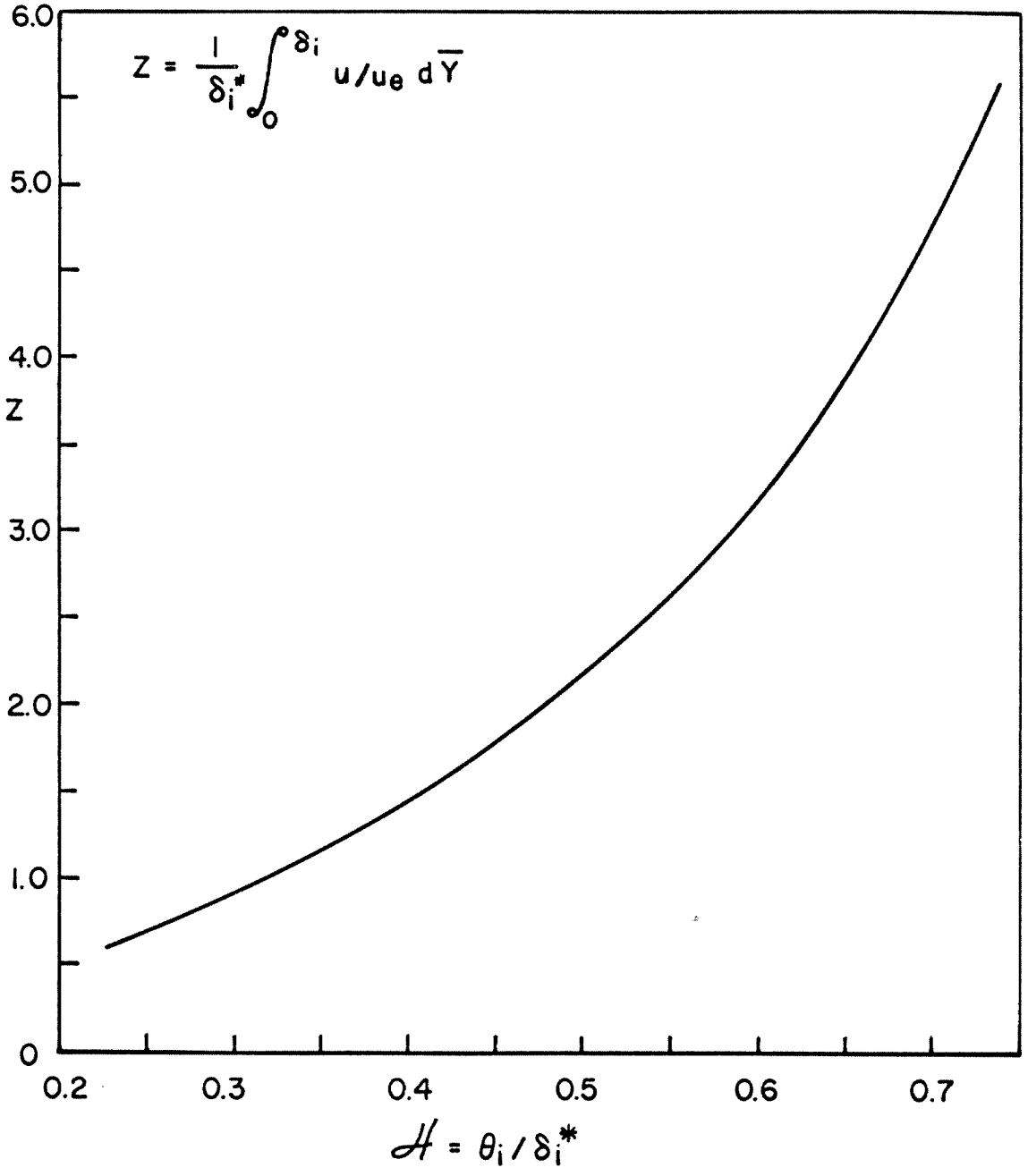

FIG. III.2 INTEGRAL FUNCTIONS, Z VS. $\mathcal{H}$

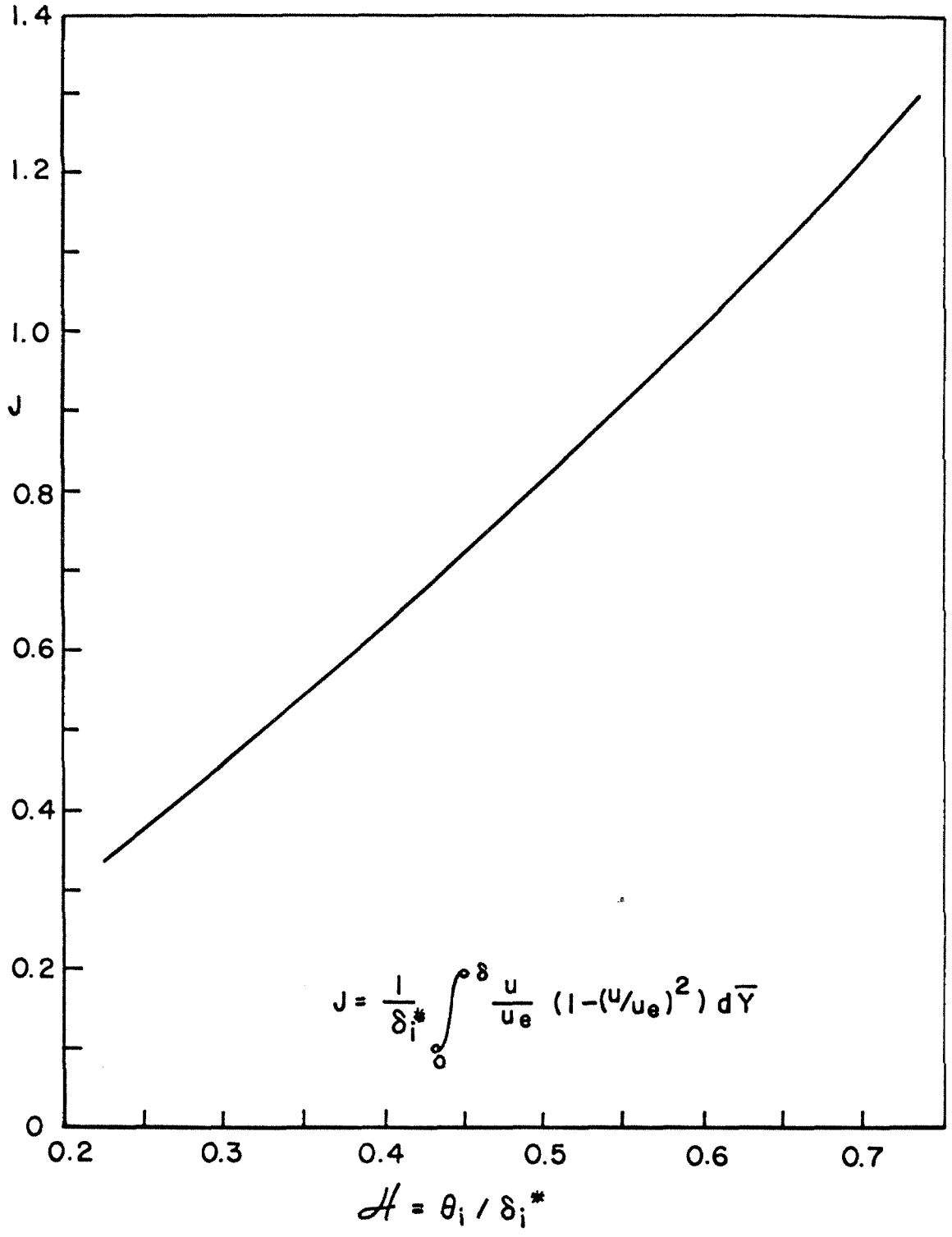

FIG.III.3 INTEGRAL FUNCTIONS ; J VS. $\mathcal{H}$

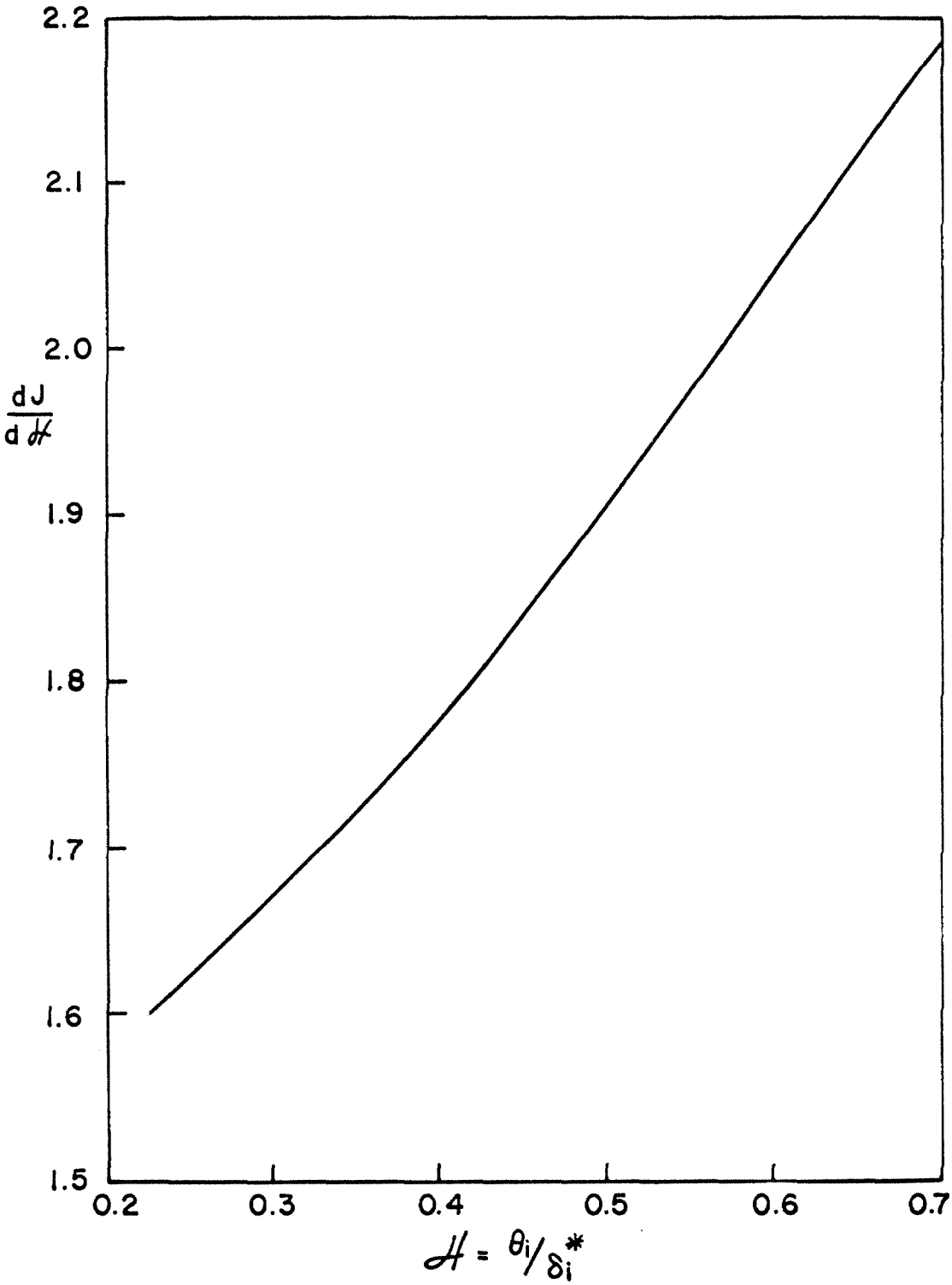

FIG III.4 INTEGRAL FUNCTIONS, $\frac{dJ}{d\mathcal{H}}$ VS $\mathcal{H}$

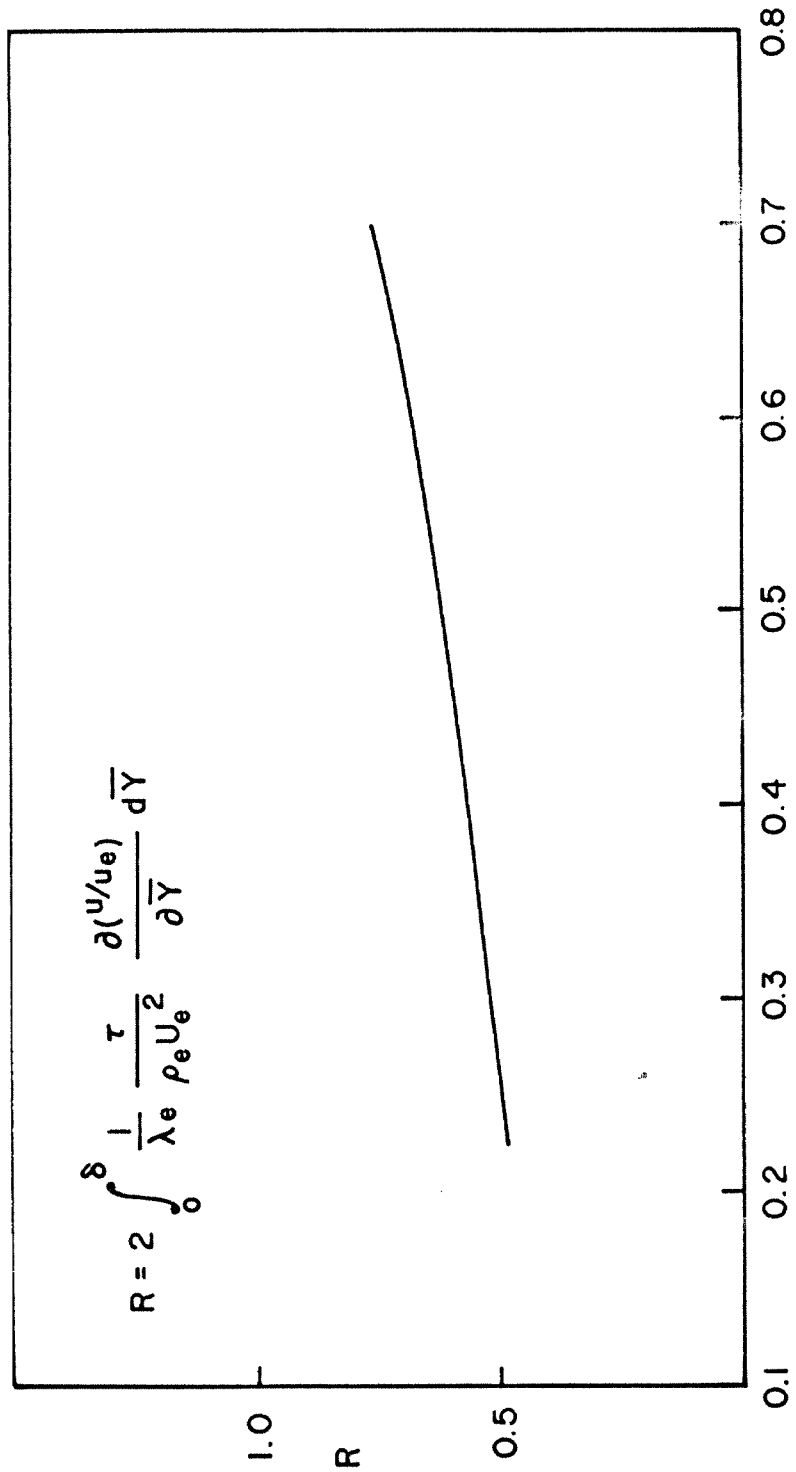

FIG. III.5 INTEGRAL FUNCTIONS, R VS $\mathcal{H}$

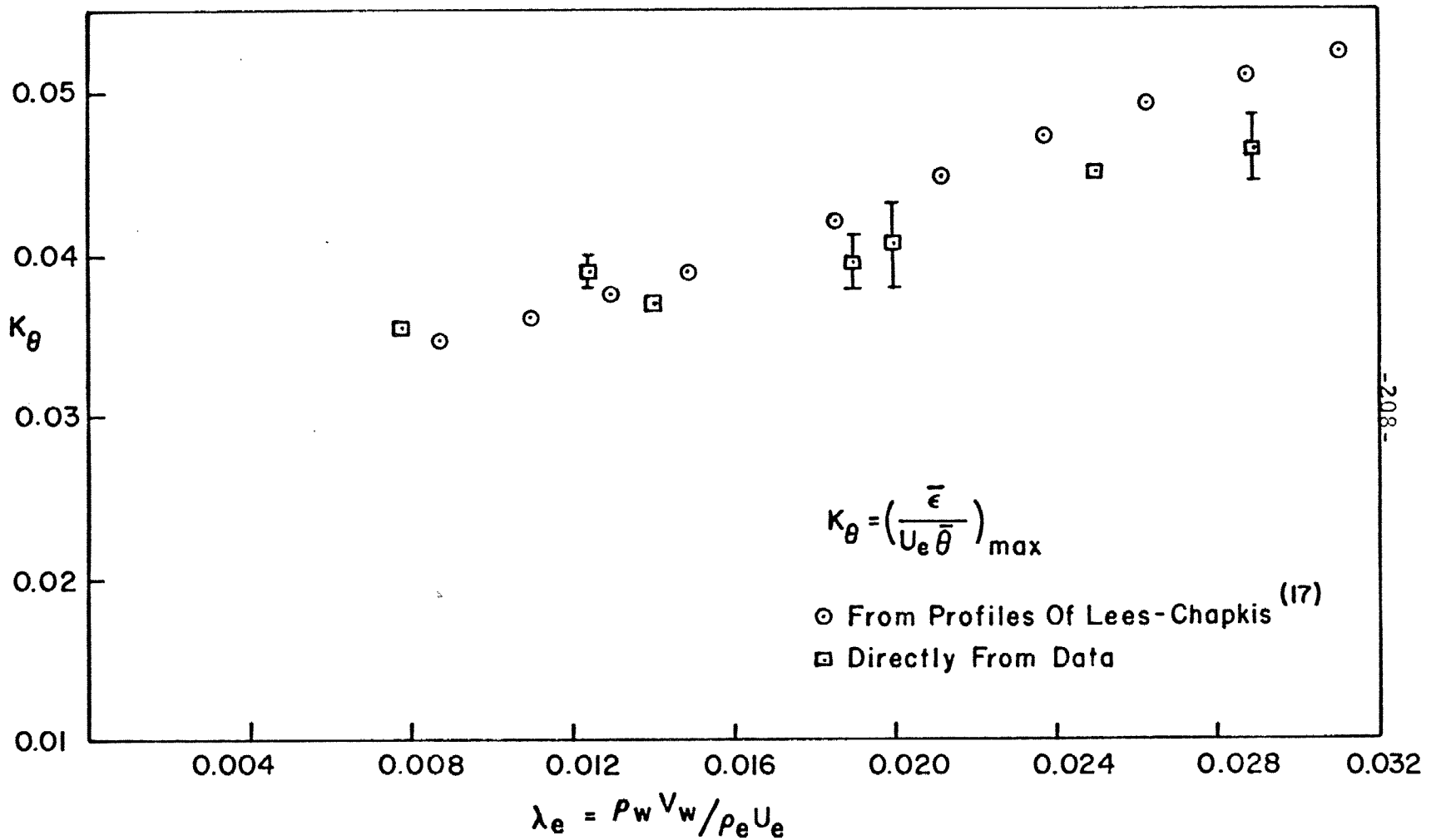

FIG III.6 VARIATION OF K_θ WITH λ_e

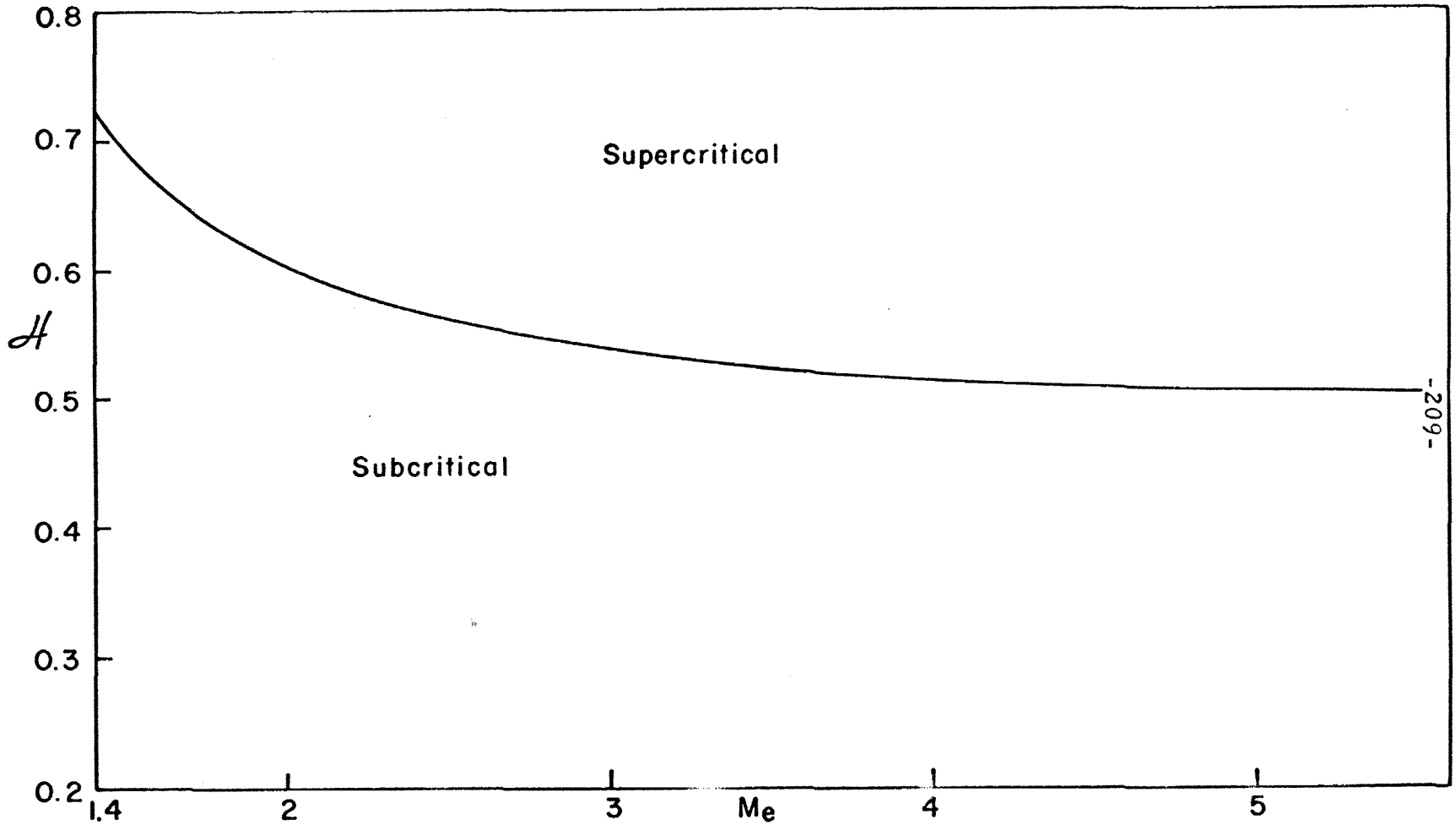

FIG.III.7 CRITICAL LINE
$D(Me, \mathcal{H}) = 0$

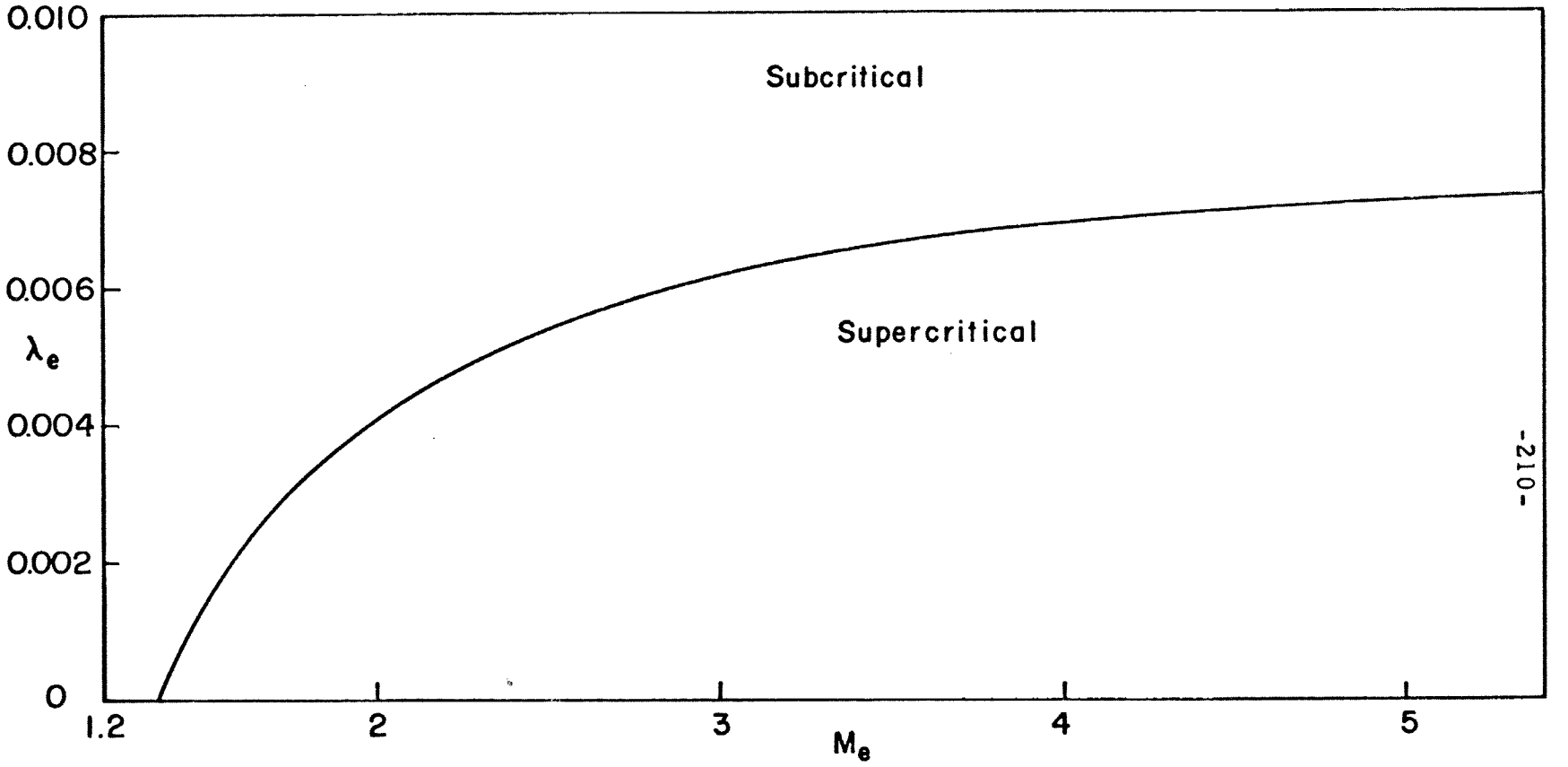

FIG.III.8 CRITICAL LINE

$D(M_e, \# = 0)$

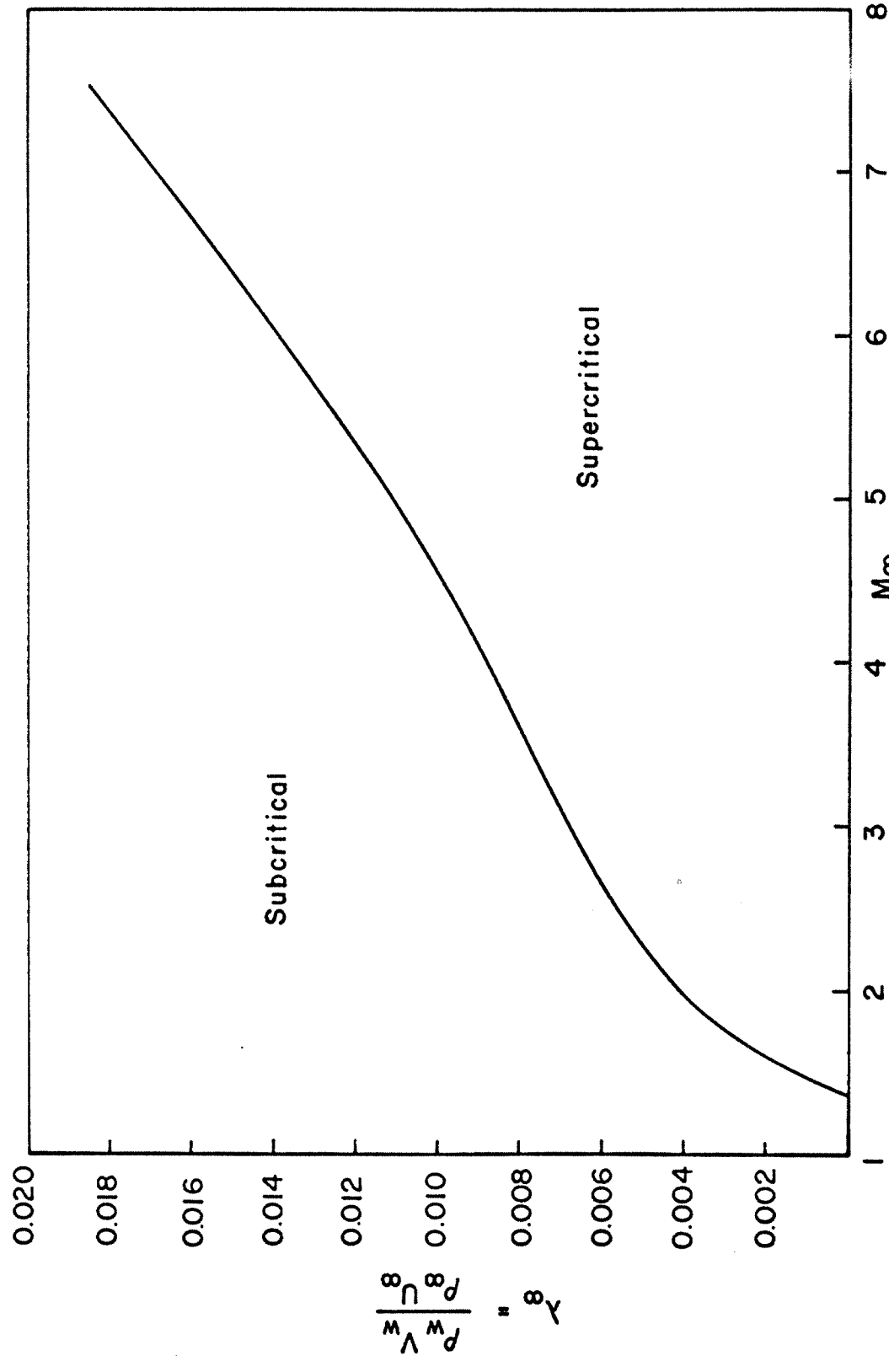

FIG.III.9 CRITICAL LINE
$D(M_e, \mathcal{H}) = 0$

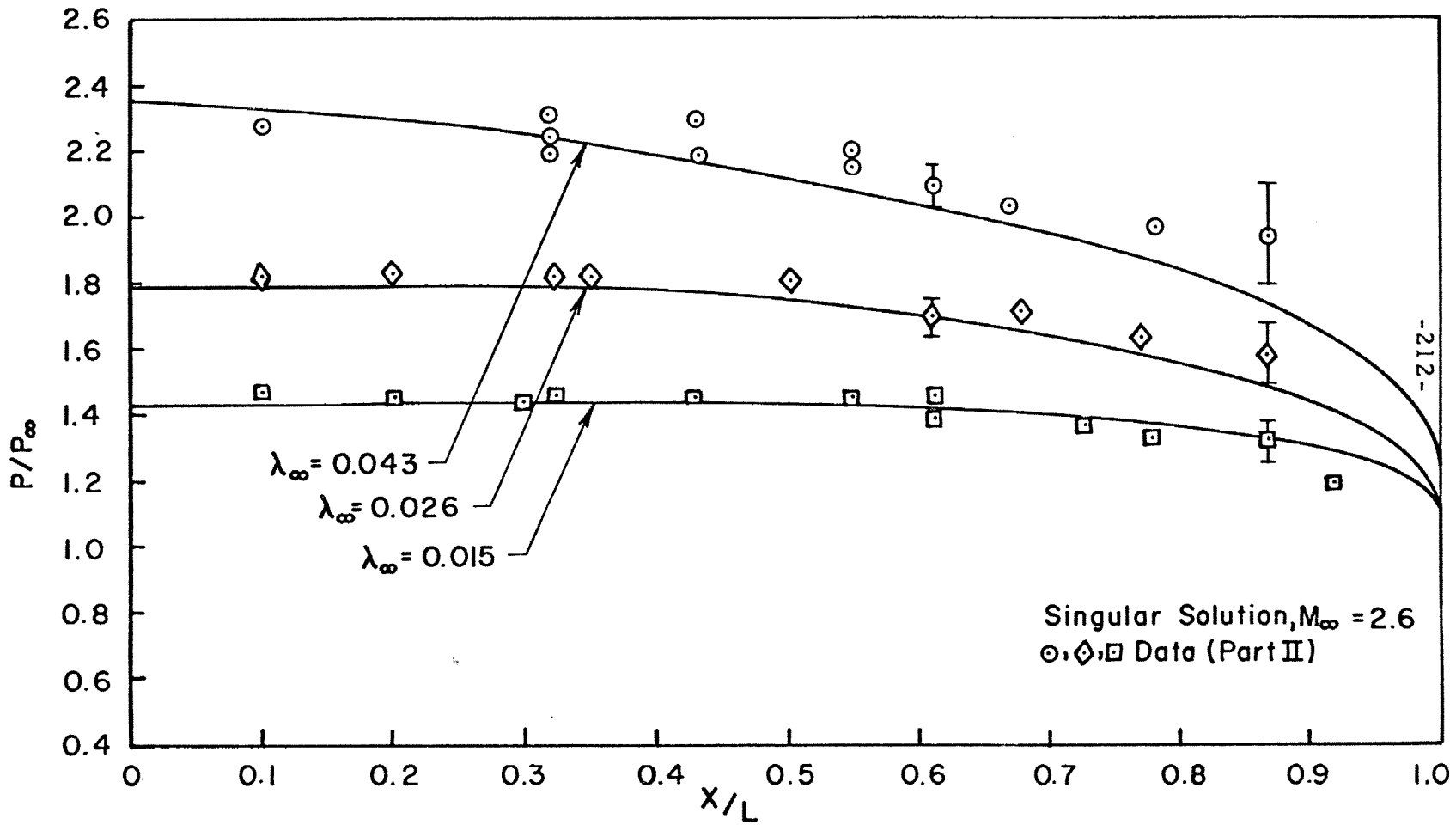

FIG. III.10 COMPARISON OF SINGULAR SOLUTION WITH DATA

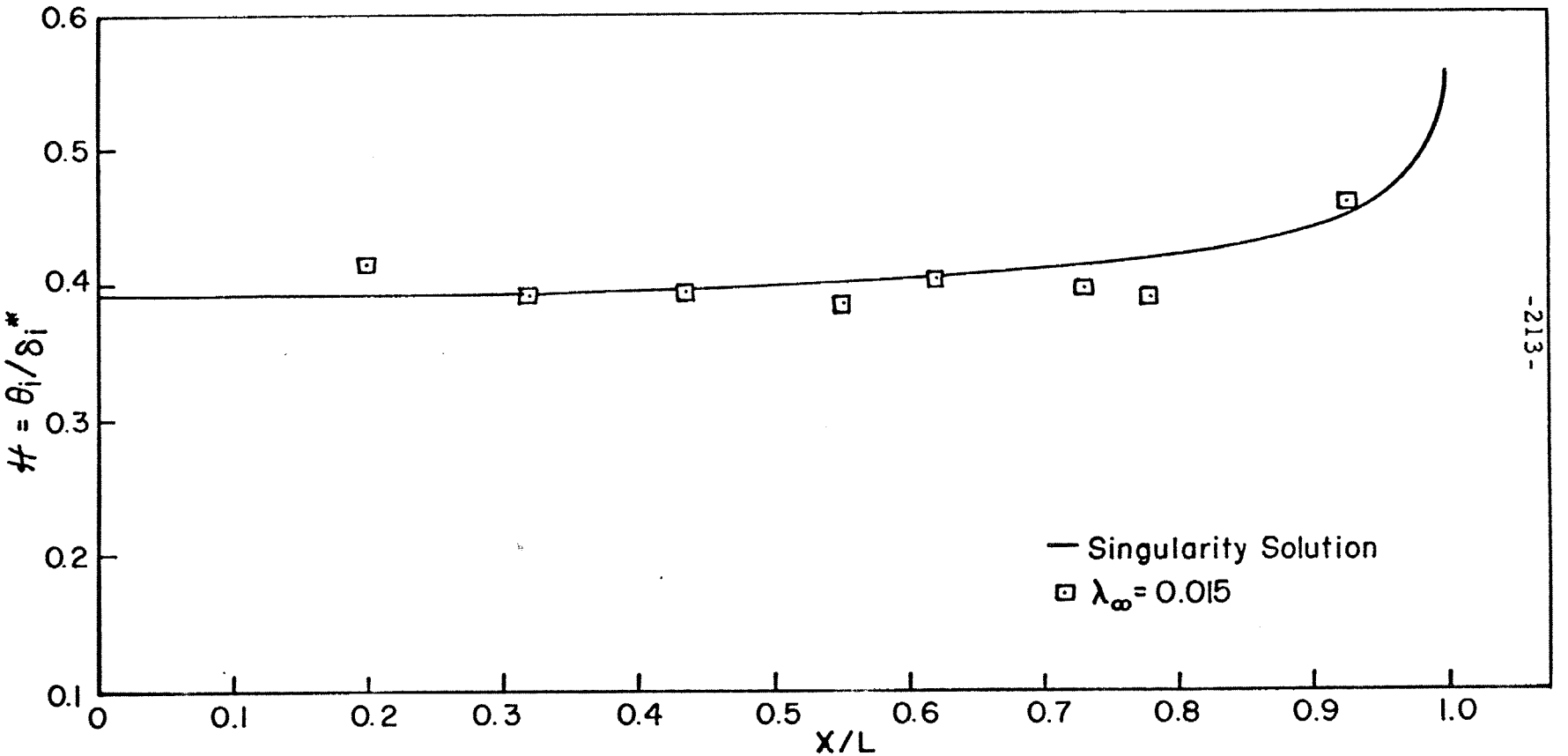

FIG.III.11 COMPARISON OF FORM PARAMETER
$M_\infty = 2.6$

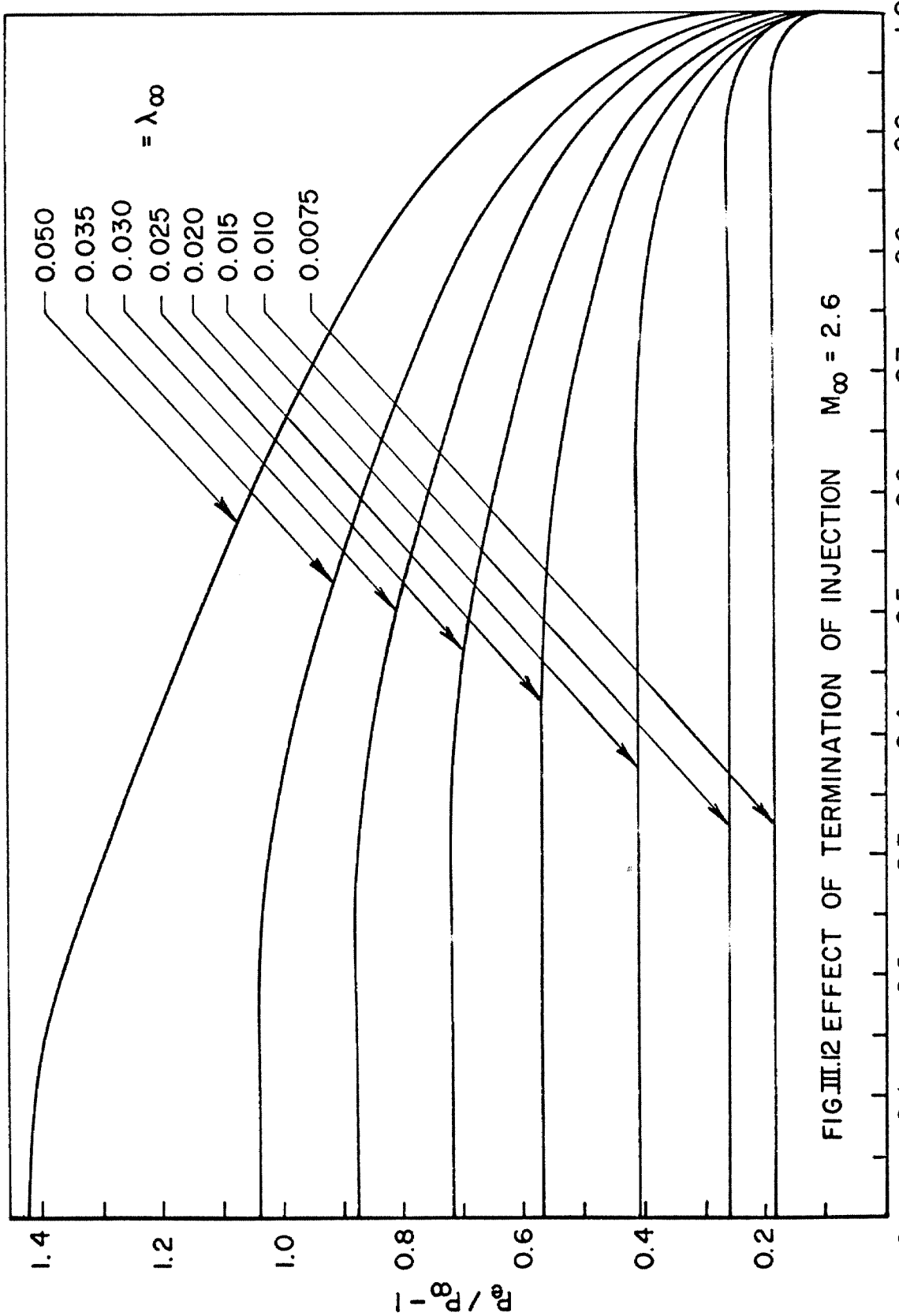

FIG. III.12 EFFECT OF TERMINATION OF INJECTION

REFERENCES

1. Pretsch, J., "Analytic Solutions of the Laminar Boundary Layer with Asymptotic Suction and Injection," Z. Angew. Math. Mech., 24, 264-267 (1944).

2. Aroesty, J. and Cole, J. D., "Boundary Layer Flows with Large Injection Rates," RAND Corp. Memo #RM-4620-ARPA (August 1965).

3. Lees, L., "Laminar Heat Transfer over Blunt Nosed Bodies at Hypersonic Speeds," Jet Propulsion 26, 259-269 (1956).

4. Cohen, C. B. and Reshotko, E., "Similar Solution for the Compressible Laminar Boundary Layer with Heat Transfer and Pressure Gradient," NACA TN 1295 (1956).

5. Libby, P. A., "The Homogeneous Boundary Layer at an Axisymmetric Stagnation Point with Large Rates of Injection," J. Aerospace Sci. 29, 48-60 (1962).

6. Radbill, J. R., "Application of Quasilinearization to Boundary Layer Equations," AIAA J. 2, 1860-1862 (1964).

7. Libby, P. A. and Chen, K. K., "Remarks on Quasilinearization Applied in Boundary Layer Calculations," AIAA J. 4, 937 (1966).

8. Hartunian, R. A. and Spencer, D. J., "Experimental Results for Massive Blowing Studies," AIAA Journal, Vol. 5, No. 8 (August 1967), pp. 1397-1401.

9. McQuaid, J., "Incompressible Turbulent Boundary Layers with Distributed Injection," Ph. D. Thesis, Engineering Department

Cambridge University (September 1966).

10. Simpson, R. L., Kays, W. M. and Moffat, R. J., "The Turbulent Boundary Layer on a Porous Plate: An Experimental Study of the Fluid Dynamics with Injection and Suction," Stanford University Rept. #HMT-2, M. E. Dept.

11. Mugalev, V. P., "The Experimental Investigation of the Subsonic Turbulent Boundary Layer on a Plate with Injection," Izvestiia Vysshikh Uchebnykh Zavedonii; Ayiationnaya Tekhnika, No. 3 (1959), pp. 72-79 (translated by J. B. Gazley), Rand Corp. Report T-142 (Dec. 8, 1960).

12. Mugalev, V. P., "Experimental Investigation of Turbulent Boundary Layers on a Plate in Supersonic Flow in the Presence of Injection of Air and CO_2. Fiziko-Takhmkeskii Institut v trudy, Moscow v. 4, 1959, pp. 152-171.

13. Segal, A., Calif. Inst. of Tech., Private Communication.

14. Zukoski, E. E., "Turbulent Boundary Layer Separation in Front of a Forward Facing Step", AIAA Journal (Oct. 1967), vol. 5, #10, pp. 1746-1753.

15. Emanuel, G. and Jones, J. P., "Compressible Flow through a Porous Plate", Aerospace Corp. Rept. #SSD-TR-66-165 Aug. 1966.

16. Behrens, W. H., "Flow Field and Stability of the Far Wake Behind Cylinders at Hypersonic Speeds," Ph. D. Thesis, Calif. Inst. of Tech., 1966.

17. Liepmann, H. W. and Laufer, J., "Investigation of Free Turbulent Mixing," NACA TN 1257 (August 1947).

18. Coles, D. F., "The Turbulent Boundary Layer in a Compressible Fluid," Rand Corp. Report R-403-PR (September 1962).

19. Danberg, J. E., "Characteristics of the Turbulent Boundary Layer with Heat and Mass Transfer", NOLTR 67-6, Jan. 23, 1967.

20. Lees, L. and Chapkis, R., "Surface Mass Injection at Supersonic and Hypersonic Speeds as a Problem in Turbulent Mixing: Part I Two Dimensional Flow", Paper #68-130 AIAA 6th Aerospace Science Meeting (submitted for publication, AIAA Journal).

21. Spaid, F. and Zukoski, E. E., "A Study of the Interaction of Gaseous Jets from Transverse Slots with Supersonic External Flow," AIAA Journal, vol. 6, #2, Feb. 1968, pp. 205-212.

22. Alber, I. E., "Integral Theory for Turbulent Base Flows at Subsonic and Supersonic Speeds," Ph. D. Thesis, Aeronautics Department, California Institute of Technology (May 1967).

23. Catherall, D., Stewartson, K., Williams, P. G., "Viscous Flow Past a Flat Plate with Uniform Injection," Proc. Roy. Soc. of London, Series A, vol. 284, March 1965.

24. Chapman, D. R., "Laminar Mixing of a Compressible Fluid," NACA TN 1800 (1949).

25. Maydew, R. C. and Reed, J. F., "Turbulent Mixing of Axisymmetric Compressible Jets (in the Half-Jet Region) with Quiescent Air", N-63-14202, March 1963.

26. Sirieix, M., Solignac, J. L., "Contribution a l'Etude Experimentale de la Couche de Melange Turbulent Isobare d'un Ecoulement Supersonique," Onera PP #327, 1960.

27. Taylor, G. I., J. A. S. 25 (1958) p. 464.

28. Lock, R. C., "The Velocity Distribution in the Laminar Boundary Layer between Parallel Streams," Quarterly J. Mechanics and Appl. Math 4, 42-63 (1951).

29. Reeves, B. L. and Lees, L., "Supersonic Separated and Reattaching Laminar Flows. I. General Theory and Application to Adiabatic Boundary-Layer/Shock Wave Interaction," AIAA J. 2, 1907-1920 (1964).

30. Klineberg, J. M., "Theory of Laminar Viscous-Inviscid Interaction in Supersonic Flow", Ph. D. Thesis, Calif. Inst. of Tech., June 1968.

31. Ko, D. R. S. and Kubota, T., "Supersonic Laminar Boundary Layer Along a Two-Dimensional Adiabatic Curved Ramp," AIAA Paper 68-109, 6th Aerospace Sciences Meeting, June 1968.

32. Victoria, K., Private Communication.

33. Sandborn, V. A. and Liu, C. Y., "On Turbulent Boundary Layer Separation," JFM (1968), vol. 32, part 2, pp. 293-304.

34. Emanuel, G., "Blowing from a Porous Cone or Wedge when the Contact Surface is Straight," Aerospace Corp. Rept. #SSD-TR-66-128, July 1966.

35. Wallace, J., Kemp, N., "Analytic Solutions to the Massive Blowing Problem. Part II: Skin Layer Analysis with Constant Blowing," AIAA Paper 68-128, 6th Aerospace Sciences Meeting, Jan. 1968.

36. Taylor, T. D., "Supersonic Flow Past a Finite Cone with Large Surface Injection or Ablation," U. S. Army AMC 68-37, April 1968, TR 3711.

37. Thomas, P. D., "Compressible Flow over a Finite Flat Plate with Massive Blowing," Lockheed Palo Alto Res. Labs. #61-78-68-8, March 1968.

38. Whittaker, E. T. and Watson, G. N., Modern Analysis, Cambridge University Press, London, 1963.

39. Muzzy, R. J., "Surface Mass Addition into a Turbulent Boundary Layer", AIAA Journal, vol. 5, #5, pp. 1029-1032.

40. Bradshaw, P., "The Turbulence Structure of Equilibrium Boundary Layers", JFM, vol. 29, part 4, Sept. 1967, pp. 625-647.